Università degli Studi di Udine
Dipartimento Politecnico di Ingegneria e Architettura

PhD Thesis

Investigation and Development of CMOS Pixelated Nanocapacitor Biosensors for Quantitative Analyses

Author:
Andrea Cossettini

Supervisor:
Prof. Luca Selmi

PhD Cycle XXXI
March, 2019

To my family...

Abstract

Dramatic health gains are expected to be established by year 2035, both for developing and already-developed countries. *Global Health* is, on one hand, a process of a worldwide development aimed at extending healthcare to developing countries and guaranteeing medical care for all; on the other hand, it also concerns the aging of populations in wealthy countries. In fact, by year 2050 almost all regions of the World will have nearly 25% of their population aged over 60 years, and quality of life will increasingly depend on a paradigm shift from *reactive* to *preventive* healthcare.

Substantial improvements and scalable transformations in Health and Care are enabled by technology advancements. *Nanotechnologies* play a key role in this respect, since they offer numerous pathways of innovation from monitoring to detection, from prevention to therapies and drug deliveries. The development of *personalized medicine* and *Lab-on-a-chip* solutions requires lots of data from patients and from the surrounding ambient, thus demanding *trillions* of sensors with low cost, low power, unobtrusive operation, and high accuracy properties.

Within this framework, engineered sensor solutions for life-sciences applications lead to the concept of *nanobiosensors.* This is the context of the present work. Among the large variety of alternative implementations, we focus on *electronic* nanobiosensors based on CMOS technology, and specifically on a 90-nm CMOS chip fabricated by NXP Semiconductors which implements massively-parallel high-frequency impedance spectroscopy sensing at nanoelectrode arrays, enabling the detection and imaging of nanoscale analytes in electrolytes and up to physiological salt concentration. While proof of concept demonstrations of the detection of many different analytes have been given with this platform, *quantitative* analyses of the results and detailed understanding of the measurement dependencies in the system parameters were still lacking. It was the purpose of this thesis to develop and improve methods, models, characterization and analysis techniques to enable not merely qualitative but dependable *quantitative* analyses with nanoelectrode biosensors.

This thesis documents my research activity on nanoelectrode impedance spectroscopy biosensors, in collaboration with NXP Semiconductors, the University of Twente, and TU–Wien, spanning from modeling and simulations to calibrations, from experimental testing and characterization to statistical analyses. A temperature-controlled microfluidic test setup is implemented for the biosensor chip from NXP, together with calibration/compensation procedures that enable unprecedented agreement between high-frequency impedance spectroscopy simulations and experiments at nanoelectrodes in electrolyte. Then, experiments are combined with detailed modeling/simulations of the nanoelectrode response to a variety of analytes, including dielectric/conductive microparticles, nanoscale charged particles and viruses. These analyses enable the quantitative understanding of peculiar features of the nanoelectrode response to analytes. Finally, advanced Bayesian statistics approaches are used to estimate parameters of the nanoelectrodes and of the analytes.

Contents

Terminology

Abbreviations and acronyms

ADC	Analog-to-Digital Converter
AFM	Atomic Force Microscope
BE	Bayesian Estimation
BSA	Bovine Serum Albumin
CBCM	Charge Based Capacitance Measurement
CCMV	Cowpea Chlorotic Mottle Virus
CDS	Correlated Double Sampling
CE	Counter Electrode
CL	Compact Layer
CMOS	Complementary Metal-Oxide-Semiconductor
CMP	Chemical Mechanical Planarization
CMV	Cucumber Mosaic Virus
CVFEM	Control Volume Finite Element Method
CSP	Compression Spring Probe
DAC	Digital-to-Analog Converter
DDS	Direct Digital Synthesis
DNA	DeoxyriboNucleic Acid
EDL	Electrical Double Layer
EIS	Electrochemical Impedance Spectroscopy
ENBIOS	Electronic Nano-BIOsensor Simulator
FWHM	Full Width Half Maximum
FPGA	Field Programmable Gate Array
HAV	Hepatitis A Virus
HFIS	High-Frequency Impedance Spectroscopy
ID	Inner Diameter
IID	Independent and Identically Distributed
ILT	Inverse Laplace Transform
IoE	Internet-of-Everything
IoT	Internet-of-Things
IPA	Isopropyl Alcohol
ISFET	Ion Sensitive Field Effect Transistors
KCL	Kirchhoff's Current Law
KDE	Kernel Density Estimator
LoC	Lab on a chip
LoD	Limit of Detection
LP	Low Power
LT	Laplace Transform

MC	Monte Carlo
MCMC	Markov-Chain Monte Carlo
MOS	Metal-Oxide-Semiconductor
MOSFET	MOS Field Effect Transistor
NTC	Negative Temperature Coefficient
OD	Outer Diameter
PB	Poisson-Boltzmann
PDD	Poisson-Drift-Diffusion
PDF	Probability Density Function
PDMS	Polydimethylsiloxane
PEEK	Polyether Ether Ketone
PID	Proportional–Integral–Derivative
PNP	Poisson-Nernst-Planck
RE	Reference Electrode
RHDV	Rabbit Haemorrhagic Disease Virus
RNA	Ribonucleic Acid
RTN	Random Telegraph Noise
SEM	Scanning Electron Microscope
SNR	Signal-to-Noise Ratio
ssRNA(+)	positive-sense single-strand(ed) RNA
UQ	Uncertainty Quantification
WE	Working Electrode

Symbols

C_A	Small-signal AC capacitance
C_E	Electrolyte spreading capacitance
C_{eff}	Effective capacitance computed from admittance modulus
C_F	Effective capacitance computed from Fourier-expansion of the input waveform
C_M	Measurement capacitance
C_P	Parasitic capacitance
C_{post}	Post-calibrated measurement capacitance
C_S	Surface capacitance
C_{SW}	Switching capacitance computed from idealized square waveforms
$C_{\square_{w/\ analyte}}$	$C_\square$ capacitance in the presence of the analyte ($\square$ denotes any above subscript)
$C_{\square_{w/o\ analyte}}$	$C_\square$ capacitance in absence of the analyte
G_A	Small-signal AC conductance
λ_D	Static Debye's length
R_E	Electrolyte spreading resistance
ω	Angular frequency

Notation

$\Delta C_{\square} = C_{\square_{w/\ analyte}} - C_{\square_{w/o\ analyte}}$	$C_{\square}$ capacitance variation upon introduction of the analyte ($\square$ can be any of the capacitance subscripts: E, eff, SW, ...)

Physical constants

ε_0	Dielectric constant of vacuum	8.854188×10^{-12}	$\mathrm{CV^{-1}m^{-1}}$
k_B	Boltzmann's constant	1.380649×10^{-23}	$\mathrm{JK^{-1}}$
N_A	Avogadro's number	6.022141×10^{23}	$\mathrm{mol^{-1}}$
q	Absolute value of electron charge	1.602176×10^{-19}	C

1 Introduction

> *"By 2035, there will be almost no poor countries left in the world."*[1]
>
> Bill Gates, *Gates Annual Letter* (2014) [1]

Poor countries are not doomed to stay poor: incomes, as well as other measures of human welfare, are rising everywhere (Africa included). In fact, the world is no longer separated into the West and the rest as in the past (Fig. 1.1), and the percentage of *very poor people* has more than halved since 1990 [1] (where extreme poverty is defined by the World Bank as living with less than US$1.90 a day, adjusted for price differences between countries and adjusted for inflation [2], see also Fig. 1.2).

---

[1] Specifically, it is meant that by 2035, almost no country will be as poor as any of the 35 countries that the World Bank classifies as low-income today, even after adjusting for inflation.

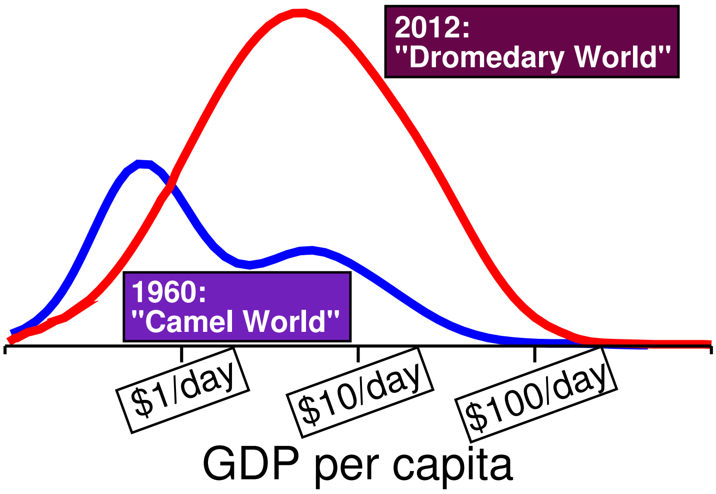

Figure 1.1: *Poverty distribution in 1960 and nowadays (2005 purchasing power parity). 50 years ago, the distribution of income looked like a "camel" with two humps, representing the developing countries and the wealthier ones. Today's world is different: more than a billion people have risen out of extreme poverty and wealth takes the shape of a centered "dromedary"-like distribution [1].*

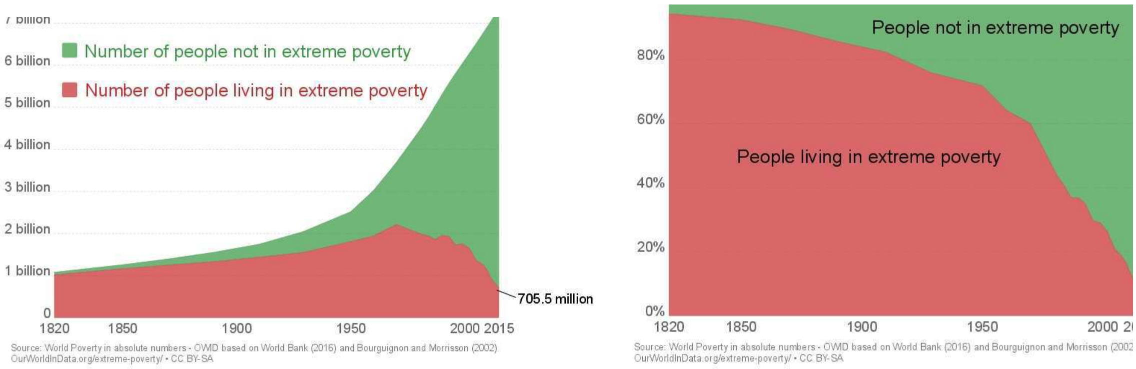

Figure 1.2: *World population living in extreme poverty (1820-2015) (images adapted from [3]). Extreme poverty is defined as living with an income lower than US\$1.90 per day (\$ adjusted for price differences between countries and adjusted for inflation). Left: absolute values. Right: relative values.*

This prediction of overcoming extreme poverty is strongly linked to and foresees a world of *Abundance*. We can define *Abundance* [4] as the World:

- without hunger;
- with medical care for all;
- with clean water and air for all;
- with clean energy for all.

A task for medical-care-for-all is to guarantee proper medical tools and assistance also to the developing countries, where health care infrastructures and deployment may be missing. This is part of a bigger picture, which entails improvements for both developing countries and for the already-developed ones, namely **Global Health**. Together with the envisioned eradication of extreme poverty, which goes along with the combination of all 4 ingredients mentioned above, Global Health entails that dramatic health gains are also expected to be established by 2035 [5].

Global Health is expected to benefit a lot from the technical innovations coming with the pursuit of Abundance. Technical Revolutions identify the shifting of the global Gross Domestic Product (GDP) leaders, which can be summarized as [6]:

- in the 18th century, GDP depended on the size of population (China/India were dominating);
- the 1st Technical Revolution provided steam, internal combustion, electricity, aeronautics, radio (Europe dominated the global GDP);
- with the 2nd Technical Revolution, transistors, computers, and Internet came into place (US and Japan became the leaders);
- the 3rd Technical Revolution fuses computing, communication, and sensing (people are freed from manual labor, and can focus on creative work).

Abundance is enabled by the 3rd *Technical Revolution* and it is expected to be reached in one generation (20 years). It is estimated that, among others, Abundance will generate the need for approximately **45 trillion sensors** [6, 7], many of which are not yet developed: this highlights the social need for sensors for health-related applications and the market implications of their deployment.

In summary, within a World moving toward abundance, trillion sensors will be required and Health-related applications will be of great relevance and highly demanded. This is the social and economic framework the present PhD thesis is related to.

1.1 Global Health 2035

The link between fighting poverty and achievements in the context of health is very strong. In fact, extreme poverty is strongly related to inequalities in health care [8]. We can consider as an example the analyses on child mortality rates: evidence suggests the existence of a causal relation between income and child mortality [9]. Provided the right investments and policy changes are adopted, it is expected that by 2035 every country will have the same child-mortality rates as U.S. had in 1980 [1] (see Fig. 1.3). This link is not surprising: many investments are required and are fundamental in achieving the foreseen goals. Between now and year 2035, while many low- and middle-income countries will develop enough to pay for this convergence themselves (and significant health gains are possible also in low-income environments [10, 11]), the poorest will still require generosity from donors [1].

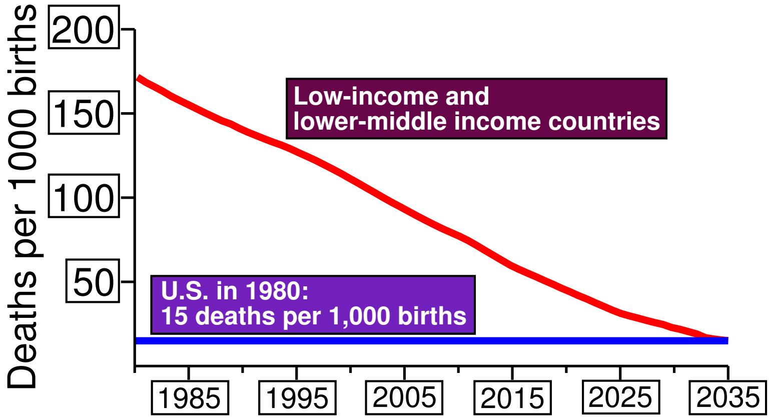

Figure 1.3: *Child mortality rates toward the year 2035. By 2035, nearly all countries can have child mortality rates as low as the U.S. had in the 1980s [1].*

What is the future of Health? What challenges await us ahead?

Global Health is not only about developing countries. While on one end it is intended as part of a process of global development (eradicating poverty, extending healthcare to developing countries which lack of deployment strategies), it also concerns aging populations of wealthy countries. In 2017 there was an estimation of 962 million people aged over 60 (corresponding to 13% of the global population). This number is growing at a rate of about 3% per year, possibly exceeding 2 billions by year 2050 and exceeding 3 billions by year 2100; by 2050, almost all regions of the world (except Africa) will have nearly a quarter or more of their populations at ages 60 and above [12,13]. While life expectancy will keep on increasing, the *quality* of life more and more will depend on a paradigm shift from *reactive* to *preventive* health care. This is particularly true for degenerative diseases, which do not reduce life

expectancy but make living hard, with increased costs for treatments and making people (usually learned-people) unproductive. This is already a reality nowadays. The *Horizon 2020* (H2020) framework addresses these questions [14]:
"Europe is facing four main healthcare challenges: (i) the rising and potentially unsustainable health and care costs, mainly due to the increasing prevalence of chronic diseases, to an ageing population requiring more diversified care and to increasing societal demands; (ii) the influence on health of external environmental factors including climate change; (iii) the risk to lose our ability to protect the populations against the threats of infectious diseases; (iv) health inequalities and access to health and care. Europe must invest in research, technology and innovation to develop smart, scalable and sustainable solutions that will overcome those challenges."

Adopting sustainable strategies and implementing a (scalable) digital transformation in Health and Care are then of primary importance. *Personalized medicine*, *Big Data* and *Artificial Intelligence* will be necessary to increase precision and efficacy of treatments and drugs. Guardian Angels [15] equipped with physico-physiological and environmental sensors will contribute to implement personalized preventive feedback loops. Both of the two scenarios (increased healthcare quality for developing countries, paradigm shift toward preventive healthcare for developed countries) will benefit from these developments.

Within the H2020 framework, large investments are planned in these areas, with a total budget of roughly 700 million euros per year [14]. Similarly, in the U.S. the share of GDP devolved to Health is expected to nearly reach 20% by year 2026, with a National Health Expenditures (NHE) growing faster than the GDP itself (Fig. 1.4) and reaching quota $5.7 trillion by the year 2026 [16].

Year 2020 is behind the corner.

We should not stop at H2020. A new (updated) vision for the future of world health care is needed. In this context, the *Global Health 2035* report by the *Lancet* Commission on investing in Health provides a new roadmap for the achievement of dramatic health gains within a generation [5].

As mentioned regarding the pursuit of abundance, substantial improvements of healthcare require technology. In the past 20 years, **new technologies** allowed the scale-up of new tools that reduced mortality rates; predictions for future trends estimate a decline of 2% in under-5 mortality thanks to the scale-up of new technologies [17]. Continued investments are then expected to result in high yield of results and benefits, and the widespread adoption of new technologies will be once again essential [5].

Investing in Health also leads to enormous payoffs: as an example we can just consider the fact that reductions in mortality rates account for about 11% of recent economic growth in low- and middle-income countries [5]. This shows that investing in Health is not only desirable from the social and ethical point of view to increase life expectancy and quality: it is also a key to occupy lead positions in future markets of expanding size.

Among the possible technologies and ways of intervention toward a new World Health, **nanotechnologies** play a key role. Apart from being an established and

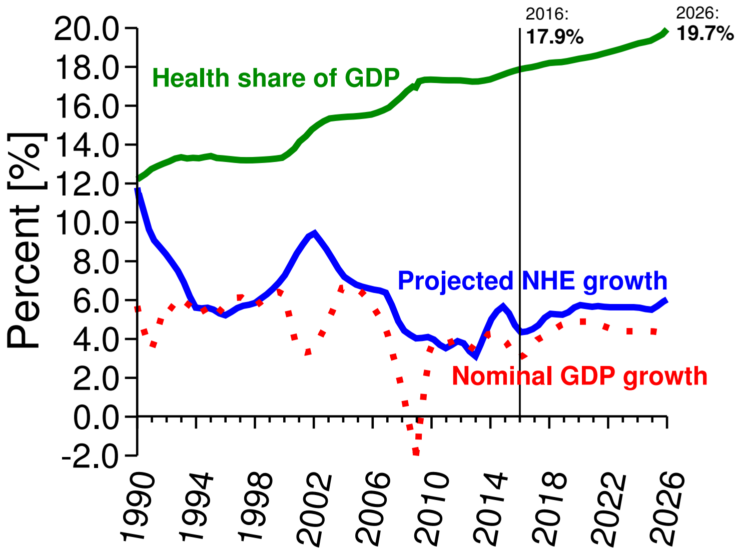

Figure 1.4: *U.S. growth in Gross Domestic Product (GDP, red), National Health Expenditures (NHE, blue), and Health Share of GDP (green) since 1990 and projected to year 2026 [16]. Predictions of NHE growth for 2017-2026 is 5.5%. Predictions of GDP growth for the same time period is 4.5%. By 2026, NHE is expected to reach $5.7 trillion.*

constantly-growing multi-billion market, nanotechnology is becoming a crucial driving force in Health, offering numerous pathways of innovation [18], from monitoring to detection, from prevention to therapies and drug deliveries. Patients' real time data will be captured instantly, processed, fused and made available to clinicians. Doctors will be able to monitor patients in real time, assisted by computers recommending the best treatments (this is already happening, see for example Dr. Watson by IBM [19]), possibly also after they leave the hospital to go home. That will enable the implementation of a new paradigm for the medicine: doctors will be in the Cloud [6]. *Lab-on-a-chip* (LoC) are also possible thanks to micro- and nanotechnology. LoCs integrate one or several laboratory functions into a single chip (e.g. [20]). This is of particular relevance for *point-of-care* diagnostics [21], especially for countries in which a proper healthcare is lacking, thanks to the capability of performing analyses without the need for laboratories.

1.2 Nanotechnology in Healthcare, the Trillion Sensors vision, and the Internet-of-Everything

Nanomedicine is a rather recent field of research, which nonetheless achieved crucial results over the years (Fig. 1.5). It spans a broad range of applications (nanomaterials for drug development, nanoelectronic biosensors for early-detection and diagnosis, ...) and enables new possible paradigms for diseases treatments (nanorobots for non-invasive diagnosis, nanodrugs for specific targets, nano-transporters

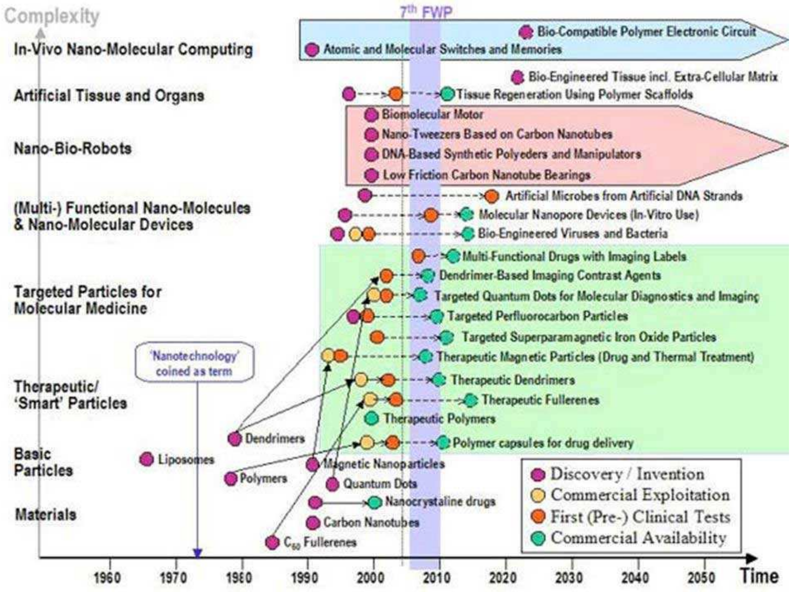

Figure 1.5: *Achievements and future prospects of nanomedicine (image from [22]).*

and nano-carriers for in-loco delivery of drugs, ...) [18].

While future Health paradigms are enabled by the unprecedented intervention capabilities offered by nanomedicine, the need for sensing, imaging, connectivity and transmission of health-related data creates a strong demand for the growing sector of the Internet-of-Things (IoT). IoT devices are already widely applied to interconnect medical resources and provide healthcare services (even though IoT is not only about health: it addresses different needs, from health to energy, from transportation to security; see Fig. 1.6) [23], and progress in nanoelectronics is paving the way for new and diverse More-than-Moore applications (sensors/actuators, biochips, ...) [24]. Heterogeneous integration of CMOS (complementary metal-oxide semiconductor) integrated circuits and SoCs with microfluidics on these bio-compatible platforms will enable *multi-sensory* platform implementations with enhanced modalities of operation, which are particularly desirable for real *personalized* medicine (sensing multiple parameters at once, specifically, for each individual patient).

Nanomedicine and IoT are fundamental enablers of the most advanced *Digital Health* paradigms. *Digital Health* is the convergence of digital and genetics revolutions to health and healthcare [26], and it represents the emerging market for mobile fitness, wellness and healthcare devices and services [6, 27]. *Digital Health* is expected to completely redefine the medical industry: diagnostics will be shifted to AI computers, and doctors will use Big Data generated by sensors and omics databases and processed by the computers on the patients' bodies.

Nanomedicine, IoT and Digital Health altogether contribute to the development of *P6 Medicine* [28], i.e. a model of medicine that is: *personalized* (thanks to a combination of technologies and nanomedicine, it is possible to "tailor specific therapeutics to the specific molecular picture of the patient" [28–31]), *predictive* (predicting diseases for healthy people, or predicting the development of diseases in already-ill subjects, by means of evidence-based methodologies [32] and even using

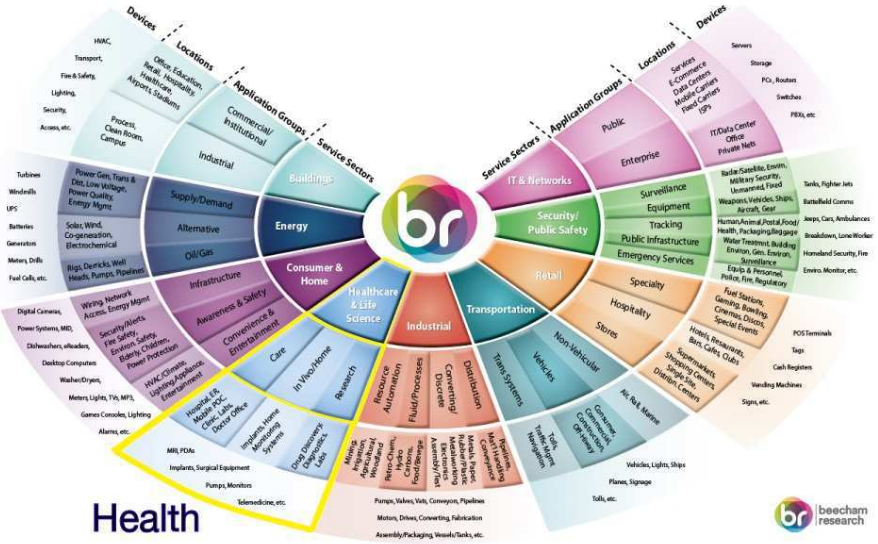

Figure 1.6: *Market segments for IoT [25]. Health is highlighted in yellow.*

personal omics profile analyses [28]), *preventive* (thanks to new assessment tools enabling early diagnostics, medicine has shifted from being just reactive to being proactive, addressing not only acute but also chronic multi-factorial diseases [28]), *participatory* (patients are informed of every aspect of their disease, their quality of life is an important parameter to be accounted for in the delivery of the cure and information is shared also about risks and uncertainties of the treatments [28, 33, 34]), *psycho-cognitive* (psychological and personal variables influence the clinical outcome, and hence taking into account the emotions and feelings of patients has become fundamental [28]), *public and population-based* (patients actively exploit the full potential of the Web, in a combination of telemedicine and e-health, where computers play a key role [35]; medicine should be shared and open-source [28]).

This paradigm clearly requires lots of data from the patients, and hence it is also driven by the availability of low-cost sensors. Sensor devices are a necessary ingredient of global digital healthcare thanks to their low cost, low power, unobtrusive operation, and accuracy properties. *Trillions* of sensors are however required to implement the depicted future [6].

Sensors are everywhere and will be even more ubiquitous in the near future. Applications to the sensing of human parameters are numerous and already commercialized (e.g. sensing of blood pressure, pulse rates, skin temperature, blood oxygenation, respiration rate, ...), as well as applications to help people in daily life (e.g. shake-stabilization for Parkinson disease patients [36, 37]). The connection between sensors (that monitor human parameters and generate data) to other processes (e.g. computers or AI to process the information), data (e.g. database stored information that help AIs taking decisions) and people (e.g. doctors) is an example of a recent and new paradigm that goes beyond IoT, namely *Internet-of-Everything* (IoE). IoE identifies the networked connection of people, data, processes and things, and it is considered as a multi-trillion market [6].

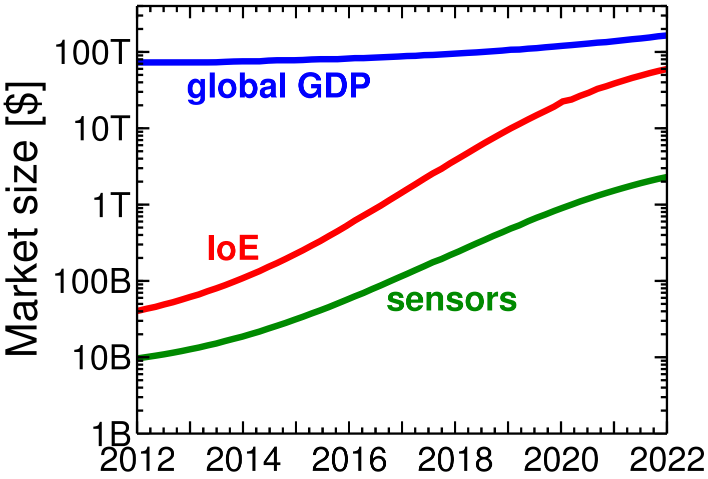

Figure 1.7: *Market forecasts for Internet-of-Everything (IoE) and sensors. IoE is expected to reach quota \$16-19 trillion by 2020, i.e. 20% of the global GDP. Networked sensors are expected to represent 5% of IoE (nearly \$1T) by year 2020. [6].*

There are certainly challenges associated with the achievements of the IoE and trillion sensors scenario, some of which include: the size of networks should be properly scaled to account for this massive amount of information (to the level of 10^{27} bytes, namely Brontobytes [6]), batteries/energy scavenging sources are required to guarantee devices lifelong power, proper algorithms are mandatory to derive useful information from these Big Data, funding is necessary [6]. However, the potential benefits are also enormous: unprecedented improvements of healthcare, creation of millions of new jobs (170M jobs by 2020, according to Cisco's forecast [6]), and large market revenues (Fig. 1.7).

To sum up, smart autonomous multi-parameter sensors really appear as a key enabler to realize these future scenarios. Within this big picture, driven by the potential benefits to the future of Global Health, we focused our research activity on the development of highly-parallel (i.e., Big Data generators) sensors for detection, imaging and characterization of individual particles at the nanoscale, possibly making a step forward in the direction of early-stage diagnostics for personalized medicine. In particular, as will be discussed in the following, Health-related applications really demand more, new, diverse and improved *nano-biosensors*, which are the main target of this thesis.

1.3 Nanobiosensors

According to the International Union of Pure and Applied Chemistry (IUPAC) definition, a biosensor is "a self-contained integrated device, which is capable of providing specific quantitative or semi-quantitative analytical information using a biological recognition element (biochemical receptor) which is retained in direct spatial contact with a transduction element" [38]. The working principle of a biosensor is then the following. An *analyte* (the component or chemical species we are interested to detect/investigate) interacts with a *biosensing component* (an element devoted to detect/recognize the analyte). The biosensing components can be, for instance, enzymes/cells that recognize the target analyte and consequently generate electroactive species (this is the case of *biocatalytic biosensors*, where a living biological system is used to speed up chemical reactions), or biological elements such as antibodies/receptors/nucleic acids, that selectively and complementarily interact with the analyte (*affinity biosensors*). Due to the interaction with the analyte, the biosensing element generates a variation of a physical quantity (e.g. modification of a mechanical, optical, or electrical state). A *transducer* is then devoted to convert the information related to the physical quantity variation into a variation in another domain (e.g. a mechanical state change can be converted in an electrical state change). Finally, a signal processing unit performs amplification and signal-conditioning of this information, and further elaborations of the data are possible (usually in the digital domain, after performing an analog-to-digital A/D conversion). Figure 1.8 shows a schematic representation of a biosensor with its main features.

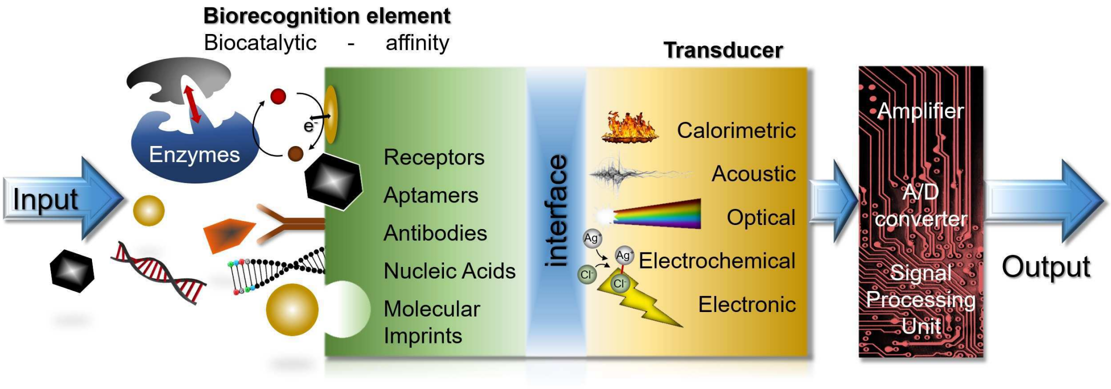

Figure 1.8: *Schematic representation of the structure of a biosensor.*

Many different sensors and imaging techniques are routinely used to assess our health status in nowadays medicine and healthcare: thermometers to measure body temperature, sphygmomanometers to measure blood pressure, stethoscopes for auscultation, radiology and MRI (magnetic resonance imaging) equipments... Devices dedicated to the monitoring and detection of biological quantities or biological parameters are also common in microbiology and analytical laboratories. However, most of these devices have been developed before the advent and deployment of nanotechnology we have experienced in recent years. Furthermore, they use macroscopic quantities of biological fluids which is often collected through invasive procedures on the patient. These are not *nano*-biosensors.

Nanobiosensors are biosensors that operate at the nanoscale by means of nano-sized transducers, interacting (detecting, imaging, analyzing, ...) with nano-sized analytes.

Why do we need *nanobiosensors*?

The analytes of interest for early diagnosis are commonly present in very low concentrations, in the range from mM (1 mol/m^3, see for example common blood test results) down to fM (10^{-12} mol/m^3, corresponding to one grain of salt diluted in several olympic-sized swimming pools), where the *molarity* [M] identifies an analyte's concentration of 1 mole in one liter (1M=1 mol/L) [39]. On top of that, biomolecules are small: bacteria are as large as 1 µm, viruses are in the range of hundreds of nanometers, proteins and nanoparticles can be even smaller (see Fig. 1.9). Thanks to the progress in nanotechnology, the size of modern nanodevices is comparable to or smaller than a large variety of biomolecules of interest. To detect small molecules with large sensing elements, one could rely on statistically relevant binding rates of analytes on large surfaces, but this strategy provides only average analyte properties on a fairly large population. Furthermore, it requires a relatively large sample volume, to guarantee the availability of a sufficiently large number of analytes for possible binding events. Differently, having transducer devices just as small as the analytes enables a *single-molecule detection* scenario: for a given analyte, a smaller biosensor size yields a greater signal-to-noise ratio of the response, possibly enabling the unambiguous identification of an individual nanoscale analyte above the noise floor. For a given concentration (large enough that the sample volume contains at least one analyte) and if one were sure to capture such analyte, then one could rely on a much smaller sample volume. On top of that, if proper modeling tools are available to aid the interpretation of single-binding events, useful information on the properties of single particles can be extracted, while collective measurements only provide information on the particles ensemble (e.g., estimating the permittivity of an individual particle or estimating the permittivity of a layer of particles agglomerate can yield different results). However, to achieve this result, the analyte has to effectively reach the biosensor itself, which entails taking into consideration the analyte transport mechanisms in the chamber. These aspects will be further expanded in the next section, after the accurate definition of the main metrics.

Nanobiosensors are of great importance to transform nowadays medicine into that of *personalized medicine*: for instance, human genome sequencing is a fundamental prerequisite to personalized medicine since a number of diseases have been related to the presence of specific genes in the genome. While a virus like HIV is described by only ∼ 9,700 base pairs and E. Coli by ∼ 4.6 million base pairs, se-

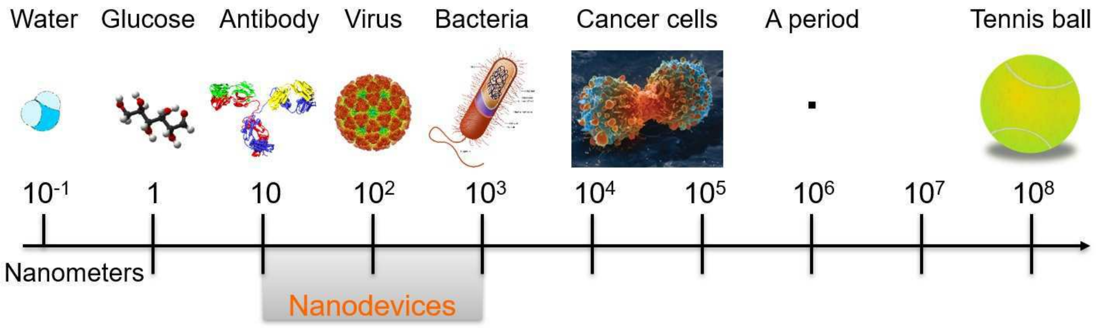

Figure 1.9: *The size of analytes compared to the size of nanodevices.*

quencing human genome requires to go through ~ 3.2 billion base pairs [39]. This is an extremely challenging task, and nanobiosensors applied to genetic sequencing offer a number of convenient features: scalability, sensitivity, large parallelism, low-cost of implementation. The activity presented in this work relates to all these attractive features.

Two examples of market-available LoC implementations of nanobiosensors are the Paradigm REAL-Time Revel system by Medtronic Minimed [40] (devoted to continuous glucose monitoring) and the IonTorrent system by Thermo Fisher Scientific [41–43] (devoted to DNA sequencing by means of non-optical technique).

Biosensors can be differentiated and classified according to a number of properties of interest. Here we identify the main distinctions, based on the way the biosensing element operates and based on the type of transduction mechanism. Since biosensors are a special kind of the more general concept of *sensors*, general figures of merit for sensors are also discussed.

1.3.1 Metrics for sensors and biosensors

Fundamental and practical figures of merit can be identified. The most relevant metrics are the following [39, 44–47]:

- *Sensitivity*: it is defined as the ratio between the output signal variation (e.g. a difference in the electric current of the transducer) and the input signal variation (e.g. a difference in the electric charge at the sensing element). In different terms, the sensitivity is the slope of the transfer characteristic curve ($S_{out} = S_{out}\left(S_{in}\right)$). A sensor is very sensitive if small variations of the sensing element state result in large variations of the output quantity. “If the sensor does not notice the analyte, it does not exist!” [39].

- *Selectivity*: it is defined as the ratio of the slopes of the transfer characteristics to the analyte of interest and to a certain interfering quantity, respectively. Therefore, the selectivity is the ratio between the sensitivity to the target analyte and the sensitivity to a source of interference. To put it another way, the selectivity represents the ability to discriminate between the target analyte and an interfering element.

- *Resolution/Limit of Detection (LoD)*: the resolution, or limit of detection, represents the quantity/amplitude of the input signal that can be detected above the noise level with an acceptable degree of confidence. It is the input quantity corresponding to an output signal of $k \cdot \sigma$, where σ represents the standard deviation of the output signal variation and k is a factor corresponding to the desired degree of confidence.

- *Repeatability*: repeatability (or test–retest reliability) represents the level of agreement between successive measurements of the same measure carried out in the same laboratory.

- *Reproducibility*: it represents the level of agreement between successive measurements of the same measure carried out in *different* laboratories.

- *Dynamic Range (DR)*: it is the ratio between the largest and smallest quantity of analyte that can be measured.

- *Response/Settling time*: it is the average time a sensor requires to capture the minimum quantity of analytes that result in a detectable response, and to change its response to a final settled value (within a tolerance range). Timing parameters are strongly related to the size of the analytes (via their diffusion coefficients) and to the structure of the biosensor itself (sensors in static environments vs sensors in flow [48]).

- *Stability*: it represents the degree of susceptibility to ambient disturbances, which can result in a drift of the output signals during measurement. This feature is particularly crucial for long-incubation steps and continuous monitoring applications [45].

- *Need for calibration*: a calibration is defined as an "operation that, under specified conditions, in a first step, establishes a relation between the quantity values with measurement uncertainties provided by measurement standards and corresponding indications with associated measurement uncertainties and, in a second step, uses this information to establish a relation for obtaining a measurement result from an indication" [46]. It should thus not be confused with simple adjustments of the measuring device (often mistakenly called "self-calibration"), nor with a mere verification of the calibration [46]. Removing the need for calibration greatly simplifies the complexity of the devices for on-body or implantable sensors [47]. However, calibration is hardly avoidable for quantitatively traceable measurements. At the nanoscale, accurate calibration is still very difficult in general, and even more so in the field of biosensors, due to the lack of standards, the limited reproducibility of the experimental conditions, etc.

- *Lifetime*: the length of time the sensor is capable to operate and generate accurate (within a specified uncertainty) output results. Clearly, this metric is strongly related to the repeatability, reproducibility and re-usability of the devices.

Trade-offs between different metrics may apply. In particular, in the following of this section we will further address the problem of achieving high sensitivities while maintaining reasonably low response times.

After the definition of the main metrics, we can now expand the discussion anticipated in the previous section concerning the size of biosensors, that is: is it convenient to shrink them down? What are the main challenges related to the scaling of dimensions? Can design guidelines be formulated to assist the design of more sensitive nanobiosensors?

As anticipated in the previous section, having transducer devices just as small as the analytes yields a greater signal-to-noise ratio of the response. However, to achieve this result, the analyte has to effectively reach the biosensor itself, which requires to account for the analyte transport mechanisms. In turn, the dynamics of this transport affects the settling time of the sensor, thus creating a link between sensitivity and settling time. This link has been studied for instance in [39, 48–51] under different assumptions as regards the mass transport mechanism. In particular, the sensitivity of the whole biosensing system depends on the mass transport effects [48], and the smaller size of the sensor may negatively impact the diffusion time to complete the measurement, hampering the detection down to the *femto*-molar level. The transport of the analytes towards the sensing elements is heavily dependent on the velocity of the fluid transporting them. If the fluid is essentially in steady state, then motion of analytes essentially depends on diffusion phenomena. In this case, the settling time for a given analyte concentration depends on the fractal dimension of the transduction elements (and nanowire devices should be privileged for high sensitivity) [51]. In case of fluid flow, however, the situation changes appreciably and other geometries might be preferable [50]. In summary, the geometry of a sensor surface dictates a number of its properties, including settling time and sensitivity [39], and the increase of the signal-to-noise ratio should be examined relative to the critical dimension of the sensor [48].

1.3.2 Label-based vs Label-free biosensing

One important distinction between sensors can be made based on whether or not the analytes are *tagged* (*labeled*) before detection events occur.

In fact, one possible approach to make it easier to detect a certain target (the analyte) is to attach a “tag” or a “label” to it. A label is an additional molecule that is connected to the target analyte. Popular labels are:

- Fluorescence labels [52–56]: typical methods include using chemicals (e.g. Maleimide-Thiol, NHS ester-Amine, ...), enzymes (e.g. Transglutaminase, Sortase, Cutinase, Biotin Ligase, ...), or tags (e.g. a genetically-tagged fluorescent protein, Halo, Aspartate, Histidine, ...) [55]; fluorescent labels are the preferred ones due to the large availability of stable and highly-sensitive fluorescence scanners.

- Chemiluminescence labels [57–61]: they are based on light-emission induced by chemical reactions, and can be used with simple instruments and without the need for light sources.

- Radioactive labels [62, 63]: they are based on radioisotopes; robustness and reproducibility are the main features, and can be used for molecular detection allowing accurate quantification of protein abundance [64].

- Electrochemically-active labels [65, 66]: they are used to improve sensitivity and/or selectivity of electrochemical nucleic-acids sensing. Species used for this purpose exhibit reversible electrochemical properties, and this guarantees an extended range of conditions under which the detection can occur. The most common type of electroactive DNA label is ferrocene [67], a redox-label that can be covalently attached to the backbone of a nucleotide signaling probe (which selectively binds to a DNA duplex) [68]. Another example is the use of aptamers that loosely binds to a neutralizer, which later functions as a signal carrier [69].

- Nanoparticle labels [70]: they are especially used for the detection of proteins and nucleic acids. Nanoparticles can be used to increase the concentration of electroactive species [71, 72], acting as seeds to deposit electrochemically detectable species [73], acting as ultra-microelectrode arrays to induce electrolysis on the substrate, or to mediate the deposition of electrocatalysts [74].

- Magnetic labels [75, 76]: they are very stable, are not affected by chemical reactions, and enable low background interference compared to optical and electrical approaches [76]. The design of magnetic labels involve the synthesis of suitable sized particles (in the nanometer-micrometer size range), their modification with biocompatible linkers and ligands, and the identification of the optimal magnetic detection technique for the desired application (e.g. spintronic sensors based on giant magnetoresistance, tunnel magnetoresistance, planar Hall effect sensors, superconducting quantum interference devices, atomic magnetometers, nuclear magnetic resonance systems, fluxgate sensors, inductive coil sensors, diamond magnetometers, and domain walls-based sensors [77–86]).

Labeling the analytes present a number of drawbacks [87]. Firstly, these methods require lengthy and troublesome pre-processing steps (real-time analyses are therefore not possible). The synthesis of labels (combining synthesis and purification) usually results in low yields [66]. Fluorescence has the disadvantage that the fluorophores are extremely sensitive to the environment conditions, such that small variations of the pH can alter the labeling. Sensing with chemoluminescence can be performed only once, and resolution and dynamic range are limited [88]. Radioactive labels raise safety concerns [89]: they require safe-handling procedures and disposal of radioactivity. Furthermore, these approaches incur in several problems due to false positives (non-specific binding of labels can occur, for instance, in the case where high concentrations of labels are applied to ensure complete labeling of all the analytes) and false negatives (e.g. due to binding site occlusions) [90, 91]. Finally, the target analytes are altered by the labels themselves (hence, inspecting the individual analyte properties becomes troublesome).

Differently, *label-free* techniques do not require the labeling sample preparation, and the analyte properties are not affected by the labels. They are based on physical parameters detection (such as optical, electrical, or acoustic properties, that are modulated in the presence of the analyte in a distinctive manner), and they are easier to operate. Thus, the analytical quality is improved, the cost is reduced, the reproducibility is improved, and real-time analyses are possible. Thanks to these favorable properties, label-free techniques are of great interest for the scientific community. Improving label-free techniques to match the commercial feasibility of current label-based methods is however a challenge [66].

In this work, the focus will be on label-free biosensors.

1.3.3 Sample preparation

Sample preparation is recognized as a critical bottleneck to translate the use of biosensors from the laboratory to clinics [92,93]. In fact, the precise design, manufacture, purification and characterization of samples are fundamental if reproducibility and well-controlled performance are required [94]. In general, sample preparation first requires to collect the specimen (e.g. blood) and to place it on a device for the actual preparation step (possibly after some preliminarily treatments, for viscous or solid samples [95, 96]). Microfluidics devices are an interesting mean to prepare samples, thanks to a number of interesting properties (small size, laminar flow, ...) that enable the application of a variety of methodologies for point-of-care preparations [92, 97, 98]. Given the widespread presence of sample preparation issues and the abundance of related documentation, for more details the reader can refer to a number of reviews [94, 99–101].

Purification of samples is necessary to remove undesired salts, primers or other contaminants, thus reducing the number of possible false-positive signals. While sample preparation is especially critical for highly-sensitive systems, where sensitivity can strongly depend on the preparation methodology [102], the final application ultimately determines the purification requirements. Surface modifications can be applied to enhance selectivity (thus reducing the false-positive events), while highly-parallel sensor systems enable to gather statistics of events and prune outliers possibly related to other analytes than the desired one. Furthermore, sensors with imaging capabilities, such as the one considered in our study, allow in principle to obtain further information about analyte shape and dynamic behavior, which can be used to select signals and separate them from other undesired responses. A highly-parallel detection platform with selectivity features would thus allow to relax the purification requirements. This is indeed the case of the chip discussed in the following of the present work, whose application to the selective detection of analytes in low-purification ambients, despite not being demonstrated in this work, appears promising.

1.3.4 Biosensing elements

Biosensor recognition elements can be both natural and laboratory-synthesized. A subset of possible recognition elements is the following (for a more extensive description, see [103]):

- Receptors [104]: we refer to transmembranes and soluble proteins that bind to specific molecules (*ligands*). The binding of the receptor induces a series of further changes in the analyte state (e.g. opening of ion channels), and these changes induced by the binding are the variations that the transducers detect. Receptors are attractive objects, since they can act both as a “receiving” and as a “sending” entity [103]. They can be synthesized to have a high affinity, such that they bind solely to a very specific target. However, they require sample preparations and the production yield can be low.

- Enzymes: they can be used to induce catalytic reactions, which produce a large variety of by-products that can be detected. Enzymes have been used, for instance, to detect HIV antibodies in serum [105]. A common disadvantage is that a reduction of the useful signal usually occurs due to interference from other chemical species [106]. However, there are examples of very successful uses of this category of recognition elements. For instance, enzyme-based biorecognition glucose sensors dominate the current world market.

- Antibodies: they have been used extensively for detection purposes in immunosensors, and their popularity increased especially after the development of monoclonal antibody (MoAb) technology [107], that enables large production of antibodies. They react with the analytes inducing modification at the level of the functional groups, enabling the detection of the reaction. A significant advantage of using antibodies is that the target does not require purification before the detection. ELISA (enzyme-linked immunosorbent assay) is a quite popular plate-based assay technique to detect substances (peptides, proteins, antibodies and hormones), in which an antigen is immobilized on a solid surface and then complexed with an antibody that is linked to an enzyme [108].

- Aptamers: these are artificially-built receptors, composed of nucleic acids strands. These ligands recognize their target primarily by shape (i.e. conformation) and not sequence [109]. Given the synthetic fabrication of these receptors (and hence the possibility to engineer their properties depending on the specific analyte that is being targeted), the types of target molecules that can be detected with aptamers is virtually unlimited.

- Nucleic acids: they act as good biosensing elements thanks to the specificity of base-pairing with their complementary sequences. Particular interest is devoted to Peptide nucleic acids (PNA). PNAs are synthetic DNAs with a polyamide backbone instead of a sugar phosphate bone [110]; as a result, the PNA strand is not as negatively charged as a DNA strand. Thanks to their superior hybridization characteristics and improved stability [111], they are preferred over other nucleic acids. The very different nature of PNA molecular structure paves the way to new detection techniques, in particular without the need of labels [103].

- Molecular imprinting: molecular imprinted polymers allow to create very stable artificial biosensing elements [103], that can detect a large variety of analytes [112].

1.3.5 Transduction mechanisms

The transduction mechanism defines another level of distinction among the biosensors.

Calorimetric/Thermometric/Pyroelectric biosensors

Calorimetric/Thermometric/Pyroelectric biosensors generate electric currents based on variations of the temperature. Biomolecules are immobilized on a temperature sensor, and the interaction between the analyte and the bio-recognition layer generates heat. In fact, almost all chemical/biological reactions involve exchange of heat [113, 114]. This heat is proportional to the molar enthalpy and the total number of reactants consumed or products formed in the reaction [113,115]. Thermistors (usually, metal-oxide) or thermopiles (usually, ceramic semiconductors) are used to measure the heat [114].

The advantages of these biosensors include stability, high-sensitivity, easy miniaturization and integration with microfluidic systems [115–117]. Furthermore, they do not require frequent calibrations and are insensitive to the optical and electrochemical properties of the sample [115]. Some of the most common and interesting applications include label-free screening of biomolecules interaction [118], DNA hybridization detection [119, 120], food-industry [121] and environmental monitoring [122].

Acoustic biosensors

Acoustic sensors comprise one or more vibrating elements that create acoustic waves [123]. Usually, the biosensing element is coupled to a piezoelectric component (usually a quartz-crystal, coated with gold electrodes) [124]. Piezoelectricity is a physical phenomenon which refers to the ability of a material to produce a voltage variation when mechanically stressed. While a number of different materials exhibit piezoelectric behaviors (quartz, tourmaline, barium, lead titanate, gallium orthophosphate, lithium niobate, lithium tantalate, crystalized topaz, zinc oxide, aluminum nitride, aluminum phosphate [124, 125]), quartz-based devices are the most common biosensors, since quarts is cheap, can be processed to yield a single crystal, can withstand chemical, thermal and mechanical stress, and is biocompatible [114]. By means of AC voltage excitation, a mechanical oscillation of the crystal is induced and the frequency of oscillations is measured [126]. Analytes attached on the surface of the electrodes (located on the crystal) change the oscillation frequency [127], and hence the mass-variation can be estimated [128]. Changes in the viscosity of the fluid can also be detected [129]. Surface Acoustic Wave devices (SAW, where the detection of analytes is based on variations of the acoustic waves that travel on the surface of a substrate between a sender and a receiver electrode) and Bulk Acoustic Wave devices (BAW, which operate in the thickness shear mode) are the main implementations [123]. Quartz is the most common material also thanks to Quartz Crystal Microbalance devices (QCM, mass sensors typically obtained by sandwiching a thin crystal between two conductive electrodes), which act as mass sensors and have been widely used and commercially available since many years [125]. Micro-cantilever are also used as mass-sensitive biosensors. Viscosity, density, and flow rate can be measured by detecting changes in the vibrational frequency [124]. An example of application of acoustic biosensors is for immunosensing [130].

Acoustic biosensors can be very sensitive [131], can operate in real time and perform label-free detection [132, 133]. However, drawbacks include lack of specificity, high interference, and calibration problems [134, 135].

Optical biosensors

Optical biosensors measure the absorbed or emitted light, and can be label-based or label-free. Due to the extremely large variety of optical biosensors, this section will be necessarily incomplete, presenting only a few alternatives. For fluorescence- and chemiluminescence-based devices, the detection is based on identifying the frequency-shifts of the radiation emitted by the (labeled-)analyte. High sensitivities and dynamic range can be obtained [136], however these sensors suffer from the drawbacks of label-based techniques. Optical-diffraction-based devices usually rely on a silicon wafer coated with a protein (via covalent bonds) and exposed to UV light through a photo mask, leading to the formation of inactive antibodies in the exposed regions. When exposed to light, this configuration provides the reference signal in absence of analytes. In the presence of analytes, instead, antigen-antibody bindings are formed and create different diffraction patterns when illuminated [115, 124]. Regarding label-free implementations, many alternatives are possible, spanning from dielectric-based to metallic-based substrates, from planar surfaces to micro/nano-patterned surfaces [137–139]. A few alternatives are offered by:

- Surface Plasmon Resonance (SPR): this is the most common type, thanks to the high sensitivity [140, 141] and to its adaptability to the detection of a large variety of analytes [142]. Surface plasmons are oscillations of the free electron density on a metal. Many different functional layers can be put on top of the conductive surface, without altering the detection capability [123]. Monochromatic light is reflected on the metal surface and, at the angle where the surface plasmons are excited, the reflected light has a minimum which can be measured [123]. In fact, interaction between analytes and biorecognition layers change the SPR. These sensors can also be implemented in arrays, thus enabling highly-parallel detection in combination with CCD (Charge-Coupled Device) cameras [143].
- Interferometry: an example is given by Biolayer Interferometry (BLI), which uses white-light interferometry to quantify biomolecules adrosbed at the end of optical fibers (at the optical fiber-biomolecular layer connection) [123, 144]. They also enable parallel analyses [145]. A strong limitation of this method is posed by poor LoD, hampering the detection of small molecules [146]. More generally, interferometer-based structures include Mach-Zehnder, Young's, Hartman, and Backscattering interferometers [147, 148].
- Diffraction gratings: they operate by measuring the reflection of light on photonic crystals (i.e., optically regular structures made of a dielectric material, forming holes and spaces in the nanometer dimension) when a biomolecule is adsorbed on the surface [123, 149]. Thanks to the cheap manufacturing process, highly multiplexed implementations are possible [123].
- Ellipsometry (ELM): it measures the changes in the state of polarization of elliptically polarized light, which is reflected at planar surfaces [123, 150]. Also in this case, CCD cameras can be used as detectors (parallel detection of analytes is possible). Disadvantages are posed by systems of unknown electrical properties.
- Waveguides: here light can be coupled into an optical waveguide to create

standing-waves. The intensity of the coupled light depends on the thickness and refractive index of the biomolecules layer adsorbed on the waveguide surface [151, 152]. Ring-resonator based biosensors are also a notable and recent implementation [147].

More details on optical-based biosensing can be found in [138, 139, 147, 148, 153] and in the references therein.

As a final remark and in view of the following discussion of purely electrical methods, it should also be noted that for optical detection it is not necessary to bound analytes on the sensor's surface: detection can be performed within the penetration depth of the evanescent wave. They are also immune to electromagnetic interference, can provide highly-parallel and multiplexed detection, and merge the advantages of other label-free techniques in cost-effective ways [148]. For all these reasons they undoubtedly represent a competitive benchmark for alternative detection techniques.

Electrochemical and electronic biosensors

Chemical reactions between immobilized biomolecules and target analytes produce or consume ions or electrons, generating variations in measurable electrical properties, such as charges, currents or potentials, that can be detected [38]. This is the basic operating principle of electrochemical biosensors [154]. These reactions generate measurable currents (*amperometric* sensors), potentials/charge accumulations (*potentiometric* sensors), or conductivity variations of the medium between electrodes (*conductometric* sensors) [154]. Identification of these reactions is however possible also by means of *impedimetric* [155, 156] and *field-effect* sensor [38].

Enzymes are the most used biosensing elements for electrochemical detection, thanks to their specific binding capabilities and biocatalytic activity [157, 158]. Since electrochemistry is a surface technique, electrochemical biosensors are sensitive to events occurring at the surface of the electrodes [159]. A typical electrochemical setup comprises a minimum of two electrodes in solution, but the three-electrodes configuration is preferred (especially in experiments with large-scale electrolytic/galvanic cells, or with nonacqueous solutions with low conductivity, i.e. with a high series resistance) [160]. A *working electrode* (WE), also known as sensing/redox electrode, serves as a transduction element in the reaction; a *counter electrode* (CE), also known as auxiliary electrode, establishes an electrical connection in the solution and helps measuring the current flow; the *reference electrode* (RE) serves to set and control in a stable way the bulk potential of the solution (and should not be placed too close to the WE) [159, 160].

Electrodes can be *ideally polarizable* (IPE, electrode at which no charge transfer can occur across the metal-solution interface due to faradaic processes, but transient currents are still possible without charge transfer) or *faradaic* (charge transfer can occur and is governed by Faraday's law, in which the amount of chemical reactions is proportional to the current flow) [160]. Given this distinction, and considering the roles the different electrodes have, WEs are typically implemented with platinum, gold, carbon (e.g. graphite) or silicon compounds, materials that approach the ideal IPE behavior; REs are commonly made of Ag/AgCl and guarantee a faradaic connection to the solution (in fact, it is necessary to provide redox species in solution to sustain the electron transfer to/from the electrode); CEs instead can be made of any convenient material, since they do not affect the behavior of the WE (usually, materials that do not produce substances by electrolysis, that could possibly reach the WE, are preferred) [159, 160].

The following classification is possible for electrochemical biosensors:

- *Amperometric/Voltammetric* [161]: they continuously measure currents resulting from oxidation/reduction of electroactive species [159]. When the current is measured at a constant potential, we refer to *amperometry*; when the potential is measured at constant current, we refer to *voltammetry.* The presence of electroactive interference in the sample can cause false current readings, and this is a major limitation of this family of biosensors [114, 162]. Very high density arrays are also possible [163], and notable implementations include interdigitated [164,165], bipolar [166], nanogap [167], and ring-disk [168] electrodes.

- *Potentiometric* [169]: they measure the accumulation of a charge and corresponding change in potential at the WE [159], essentially providing information about the ion-activity [170]. They do not chemically influence the samples, hence are the ideal candidate sensors for applications with very tiny samples (e.g., femto-L volumes) [159, 171]. Examples of application are the detection of the pH (i.e., the concentration of H^+ ions) or selective ion concentrations in solutions. Many potentiometric devices are based on field effect transistor (FET) devices. Ion-selective electrodes are in particular extremely used in clinical chemistry, thanks to their selectivity, simplicity, rapidity, low cost and maintenance-free measurement [114].

- *Conductometric* [172, 173]: they measure the ability of an analyte/medium to conduct DC or AC/transient electrical currents between electrodes. They are mostly associated with enzymes (where the ionic strength of a solution between two electrodes is altered by enzymatic reactions) [159]. *Capacitive biosensors* also fall within this category [174]. These kinds of biosensors are of great interest, especially in combination with nanostructures (e.g., nanowires [175]). They are very convenient because no reference electrode is required (since these sensors detect changes in the conductivity, or resistance, between two electrodes), they are cheap to fabricate, and there is the possibility of miniaturization, parallelization in device arrays, and direct electrical response [114,176].

- *Charge-effect*: Ion Sensitive Field-Effect Transistor (ISFET) devices are a notable example of charge (or field) effect biosensors [177]. Surface charges induced by the analytes or variations in the solution modify the conductivity of the field-effect device, thus leading to the detection (e.g., variations in the pH of the electrolyte). Recent developments include nanoribbons (NR) [178–180] and FinFET [181] implementations, thanks to the opportunity offered by CMOS-integration.

- *Impedimetric* [182, 183]: they measure the electrical impedance between two electrodes in AC, with a constant DC bias superimposed. A small-signal sinusoidal excitation is applied, sweeping its excitation frequency and measuring the resulting current at the electrode. The ratio between the measured current and applied voltage (at different frequencies) gives the impedance spectrum. This is referred to as Electrochemical Impedance Spectroscopy (EIS) [184]. A major strength of EIS is that it interrogates different sample properties in different frequency ranges.

If no electrochemical reactions occur in the solution, detection/characterization of analytes and electrolyte properties is still possible by means of essentially the same basic techniques. As an example, sedimentation of dielectric microparticles on nanoelectrodes can be monitored by means of impedimetric measurements (impedance spectroscopy), possibly identifying properties of the analyte (size, permittivity) without the need for electrochemical reactions: the mere presence of the analyte (which occupies a part of volume that was previously occupied by electrolyte), in fact, alters the electrical properties (impedance) of the medium. This is the case of electronic biosensors (i.e., biosensors based on electronic transduction without electrochemical reactions causing the variations of the input physical quantity), which are the subject of this thesis.

1.3.6 Impedance-based sensing

Impedance sensing is performed by applying small sinusoidal voltage signals $V(\omega)$ at different frequencies ($f = 2\pi\omega$) to a sample (e.g. by means of an electrode), while simultaneously recording the resulting current $I(\omega)$. The *impedance* is the ratio between the frequency dependent complex numbers $V(\omega)$ and $I(\omega)$: $Z(\omega) = V(\omega)/I(\omega)$. Results are also commonly displayed in terms of *admittance*, i.e. the reciprocal quantity of impedance: $Y(\omega) = 1/Z(\omega) = I(\omega)/V(\omega)$.

The impedance is, in general, frequency-dependent. Hence, it has a non-constant amplitude and phase spectrum. Impedance spectroscopy is dedicated to measuring the amplitude and phase (or real and imaginary part) of this impedance spectrum, to gather information about the sample under test.

The many possible architectures of impedance analyzers can essentially be grouped in two main categories, distinguished based on the way the impedance is calculated starting from the measurement of the current induced by the applied voltage stimulus [185, 186]:

- those that use a wide spectrum of frequencies for the input voltage and calculate the impedance by Fast Fourier Transform (FFT) of the applied signal and measured current. This solution usually yields poor sensitivity and signal-to-noise ratio (SNR); furthermore, and a large amount of power and memory are required [185].

- those that use coherent-detection, by means of quadrature detection or lock-in amplifiers. Since the applied signal power is concentrated in a single frequency and the output is tuned within narrowband filters, higher SNR is obtained and the linear mode of operation is maintained [185].

For a more detailed description of different architectures of impedance spectroscopy circuits, the reader can refer to the following reviews [185–188].

Alternatives to impedance analyzers are also possible. As a notable example, we cite the charge-based capacitance measurement (CBCM) approach [189, 190]. This is the approach that was followed for the development of the biosensor platform investigated in this thesis. While CBCM techniques cannot replace general-purpose impedance analyzers, for specific applications (e.g., biosensing) they present significant benefits compared to conventional lock-in architectures (e.g., smaller area occupation, which enables the implementation of matrices of sensors with smaller intra-sensors pitch).

The physical systems of interest for impedimetric sensing can be conveniently modeled by means of combinations of linear lumped-element electric components. In particular, for the physical systems under study in the context of biosensing, the impedance under investigation is always passive (e.g., pure delay or all-pass behaviors are not possible, since they would inevitably produce impedances with negative real parts in certain frequency bands) and can be modeled with equivalent lumped element circuits made of mixed resistance-capacitance components (not even inductive). Over any finite frequency range of interest, these responses can always be approximated to arbitrary accuracy with RC networks of adequate complexity (e.g. using the systematic methods developed by Foster and Cauer [191–193]).

A relevant element is given by the portion of electrolyte in close proximity to the electrode, often denoted as the electrical double layer (EDL, see next section). If we assume the electrode to be ideally flat and extremely thin, the EDL of an impedimetric sensor can be described by an ideal capacitor. In practice, however, surface roughness and porosity of the electrode result in a distribution of local time-constants, which can be modeled by means of *constant phase elements* (CPE) [185, 194], whose impedance reads:

$$Z_{CPE}\left(\omega\right) = \frac{1}{\left(j\omega\right)^{\alpha} Q_0} \tag{1.1}$$

where α represents a non-ideality factor (for $\alpha = 1$ an ideal capacitor with capacitance equal to Q_0 [F] is obtained; for $\alpha = 0$ an ideal resistor with resistance equal to $1/Q_0$ [Ω] is obtained; for $\alpha \neq 1$ an impedance with constant phase (-90α)° is obtained). For reasonably smooth electrodes, typical values of α are in the range 0.8-0.9.

Together with surface roughness, also diffusion processes of ion species result in deviations from purely resistive-capacitive behaviors. In particular, redox reactions are usually modeled by means of a Warburg diffusion element (Z_W). A *Warburg impedance* accounts for the mass-transport limitations of redox currents at low frequency [185] and is represented by a CPE with $\alpha = 0.5$ (i.e. an impedance which depends on the square root of the angular frequency, $Z_W \sim 1/\sqrt{\omega}$). An equivalent circuit commonly used in EIS analysis is the Randles circuit [195], shown in Fig. 1.10 (a).

For modeling purposes, we will approximate the EDL as an ideal capacitance [185]: in fact, as will be discussed in the following, given the advanced fabrication process used to fabricate the nanoelectrodes in CMOS technology as discussed in this thesis, large values of $\alpha \simeq 1$ are realistic. The Warburg impedance will also be neglected in this thesis: as will be discussed in Chap. 2, essentially zero DC bias

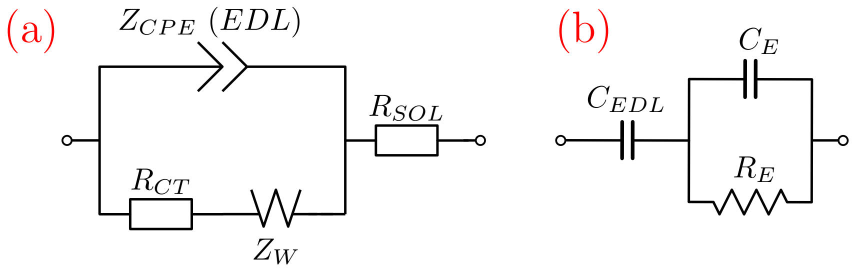

Figure 1.10: *(a) Randles equivalent circuit model, composed by the bulk solution resistance R_{SOL}, the EDL constant phase element Z_{CPE} (which models non-Faradaic phenomena), and the series of a charge-transfer resistance R_{CT} and a Warburg impedance Z_W (modeling Faradaic phenomena) [185,195]. (b) Simplified model valid for nearly-ideal electrode surface properties and in the absence of redox reactions, composed by the EDL capacitance C_{EDL}, and R_E and C_E representing the spreading resistance and spreading capacitance of the electrode to the electrolyte, respectively.*

will be applied between the gold working- and counter-electrodes of the biosensor platform, and redox reactions do not occur. These two simplifications allow us to simplify the Randles equivalent circuit, considering instead the model shown in Fig. 1.10 (b) and thoroughly discussed in the following of the thesis. Modeling and interpretation of measured impedance spectra is not trivial, especially due to the large number of parameters and phenomena that can affect the result (e.g., temperature, surface roughness, ...) [196]. Since the physical meaning of the lumped element components we use to model the system should always be preserved, usually simpler (approximated) models are to be preferred [185]. This will indeed be our approach, and equivalent circuit models for the biosensor under investigation will be discussed in Chapter 3.

1.4 The Electrical Double Layer at low and high frequencies

If we neglect airborne particles and gas sensing applications [197], electrolytes are the most common ambient where biomolecules can be found, and hence are of primary interest for sensing applications. In particular, all humans and many animals need water electrolytes to survive. Biosensing in electrolyte can however be challenging for a number of reasons, and notably due to the *screening* of the sensor's signals caused by the formation of the *Electrical Double Layer* (EDL) [160]. In fact, while on one hand this phenomenon guarantees high sensitivity to surface reactions, it severely hampers the detection of analytes that are not in close contact with the sensor. In the following we will discuss this aspect in more detail.

When a charged metal surface is put in contact with an electrolyte, ions that have an opposite polarity (with respect to the polarization of the metal surface) are attracted by the charged surface. These ions (called *counter-ions*, due to their opposite polarity) tend to accumulate on the sensor's surface, and thus create a

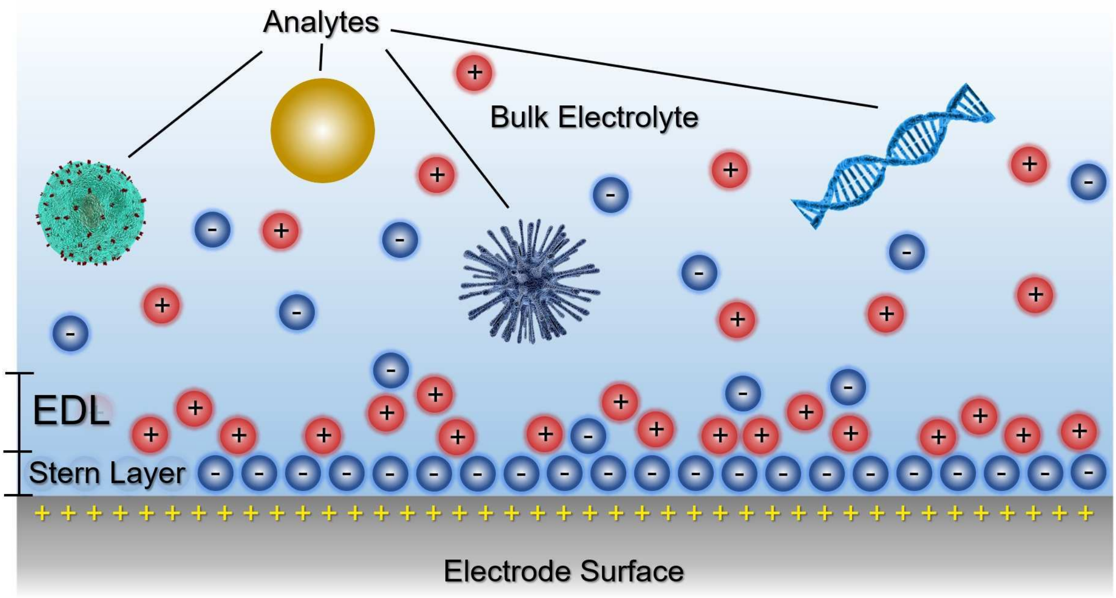

Figure 1.11: *Sketch representing the Electrical Double Layer (EDL). Analytes located far from the sensor's surface are difficult to be detected due to the screening of the electrode's signals.*

dipole and a thin layer with reduced water content and permittivity with respect to bulk electrolyte. The thickness of this layer is in the order of the size of the atoms (a few Å), and it is called *Stern layer*. While counter-ions are attracted to the sensor's surface, for the same reason *co-ions* (ions that have the same polarity as the charged surface) are depleted from the sensor's surface and form the *diffuse layer*. The Stern and diffuse layer together form the so-called electrical double layer, which is accurately described in the continuum by the Gouy-Chapman-Stern theory [198–201] and is schematically represented in Fig. 1.11. The main consequence of the formation of the EDL is that a potential drop occurs at the sensor's surface. The high electric field therein polarizes the water molecules. Therefore, a low-permittivity layer is interposed between the sensor and the bulk electrolyte. This layer hampers the sensing of analytes located far from the sensor's surface [202]. The distance up to which the screening by the EDL occurs is identified by the *Debye length* parameter:

$$\lambda_D = \sqrt{\frac{\varepsilon_{el} k_B T}{\sum_m^{N_{ions}} Z_m^2 q^2 n_{0,m}}} \simeq \sqrt{\frac{\varepsilon_{el} k_B T}{2q^2 n_0}} \tag{1.2}$$

where ε_{el} is the permittivity of the electrolyte, k_B is the Boltzmann's constant, T is the absolute temperature, q is the absolute value of the electron charge, N_{ions} is the number of ions species in the electrolyte, and Z_m and $n_{0,m}$ are the valence and ion concentration of the m-th ion species. Under the simplifying assumption of having a 1:1 symmetric electrolyte [203], the expression can be simplified as in the last term of Eq. 1.2, where n_0 is the ion concentration in the bulk of the electrolyte. Eq. 1.2 highlights the dependency of the Debye length from the inverse of the square root of the ion concentration. The Debye length is roughly 1 nm at physiological salt concentrations.

One possible approach to enable sensing across a larger distance from the electrode's surface is to increase the screening distance (namely, the Debye length) by reducing the salt concentration of the electrolytes [204–206] (the parameter n_0 in Eq. 1.2); however, lowering the ionic strength is not a good solution for the detection of biomolecules since it can alter their properties, or even denature and ultimately destroy them.

Another solution is offered by magnetic beads [75]. Magnetic beads can be linked/coated with receptors such as antibodies, strepadivin, or DNA to obtain a specific interaction with the target, then squeezed against the surface using an external magnet, finally recovering it for further studies. This way, the target analyte can be forcefully moved onto the sensor's surface. This however implies the labeling of the analyte (these magnetic beads are used as tags in place of conventional labels), with the known drawbacks.

A different approach is to operate the biosensor with transient or high-frequency signals [207–209]. In fact, while the low frequency signals are slow enough to allow the ions to move and rearrange themselves (thus forming the screening EDL), high-frequency signals are faster than the dynamics of the single ions. As a consequence, the single ions and the EDL are not given enough time to adjust to the AC bias perturbations. In this case, the electric field penetrates further from the electrode and probes analytes located at a larger distance. Simultaneously, sensitivity to small adsorbates within the EDL is diminished compared to low-frequency detection.

To further address this point, we can consider as a simple model system a hemispherical electrode in contact with a physiological salt concentration (150 mM) electrolyte [210]. By using the model in [211], we can define the relative sensitivity (with respect to the electrode's area) to local (surface or bulk) processes (e.g. the presence of an analyte) as $|\,(r_0 E_r/V)^2\,|$, where r_0 is the radius of the electrode, V is the voltage applied to the electrode, and E_r is the amplitude of the local electric field) [210] (this expression can be derived from [211], where the admittance variation induced by the presence of an analyte was demonstrated to be proportional to the square of the local electric field strength). Three frequency ranges can be identified, discriminated by two distinct frequency points, as shown in Fig. 1.12. The first frequency of interest is the frequency point from which we start to overcome the EDL screening. It is geometry-dependent and is heuristically given by

$$f_1 = \frac{1}{2\pi R_E \left(C_{EDL} + C_E\right)} \tag{1.3}$$

where C_{EDL} represents the capacitance of the double layer, and R_E and C_E are the electrolyte spreading resistance and capacitance, respectively. For an 85 nm radius electrode in 150 mM solution, we have $f_1 \approx 3.3$ MHz. The second frequency of interest is the so-called electrolyte dielectric relaxation cut-off frequency:

$$f_2 = \frac{1}{2\pi R_E C_E} = \frac{\sigma_{E,DC}}{2\pi\varepsilon_E} \tag{1.4}$$

where we indicated as $\sigma_{E,DC}$ the DC conductivity of the electrolyte, and as ε_E its permittivity. Again, for an 85 nm radius electrode in 150 mM solution, we have

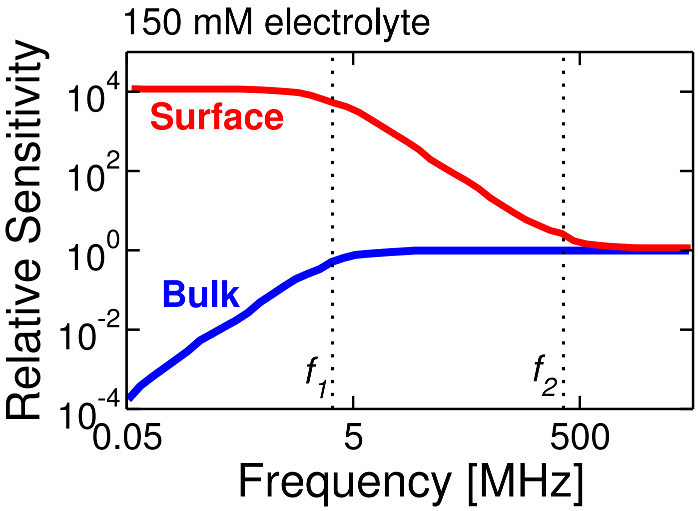

Figure 1.12: *Relative sensitivity to surface and bulk processes as a function of frequency for a simple model system (hemispherical electrode with* r_0 *=85 nm radius). The relative sensitivity is defined as* $|\,(r_0 E_r/V)^2\,|$ *(where* V *is the voltage applied to the electrode and* E_r *is the amplitude of the local electric field) [210]. See also Tab. 1.1.*

$f_2 \approx 360$ MHz. For this model system, the two frequencies can be related to each other as:

$$f_1 \approx \frac{f_2}{1 + \frac{r_0}{\lambda_D}} \tag{1.5}$$

where $\lambda_D \simeq 0.8$ nm is the Debye's length.

We can thus create Table 1.1, representing the sensitivity properties at the different frequency ranges.

Frequency range	**Bulk sensitivity**	**Surface sensitivity**
$f < f_1$	Low “blocking” double layer	High saturated at low frequency
$f_1 < f < f_2$	Nominal “transparent” double layer	High still exceeding bulk sensitivity
$f > f_2$	Nominal “vanished” double layer	Nominal same as bulk sensitivity

Table 1.1: *Relative sensitivity to surface and bulk electrolyte: identification of the main frequency ranges and the related properties. See Fig 1.12. Table adapted from [210].*

As f_2 is approached, the AC field from the nanoelectrode penetrates fully the electrolyte and measurements become less sensitive to hardly controllable surface defects and contamination. Hence, being able to operate at frequencies higher than the dielectric relaxation frequency is extremely convenient, even though very challenging (as will be discussed later).

Considering large (millimeter-sized) electrodes, f_1 can be lower than 1 kHz. Being able to probe analytes far from the electrode's surface is thus easily achievable for macro-scaled objects; differently, to both overcome the Debye screening and at the same time achieve high sensitivity for the detection of nanoscale analytes, using nanoscale electrodes and frequencies above 1 MHz appears essential.

In this PhD thesis, we will focus on the opportunities offered by operating at frequency $> f_1$ or possibly even $> f_2$. More details about the Physics of electrolytes, and the screening and EDL theory will be given in Sect. 3.1

1.5 Electronic biosensors, high-frequency impedance spectroscopy, and nanoelectrode arrays

While the selectivity of biosensors essentially depends on the properties of the biorecognition layers, performance parameters like sensitivity, dynamic range, and limit of detection strongly depend on the physicochemical properties of the transducer, which can be improved by proper engineering of materials and designs [212]. A way to achieve high sensitivity to macromolecular entities is offered by using nanoelectrodes, with a size comparable to that of the target analyte [209]. In this case, however, the small dimension of nanoelectrodes can severely reduce the event-rates of interactions between a single nanoelectrode and nano-sized analytes (e.g. nanoparticles or viruses) [209]. A solution is offered by employing a large number of nanoelectrodes, individually addressable and organized in dense 2D-matrix structures: this allows to enhance the binding-rates, and enables massively-parallel highly-sensitive sensing [209]. As will be clear in the following, this is essentially enabled by CMOS technology, and it represents the next-level of miniaturization from common microelectrode array (MEA) implementations, namely *nano*electrode arrays (NEA).

Despite its long history, so far Electrochemical Impedance Spectroscopy (EIS) received limited attention at the nanoscale. Recent developments in nanotechnology, however, allow miniaturizing and integrating EIS sensors in CMOS technology [213]. In fact, nanoscale electrochemical devices are perfectly suited as signal transduction elements for integration with solid-state electronics [209], also because the requirements for materials fabrication methods for integrated circuits (IC) and electrodes are mostly compatible. Thanks to the low power consumption and enhanced sensitivity upon miniaturization, electrochemical methods combined with nanoscale electronics pave the way to a number of applications where they can provide outstanding performances. In particular, they enable highly-parallel sensing and high-sensitivity [190, 209, 214–219]. Examples of highly sensitive realizations include the implementation of CMOS DNA sensor arrays [216, 220], the possibility to perform both recording and stimulation of cellular activity [221–226], and capacitance measurements that even achieve the zepto-Farad resolution [227, 228].

EIS is capable of investigating different sample properties at different frequencies. In the absence of faradaic contribution and at low frequencies, it probes the region within the EDL, hence it is very sensitive to chemical processes occurring at the surface of the electrode [209]. However, extending the sensing capabilities beyond the EDL is desirable in a number of applications (for example, just consider that at physiological concentrations the Debye length is much smaller than the size of a regular IgG antibody or a virus, see Fig. 1.9), and a limited ability to do so has proven a major hurdle for transducers based on field-effect detection [51, 202, 229–231].

As discussed in the previous section, operating at high-frequencies is an elegant solution to overcome the Debye's screening. However, high frequencies of operation is a noted obstacle for integrated impedimetric biosensors, and it hampers the detection of analytes far from the sensor's surface [51, 207, 229, 230, 232]. In fact, the admittance of individual nanoelectrodes in contact with physiological solution is in the order of femto-Farad [160], i.e. orders of magnitude smaller than the capacitance of sub-cm long coaxial-cables. Performance of conventional EIS systems are in fact limited by stray capacitance, and rarely exceed 1 MHz operating frequencies [206, 233, 234]. As a result, very few groups developed approaches to perform EIS with nanoscale electrodes.

One possible approach to address the issue is to connect multiple nanoeletrodes in parallel, in such a way that the total admittance becomes larger than the admittance of the interconnection: this way, it is possible to probe analytes beyond the EDL, at the price of having to rely on measurements averaged over multiple electrodes. Interdigitated electrodes [235] and nanogap electrodes [236] are slight variations of this approach. Alternatively, frequency-mixing can also be applied: exploiting the non-linear behavior of ISFET sensors, the response to modulated high-frequency excitations can be converted to low frequency for the actual extraction of the information [207, 237].

Operating individual nanoelectrodes at high frequency at physiological salt concentrations can thus be achieved only by substantially reducing the parasitic impedance. In turn, this is only possible with advanced CMOS fabrication processes [190, 238, 239] and co-design approaches of electrodes and electronics [240]. In fact, the desire to reach high modulation frequency at the nanoelectrodes (to overcome Debye screening) forced to use simple and compact stimulus/readout circuitry for the implementation of the biosensor described in this thesis (as the CBCM technique can provide). As will be clear in the following, staying close to the most advanced CMOS processes is also necessary to maximize the signal-to-noise ratio. The opportunities offered by advanced CMOS technology, in particular the capability to implement high-performance low-power circuits, with record integration density and nearly 100% yield, make CMOS-based nanobiosensors a most-promising technology, in such a way that it can be envisioned that "what can be sensed by CMOS will be sensed by CMOS" [210]. Relying on the most advanced CMOS process thus enables to perform high-frequency impedance spectroscopy (HFIS) at nanoelectrodes for label-free real-time detection and imaging. Finally, another advantage of CMOS-based devices that should be mentioned is the low-cost. While a single microscope for optical systems costs 30-400 k$ (depending on the application), the cost of a single CMOS chip is 4-5 orders of magnitude lower (depending on the production volume)[2]. This enables massively parallel imaging, with a large number of chips

---

[2] the advantage in terms of cost is especially visible under the hypothesis of having re-usable chips, as is to a large extent the case with the chips discussed in this work (better explained in Sect. 4.3).

running in parallel.

All the aforementioned benefits offered by CMOS technology are integrated in the CMOS pixelated biosensor platform described in this thesis, which is devoted to investigating high-frequency impedance spectroscopy and imaging of a large variety of analytes. The platform is suited for many applications, including but not limited to: determination of concentrations of analytes, cytometry, real-time imaging of the behavior of cells, identification of the efficacy of bactericidal treatments for food-industry applications (e.g. discrimination between live and dead cells), selective identification of analytes (by means of surface functionalization), ...

1.6 Summary and scope of the work

In this chapter we have introduced the motivation for intense developments of sensors for health applications and provided a general description of different kinds of nano-biosensors. We have highlighted a few interesting properties that would be desirable in advanced nanobiosensors, such as label-free detection, real-time imaging mode of operation, capability to detect analytes at the nanoscale with high sensitivity and selectivity, massively-parallel and high-throughput capabilities. Electronic nanobiosensors based on impedimetric measurements at NEAs address these target properties in a competitive way compared to common optical methods and have huge potential of improvement.

In the context of electronic biosensors, we have seen that advanced CMOS technology provides crucial benefits. In fact, thanks to the continuous improvements of CMOS technology [241], higher frequencies, smaller electrodes, and higher array densities will be possible [209]. Provided that the SNR is maintained, smaller electrodes enable detection at the level of single-molecules (see Fig. 1.9); higher array densities enable spatial resolution superior to optical imaging; higher frequencies of operation enable to exceed the electrolyte dielectric relaxation cut-off frequency (f_2, beyond 300 MHz at physiological salt concentrations), thus accessing a frequency range where the response is independent of the ionic conductivity of the electrolyte itself, and therefore improving the robustness of the sensing [209]. Also the co-design of electrode and electronic readout circuits is of fundamental importance.

Until now, very few platforms revealed the capability to operate at frequencies above 1 MHz or as high as 50 MHz [214,238,242,243] combined with high-resolution label-free real-time imaging of particles, cells, and emulsions. The CMOS pixelated nanocapacitor biosensor platform developed by NXP Semiconductors [190,209,214, 215] is thus a unique system in the nanobiosensors scenario: it implements a matrix of 256×256 nanoelectrodes (when immersed in fluid they form metal/liquid nanocapacitors) enabling massively-parallel label-free real-time dynamic imaging and HFIS beyond the dielectric relaxation cut-off frequency of the electrolyte up to nearly physiological salt concentrations (maximum frequency of operation: 70 MHz).

Proof of concept demonstration of the detection and imaging of a number of different analytes has been given with this platform (microparticles, nanoparticles, cells, oil emulsions, viruses) [190,209,214,215]. However, quantitative analysis of the results and detailed understanding of the measurement dependencies in the system parameters is still lacking.

It is thus the purpose of this thesis to investigate the potential of this innovative platform for quantitative nano-biosensing applications. In particular, the main goal of this work has been to improve the measurement system and demonstrate its capabilities from the quantitative point of view (with the aid of analytical, numerical and statistical models), possibly understanding and characterizing all the main effects that might influence the outcome of experiments.

The thesis is structured as follows (the corresponding author's references are linked):

- **Chapter 2** presents the CMOS pixelated nanocapacitor biosensor platform at the basis of this PhD thesis. The concept and implementation of the CMOS chip, the realization of a temperature control system and a microfluidic setup are discussed, together with a comparison with state-of-the-art chips for impedance sensing. The content of this chapter was partly published in [209] [190].
- **Chapter 3** presents analytical, numerical and statistical models to aid the study of nanoelectronic biosensors and analytes. The topics covered include: an introduction to the nanobiosensor simulator (ENBIOS) used in this thesis, the implementation of two simulation tools for the nanoHUB.org portal [244] [245] [246], an analytical model to interpret measurements performed by means of CBCM (as is the case for the NXP platform) [190], a methodology to simulate (by means of ENBIOS) the response of a biosensor due to arbitrarily-shaped input voltage waveforms, a compact-model and simulation study of the HFIS response of the nanoelectrodes to small viruses [247] [248], a parameter-estimation and uncertainty quantification statistical approach based on Bayesian inference [249] [250].
- **Chapter 4** presents experiments in uniform environments (electrolytes, without analytes) [190]. The implementation of calibration strategies to avoid and/or compensate systematic errors are discussed [190], analyses of possible root causes for residual discrepancies between simulations and measurements are presented [251], and the parameter-estimation statistical approach is used to determine system parameters [249] [250]. At least one more journal paper is in preparation on these topics.
- **Chapter 5** presents results in the presence of analytes. Oil droplets are considered as a test case to implement calibration curves to estimate the size of analytes, experiments with dielectric microparticles are presented together with Bayesian extraction of parameters, conductive microparticles are extensively analyzed to understand their peculiar features, and simulations of nanoparticles are performed to reveal the platform detection limits. At least one more journal paper is in preparation on these topics.

The work of this thesis thus spanned a wide range of activities: modeling, numerical simulations, calibrations, implementation of experimental setups, experiments with subsequent verification and interpretation of results, statistical analyses. These activities have been enabled by a network of collaborations, in particular:

- NXP Semiconductors (Dr. Frans Widdershoven), who provided us the CMOS biosensor platform most of the activity of this PhD has been based on, and constantly suggested ideas and models to aid the interpretation of experimental results and to design new experiments;

- University of Twente (Prof. Serge G. Lemay, Dr. Cecilia Laborde, Dr. Christophe Renault), who performed a significant part of the experiments shown in this thesis and provided the corresponding measurements;

- Technical University of Wien (Prof. Clemens Heitzinger, Dr. Jose A. Morales Escalante, Leila Taghizadeh, Benjamin Stadlbauer, Daniel Pasterk), who developed the Markov-Chain Monte Carlo statistical analyses approach and performed the Bayesian estimation analyses.

2 CMOS Pixelated Nanocapacitor Biosensor Platform

In this chapter we describe the CMOS pixelated nanocapacitor biosensor chip (originally developed and kindly provided by NXP Semiconductors) which is at the basis of this PhD thesis [190]. The chip is an improved version of a 90 nm CMOS integrated circuit featuring a nanocapacitor array, readout and A/D conversion circuitry, and a Field Programmable Gate Array (FPGA)-based interface board with NIOS II soft processor [190]. In particular, we describe the assembly of a microfluidic and temperature-control packaging, which turn the chip into a fully-electronic label-free biosensing platform capable to operate at high frequency and thus to overcome the Debye screening limit over a wide range of electrolyte salt concentrations.

Sect. 2.1 describes the NXP chip processing, the PCB, and the socket. Sect. 2.2 and 2.3 present the microfluidics, the temperature control setup, and the mounting we implemented at the Nanoelectronics Lab in Udine. We leave to next chapters the detailed description of the calibration and compensation procedures we developed to reduce systematic errors (Chapter 4). Finally, in Sect. 2.4 we present a benchmark analysis of the platform compared to other implementations.

We acknowledge F. Widdershoven (NXP Semiconductors) for developing, sharing the fabrication details, and providing us the chips and the board, and Prof. M. Sortino (University of Udine, LAMA FVG Advanced Mechatronics Laboratory) for the help with drilling and 3D printing operations (Sect. 2.1.3 and 2.2).

The content of this chapter is partly published in [190] [209].

2.1 The chip and the board

2.1.1 Concept and implementation

The core of the chip consists of 65,536 individually addressable gold-copper nanoelectrodes of 90 nm nominal radius, arranged in a 256×256 array with 550nm×720nm, 600nm×720nm or 600nm×890nm column/row pitch (different chip versions). The chip has been designed for Charge Based Capacitance Measurements (CBCM) [189] at switching frequencies up to 300 MHz. Fig. 2.1 shows a chip photo, highlighting the main circuit blocks, Fig. 2.2 shows the organization and architecture of the array of nanoelectrodes, Fig. 2.3 shows an essential schematic of one sensor cell and column read-out circuit, and Fig. 2.4 shows a block diagram of the main components of the sensor and control-board architecture.

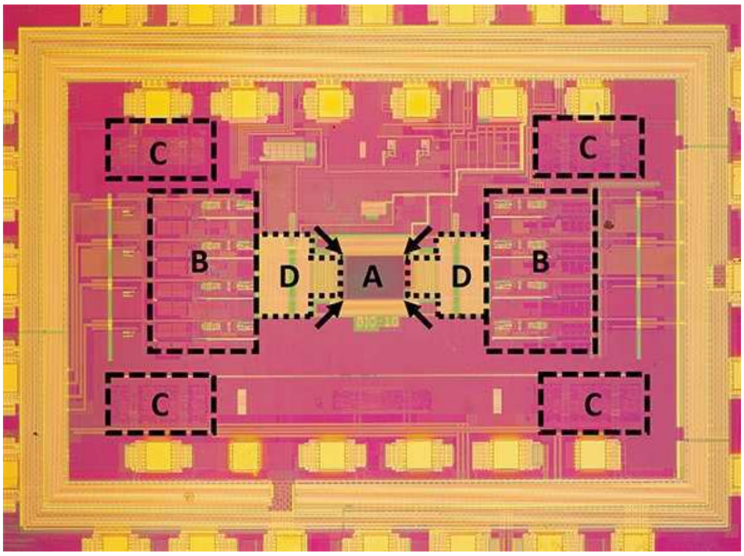

Figure 2.1: *Photo of the chip, highlighting the matrix of 256×256 nanoelectrodes (A), the 4 temperature sensors (arrows), the 8 A/D converters (B), the 4×64 data accumulation registers (C), and the 2×128 column read-out circuits (D). The chip size is 3.2×2.1 mm^2. Published in [190].*

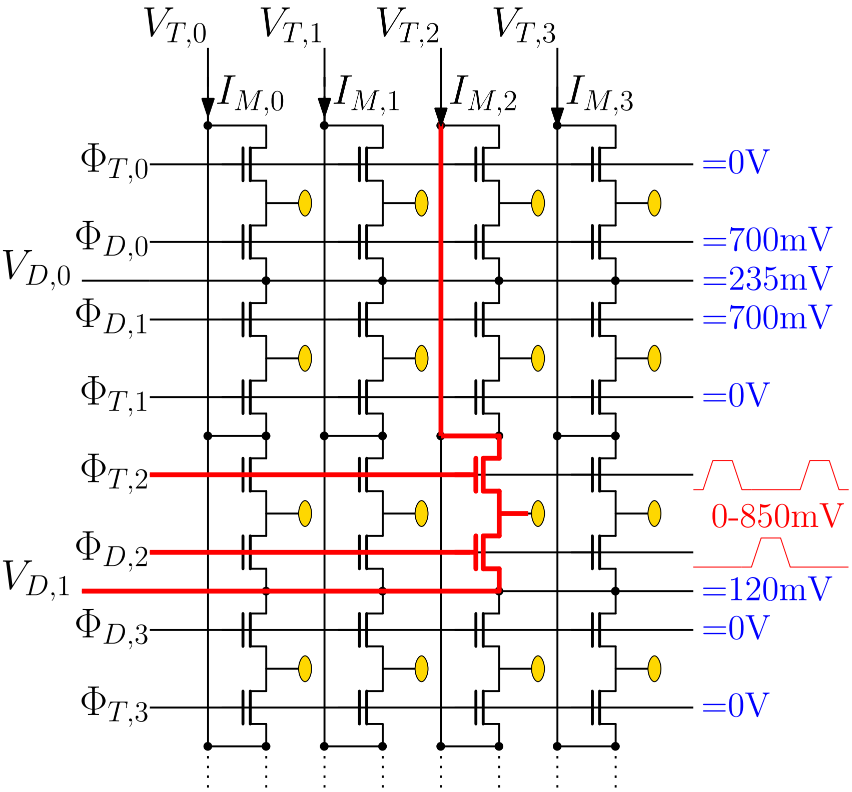

Figure 2.2: *Architecture of the array, highlighting in red a single sensor cell. The gold disks represent the nanoelectrodes. Published in [190].*

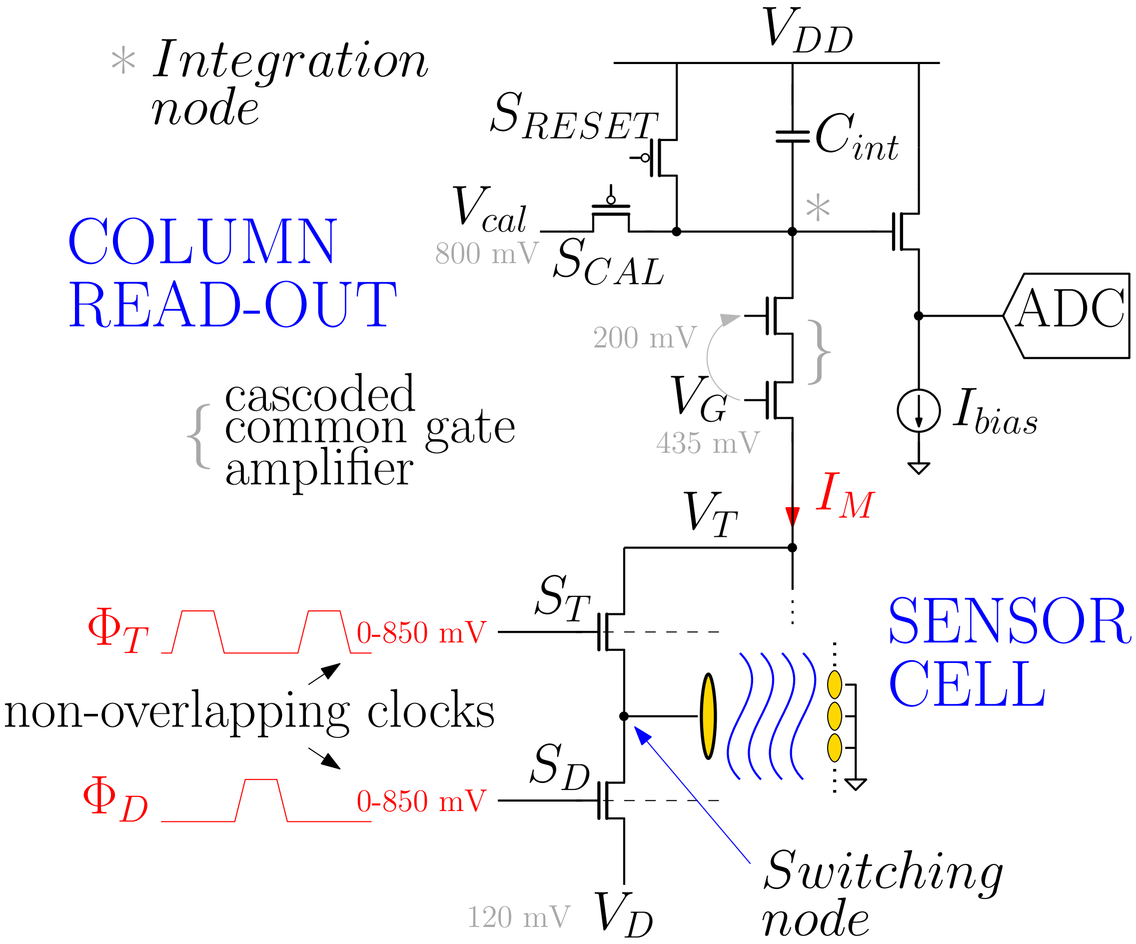

Figure 2.3: *Schematic of a selected sensor cell (see also Fig. 2.2), coupled to its column read-out circuit. Gold disks represent the nanoelectrodes. The cascoded common gate amplifier controls the column voltage* V_T*, and passes the column current* I_M *to the integration capacitor* C_{int} *(480 fF).* I_M *is equal to the average sensor cell current (averaged by the column's parasitic capacitance). At the end of a charge integration period (started by opening switch* S_{RESET}*), the ADC samples the voltage on the integration node (labeled *). Immediately after, it samples the calibration voltage* V_{cal} *(800 mV), passed to the integration node via switch* S_{CAL}*, and converts the difference of the 2 samples. This implements a Correlated Double Sampling (CDS) scheme, which suppresses* $1/f$ *noise and drift in the A/D conversion path. Typical voltage values are also indicated. Published in [190].*

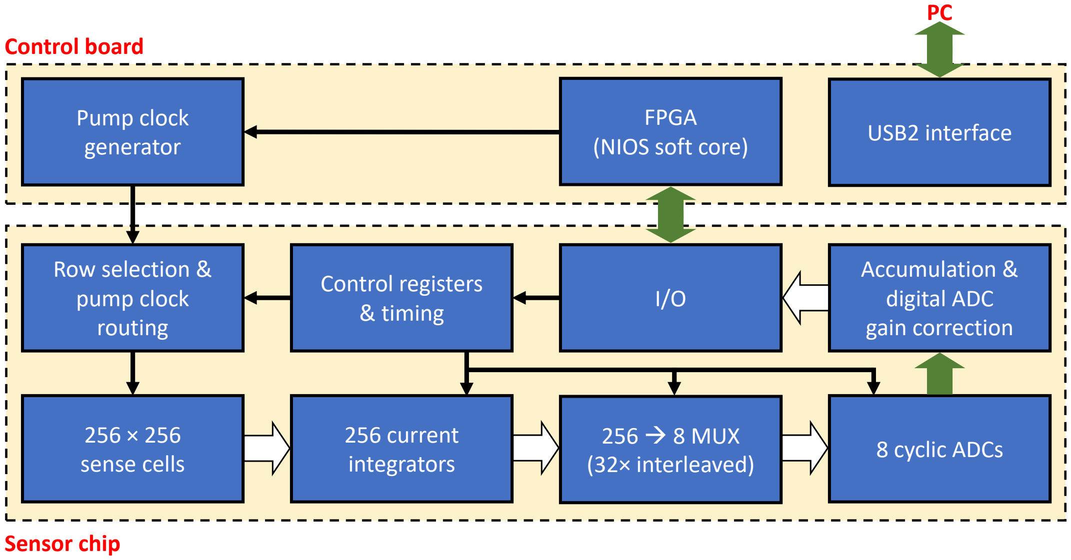

Figure 2.4: *Architecture of the sensor chip and control board (image adapted from [214]).*

CBCM is implemented with two minimum-size ($W/L = 200\text{nm}/90\text{nm}$) switch transistors S_T and S_D per sensor cell, that repetitively charge and discharge the capacitance of a nanoelectrode, connected to the switching node, to the potentials V_T and V_D, respectively. S_T and S_D are controlled by off-chip generated non-overlapping clocks (Φ_T, Φ_D) with programmable frequency and pulse shapes. To avoid interference in ground return paths on the chip, Φ_T and Φ_D are imported on the chip as 2 differential clock pairs, that are routed differentially all the way to the row selection circuitry alongside the array, where the non-inverted clock signals are passed on to a selected row of sensor cells. The clock waveforms for measurements at 50 MHz switching frequency typically have 1 ns rise and fall times, 7 ns high times, and 10 ns delay between the Φ_T and Φ_D pulses. Clock waveforms at different frequencies maintain the same rise/fall times, while scaling the high time and the delay accordingly. These parameters can be programmed via the chip control software.

A full row of 256 sensor cells is selected (e.g. row $m = 2$ in Fig. 2.2) by passing the clock signals Φ_T and Φ_D, and the discharge potential V_D, to the row's $\Phi_{T,m}$, $\Phi_{D,m}$ and $V_{D,k}$ terminals ($k = \left\lfloor \frac{m}{2} \right\rfloor$, where the floor operator $\lfloor \cdot \rfloor$ rounds down to the nearest integer; i.e. $\Phi_{T,2}$, $\Phi_{D,2}$ and $V_{D,1}$ in the example) via on-chip analog switches, controlled by an on-chip row decoder. All other rows (i.e. rows 0, 1, 3, 4, ... in the example) are disabled with a logic low DC potential on their respective $\Phi_{T,m}$ terminals.

The nanoelectrodes of the adjacent row, that shares the same $V_{D,k}$ line with the selected row (i.e., row 3 and line $V_{D,1}$ in the example), are made floating with a logic low DC potential on that row's $\Phi_{D,m'}$ terminal ($m' = 4\left\lfloor \frac{m}{2} \right\rfloor - m + 1$; i.e. $\Phi_{D,3}$ in the example). This insulates these nanoelectrodes from the discharge potential V_D.

A "fluid" DC potential V_{FL} is put on the $V_{D,k'}$ lines of all other non-selected rows ($k' \neq k$; i.e. $V_{D,0}$, $V_{D,2}$, $V_{D,3}$, ... in the example), and passed on to the nanoelectrodes by putting a logic high DC potential on the respective $\Phi_{D,m''}$ terminals ($\left\lfloor \frac{m''}{2} \right\rfloor \neq k$; i.e. $\Phi_{D,0}$, $\Phi_{D,1}$, $\Phi_{D,4}$, $\Phi_{D,5}$, ... in the example). These electrodes provide an AC return path for the modulation signal on the selected nanoelectrodes.

This selection scheme effectively constitutes a single large reconfigurable on-chip counter electrode, at a DC voltage V_{FL}, that is typically set to the time-averaged DC level of the modulation signal on the selected nanoelectrodes. With this row selection scheme and V_{FL} potential, the long-term net DC charge transport through all nanoelectrode surfaces, mediated e.g. by redox-active species in the fluid, is always averaged out to zero, preventing unwanted electrochemical modifications of the electrode surfaces. This is an important prerequisite for long-term stable measurements in electrolytes.

The array and row-selection electronics of the chip version with the largest (890nm) row pitch are slightly modified: each row of nanoelectrodes has its own selectable discharge line, so that the nanoelectrodes of both non-selected rows adjacent to the selected row can be connected to V_{FL}. This way, the adjacent row of electrodes is not floating; instead, the selected nanoelectrodes are surrounded by a fully symmetrical AC return path, at the expense of a slightly larger sensor cell area. In the array of the chip version with 550nm column pitch, odd and even columns are placed mirror-imaged with respect to each other. This way, groups of 2×2 sensors cells can share a single discharge line contact. This gives the smallest sensor cell area, at the expense of non-identical misalignment sensitivity of the odd and even sensor cells of a selected row. The latter can result in well defined measurement patterns, clearly visible in capacitance maps.

This combination of small-radius actively modulated on-chip nanoelectrodes with a much larger reconfigurable counter electrode at micrometer proximity is a critical enabler for CBCM at MHz - GHz switching frequencies, without being limited by the electrolyte series resistance. To be able to reach a similar high-frequency operation with off-chip modulation, the electrolyte series resistance, loaded by the parasitic capacitive coupling to the entire wetted chip surface (including disabled nanoelectrodes) surrounding the selected nanoeletrodes, would require placing a large external counter electrode plate at few-micrometer distance above the chip surface. Apart from the fact that such a system cannot be manufactured without drastically modifying a mature CMOS flow, the narrow gap between the counter electrode and the chip surface would constitute a huge resistance for the fluid flow. Such a system, if reliably manufacturable at all, would be very impractical.

The capacitance of a nanoelectrode in $(row, column) = (i, j)$ is determined by selecting row i, and measuring the average charge/discharge DC current I_M per cycle of column j (see Fig. 2.2 and Fig. 2.3). Therefore, the measurement capacitance (C_M) can be expressed as:

$$C_M = \frac{Q_s}{\Delta V} = \frac{I_M}{f_s \Delta V} \tag{2.1}$$

where f_s is the switching frequency, $\Delta V = V_T - V_D$ is the charge/discharge modulation amplitude, and Q_s is the average charge transferred through the sensor cell per charge/discharge cycle (if we indicate as Q_{TOT} the total charge transferred by a sensor cell in N_{cyc} switching cycles, we can express $Q_s = Q_{TOT}/N_{cyc}$). While the discharge node of the nanoelectrode (at voltage V_D) is directly controllable, the transfer voltage node (at voltage V_T), instead, is not directly accessible and it is controlled only in an indirect way via the cascoded common gate amplifier (see Fig. 2.3). The measurement capacitance information thus requires to make an assumption on the value of V_T, which we indicate as $V_{T,E}$. Consequently, the measurement capacitance provided by the platform can be expressed as Eq. 2.1 using $\Delta V = V_{T,E} - V_D$. Differences between the *a-priori* definition of $V_{T,E}$ and the actual value of V_T can be easily corrected after the measurement (see Chapter 4).

Typical values of V_D and V_T are in the ranges of 80 – 160 mV and 280 – 360 mV, respectively, with a maximum $V_T - V_D$ of 200 mV. For typical values of C_M in the range 0.6 – 4 fF, the maximum column current I_M at $f_s = 70$ MHz is 56 nA. Therefore, the input transistor (W/L = 600nm/300nm) of the common-gate amplifier in Fig. 2.3 is always biased in the sub-threshold regime.

The voltages of the charge-integration nodes (* in Fig. 2.3) of the 256 column read-out circuits are digitized by 8 analog-to-digital converters (ADC), running in parallel (Fig. 2.4).

The 13-bit ADCs have a cyclic "1.5 bit/cycle" architecture, with built-in noise suppression (by Correlated Double Sampling (CDS), see caption of Fig. 2.3), similar to the ADC described in section 3B of [252] (same architecture but different component values; for convenience, the architecture of [252] is reported in Fig. 2.5). They run at clock frequencies of 1 – 45 MHz, that can be derived from the non-overlapping clocks with an on-chip clock recovery circuit and an optional clock divider (divide-by-2; required for non-overlapping clock frequencies of 45 – 90 MHz). For non-overlapping clock frequencies above 90 MHz, the ADC can be clocked with an external clock. In practice, we always use the clock recovery circuit combined with the clock divider, to guarantee a 50% duty cycle for the ADC clock.

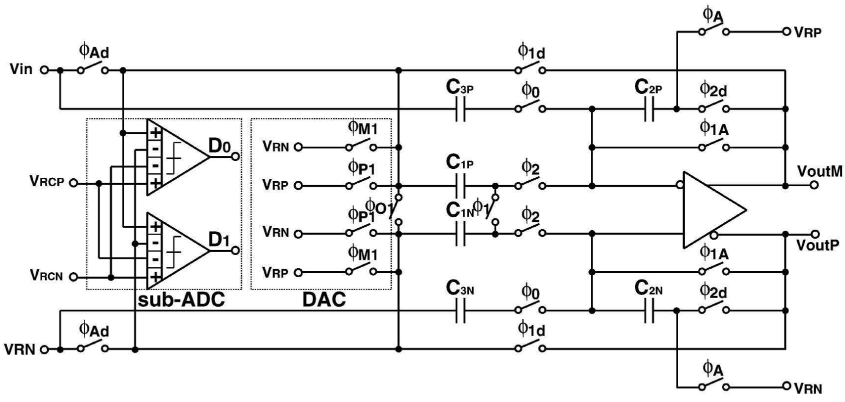

Figure 2.5: *Architecture of the "1.5 bit/cycle" ADC with built-in noise suppression of [252]. Image taken from [252].*

Although the ADCs have been designed for 13 bits resolution, their actual resolution is limited to 9 – 10 effective number of bits[1]. The root cause of this limitation is still not fully understood, but it involves a correlated noise or cross-talk component that cannot be averaged out. Although this limits the sensitivity of single-electrode capacitance measurements to 0.5 – 1 aF (1-sigma noise level), it does not block the

---

[1] a value that is also related to the switching frequency

use of the chip for many interesting single-particle detection and imaging applications (see Sect. 5.3), or applications where signals of multiple nanoelectrodes can be averaged (e.g. for protein or DNA/RNA detection).

Each ADC processes a group of 32 consecutive odd or even columns in time-division multiplexing mode (MUX not shown in Fig. 2.3). In particular, even/odd columns are processed by the ADCs located on opposite sides of the chip (left and right B-areas in Fig. 2.1, respectively). With the clocks Φ_T and Φ_D of the selected row running continuously, the charge integrators of the 32 columns are started one after another at integer multiples of the number of clock cycles required for 1 A/D conversion (this number depends on the settings of the ADCs). After integration for a programmable number of non-overlapping clock cycles (which determines the integration time), the voltage on the charge-integration node of a column is sampled by the A/D converter, applying CDS, and subsequently reset and restarted, while the other 31 charge integrators continue integrating. Then the next column is processed. This sequence through 32 consecutive columns is repeated $1 - 127$ times (programmable), where the ADC outputs are column-demultiplexed, and accumulated in 256 on-chip data accumulation registers (the 4 blocks labeled "C" in Fig. 2.1; see also Fig. 2.4).

After data accumulation is completed for all columns, the contents of the 256 registers are exported via a serial output bus (Fig. 2.4). Then the next row is selected and processed (to avoid cross-talk from the serial output bus, charge integration is postponed during serial output). Fig. 2.6 shows a representation of this row-wise activation of the nanoelectrodes.

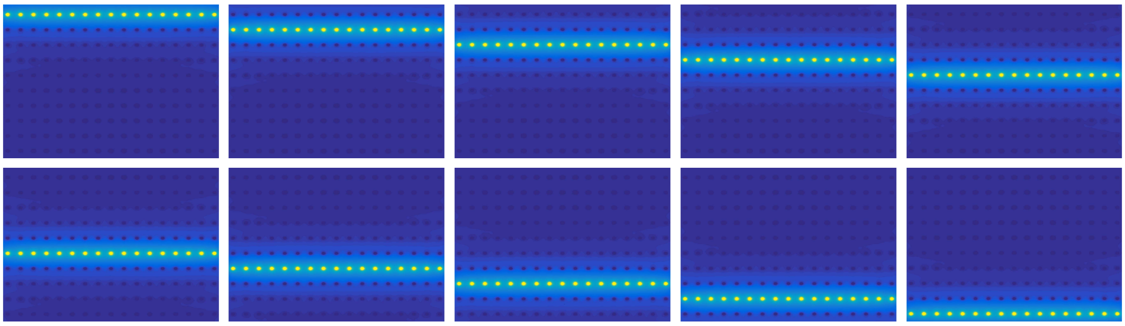

Figure 2.6: *Sequence of AC voltage maps (at 50 MHz in a 150 mM electrolyte, obtained by means of simulations, as described in Sect. 3.2) representing the row-wise activation of the nanoelectrodes of the platform. The bright yellow circles are the activated working electrodes, whereas the dark-blue circles are the de-activated counter electrodes.*

On-chip accumulating the ADC outputs of a full row of 256 selected sensor cells can be used for increasing the signal/noise ratio and decreasing the serial-out duty cycle (during which the sensor does not measure). On a dedicated test board, with clock signals generated by a multi-channel high-frequency pulse generator, connected to the chip by 50-Ω terminated rigid coax cables, the chip's CBCM circuitry was verified to work properly up to 320 MHz (using externally clocked ADCs). However, for use in biochemical laboratories, the chip is operated in a self-contained system with on-board pulse generation circuitry that can support a maximum non-overlapping clock frequency of 70 MHz (see Sect. 2.1.3).

The lower frequency limit is determined by the leakage currents of the non-selected switching transistors. For switching frequencies below 1 MHz, I_M drops to a level that approaches the total leakage current of all non-selected cells of the same column. This results in non-negligible offset errors in the measured capacitance. First-order corrections for leakage currents (described in Sect. 4.4.1) could not fully remove the errors, suggesting additional effects being involved as well (e.g., the ADCs require a minimum clock frequency to prevent leakage of the charges stored on their capacitors). This issue is subject to ongoing investigation. Pending the results, we limit the lowest frequency to 1 MHz.

The number of switching cycles is typically set to 1408 for most measurements at higher frequencies, but can be reduced if larger values of C_M are expected (e.g. at lower switching frequencies and/or high-salt electrolytes) to keep the voltages on the charge integration nodes within the linear input range of the ADCs. This value is set by the user via the control software. Under nominal operating conditions, the chip produces 4.5 frames/s at 50 MHz switching frequency and 9 on-chip data accumulations per row. With ADC clocks derived on-chip from the switching clock, the frame rate is proportional to the switching frequency. Therefore, at 1.6 MHz it takes about 7 seconds to acquire a complete frame. At a lower number of data accumulations, the frame rate becomes limited by the data transfer time over the serial output bus, with a maximum of about 10 frames/s at 50 MHz.[2] Measurement capacitance images are available in real time. The supply voltage is 1.2 V. With nominal settings, the chip consumes 15 mW at 50 MHz switching frequency (80% by the 8 ADCs).

The variance of the statistical fluctuations in the charge transferred by a sensor cell in N_{cyc} charge/discharge cycles (i.e., in $2N_{cyc}$ switching steps) is [209]:

$$\sigma_Q^2 = 2N_{cyc}k_BTC_M \tag{2.2}$$

where k_B is the Boltzmann's constant. Remembering that Q_s is the average charge transferred through the sensor cell per charge/discharge cycle, and indicating as Q_{TOT} the total charge transferred in N_{cyc} cycles, we can relate the capacitance change (induced for example by the binding of an analyte) $\Delta C_M = C_{M_{w/\ analyte}} - C_{M_{w/o\ analyte}}$, to a charge change as:

$$\Delta Q_{TOT} = Q_{TOT_{w/\ analyte}} - Q_{TOT_{w/o\ analyte}} = N_{cyc}\left(V_T - V_D\right)\Delta C_M \tag{2.3}$$

Consequently, we can express the intrinsic signal-to-noise ratio (SNR) as [209]:

$$SNR = \left(\frac{\Delta Q_{TOT}}{\sigma_Q}\right)^2 = \frac{N_{cyc}\left(V_T - V_D\right)^2\left(\Delta C_M\right)^2}{2k_BTC_M} \tag{2.4}$$

Equation 2.4 motivates the need for advanced CMOS in order to maximize the signal-to-noise ratio:

---

[2] for a given measurement time, increasing the frame rate requires either to reduce the number of switching cycles (which, however, must be chosen in order to guarantee the linear operation of the ADCs) or to reduce the number of data accumulations. A lower number of averages results in a lower suppression of noise, ultimately reducing the accuracy.

- First, ΔC_M increases with decreasing nanoelectrode dimensions, calling for electrodes with a size as small as possible

- Second, decreasing C_M gives less noise. The measurement capacitance can be expressed as the sum two contributions (this point will be extensively discussed in Sect. 3.3, especially in Fig. 3.11): the bare nanoelectrode capacitance and a parasitic capacitance. While nanoelectrodes with a small capacitance still can be made with non-CMOS methods (such as electron-beam lithography), achieving small parasitics really requires the unique sub-micrometer dense integration capabilities of modern CMOS technology.

2.1.2 Chip fabrication and nanoelectrode processing

Manufacturing of the wafers consisted of two main parts: an (almost) standard CMOS part, done by TSMC in a mature production fab (Hsinchu, Taiwan), followed by a post-processing part, done in the cleanrooms of IMEC (Leuven, Belgium) and Philips Innovation Services (Eindhoven, Netherlands).

The initial part starts with a TSMC default 90nm low-power (LP) CMOS flow, processed up to and including the metal-4 Chemical Mechanical Planarization (CMP) step. Next, a 75nm/300nm/150nm (bottom up) nitride/oxide/nitride stack was deposited, which serves as a moisture barrier to protect the underlying CMOS. Via-4 holes (exposed 130nm×130nm), arranged in 256×256 arrays with column/row pitches of 550nm×720nm, 600nm×720nm or 600nm×890nm (on different chip versions), were exposed and etched in the moisture barrier (the etching widens the holes' apexes somewhat). The via-4 holes land on patterned minimum-area metal-4 pads, vertically connected to the common source/drain regions of underlying pairs of switch transistors (the switching nodes in Fig. 2.3) by minimum-area contact/metal-1/via-1/metal-2/via-2/metal-3/via-3 pillars (see Fig. 4 of [214]). Next, 100µm×100µm bond pad openings were exposed and etched in the moisture barrier, using a TSMC-proprietary method that protects the already formed via-4 holes. Then, a Ta/TaN diffusion barrier was deposited conformally over the patterned moisture barrier, also covering the sidewalls and bottom regions of the via-4 holes and bond pad openings. Finally, the high aspect-ratio via-4 holes and bond pad openings were filled simultaneously with a copper layer that extends 1µm above the surface of the moisture barrier (about 0.5µm in the bond pad regions), as needed to be able to planarize the copper with a copper-CMP step in advanced CMOS copper processes. Here the (almost) standard CMOS processing part ends.

The post-processing part starts with transferring the wafers to the IMEC 300mm cleanroom. Here, the copper layers on the wafers were planarized and thinned with a copper-CMP tool, equipped with an eddy current sensor that monitors the remaining copper thickness during polishing. The CMP was stopped at a target thickness of 120nm, to preserve the underlying Ta/TaN diffusion barrier (see next paragraph).

Next, the wafers were cut into 45mm×45mm squares for further post-processing in the pilot cleanroom of Philips Innovation Services. The actual copper thickness was measured on wafer residues. Gold was sputtered on the thinned copper and annealed to inter-diffuse with the copper into a uniform gold-copper alloy. The deposited gold thickness was tuned to end at cubic $Au_{0.66}Cu_{0.34}$ and $Au_{0.3}Cu_{0.7}$

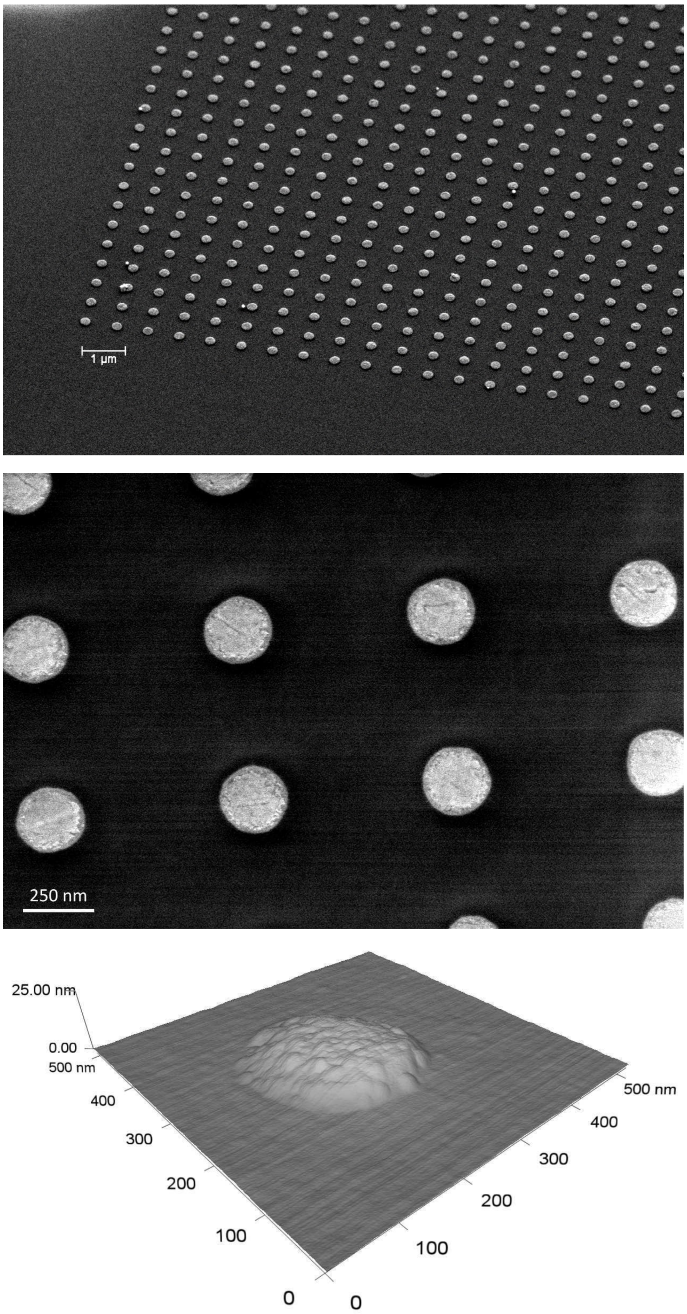

Figure 2.7: *Tilted overview (top) and perpendicular zoomed-in (middle) Scanning Electron Microscope (SEM) images of nanoelectrodes on a 600nm×720nm pitch (white spots in the top picture are polishing slurry particles, left behind because of insufficient post-CMP cleaning). Bottom: contact-mode Atomic Force Microscope (AFM) image of a nanoelectrode protruding 11 nm above the chip surface (the similar-looking hemispherical structures are an AFM tip convolution artifact). Images kindly provided by Univ. Twente. Published in [190].*

phases on the array and bond pad regions, respectively. Cubic phases were chosen to avoid build-up of microscopic stress and defects in the alloy, caused by phase transformations during cooling-down. The gold fractions of the alloys are determined by the average local thickness of the thinned copper layer in the array and bond pad regions. During the anneal, the preserved Ta/TaN double layer acts as a diffusion barrier for copper and gold atoms, to prevent the metals from diffusing into the underlying CMOS layers. In addition, the Ta/TaN is a good adhesion layer for the formed gold-copper alloy, required to prevent delamination from the moisture barrier during subsequent gold-copper polishing. In fact, delamination of gold-copper flakes during polishing can rip nanoelectrodes out of the via-4 holes; this was the main defect mechanism in a first version of the gold-copper manufacturing process that didn't preserve the Ta/TaN double layer and resulted in a large number of faulty electrodes in the array.

The gold-copper alloy was patterned with a damascene-like polishing step that stops selectively on the underlying Ta/TaN diffusion barrier. Then the barrier was removed with a conventional barrier-removal polish step, to electrically separate the nanoelectrodes (Fig. 2.7) and bond pads.

Because, with this approach, all critical geometrical features were defined with state-of-the-art CMOS equipment (193-nm lithography, dry etching) in a production cleanroom with nearly perfect process control, and the gold-copper post-processing flow is essentially like a state-of-the-art copper damascene flow, fully functional sensor chips were made with high yield and low spread. This clearly proves the advantage of staying close to state-of-the-art CMOS processing.

Sensor chips were separated from full-thickness wafers (no backside grinding) by first cutting 100µm wide V-grooves in the saw lanes with a 45°tapered blade, and then cutting though the wafers with a 50µm thick blade. The thick bare dice with 45°beveled front-side edges can be handled conveniently with tweezers, and inserted easily upside-down in a compression spring probe (CSP) socket (Sect. 2.1.3).

2.1.3 Socket, PCB, and FPGA-interface

Disposable bare sensor dice are mounted upside down in an ARIES Electronics CSP (Compression Spring Probes) socket (poly ether ketone, PEEK, material) with gold-plated heat-treated BeCu contacts [253] [254]. The sockets are modified with 2 drilled fluidic ports (500-µm diameter) and an optional milled microfluidic channel (150-µm deep and 500-µm wide) in the bottom (part no. A1924-314-23-2 and A3592-314-23_1, respectively). Fig. 2.8 (bottom-right) shows the version without milled microfluidic channel.

A laser-cut Polydimethylsiloxane (PDMS) guard ring defines and seals the microfluidic chamber, and protects the chip's bond pad ring from the liquids. A PDMS sheet (250 µm thick) was cut at 1000 mm/s speed and 13 W power with a commercial CO_2 laser cutter machine. During the cuts, the PDMS layer sits on a steel metal plate to help heat dissipation, which results in sharper edges. Alternatively, molding of liquid PDMS is possible. In a socket without milled microfluidic, this seal creates a fluidic chamber with a volume of about 50 nL. In a socket with milled microfluidic channel, a similar volume can be realized with a thinner PDMS ring (typically 100-m or less). Fig. 2.8 (bottom-left) shows the PDMS ring placed on the chip. Closing the lid and clamp of the socket presses the chip on the PDMS ring, with its bond pads against the spring pins. As an alternative mounting approach,

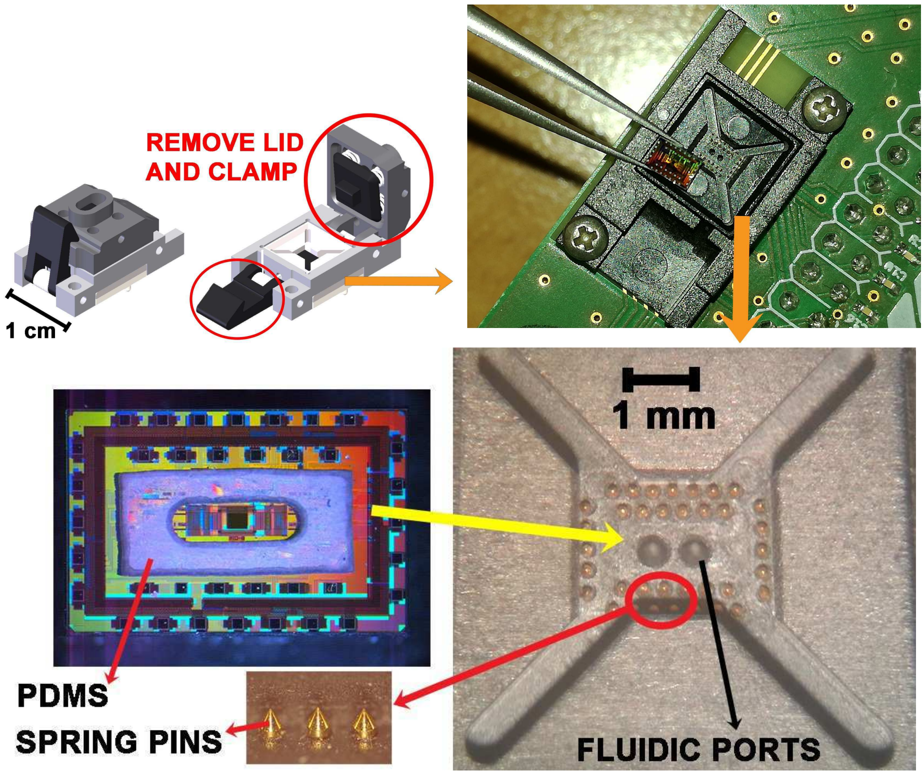

Figure 2.8: *Drawings and photos of the socket and its mounting. Top left: 3D rendering of the socket assembly [254]. The lid and clamp are removed before connecting the socket to the PCB. Top right: photo of the socket mounted on the PCB, together with a chip held with tweezers. Bottom right: detail of the contact spring pins and fluidic ports in the socket. Bottom left: photo of the chip with a PDMS seal ring (the opening, at the center of the seal, is the fluidic chamber that is filled with electrolyte), and optical microscope photo of the spring pins. The chip is inserted upside-down in the socket. Published in [190].*

a 3D printed metal finger (Fig. 2.9 inset) can be pressed on the backside of the chip (instead of the standard lid), thereby creating a good thermal connection to an external temperature control system (Sect. 2.2). Thermal paste ensured a good coupling to the Peltier thermal mass. Use of paste between chip and finger is avoided to prevent the risk of contamination of the fluids in the chamber. Liquids are pumped through the fluidic chamber via PEEK tubes (outer diameter OD=510-µm, inner diameter ID=255-µm), press-fitted into the fluidic ports.

As shown in Fig. 2.8 (top right) and Fig. 2.9, the socket is mounted on a dual-layer PCB, connected with a 40-core flat-cable to a control system, based on an Altera Cyclone III FPGA, partially used to run a NIOS II soft processor. Programmable non-overlapping clock generators are built around an AD9959 direct digital synthesizer (DDS) chip and 2 AD5390 16-channel 14-bit Digital-to-Analog Converter (DAC) chips, both from Analog Devices. The DAC outputs set clipping and offset voltages, and control current sources of a high-frequency analog circuit that transforms the DDS sine-wave outputs into non-overlapping clock pulses with programmable high and low levels, and rise, fall and high times.

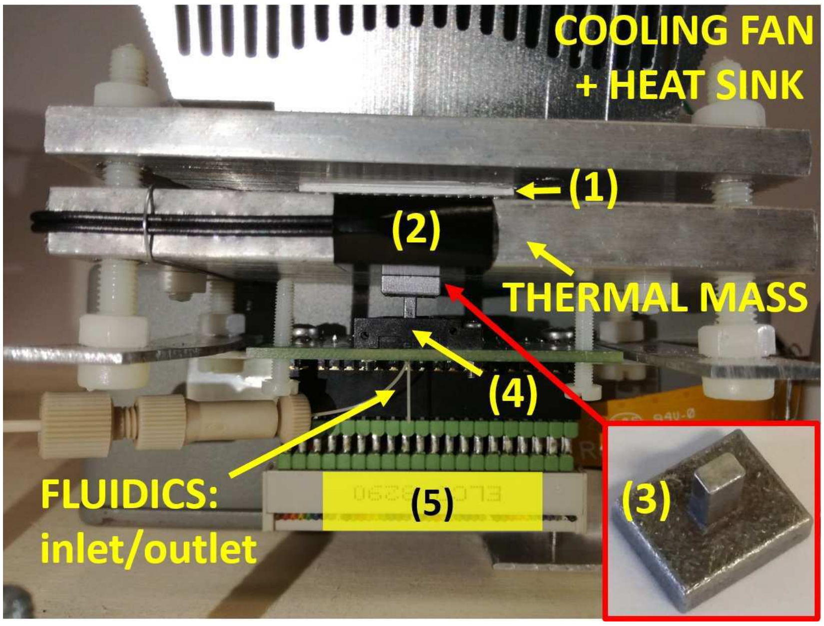

Figure 2.9: *Chip/controller and indication of the various parts. A Peltier element (1) thermally connects the heat sink to an aluminum thermal mass. An NTC temperature sensor (2) is mounted in a small hole in the thermal mass (and is protected by a piece of black adhesive tape to prevent it from moving). Thermal contact to the backside of the chip is created via a 3D printed* $Al_{0.94}Si_{0.06}$ *alloy heat finger (3, inset). The socket (4) is used without lid and clamp. A 40-pin connector (5) and 40-core flat cable provide the electrical connection to the FPGA-based control system. Published in [190].*

The non-overlapping clocks are exported as differential pairs, and routed through signal-ground-signal wire triples over a 5-cm long 40-core flat cable to the sensor chip outside the control system's enclosure. The clock wires are driven by 118-Ω source impedances, that minimize ringing in the clock signals at the sensor chip terminals. To keep the system compact and simple, all other control signals and voltages are routed through adjacent wires of the same flat cable. Residual ringing in the clock signals, caused by the non-ideal transmission line properties of this construction, limits the maximum useful switching frequency to 70 MHz.

The original design of the PCB implemented 400 µm wide holes for the fluidic ports, not wide enough to fit the 510 µm tubes eventually used in this thesis (*Upchurch Scientific* PEEK tubing, part number *1542*). Fig. 2.10 shows a photo of the original holes of the PCB. Since there is enough room for enlarging the hole to the desired size, a re-design of the PCB was not necessary. The holes have been successfully enlarged using a computer numerical control (CNC) milling machine, mounting a 0.55 mm drill bit (we acknowledge support from Prof. M. Sortino and LAMA FVG Advanced Mechatronics Laboratory); this allowed the tubes to be correctly press-fitted in the socket.

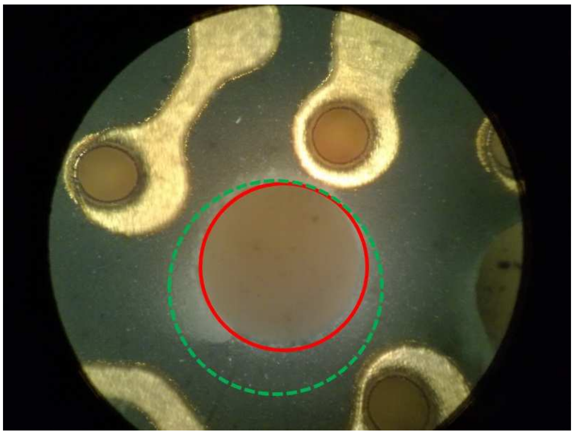

Figure 2.10: *Zoom over one fluidic hole in the PCB. The 400 µm width of the hole (red circle) is not large enough to host the 510 µm tubes. However, there is enough space to enlarge the holes to 510 µm width (dashed green circle) by precision milling.*

2.2 The temperature control system

Being able to operate at well controlled temperature is of critical importance for biosensing. To this end, we developed a temperature control setup based on a Peltier cell.

Fig. 2.9 shows a zoom of the board/socket/temperature control parts. The backside of the chip is pressed by a narrow metal finger, in thermal contact to a thermal mass. The finger was 3D printed in $Al_{0.94}Si_{0.06}$ alloy to ensure low surface roughness and high surface parallelism (we acknowledge Prof. M. Sortino). A temperature control system made of a Peltier cell (model ET-127-10-13), thermal masses (material: Aluminum), and a heat sink with cooling fan were designed to dynamically regulate the chip temperature over a temperature range from 10 to 75 °C (at 22 °C room temperature). This broad temperature range enables to inspect physicochemical phenomena and analytes which are of interest at specific operating temperatures, like for instance imaging of tumor cells (at human body temperature) or DNA hy-

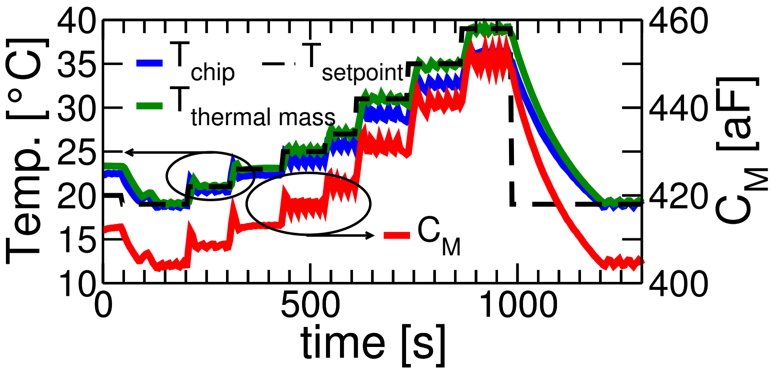

Figure 2.11: *Measurement capacitance (C_M) in air at 50 MHz while dynamically changing the temperature controller set point ($T_{setpoint}$). On-chip and thermal mass temperature sensor readings (T_{chip}, $T_{thermal\ mass}$) are also shown. Published in [190].*

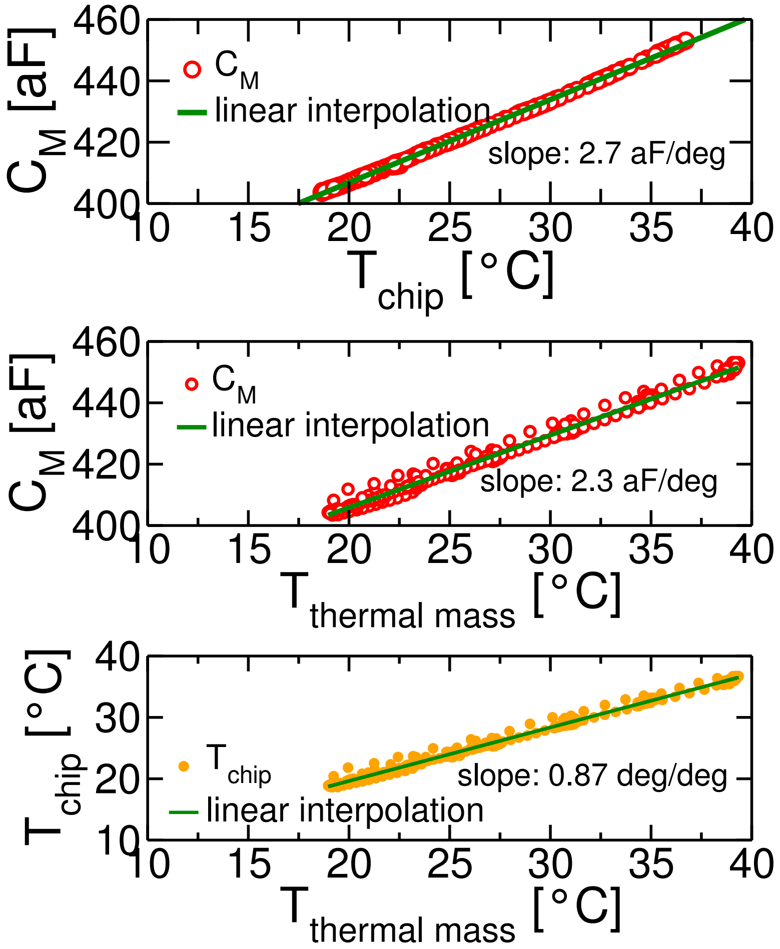

Figure 2.12: *Correlation between the measured quantities of Fig. 2.11. Top: a strong correlation is observed between* C_M *and the on-chip measured temperature. Middle:* C_M *versus* $T_{thermal\ mass}$ *exhibit a small hysteretic behavior, caused by the transients between successive temperature set points (the heat takes some time to flow away from the chip to the thermal mass and finally to the heat sink). Bottom: correlation between the on-chip and thermal mass temperature readings.*

bridization/melting processes (from 50 °C and above). The control algorithm is either a simple on-off sequence or a Proportional–Integral–Derivative (PID) function, where we use a Negative Temperature Coefficient (NTC) thermistor inserted inside of the thermal mass (label 2 in Fig. 2.9) to provide a reference temperature for the Peltier controller (LairdTech PR-59). Fig. 2.11 shows the chip/thermal mass temperature (T_{chip}, $T_{thermal\ mass}$) and measurement capacitance waveforms (C_M) corresponding to a piecewise-constant change of the temperature setpoint (dashed black curve). Measurements are done in air at 50 MHz switching frequency. Here the temperature is intentionally regulated with a coarse on-off algorithm, generating small rapid temperature ripples around the setpoint, to highlight the strong correlation between the chip temperature and the measured capacitance (mainly via the temperature-sensitivity of the gate-source voltages of the sub-threshold-biased bottom transistors of the cascoded common gate amplifiers in the column read-out circuits; see Fig. 2.3). Fig. 2.12 (top) demonstrates a strong correlation between T_{chip} and C_M, as expected, with a temperature coefficient of approximately 2.7 aF/degree. With the signals from the 4 on-chip temperature sensors, this coefficient can be used to compensate for temperature variations during measurements. Fig. 2.12 (middle) demonstrates the correlation between C_M and the temperature reading on the thermal mass, with a temperature coefficient of approximately 2.3 aF/degree. In this case a small hysteresis is present, caused by the transients between successive temperature set points (the heat takes some time to flow from the chip to the thermal mass). Finally, Fig. 2.12 (bottom) shows the correlation between the temperature reading on-chip and in the thermal mass, with a coefficient of approximately 0.87 degree/degree. This proves that the thermal contact between the thermal mass and the chip, via the 3D-printed metal finger, is good.

2.3 Microfluidics

In this section we describe the microfluidics setup we implemented to fill the fluidic chamber of the chip with (sequences of) liquids (electrolytes, with or without suspended analytes). Unless otherwise stated, all the microfluidic components we describe in this Section have been manufactured by *IDEX H&S* [255] (and have been purchased from *Microcolumn S.r.l.* [256]), and are made of PEEK material. In fact, the biocompatiblity of PEEK material provides high chemical resistance to almost all fluids of interest for biosensing [257, 258].

2.3.1 PDMS seal rings

As anticipated in Sect. 2.1.3, a PDMS guard ring is used to define and seal the microfluidic chamber. To fabricate the PDMS seal, we started from a 250 µm thick PDMS sheet (*Shielding Solutions Ltd.* [259], part number *SSP-M823-010*), which was provided as a PDMS sheet attached to an acrylic sheet. A commercial CO_2 laser cutter machine (*LVTC* model family from *Laser Veronese* [260]) was used to cut the PDMS sheet in pre-defined shapes (we acknowledge support from *3D Project Lab* [261]).

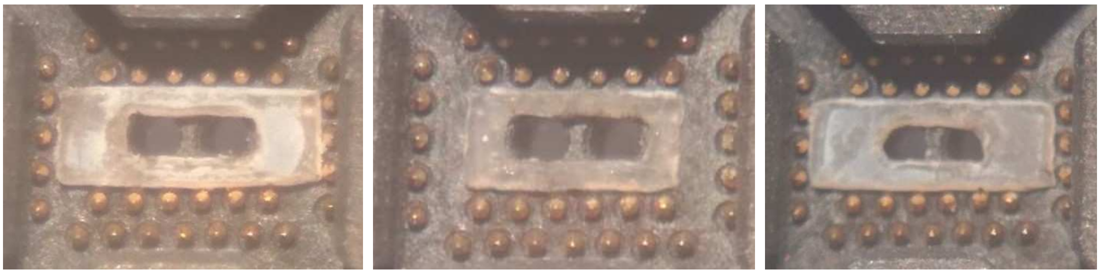

Figure 2.13: *Photo of the PDMS seal inserted in the socket with nominal outer dimension of 1.1×2.9 mm and inner opening of 0.25×1.2 mm. Left: PDMS seal with nominal dimensions. Center: PDMS seal with smaller outer dimension (1.1×2.3 mm). Right: PDMS seal with smaller inner dimension (0.2×1.0 mm).*

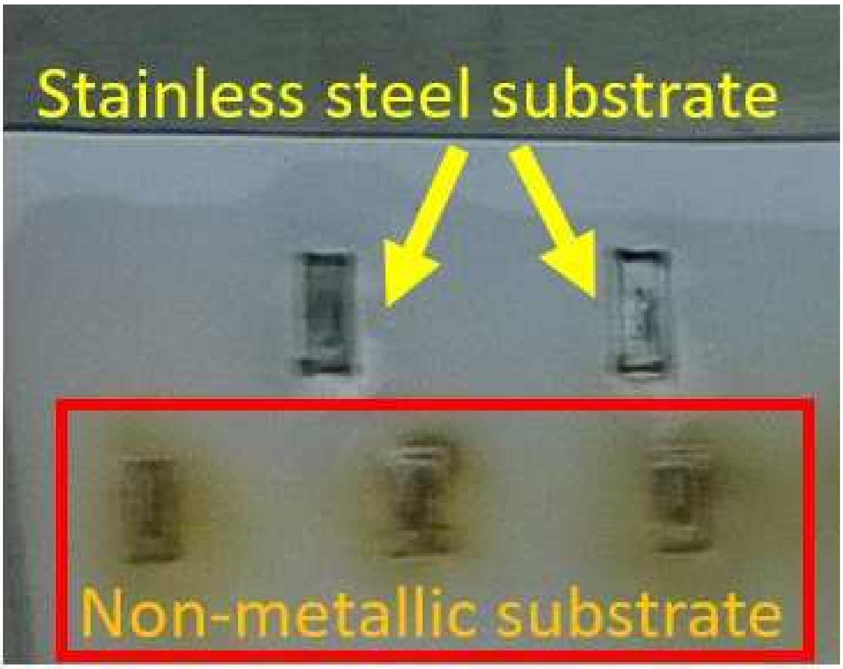

Figure 2.14: *Comparison between PDMS laser cut using a non-conductive (bottom, highlighted in red) or conductive (top, highlighted in yellow) substrates.*

First, the PDMS sheet (along with the acrylic sheet) was positioned on a non-conductive substrate (with the PDMS facing upwards). Different laser power and cut speed have been tested, and the better results (in terms of smoothness of the edges and minimization of burning residues) have been obtained with a speed of 1000 mm/s and 13 W power. Fig. 2.13 (left) shows a PDMS seal ring inserted in the socket. The size of the seal guarantees the electrical connection between the chip and the socket's probes, as well as stability of the seal during mounting (the outer edge nearly touches the spring probes of the socket). Fig. 2.13 (center) shows a seal with smaller outer dimension: due to the smaller width of the seal, during mounting it is more likely to have a misalignment of the central opening w.r.t. the array of the chip. Fig. 2.13 (right) shows a seal with smaller inner dimension: since the seal partly overlaps on the fluidic holes, it is more likely that some liquids leak out of the chamber.

Then, we considered using conductive (stainless-steel) substrates during the cut: in fact, thanks to the thermal conductance of a metal substrate, this allows to reduce the burning effects on the PDMS sheet. This phenomenon is shown in Fig. 2.14, where the advantage of using metallic substrates is clearly visible.

After the cut of the PDMS ring, a cleaning process is required. This is typically performed doing subsequent washing steps in acetone and isopropyl alcohol (IPA), that helps removing the possible laser burning residues. Liquids have been purchased from *Sigma Aldrich* [262].

PDMS is made by polymerizing silicone oil; however 100% polymerization cannot be achieved and this can result in having small amounts of non-reacted silicone oil that slowly diffuse to the surface over time: consequently, the surface of the

PDMS can get hydrophobic (making it hard to remove air bubbles in the fluidic chamber) [263]. To remove residual silicone oil from the PDMS surface, we soak the PDMS seals in IPA, heating it up in a temperature-controlled stove to about 70 °C for a few hours. The beaker in which we place the PDMS+IPA is sealed, in order to avoid evaporation of the hot IPA. This is the final step before using the PDMS seals for experiments.

2.3.2 Injection setup

As introduced in Sect. 2.1.3, liquids are pumped through the fluidic chamber via PEEK tubes, press-fitted into the fluidic ports (this is necessary due to the impossibility of gluing PEEK to the socket for its chemical resistance). Fig. 2.15 shows a sketch of the microfluidics setup we implemented.

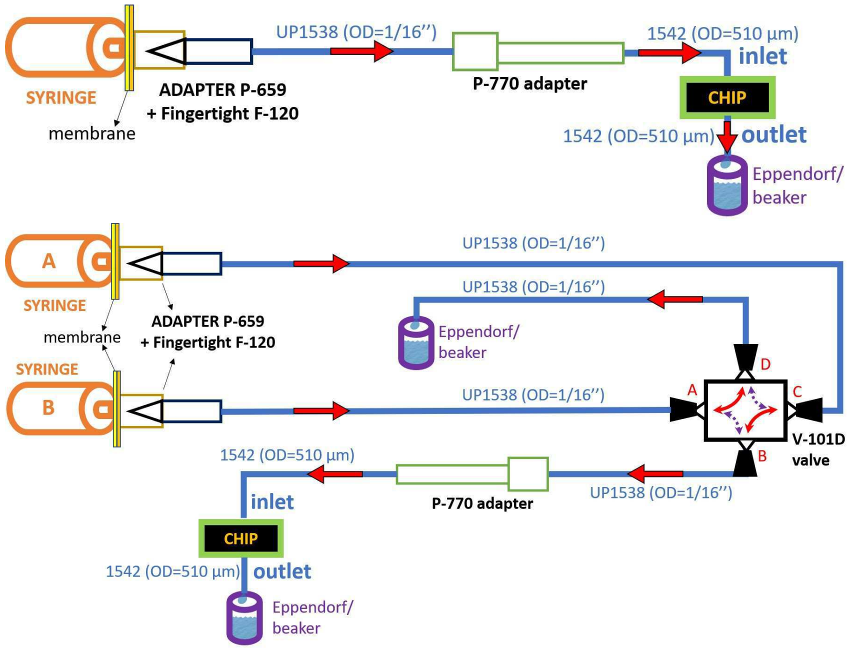

Figure 2.15: *Sketch of the microfluidics setup. Top: simple setup with a single syringe. Bottom: improved setup with a switching valve, allowing for switching between different fluids without introducing air bubbles in the fluidic chamber. Arrows indicate the direction of the liquid flow. See Fig. 2.17 for pictures of the different parts.*

Two PEEK tubes with (OD,ID)=(510µm,255µm) (produced by *Upchurch Scientific*, part number *1542*) are press-fitted into the fluidic ports of the PCB/socket assembly: one tube acts as an *inlet*, one tube as an *outlet* port for the fluids. Liquids going through the outlet tube are collected (but never reused), for instance with a small beaker or with Eppendorf tubes. An adapter (part no. *P-770*) is used to connect the inlet *1542* tube to a common (OD,ID)=(1/16in,0.04in) tube (part no. *UP1538*). A tube sleeve (part no. *F-187*) is used to fixate the *1542* tube in the adapter. A disposable syringe is used to inject the fluids into the system. Another adapter (part no. *P-659* and *fingertight F-120*) is used to link the Luer-Lock connector of the syringe to the tube. A membrane can also be connected at the output of the syringe if required, e.g. to filter possible impurities larger than a certain dimension.

This minimal setup (Fig. 2.15, top) allows to perform experiments with a single fluid. Analyzing different samples (e.g. different electrolytes, or the same electrolyte with an addition of analytes) is troublesome because it requires changing the syringe (replacing the connected syringe with a second one, filled with the new sample). During the removal/connection of the syringes, air bubbles are easily created in the tubes, flow through the fluidic chamber, and can alter the measurement if not creating areas of the array's surface not perfectly wetted (as will be illustrated in Sect. 4.3, in fact, the first step of every measurement with liquids is to inject IPA, which allows to properly fill the whole fluidic chamber thanks to its wetting properties; the introduction of air bubbles, especially if the next fluid to be injected is not IPA, can cause part of the surface of the array to remain dry).

In order to overcome this limitation, two syringes can be used together with a switching valve (part no. *V-101D*), as shown in Fig. 2.15 (bottom). With this approach, while one syringe (syringe A in the drawing) is directly connected to the fluidic chamber running the experiment (valve connection B-V in the scheme), the second one (syringe B) is *priming* the tube (i.e. filling the tube with liquid to remove all air prior to actually using that secondary liquid), filling it with the second liquid to be tested (which is temporarily being directed toward a waste container, valve connection A-D in the scheme). These connections are represented by the red arrows in valve of Fig. 2.15 (bottom). As soon as it is required to switch liquid, the valve is actuated, switching from the red-arrows to the purple-dotted-arrows configuration. A new liquid (that of syringe B) is then pumped through the chip, without introduction of air bubbles. Clearly, the longer the tube going from the valve to the chip is, the longer the transition time from one fluid to the new one becomes (typical transition times are in the order of ∼1 min when operating at 50

Figure 2.16: *Photo of the NE-300 automated syringe pump used for injecting the fluids in the experiments.*

µL/min pump rates, see below).

Manual control of the syringes is inaccurate and cannot guarantee a constant fluid rate. To overcome this limitation, automated syringe pumps are used to regulate the injection of the syringes (part number *NE-300* of *New Era Pump Systems, Inc.* [264], purchased from *KF TECHNOLOGY S.r.l.* [265]). Fig. 2.16 shows the *NE-300* syringe pump, together with a disposable syringe. Automatic syringe pumps deliver the liquids to the chip at controlled rates (typically, in the range 5–50 µL/min). Along with a sub-µL/min fluid rate accuracy, the pump also allows monitoring the total volume which is injected. Thanks to this information, the total volume of the tube between the switching valve and the chip can be easily estimated a-priori, thus allowing to accurately identify the moment when the new liquid reaches the fluidic chamber.

Fig. 2.17 shows a photo of the full setup. The syringe pump holds a syringe filled with electrolyte. The tube is connected to the valve, which is held in place with screws for ease of operation (we intend to avoid movements of the tubes while manually activating the valve). The connection to the PCB/socket, as well as the adapter for the transition from the 1/16in to the 510µm tube are shown. The outlet tube is very short (to minimize flow resistance), and a small beaker can be easily placed beneath it to collect the fluids.

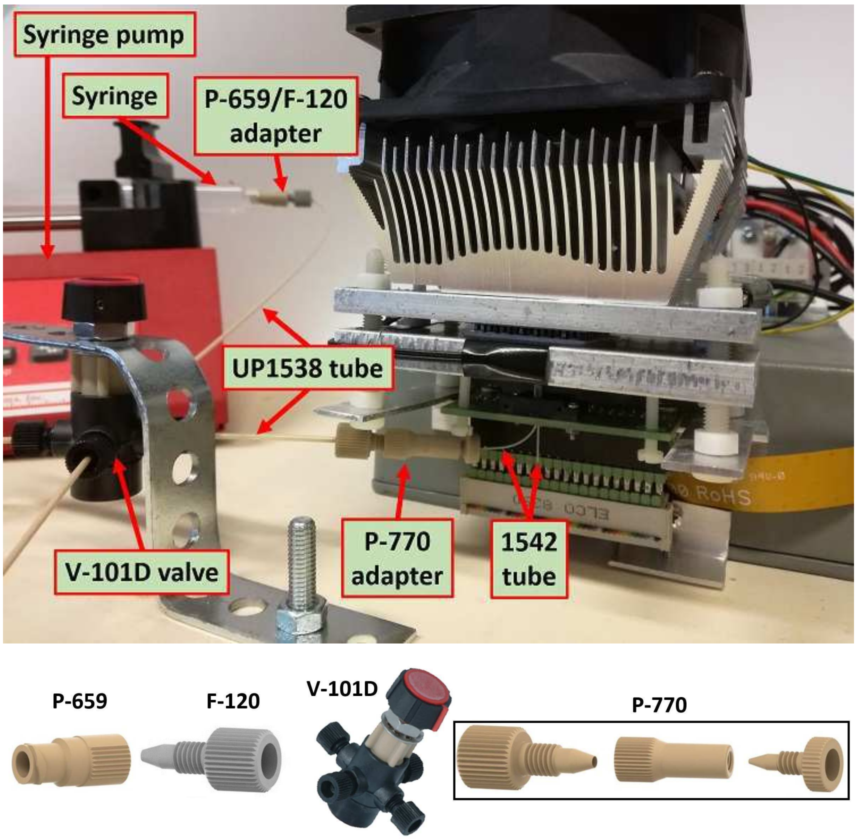

Figure 2.17: *Top: photo of the complete system (biosensor platform, temperature controller, and microfluidics part). The main fluidic parts are labeled. Bottom: detail of the valve and main connectors.*

The described setup does not enable a direct control of the temperature of the injected fluids. However, this would be possible by coupling the tubes to the thermal mass beneath the Peltier cell.

2.3.3 Leakage of liquids and countermeasures

As mentioned in Sect. 2.3, syringe pumps are typically actuated at few µL/min pump rates. Excessive liquid pressure (which can be possible if the syringes are manually controlled) along with poor positioning of the metal finger (namely, significant non-parallelism of the metal finger w.r.t. the chip) can lead to leakage of fluids. In that case, in fact, the pressure of the chip on the PDMS seal ring is not uniform along the periphery, and the part with lower mechanical pressure may not contain the high-pressure liquid. As an example, Fig. 2.18 shows two subsequent photos of an experiment with liquids with manually-actuated syringes and a slight misalignment of the metal finger. The top picture shows a water droplet being correctly expelled from the outlet tube. As the experiment proceeds (bottom figure), the extra-pressure leads to the water not being contained by the PDMS seal, thus leaking in the socket. For this reason, using automated syringe pumps at controlled (and low) pump rates, as well as proper mounting of the setup (for instance using auxiliary screws as spacers to achieve a better parallelism, see the white plastic screws in Fig. 2.18) is mandatory to minimize if not eliminate the leakage.

Another possible source of leakage is a bad insertion of the tubes in the socket. In fact, if the tubes are not properly press-fitted in the holes of the socket, the liquid may leak from the bottom side of the PCB, before even reaching the fluidic chamber and the PDMS. This is shown in Fig. 2.19, and it highlights the importance of accurate connection between all the components of the system.

Leakage of fluids is the major failure mode of the system. As an alternative mounting, we have also considered operating in withdrawal mode. In fact, operating the syringes in withdrawal mode creates a local depression in the fluidic chamber, increasing the adherence of the PDMS seal to the chip/socket and thus helping in preventing leakage at the ultimate risk of generating air bubbles.

The setup of Fig. 2.15 can also be used for withdrawal operation (provided that the syringe pumps are enabled to operate in such a way). Only one syringe is required for the purpose. The Eppendorf/beaker contains the liquid to be tested, and when actuated the syringe draws the liquid out of it. The arrows in Fig. 2.15 then go in the opposite direction with this mode of operation. However, a major drawback of this setup is that operating with different liquids (or operating for long time) requires to replace the beaker, thus exposing the tube to air generating air bubbles.

One simple improvement is shown in Fig. 2.20 (top). Here we try to minimize the number of required components, hence we use only the elements already included in the inject-only setup. Syringe A operates in withdrawal mode, drawing the liquid out of the beaker placed under the chip. To avoid exposing tubes to air (e.g. when the beaker runs out of liquid), we make use of the second syringe (syringe B): we operate it in inject-mode, connect it with a tube to the same beaker, and make it refill it at need (or constantly adding liquid to it during the experiment). With this

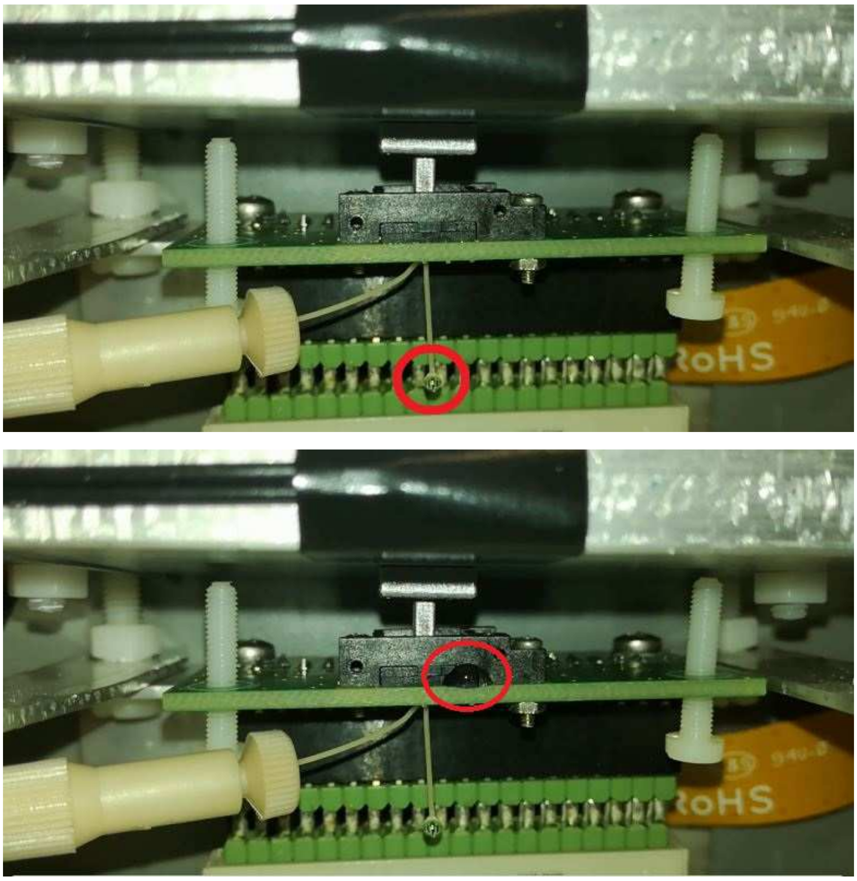

Figure 2.18: *Top: photo zoomed over the chip/socket/finger elements during a measurement with liquids. A droplet flowing out of the outlet tube is visible. Bottom: due to excessive injection pressure and not-good alignment of the metal finger, leakage of fluids occurred in the socket.*

approach, long experiments can be performed without incurring in running out of test samples (the beaker is constantly replenished by syringe B). If a new liquid is to be tested, the injection of syringe B is stopped, the syringe is replaced with a new one (containing the new test sample), and the injection is re-actuated. Given the typical low pump-rates, the time required to replace the syringe is lower than the time syringe A takes to draw out all the liquid remaining in the beaker. Hence, the tube is never exposed to air. The major drawback is evident when two different liquids are to be tested. When we change the sample of syringe B and make it spill its content in the beaker, since the beaker will never be completely emptied (by syringe A) before we add the new sample (because we do not want to expose the tube to air), then a mixture of the two samples is obtained. However, while at first syringe A draws out of the beaker a mixture of two liquids (the old and the new one), after some time (keeping on spilling the new liquid in the beaker) the old liquid gets so diluted (by the new one) that we can assume only the new liquid remains in the beaker. Clearly, if the liquid level in the beaker is very low before we replenish it, the time needed for completely substituting the content of the beaker with the new sample is shorter. However, if the "old" sample to be replaced does

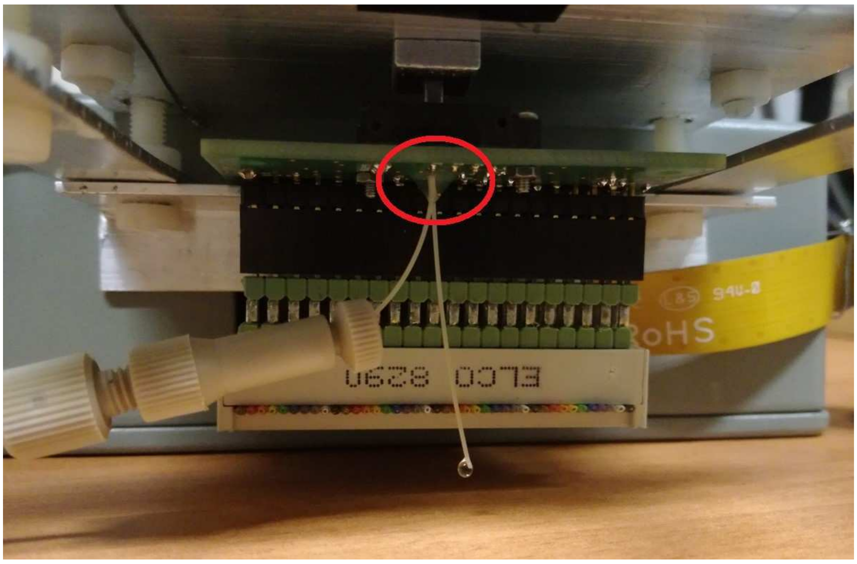

Figure 2.19: *Photo of the chip/socket/finger elements during a measurement with liquids. The tubes have not been properly press-fitted in the socket. As a result, leakage of liquids originated from the bottom of the PCB.*

not properly mix up with the new one (e.g. for water and oils, or in the presence of analytes that possible sediment at the bottom of the beaker), then this approach is not applicable.

One further improvement that allows both injection and withdrawal operation is shown in Fig. 2.20 (middle). The extra components required to build this setup consist in a second adapter for the 1/16in-to-510µm tubes transition and a second switching valve (and possibly a third syringe, with its pump). Using this setup in injection mode is straightforward. The upper part of the scheme works as for Fig. 2.15 (bottom), with one syringe (A) injecting liquids in the chamber, and the second syringe (B) *priming* the secondary tube. In the bottom part of the scheme, the second valve simply requires to connect the chip to one waste container to collect the outlet liquids (valve connection A-D). Syringe C is not used in this configuration (hence a total number of 2 syringes is required). If liquid withdrawal operation is required, instead, one of the two top syringes is not used, and syringe C comes into place. Connections A-D are performed for both valves, allowing the syringe A to withdraw liquid from the container connected to port D of the bottom valve. In the meantime, thanks to the connection C-B of the bottom valve, syringe C is operated to prime the tube (that connects port B of the valve to the liquid container). When a switch of liquids is required, the bottom valve is actuated. The top valve in principle does not need to be actuated during the whole experiment (the only exception is if the withdrawing syringe is filled completely: in that case, the third syringe, B, is required, the top valve is actuated, and syringe B continues the withdrawal of the liquid, while in the meantime syringe A can be emptied).

While this setup is straightforward and easy-to-use, it may require one extra syringe pump, which is an expensive component. An optimized version of the design is shown in Fig. 2.20 (bottom), where no extra syringes/pumps are required. For injection mode, both valves implement the connections A-D, B-C. While one valve is

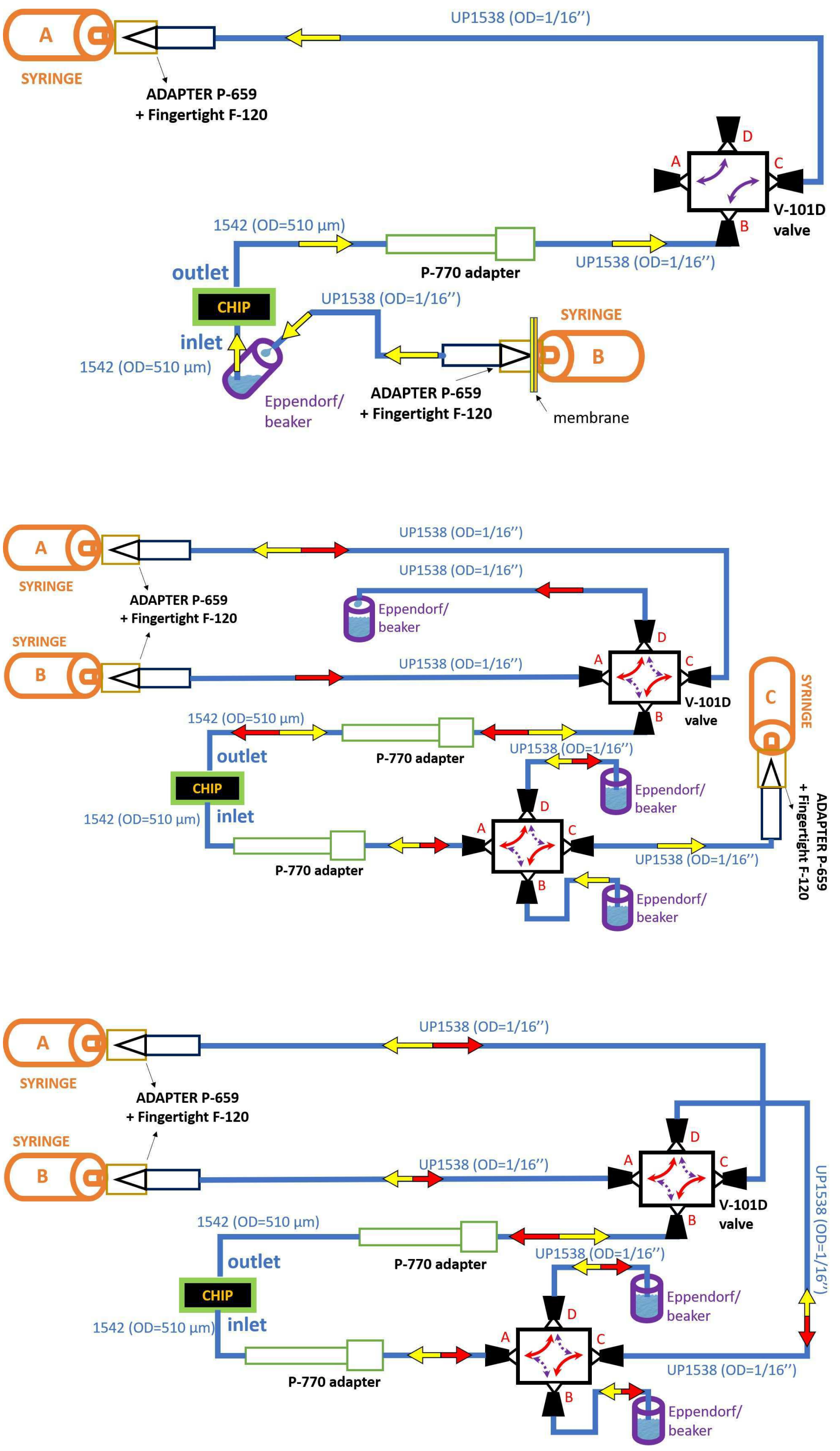

Figure 2.20: *Sketch of microfluidics setups for injection and/or withdrawal operation. Red/yellow arrows indicate the flow of liquids (in inject/withdrawal mode, respectively). Top: setup for using the inject-setup elements to operate in withdrawal mode without the need to purchase extra components. One syringe draws liquids out of the beaker/Eppendorf, while a second syringe replenish it. Middle: simple extension of the inject-only setup, enabling both injection and withdrawal operation. This requires having 3 syringe pumps. Bottom: optimized design that minimizes the need for extra components.*

used to direct the liquid from syringe A to the chamber (the waste is collected by the container on the port D of the bottom valve), syringe B performs the priming of the tubes. Changing electrolyte requires only to actuate the top valve. For withdrawal operation, the starting configuration is again A-D B-C for both valves. Again, while syringe A fills the fluidic chamber, syringe B primes the tubes. To change the electrolyte, the bottom valve has to be actuated. If the syringes are operated at exactly the same pump rates, in principle they would be completely filled at the same time. This would be a problem, because it would require pausing the experiment to replace the withdrawing syringe with an empty one. However, since the syringe operated for the priming of the tube is not involved in running experiment, we can easily operate it at a different pump rate. On top of that, if possible, we also have the option of running experiments with different electrolytes for slightly different duration. By doing so, we can guarantee that the two withdrawing syringes are never completely filled at the same time. The priming can also be paused to empty the syringe and resumed (allowing enough time to withdraw the air bubbles that possibly got into the tube in the meantime). By using this scheme, a reduction of costs is achieved.

A withdrawal setup is now routinely used in our experiments, since it essentially eliminated all leakage problems thus allowing us to safely manage electrolytes with high salt-concentrations near physiological limits (that can be corrosive for the board hosting the socket of the chip).

2.4 Biosensor platform performance and benchmarking

To benchmark this platform with existing literature, Table 2.1 compares key features and performance indicators of the chip described in this Chapter with published planar interdigitated, microelectrode, and nanoelectrode arrays (for other non-CMOS approaches, the reader can refer to the list of references reported in Sect. 1.3.5).

While not being identical to a true amplitude/phase impedance measurement[3], the proposed frequency-sweep CBCM measurements enable much higher nanoelectrode surface density and lower power consumption at high modulation frequency. This concept thus represents a valid alternative, especially for the envisioned (bio)-sensing applications (where the measured impedance can be modeled as the combination of resistive and capacitive lumped elements, see Chapter 3). The small size and density of sensors is a fundamental prerequisite for enabling detection and HFIS of small nanoscale analytes. While some architecture (as [243]) has been reported

---

[3] This measurement system is not meant to replace a general-purpose impedance analyzer: in fact, it does not allow to determine the complex impedance of an arbitrary load. Thus, the specific field of application (electrolytes with functionalization layers, analytes, etc.) has to be considered when comparing this platform to different implementations. In these cases, the impedance under investigation is always passive (e.g. it never exhibits pure delay or all-pass behaviors), it can always be modeled up to arbitrary accuracy with equivalent lumped element circuits made of mixed resistance-capacitance components, and the values of the model elements can be reconstructed via fitting procedures on the multi-frequency measurements (see Sect. 3.3 and Sect. 4.5).

to operate at even higher frequencies, much smaller spatial resolution and larger dissipated power characterize these implementations.

Following our earlier discussion about the challenges to operate at high frequencies with nanoscale electrodes, Fig. 2.21 shows a direct comparison of this platform to other implementations. The work described in this thesis is located at bottom-right corner, corresponding to the small sensor areas and high frequency of operation, largely leaving behind the other proposed solutions. As a further comparison, we also show in Fig. 2.22 a similar map, comparing different chips considering, as figures of merit, the density of sensors (i.e., the pixel area) and the maximum frequency (f_{MAX}) over the dissipated power (P_{diss}). These metrics corroborate the conclusion that the platform described in this thesis has distinct and unique features and merits compared to other chips: the sensors density is extremely higher than the other implementations, and the f_{MAX}/P_{diss} ratio is on the high-side, allowing to reach the upper-right corner of the plot.

These results demonstrate the opportunities offered by state-of-the-art CMOS process technology.

Ref.	**Tech.**	**Sensor site**	**# sensors**	**Sensors /mm^2**	**Measured quantity**	**Method**	**Freq. range**	P_{diss} **[mW]**	**Imaging?**
[232]	180-nm CMOS	MEA (Au) 22×22µm	9,216	1,111	|Impedance|	EIS	100 Hz- 1 MHz	N/A	
[238]	350-nm CMOS	MEA (Au) 40×40µm	100	204	Admittance	I/Q	10 Hz- 50 MHz	84.8	
[266]	130-nm CMOS	MEA (Au) 28×28µm + PDA	5,120[a]	297	|Impedance|, ExC, OD	I/Q	100 kHz- 2 MHz	N/A	yes (optical)
[267]	130-nm CMOS	4-WE (+CE,RE) (Au) 2×2µm[b]	64[c]	17	Admittance	I/Q	0.1 Hz- 10 kHz	1.8	
[268]	130-nm CMOS	MEA (TiN) 8.75 µm^2	16,384	4,444	Impedance, ExC, InC	SW mod/dem	1 Hz- 10 MHz[d]	95	yes
[243]	250-nm CMOS	IMEA (Al/Al$_2$O$_3$) 100×100 µm	5	500	Capacitance	C2f	8 kHz- 291 MHz	29	
[217]	180-nm CMOS	MEA (Pt) 7.5×3 µm	59,760	5,487	Impedance	Lock-in	1 Hz- 1 MHz	86	yes
This chip [190]	90-nm CMOS	NEA (AuCu) $r_{el} = 90$nm	65,536	2.53×10^6	Switching capacitance	CBCM	1 MHz- 70 MHz	15	yes

a. grouped in 1 electrode + 4 photodiodes per sensing site. b. one WE sized 55×55 µm, one WE sized 5×5 µm, two WE sized 2×2 µm. c. 16-channels, each one with 4-WE. d. range for HFIS.

C2f: capacitance-to-frequency conversion, CBCM: Charge-based capacitance measurement, CE: counter electrode, ExC: extra-cellular potentials, IMEA: interdigitated MEA, InC: intra-cellular potentials, I/Q: I/Q demodulation, IS: impedance spectroscopy, MEA: micro-electrode array, NEA: nano-electrode array, OD: optical detection, PDA: photodiodes array, Pdiss: dissipated power, RE: reference electrode, SW mod/dem: square-wave modulation/demodulation, WE: working electrode

Table 2.1: *Comparison of chip performance with literature.*

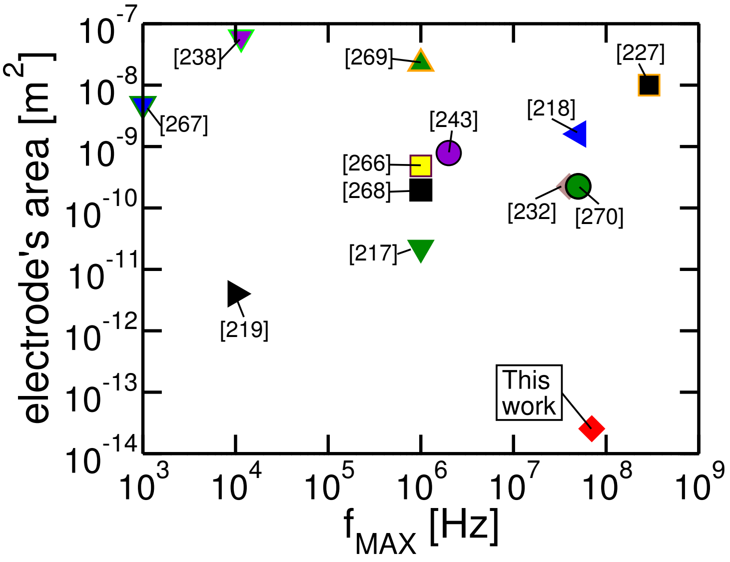

Figure 2.21: *Comparison of chip performance with literature based on the area of individual sensors vs maximum-frequency (f_{MAX}). The size value we used for [267] is the smallest among their three implementations (55×55 μm^2, 5×5 μm^2, 2×2 μm^2). The size value we used for [227] is the size of the input bonding pad (150×150 μm^2).*

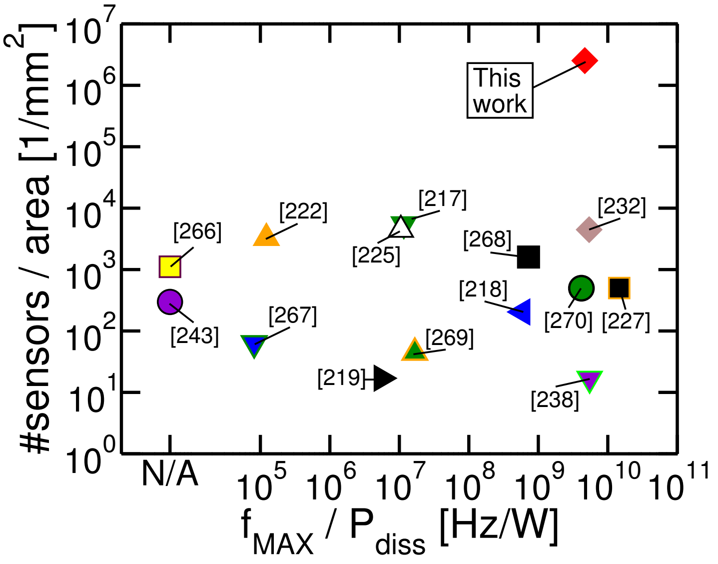

Figure 2.22: *Comparison of chip performance with literature based on density of sensors (no. of sensors per unit area) vs maximum-frequency over dissipated power ratio (f_{MAX}/P_{diss}).*

2.5 Summary

This chapter presented the CMOS pixelated nanocapacitor biosensor platform at the basis of this thesis. The chip has been originally developed by NXP Semiconductors and presents a number of remarkable features for (bio)sensing applications:

- the nanoscale dimension of electrodes (90 nm radius) is comparable to some of the smallest analytes (e.g. viruses), and can enable single nanometer-sized particle detection;
- the small intra-electrode pitch (as small as 550 × 720 nm), combined with the fast scan rate and the real-time operation, enable massively parallel imaging with high pixel density;
- the advanced CMOS fabrication process guarantees low parasitics and a high yield, with nearly zero defects;
- the high-frequency of operation (up to 70 MHz) enables to overcome the first cut-off frequency of electrolytes (f_1), and it paves the way for future developments approaching the dielectric relaxation frequency (f_2) at physiological salt concentrations.

All these features can be further improved thanks to technology scaling (possibly enabling pixel densities higher than optical systems, and maximum operating frequencies higher than f_2).

While the chip and interface board had already been designed by NXP Semiconductors, the author's contributions to this chapter include the development of the thermal control system (from the identification of specifications, to the definition of the bill of materials, the assembly, and the final experimental testing with related analyses), the development of the microfluidic setup (also including the adjustments of the PCB to fit the microfluidic tubes, the fabrication of the PDMS seal rings, the assembly of components and experimental testing, and the implementation of countermeasures to overcome the leakage of liquids), and the benchmark analyses.

The temperature control system we designed allows to operate the chip in a wide range of temperature conditions, suited for different kind of analyses. Besides, thanks to the identification of the relation between the measurement capacitance and the on-chip temperature, compensating for temperature-variations during measurement is also possible.

Finally, details about the implementation of a microfluidic setup have been provided, discussing the main difficulties (in particular, leakage of liquids). The setup we implemented allows to operate the chip in dry as well as with electrolytes, overcoming the issue of leakage of salty liquids that could possibly damage the board, and enabled us to perform experiments with analytes in our lab.

In summary, this platform really appears as a unique system for biosensing applications, enabling metrology of biological quantities at the nanoscale.

3 Analytical, Numerical and Statistical Models

This chapter is devoted to presenting analytical, numerical and statistical models for nanoelectronic biosensors and analytes.

In Sect. 3.1 we introduce the Poisson-Boltzmann and Poisson-Nernst-Planck (Poisson-Drift-Diffusion) formalism to describe electrolytes in DC and small-signal AC regimes. Section 3.2 is devoted to briefly presenting an electronic nanobiosensor simulator (ENBIOS, originally developed by F. Pittino [269]), which will be extensively used in this thesis; the porting of two simulation platforms (based on ENBIOS) on the nanoHUB.org portal will also be discussed. In Sect. 3.3 we present the *switching capacitance* model, which will be used to interpret the experimental data generated by the biosensor platform of Chapter 2, while in Sect. 3.4 we discuss about modeling the biosensor response to arbitrary input voltage waveforms. Sect. 3.5 is devoted to present compact geometrical/electrical models to study the response of the platform to viruses. Finally, Sect. 3.6 presents a Bayesian statistical technique to extract parameters and quantify uncertainties.

We acknowledge F. Widdershoven (NXP Semiconductors) for developing the original formulation of the switching capacitance model, and C. Heitzinger and his group at TU–Wien (J. A. Morales Escalante, L. Taghizadeh, B. Stadlbauer, D. Pasterk) for implementing the Bayesian estimation algorithm described in Sect. 3.6 and running the Markov-Chain Monte Carlo parameter extractions shown in this thesis.

The content of this chapter is partly published in [190, 245–250].

3.1 The PB-PNP framework and models for electrolytes and EDL

Here we report the essentials of a numerical modeling framework adequate to describe the nanocapacitor array and analogous biosensor systems [180, 181, 190, 206, 209, 214, 215, 220, 239, 270–272].

The basic Physics and the underlying mathematical modeling is well captured by the simple 1D-symmetry electrode-structure depicted in Fig.3.1 (top). An electrolyte region is defined between one ideally polarizable working electrode, WE (i.e. one electrode that carries no DC current) biased at constant DC voltage (V_{DC}=0 V in our case) and the grounded counter electrode (CE). A small-signal AC excita-

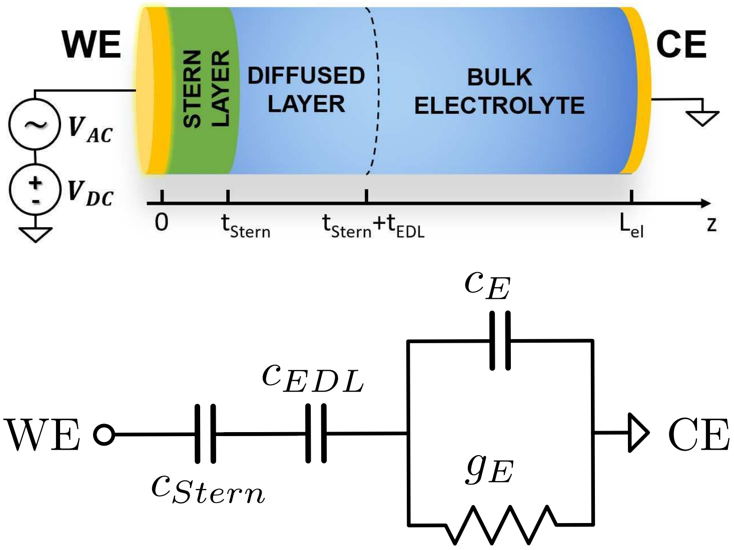

Figure 3.1: *Top: sketch of a simple 1D-symmetry structure capturing the essential Physics of a nanoelectrode in contact with an electrolyte. Bottom: lumped element equivalent circuit to represent the admittance per unit area* Y *of the 1D system according to the Gouy-Chapman-Stern theory (*$t_{Stern} + t_{EDL} << L_{el}$*).*

tion, V_{AC} is added to the WE's DC potential. According to established electrolyte Physics [160], ions and water molecules create a thin layer of dipoles at the interface between the WE and the electrolyte (Stern layer), which then extends into a thicker diffusion layer with non-negligible space charge density with respect to the neutral bulk electrolyte (EDL).

The mathematical modeling framework for this system is given by the Poisson-Boltzmann equation in the equilibrium DC regime, and the Poisson-Nernst-Planck equations for the linearized small signal AC regime [51, 269, 273–278]. A more detailed description can be found in [203, 279].

3.1.1 DC formulation

Under the equilibrium conditions that describe the system in Fig. 3.1 (top) at zero DC currents, the model equation for the DC problem is the so-called Poisson-Boltzmann (PB) equation [160], which reads:

$$\begin{aligned} \nabla \cdot (\varepsilon(\vec{r})\nabla V_0(\vec{r})) &= -\rho_{0_f}(\vec{r}) - \rho_{0,nl}(\vec{r}) \\ &= -\rho_{0_f}(\vec{r}) - q\sum_{m=1}^{N_{ions}} Z_m n_{0,m}^{\infty} \exp\left(-\frac{Z_m q\left(V_0(\vec{r}) - V_{ref}\right)}{k_B T}\right) \end{aligned} \tag{3.1}$$

where V_0 is the DC potential, q is the elementary charge, k_B is the Boltzmann's constant, ε is the dielectric permittivity, and T is the absolute temperature. For the simple 1D system, the spatial coordinate $\vec{r}$ simply corresponds to the monodimensional z-coordinate $z \in [0, L_{el}]$. The charge density is given by spatially immobilized charges ($\rho_{0,f}$) and mobile ion charges in the electrolyte ($\rho_{0,nl}$). The mobile charges are expressed with the last summation term in Eq. 3.2. Their DC concentration can be expressed as:

$$\tilde{n}_{0_m}(\vec{r}) = n_{0_m}^{\infty} \exp\left(-\frac{Z_m q \left(V_0(\vec{r}) - V_{ref}\right)}{k_B T}\right) \tag{3.2}$$

and it depends on the signed valence and the bulk concentration of each (m-th) ionic species (Z_m and $n_{0,m}^{\infty}$), on the number of ions species (N_{ions}), and on the reference potential in the bulk of the electrolyte (V_{ref}).

For a system with semiconductor regions (to model for instance ISFET devices), transport equations for the DC current should also be included. However, in the following of this thesis, we assume no DC currents flow through the electrolyte (which is a reasonable assumption, since the gold nanoelectrodes of the platform do not sustain DC currents), thus no more ingredients are required to model the Physics in DC.

Dirichlet boundary conditions are applied on the electrodes, whereas Neumann conditions are used for the other boundaries [203].

3.1.2 AC formulation

The AC model is described by the Poisson-Nernst-Planck (PNP) equations (otherwise denoted as Poisson-Drift-Diffusion, PDD), which are formulated in the time-harmonic small-signal (i.e. linearized) approximation. Under this assumption, the small-signal concentration of the ions can be expressed as:

$$\tilde{n}_m(\vec{r}) = n_{0_m}(\vec{r}) \frac{q Z_m}{k_B T} \left(\tilde{\phi}_m(\vec{r}) - \tilde{V}(\vec{r})\right) \tag{3.3}$$

where $\tilde{V}$ is the electrostatic potential phasor, $\tilde{\phi}_m$ is the pseudo-potential of the m-th ionic species, and n_{0_m} is the DC ion concentration of the m-th ionic species.

After linearization of Eq. 3.2, we obtain the AC Poisson equation:

$$\nabla \cdot \left(\varepsilon(\vec{r}) \nabla \tilde{V}(\vec{r})\right) + \sum_{m=1}^{N_{ions}} \frac{q^2 Z_m^2}{k_B T} n_{0_m}(\vec{r}) \left(\tilde{\phi}_m(\vec{r}) - \tilde{V}(\vec{r})\right) = 0 \tag{3.4}$$

The currents are described by the Drift-Diffusion equations, which take the following form after linearization (again, assuming that the electrolyte is in equilibrium and no DC current is flowing):

$$q Z_m \mu_m \nabla \cdot \left(n_{0_m}(\vec{r}) \nabla \tilde{\phi}_m(\vec{r})\right) - j\omega n_{0_m}(\vec{r}) \frac{q Z_m}{k_B T} \left(\tilde{\phi}_m(\vec{r}) - \tilde{V}(\vec{r})\right) = 0 \tag{3.5}$$

where μ_m is the mobility of the m-th ionic species, j is the imaginary unit, and ω is the angular frequency. This allows to compute the AC current density ($\tilde{J}$) as the summation of the displacement ($\tilde{J}_D$) and ionic current densities ($\tilde{J}_m$) as:

$$\tilde{J} = \tilde{J}_D + \sum_{m}^{N_{ions}} \tilde{J}_m = -j\omega\varepsilon \nabla \tilde{V}(\vec{r}) - \sum_{m}^{N_{ions}} q^2 Z_m^2 \mu_m n_{0_m} \nabla \tilde{\phi}_m(\vec{r}) \tag{3.6}$$

This completes the PNP formulation.

3.1.3 Analytical model for a 1D electrode-Stern-electrolyte system

Considering the 1D structure of Fig. 3.1 (top), analytical calculations can be worked out in the PB-PNP formalism for the simple case where the WE's DC potential is zero. The solution can be interpreted with the equivalent circuit drawn in Fig. 3.1 (bottom), where the Stern layer capacitance (c_{Stern}), the EDL capacitance (c_{EDL}), and the bulk electrolyte conductance and capacitance (g_E and c_E) are all quantities per unit area which are given by [203]:

$$\begin{cases} c_{Stern} = \frac{\varepsilon_{Stern}}{t_{Stern}} \\ c_{EDL} = \frac{\varepsilon_{el}}{\lambda_D} \\ c_E = \frac{\varepsilon_{el}}{L_{el}} \\ g_E = \sigma_{el}/L_{el} \end{cases} \tag{3.7}$$

where ε_{Stern} and t_{Stern} are the permittivity and the thickness of the Stern layer, respectively, $\varepsilon_{el} \simeq 78\varepsilon_0$ is the permittivity of the bulk electrolyte, L_{el} is the length of the electrolyte region, λ_D is the Debye length, and $\sigma_{el} = \sum_m Z_m^2 q^2 \mu_m n_{0,m}$ is the electrolyte conductivity (where Z_m, μ_m and $n_{0,m}$ are the valence, the mobility in units of m/Ns and the concentration of the ions in units of m^{-3}, respectively). Dielectric materials (i.e. materials without ions) have essentially infinite spreading resistance and are modeled as a simple capacitance value set by their permittivity: $c_{diel} = \varepsilon_{diel}/L_{el}$.

The analytical expression of the admittance (as a function of the angular frequency, ω) for the circuit model in Fig. 3.1 (bottom) is given by:

$$Y_{a.m.}(\omega) = \left(\frac{1}{j\omega C_{Stern}} + \frac{1}{j\omega C_{EDL}} + \frac{1}{G_E + j\omega C_E} \right)^{-1} \tag{3.8}$$

whose capacitive component is simply expressed as:

$$C_{a.m.}(\omega) = \frac{1}{\omega} \Im \left[\left(\frac{1}{j\omega C_{Stern}} + \frac{1}{j\omega C_{EDL}} + \frac{1}{G_E + j\omega C_E} \right)^{-1} \right] \tag{3.9}$$

where the terms of Eq. 3.7 are de-normalized via the cross-section area of the 1D-system: $C_\square = c_\square \mathrm{Area}$ and $G_\square = g_\square \mathrm{Area}$.

We will make use of this analytical model ("a.m.") in Sect. 3.6.

3.2 Electronic Nanobiosensor Simulator (ENBIOS)

The analytical models (presented in the following of this chapter) and the signal transduction mechanisms of the nanoelectrodes array platform (see the previous chapter) have been investigated in detail by means of 3D finite-element-method (FEM) numerical simulations. In particular, we employ ENBIOS (Electronic NanoBIOsensor Simulator), a MATLAB-based electronic nanobiosensor simulator based on the Control Volume Finite Element Method (CVFEM) discretization method [269], which solves self-consistently the PB equation in steady state and the coupled PNP equations in the time harmonic linearized small signal regime for all ion species in the electrolyte. The simulator first computes the DC solution, then it solves the AC problem over the frequency points specified by the user. The simulator guarantees the global conservation of the currents at the domain boundaries, thus enabling the calculation of very tiny variations of the admittance of the systems under study [203].

The definition of the geometries and the generation of tetrahedral grids is performed via the *netgen* mesh generator [280]. The working (WE) and counter (CE) electrodes are modeled by Dirichlet boundary conditions, whereas a Neumann condition is imposed to the other boundaries. For the simple 1D-system of Fig. 3.1 (top), we can express the AC current at the working electrode ($\tilde{I}$) simply as $\tilde{I}$=Area$\times\tilde{J}$ (where “Area” identifies the cross-section area of the 1D geometry). For arbitrary 3D-structures, the current at the electrodes derives from more complex calculation based on the current density fluxes, which are computed on the surfaces of the control volumes. More details on the calculation of the electrode currents can be found in [269]. Once the current at the electrode is computed, we can derive the admittance as $Y_A = \tilde{I}/V_{AC}$, where V_{AC} is the electrode’s AC potential and $\tilde{I}$ is the total AC current at the electrode. Small-signal AC models and numerical simulations produce a complex electrode admittance that can be formally interpreted as a conductance in parallel with a capacitance, namely:

$$Y_A = G_A + j\omega C_A \tag{3.10}$$

In general, the conductance G_A and the capacitance C_A are frequency-dependent real numbers, related to each other via the Kramers-Kronig relations [281, 282].

We include a dielectric layer on top of the nanoelectrodes (when we simulate them in electrolyte) to mimic the Stern compact layer (CL). Unless otherwise stated, we model the CL as a dielectric layer with thickness equal to the atomic radius (t_{Stern} = 0.25 Å) and relative permittivity $\varepsilon_{r,Stern} = 7$ [203], consistently with standard capacitance values per unit area of the compact layer ($\approx$ 20 µF/cm^2), as reported in literature [283].

To study the response of the nanoelectrode array platform (a full-3D problem), we simulate arrays of 5×5 to 25×35 nanoelectrodes, with intra-electrodes pitch along the x- and y-directions (p_x and p_y) equal to $(p_x, p_y) = (600, 720)$ nm or $(p_x, p_y) = (600, 890)$ nm. The size of the simulation domain is chosen large enough to render effects of the domain boundaries on the results negligible. Simulations of the nanoelectrodes in the presence of large analytes (e.g., microparticles) require using large arrays.

To mimic the parallel operating principle of the chip, we typically apply a time-harmonic small signal AC excitation to all nanoelectrodes of the central row of the array, and we calculate the admittance of the central electrode of that row as a function of the AC modulation frequency. If calculating the response at multiple electrodes is required (e.g. to replicate the imaging capabilities of the platform in the presence of an analyte), we perform simulations with different excitation patterns (e.g. subsequently activating different rows), extracting the admittance of multiple electrodes of the activated row (see Fig. 2.6).

Fig. 3.2 shows a sketch of a typical 3D system simulated with ENBIOS. We consider a matrix of nanoelectrodes (default size: 7 × 7 electrodes) with radius r_{el} and intra-electrode pitches p_x and p_y. Electrodes are labeled according to the row/column number, where the labeling starts at the central electrode of the array: we indicate as $e_{i,j}$ the electrode on the i-th row above (along the y-direction) the central row and on the j-th column on the right side (along the x-direction) of the central column. e_{00} is the central electrode of the array. A spherical particle with radius r_p is suspended above the plane of the nanoelectrodes. We indicate as d_x and d_y the lateral displacements (along the x- and y-directions) of the centroid of the particle with respect to the center of electrode $e_{0,0}$, and as d_z the vertical distance between the bottom surface of the particle and the plane of the array (the z-coordinate of its center is therefore $r_p + d_z$). Unless otherwise stated, in the following of the thesis the "default" simulation setup has the parameters listed in Tab. 3.1.

The permittivity of the electrolyte (ε_{el}) is modeled by means of the double time constants Debye model [203, 284], thus accounting for the relaxation processes of water molecules that affect the permittivity at high frequencies. The mobility of ions and the parameters of the double time constants model are computed as a function of the temperature, according to the models described in [203, 285]. More details about ENBIOS can be found in [203, 269].

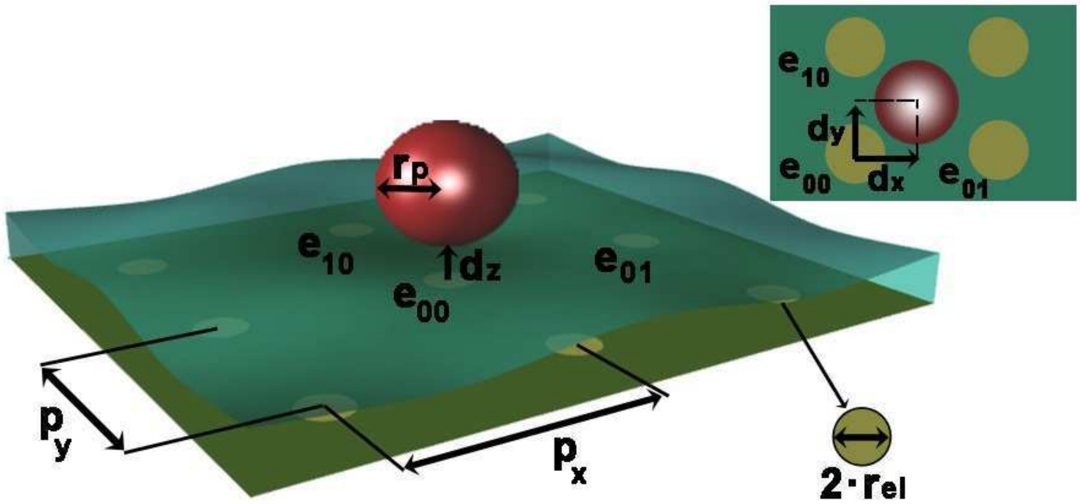

Figure 3.2: *Sketch of typical 3D systems that are studied in this thesis. We consider a matrix of nanoelectrodes with radius r_{el} and intra-electrode pitches p_x and p_y. Each electrode is labeled according to its row/column number (e_{ij}), where we start the labeling as e_{00} at the central electrode of the array (the first neighbor electrodes on the same row are $e_{0,1}$ and $e_{0,-1}$, and the first neighbor electrodes on the same column are $e_{1,0}$ and $e_{-1,0}$). A sphere with radius r_p models an analyte (particle), suspended above the plane of the nanoelectrodes. We indicate as d_x and d_y the lateral displacements (along the x- and y-directions) of the barycenter of the particle with respect to the center of electrode $e_{0,0}$, and as d_z the vertical distance between the bottom surface of the particle and the plane of the array (hence, if the analyte is a sphere, the z-coordinate of its barycenter is simply $r_p + d_z$).*

Parameter	**Symbol**	**Value**
Radius of nanoelectrodes	r_{el}	90 nm
Intra-electrode pitch along x-direction	p_x	600 nm
Intra-electrode pitch along y-direction	p_y	890 nm
Number of rows	n_{rows}	7
Number of columns	n_{cols}	7
Active (working) electrodes	WEs	$e_{0,j}\ \forall j$
Counter electrodes	CEs	$e_{i,j}\ \forall i \neq 0$
Thickness of Stern compact layer*	t_{Stern}	0.25 Å
Relative permittivity of Stern compact layer*	$\varepsilon_{r,Stern}$	7
Temperature	T	298.16 K
Relative permittivity of dielectric particle	ε_p	2.6
Relative permittivity of conductive particle	ε_p	6.9
Conductivity of conductive particle	σ_p	6.3×10^7 S/m

* only for simulations in electrolyte, neglected with dielectric ambient materials.

Table 3.1: *Default ENBIOS simulation parameters.*

In the following, simulation results will be shown for frequencies as high as 10 GHz, way higher than the actual maximum measurement frequency of the biosensor platform of Chapter 2 (70 MHz). This is done to anticipate the understanding of the behavior at higher frequencies (for possible future developments of the biosensor system), since having a wider spectrum can yield more robust estimation of parameters (see for instance Sect. 3.6), and because the high-frequency part of the spectrum is of great importance. In fact, at higher frequencies the sensitivity to spurious charges at the surface of the electrode is reduced (see Fig. 1.12 and Tab. 1.1) and the signal achieves a higher penetration in the electrolyte (as discussed in Sect. 1.4 and shown in Fig. 3.3).

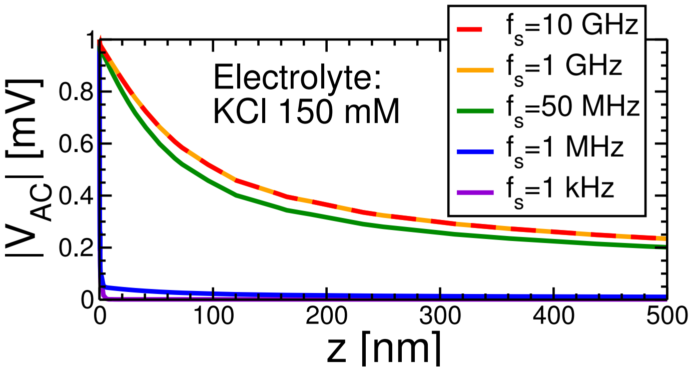

Figure 3.3: *Amplitude of AC signals at different frequencies as a function of the distance from the surface of the electrode (resulting from an excitation of 1 mV of the 3D system sketched in Fig. 3.2), for an electrolyte at physiological salt concentration (150 mM). High frequencies enable to achieve a higher penetration of the signals in the electrolyte.*

3.2.1 Porting of ENBIOS on nanoHUB.org

nanoHUB.org [286–288] is a web portal dedicated to research, education and collaboration in the field of nanotechnology. To date, it offers more than 6,000 resources (including courses, presentations, teaching materials, ...) with more than one million individual visitors in the last year. In particular, nanoHUB offers free online simulation tools, developed and made available by researchers around the world. These tools are a valuable resource both for research and for teaching purposes, both for students and professors. Given the high-visibility offered by the portal and the opportunity of receiving useful feedback from the users, we decided to make available to the scientific community two impedance-spectroscopy simulation tools powered by ENBIOS: "ENBIOS-1D Lab" [244, 245] and "ENBIOS-2D Lab" [246].

ENBIOS-1D Lab

ENBIOS-1D Lab (first published in 2016 [244], last version of the tool: v3.0 [245]) is a tool devoted to simulating simple 1D structures, helping users in understanding the basic principles of DC and AC operation of electronic biosensors. Fig. 3.4 shows the graphical user interface (GUI) of the tool.

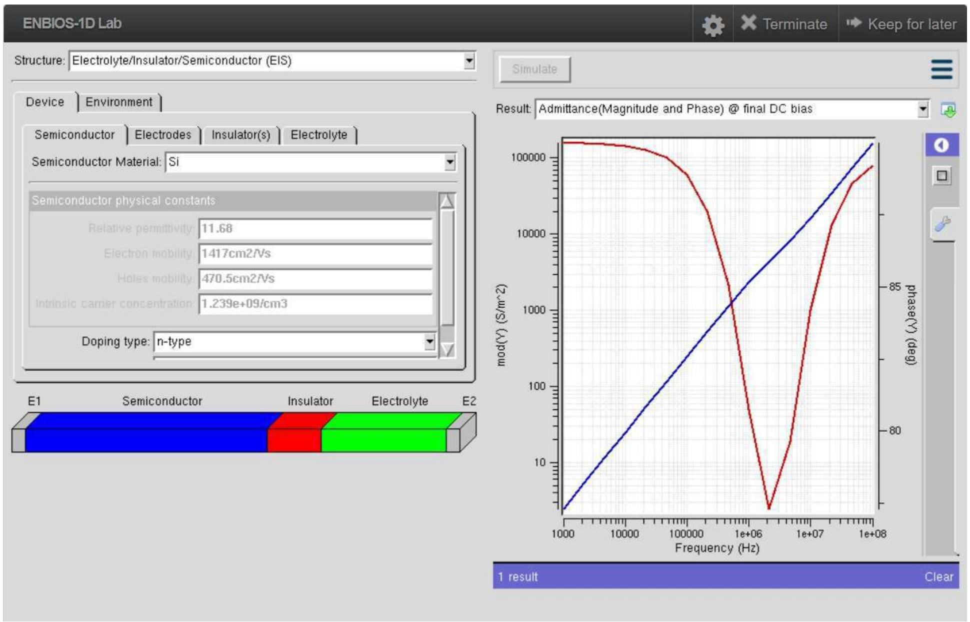
Structure: Electrolyte/Insulator/Semiconductor (EIS)

Semiconductor Material: Si

Relative permittivity: 11.68
Electron mobility: 1417cm2/Vs
Holes mobility: 470.5cm2/Vs
Intrinsic carrier concentration: 1.239e+09/cm3

Doping type: n-type

Result: Admittance(Magnitude and Phase) @ final DC bias

Figure 3.4: *GUI of the ENBIOS-1D Lab tool.*

Three possible 1D structures (defined between two electrodes, E1 and E2) can be simulated with this tool, as shown in Fig. 3.5: an electrolyte (E), an electrolyte-insulator (EI), or an electrolyte-insulator-semiconductor (EIS). Among the different features, this tool also enables to simulate semiconductors and DC/AC site-binding charges (these topics are not discussed in this thesis; for more details see [203, 279]).

The user can set his preferred simulation options parameters, related to the environment and to the device. In particular, the user can:

- Choose the semiconductor material: either using the pre-defined models (for

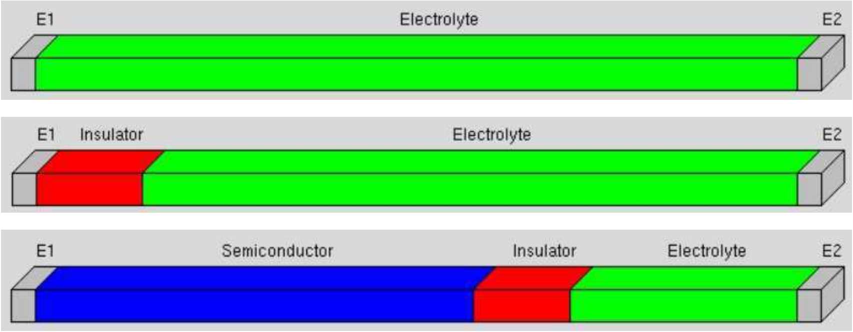

Figure 3.5: *Structures available for simulation in the ENBIOS-1D Lab tool (electrolyte, electrolyte-insulator, electrolyte-insulator-semiconductor.*

Silicon and Germanium), or defining his own semiconductor parameters (permittivity, electron/holes mobility, intrinsic carrier concentration), also indicating the preferred doping concentration;

- Set the counter electrode either as ideally-polarizable or faradaic (the working electrode is always set as ideally-polarizable, since the DC current is not implemented);
- Choose the insulator material: either using the pre-defined models (SiO_2, Al_2O_3, HfO_2, Ta_2O_5) or defining his own insulator parameters (relative permittivity and site-binding-related parameters);
- Include a dielectric compact layer at the interface with the electrolyte (specifying the thickness and permittivity, as well as including a surface charge);
- Choose the electrolyte: indicating the salt concentration of (even multiple) pre-defined electrolytes (NaCl, KCl, $NaNO_3$, KNO_3);
- Set the pH of the electrolyte: for instance by adding to the solution strong acids/bases (HCl, HNO_3, NaOH, KOH) at arbitrary concentration;
- Enable the DC and/or AC site-binding models [279];
- Set the operating temperature;
- Define the frequency range for HFIS analysis.

Similarly, the user has access to a number of different results visualization windows. In particular, the user can inspect DC quantities profiles as a function of the spatial coordinate in the domain:

- Potential;
- Ion/carrier concentrations;

AC quantities profiles (at the different frequencies, expressed as magnitude/phase or real/imaginary part) as a function of the spatial coordinate in the domain:

- Potential;
- Ion/carrier concentrations

and AC quantities as a function of frequency:

- Admittance/Impedance as magnitude/phase spectra;
- Admittance/Impedance as real/imaginary part spectra;
- Admittance/Impedance as Cole-Cole plots [289, 290].

To date, ENBIOS-1D Lab has been effectively used worldwide by 175 unique users (Fig. 3.6) for a total number of more than 1,000 simulation runs (Fig. 3.7).

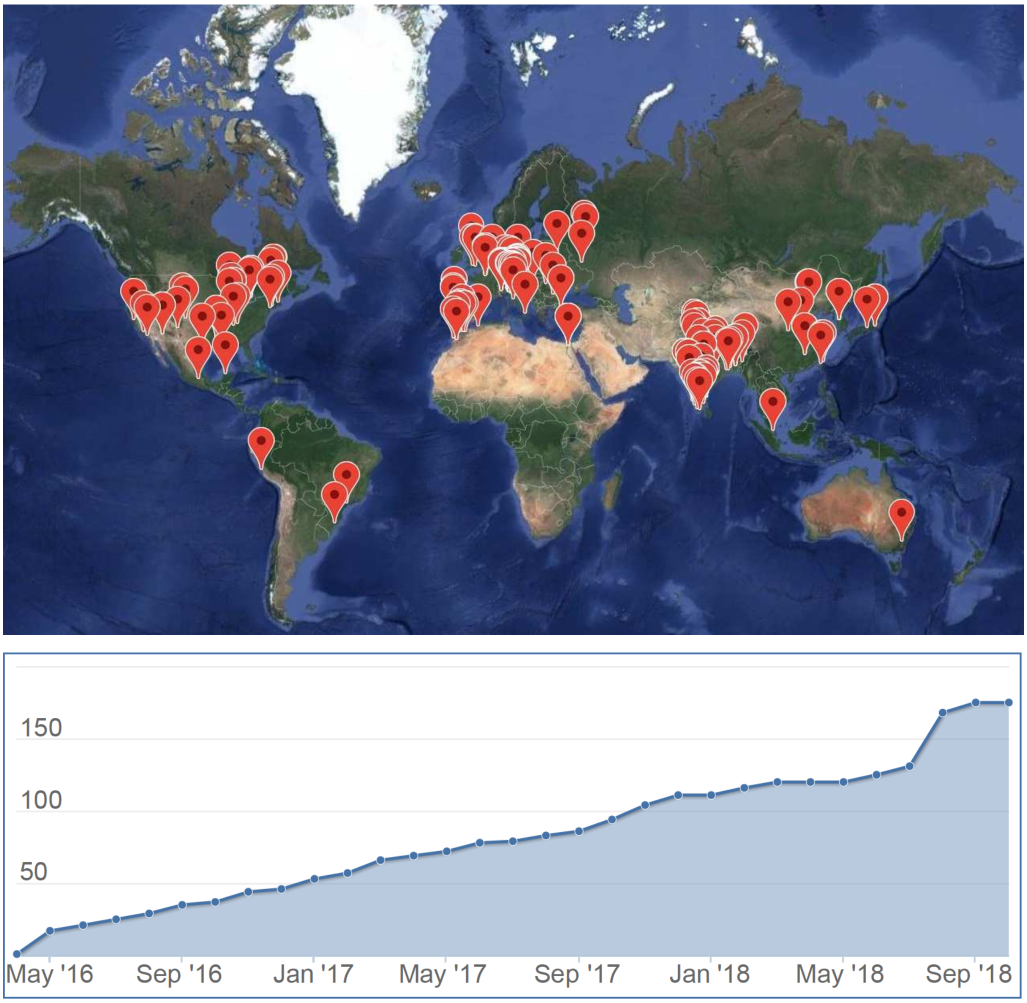

Figure 3.6: *Users of ENBIOS-1D Lab: location (top) and cumulative number (bottom) of unique simulation users (October 1^{st}, 2018).*

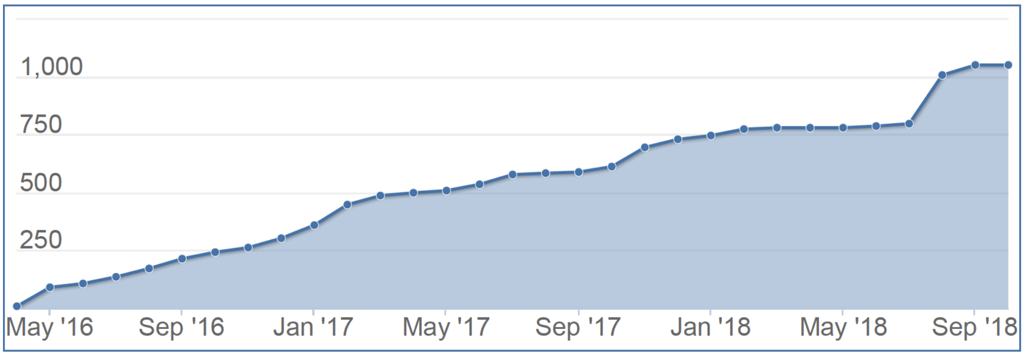

Figure 3.7: *Number of ENBIOS-1D Lab cumulative simulation runs (October 1st, 2018).*

ENBIOS-2D Lab

ENBIOS-2D Lab [246] is a tool devoted to simulating ISFETs. Fig. 3.8 shows the graphical user interface (GUI) of the tool.

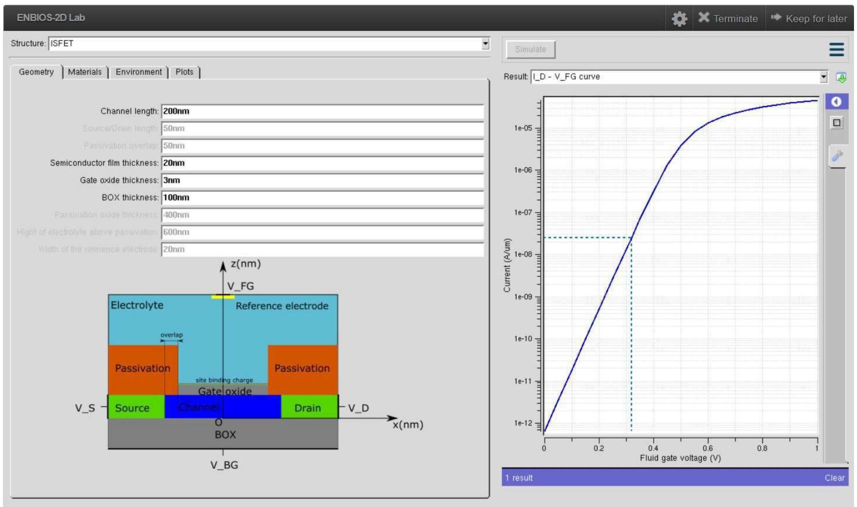

Structure: ISFET

Channel length: 200nm
Source/Drain length: 50nm
Passivation overlap: 50nm
Semiconductor film thickness: 20nm
Gate oxide thickness: 3nm
BOX thickness: 100nm
Passivation oxide thickness: 400nm
Hight of electrolyte above passivation: 600nm
Width of the reference electrode: 20nm

Result: I_D - V_FG curve

Figure 3.8: *GUI of the ENBIOS-2D Lab tool.*

The ISFET device is taken as a silicon-on-insulator (SOI) MOS device in which the gate electrode is separated from the channel by the electrolyte. A sketch of the structure is also shown in Fig. 3.8. More details can be found in [279].

The features described for the ENBIOS-1D Lab tool are also available in ENBIOS 2D-Lab. Given the more elaborated geometry, more parameters can be tuned by the user (e.g. channel length, semiconductor and oxide thickness, ...). The geometry has a 2D-symmetry: the output DC and AC quantities can be plotted both along the x-direction (the direction of the channel) and along the z-direction (the direction perpendicular to the channel), and the frequency spectra are available as well (magnitude/phase, real/imaginary part, Cole-Cole plots). Finally, the $I_{DS} - V_{FG}$ characteristics (the channel current as a function of the "fluid gate" potential) can also be extracted.

To date, ENBIOS-2D Lab has been effectively used worldwide by more than

200 unique users (Fig. 3.9) for a total number of more than 1,200 simulation runs (Fig. 3.10).

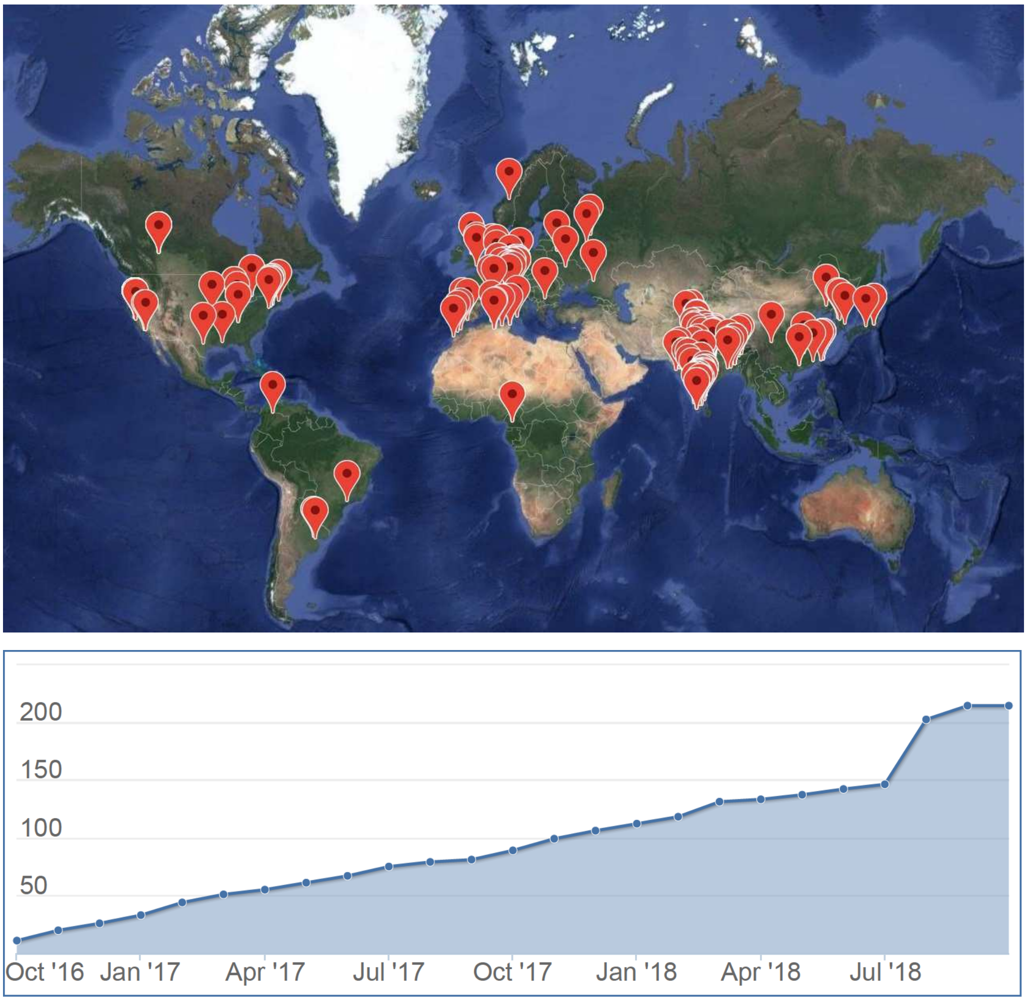

Figure 3.9: *Users of ENBIOS-2D Lab: location (top) and cumulative number (bottom) of unique simulation users (October 1^{st}, 2018).*

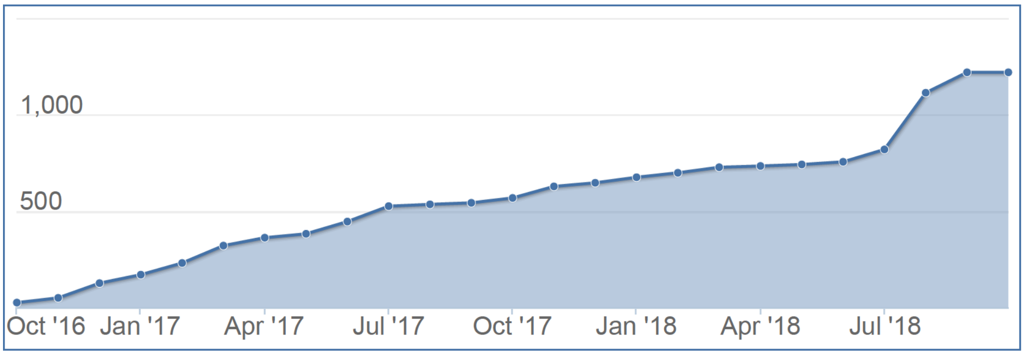

Figure 3.10: *Number of ENBIOS-2D Lab cumulative simulation runs (October 1^{st}, 2018).*

3.3 Modeling of the switching capacitance

Because of the switching operation of the sensor cells, the measurement capacitance C_M provided by the biosensor platform (Eq. 2.1) is not directly comparable to the AC capacitance C_A (see Eq. 3.10), as obtained from small-signal AC models or simulations at $\omega = 2\pi f_s$ (f_s being the switching frequency). To overcome this limitation, a switching model has been developed [190, 203, 291], based on a simplified equivalent circuit of a sensor cell with a nanoelectrode in contact with an electrolyte (Fig. 3.11). The circuit of Fig. 3.11 is similar to the model for the 1D structure of Fig. 3.1. In fact, the response of an individual nanoelectrode in contact with electrolyte is governed by the same physical principles described for the 1D system. The circuit has 4 constant (frequency-independent) components: R_E and C_E are the spreading resistance and spreading capacitance of the nanoelectrode to the electrolyte, C_S is the surface capacitance of the Stern layer in series with the EDL capacitance at the electrolyte/electrode interface (functionalizations of nanoelectrodes, if present, are also included in this term), and C_P is the parasitic capacitance of the switching node. Therefore, compared to the circuit of Fig. 3.1, the presence of the parasitic capacitance C_P is the main difference. Given the different geometry of the electric field flow lines that spread toward adjacent electrodes, the calculation of the values of the circuit components cannot be performed by means of the simple relations of Eq. 3.7. The AC admittance of this equivalent circuit can be expressed as:

$$Y_{el}\left(\omega\right) = \frac{j\omega C_S\left(1 + j\omega R_E C_E\right)}{1 + j\omega R_E\left(C_E + C_S\right)} + j\omega C_P \tag{3.11}$$

It is worth pointing out that this model does not reproduce the effects of analytes in proximity of the electrode. More complex circuit topologies should be adopted in such cases (as discussed in Sect. 4.5)

This equivalent circuit is alternatively charged/discharged by the two switch transistors, which can be modeled as two switches S_T and S_D, connected to the charge and discharge voltages V_T and V_D, respectively. Using the information of the timing parameters of the non-overlapping clocks (Φ_T and Φ_D, see Fig. 2.2), the average current pumped through the sensor cell ($f_s C_{SW}\left(V_T - V_D\right)$) from V_T to V_D

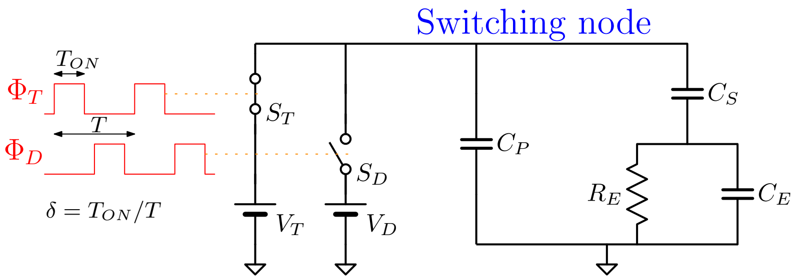

Figure 3.11: *Equivalent circuit of the switching model. C_P is the parasitic capacitance, C_S is the surface capacitance (the Stern layer in series with the double layer), R_E and C_E are the spreading resistance and spreading capacitance of the electrode to the electrolyte. The switches (S_T and S_D) connect the switching node to the charging or discharging voltages (V_T and V_D), as in Fig. 2.2. Published in [190].*

can be derived. The *switching capacitance* is given by:

$$C_{SW} = \gamma \left(C_S + C_P \right) \tag{3.12}$$

where $\gamma = \gamma \left(f_s, \delta, C_P, C_S, C_E, R_E \right)$ is a function of the time parameters (switching frequency, f_s, and duty cycle, δ) and of the lumped element components of the equivalent circuit, and it represents a *charge pump efficiency factor.* We report in Appendix A.1 a complete derivation of this expression and all its parameters.

The values of R_E, C_E and C_S can be estimated by fitting the AC admittance of the right branch of Fig. 3.11 (i.e. Y_{el} without the parasitic capacitance term, namely $Y = \frac{j\omega C_S(1+j\omega R_E C_E)}{1+j\omega R_E(C_E+C_S)}$, see Eq. 3.11) to the AC admittance Y_A, modeled or simulated with or without analyte on (or near) the nanoelectrode surface [211]. In particular, under the assumption that the AC admittance is extracted over a sufficiently broad frequency range (such that the low- and high-frequency limits can be extracted), the parameters can be calculated starting from the AC capacitance spectrum (see Eq. 3.10) as:

$$\begin{aligned} C_S &= \lim_{\omega \to 0} C_A \\ C_E &= \frac{1}{\frac{1}{C_\infty} - \frac{1}{C_S}} \\ G_E &= \frac{1}{R_E} = f_2 C_E \end{aligned} \tag{3.13}$$

where $f_2 = \sigma_{el}/2\pi\varepsilon_{el}$ is the usual electrolyte dielectric cut-off frequency, and $C_\infty = \lim_{\omega\to\infty} C_A$ is the high-frequency limit value of the AC capacitance. Table 3.2 reports values of the parameters extracted for different ambient materials for $r_{el} = 90$ nm. Similarly, Tab. 3.3 reports the same values for the case $r_{el} = 75$ nm. For comparison, values extracted for the 1D-system of Fig. 3.1 are also included. For a direct comparison, we computed the parameters for the 1D system considering a cross-section area equal to the area of nanoelectrodes, and setting $L_{el} = p_y$ (since we actuate the electrodes along one row, the closest distance between a WE and a CE is given by the pitch along the y-direction). The differences in values are evident and are caused by the different profile of the electric field flow lines. A first hint on the properties of the current fluxes (from WEs to CEs) could be obtained by estimating, for each ambient material, the value of Area and L_{el} to be used in the 1D-system that guarantees a matching between the parameters of the 1D model and the parameters extracted by means of ENBIOS simulations.

The value of C_P can be extracted from experiments (in dry experiments $|Y| \ll \omega C_P$, so the measured capacitance in air is very close to C_P). As will be discussed in Chapter 4, the value of C_P is essentially equivalent to the parasitic capacitance extracted from the physical layout of the sensor cells; therefore, it is always possible to discriminate C_P from C_S, also if the parasitics were not dominant over C_S in dry. The switching capacitance model based on Fig. 3.11 will be extensively used in this thesis for the theoretical predictions (that is, we extract the AC admittance from ENBIOS simulations, compute the lumped element values as per Eq. 3.13, and compute C_{SW} according to Eq. 3.12). The simplified lumped element model of Fig. 3.11 will thus be used to translate the simulated AC small signal impedance into

	Fig. 3.11			**Fig. 3.1**		
Dielectrics[*]	**$\mathrm{C_S}$ [fF]**			**$\mathrm{C_S}$ [fF]**		
air	0.0027			0.0003		
IPA	0.0483			0.0056		
Electrolytes	**$\mathrm{C_S}$ [fF]**	**$\mathrm{C_E}$ [fF]**	**$\mathrm{R_E}$ [MΩ]**	**$\mathrm{C'_S}$ [fF]**	**$\mathrm{C_E}$ [fF]**	**$\mathrm{R_E}$ [MΩ]**
milliQ	0.2091	6.8772	67377	0.0183	0.0245	1.8×10^7
KCl 1mM	1.5214	0.2342	197.85	1.4229	0.0245	1866
KCl 1.5mM	1.7668	0.2292	134.72	1.6587	0.0245	1244
KCl 10mM	3.2484	0.2159	21.41	3.0246	0.0245	186.7
KCl 15mM	3.6007	0.2142	14.36	3.3441	0.0245	124.4
KCl 50mM	4.5593	0.2096	4.36	4.2466	0.0245	37.33
KCl 100mM	4.9969	0.2059	2.19	4.6962	0.0245	18.66
KCl 150mM	5.2137	0.2028	1.46	4.9273	0.0245	12.44
KCl 500mM	5.7376	0.1827	0.44	5.4689	0.0245	3.73

[*] dielectric materials have essentially infinite spreading resistance and are modeled as a simple capacitance value.

Table 3.2: *Estimation of the lumped element components C_S, C_E, R_E of Fig. 3.11, extracted for different ambient materials by means of ENBIOS simulation with default simulation parameters and $r_{el} = 90$ nm. For comparison, values for the lumped elements of the 1D model of Fig. 3.1 are also indicated. The values for the 1D system have been computed using Area=πr_{el}^2 and L_{el}=720 nm (i.e. the pitch along the y-direction, since we operate activating all the electrodes along one row) and indicating as $C'_S = C_{Stern}C_{EDL}/(C_{Stern} + C_{EDL})$.*

	Fig. 3.11			**Fig. 3.1**		
Dielectrics[*]	**$\mathrm{C_S}$ [fF]**			**$\mathrm{C_S}$ [fF]**		
air	0.0023			0.0002		
IPA	0.0406			0.0039		
Electrolytes	**$\mathrm{C_S}$ [fF]**	**$\mathrm{C_E}$ [fF]**	**$\mathrm{R_E}$ [MΩ]**	**$\mathrm{C'_S}$ [fF]**	**$\mathrm{C_E}$ [fF]**	**$\mathrm{R_E}$ [MΩ]**
milliQ	0.1741	6.5213	71054	0.0127	0.0170	2.6×10^7
KCl 1mM	1.0717	0.2014	230.01	0.9882	0.0170	2688
KCl 1.5mM	1.2420	0.1963	157.29	1.1519	0.0170	1792
KCl 10mM	2.2788	0.1827	25.29	2.1004	0.0170	268.8
KCl 15mM	2.5263	0.1811	16.99	2.3223	0.0170	179.2
KCl 50mM	3.2004	0.1767	5.18	2.9491	0.0170	53.75
KCl 100mM	3.5086	0.1734	2.60	3.2613	0.0170	26.88
KCl 150mM	3.6613	0.1707	1.74	3.4218	0.0170	17.92
KCl 500mM	4.0307	0.1537	0.52	3.7979	0.0170	5.38

[*] dielectric materials have essentially infinite spreading resistance and are modeled as a simple capacitance value.

Table 3.3: *Same as Tab 3.2 for $r_{el} = 75$ nm.*

a switching capacitance (not vice-versa). This model is the simplest one that preserves the basics of the Physics of operation implemented with full three-dimensional geometrical accuracy in the FEM simulator (RC behavior of the electrolyte, EDL capacitance, parasitic capacitance). More complex models may be used as well, not only to translate the AC small signal simulations into a switching capacitance, but also to interpret experimental results. This will be discussed in Sect. 4.5.

In Fig. 3.12 (green dashed curve), we show typical switching capacitance spectra in electrolyte, where the low frequency part of the response is essentially governed by the surface capacitance C_S, as per the EDL screening theory. In this figure we also compare the switching capacitance to the AC capacitance (C_A) and to the *effective capacitance* [215], which is defined as:

$$C_{eff} = |Y_A|/\omega \tag{3.14}$$

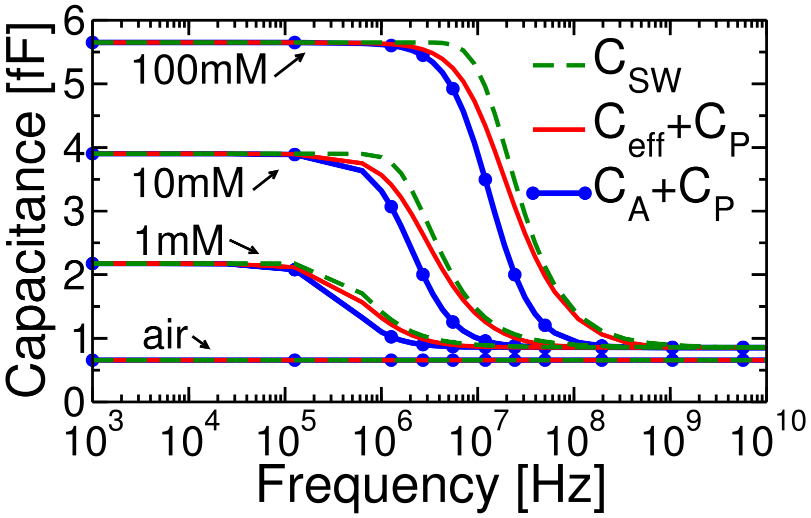

Figure 3.12: *Comparison between AC capacitance (C_A), effective capacitance (C_{eff}) and switching capacitance (C_{SW}) spectra for nanoelectrodes with radius r_{el} =90 nm in dry or in NaCl electrolytes at different salt concentrations. The parasitic capacitance used for the calculation of C_{SW} is C_P =0.65 fF. C_P is also added to C_A and to C_{eff} to allow a direct comparison between the different capacitance models. The duty cycle for C_{SW} is $\delta = 35\%$.*

As was demonstrated in [215], C_{eff} appear as a good empirical approximation of the actual switching capacitance of the system. Fig. 3.13 instead highlights the impact the duty cycle has on the C_{SW} spectra: for higher duty cycles (i.e., for longer charging phases) a rigid shift of the curve toward higher frequencies occurs. Furthermore, Fig. 3.14 shows how C_{SW} is affected by variations of the lumped element model parameters: variations of the surface capacitance C_S affect the low-frequency part of the spectrum, variations of C_P result in a nearly rigid vertical shift of the curves, variations of C_E change the response in the high-frequency limit, and variations of R_E appear as a shift of the cut-off frequencies of the spectra.

If an analyte is present in the electrolyte, the electric field is perturbed and the capacitance spectrum changes. Considering the switching model, in the same

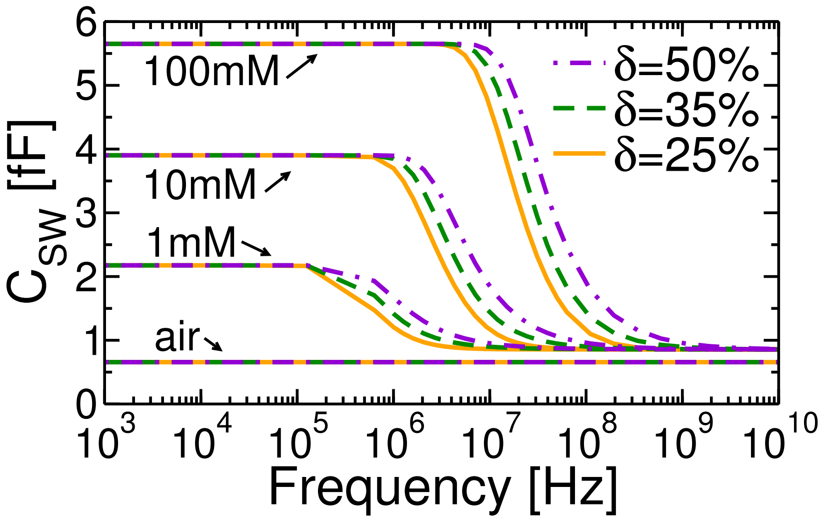

Figure 3.13: *Comparison between switching capacitance (C_{SW}) spectra for different duty-cycle (δ) values. The electrolyte is NaCl and we used C_P =0.65 fF. Higher duty cycles result in a rigid shift of the curved toward higher frequencies.*

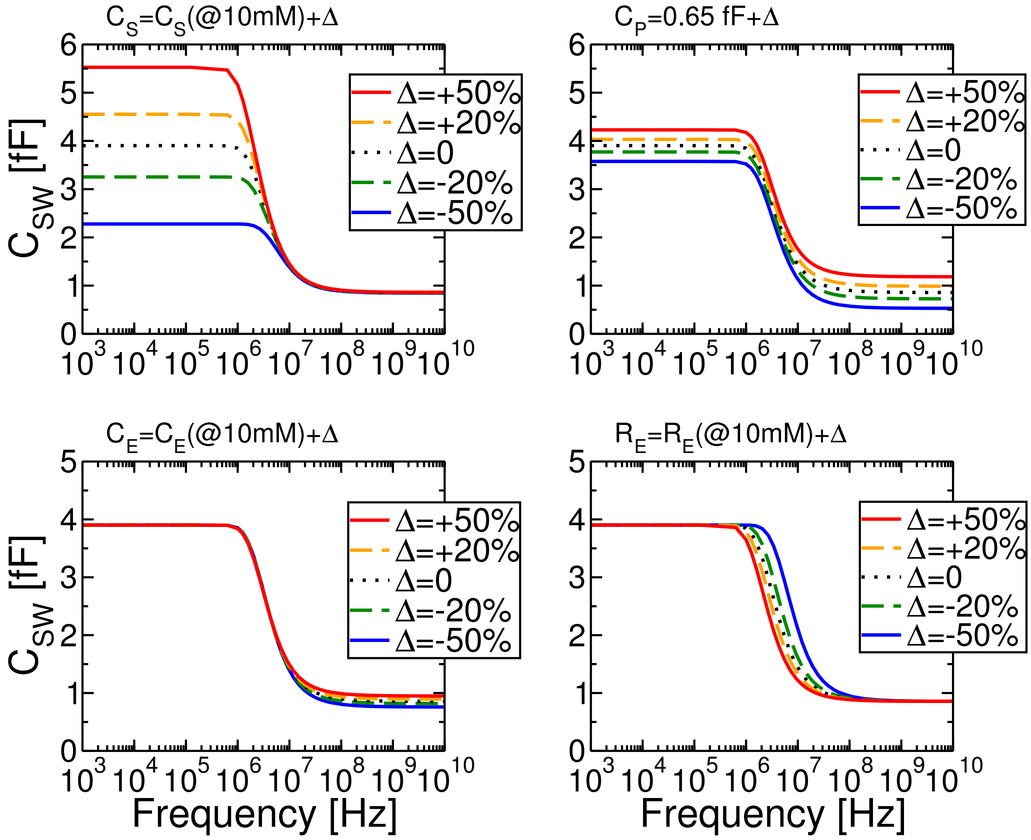

Figure 3.14: *Comparison between switching capacitance (C_{SW}) spectra for variations of the lumped-element model parameters of Fig. 3.11. The nominal values correspond to the 10 mM salt concentration of Tab. 3.2 (left).*

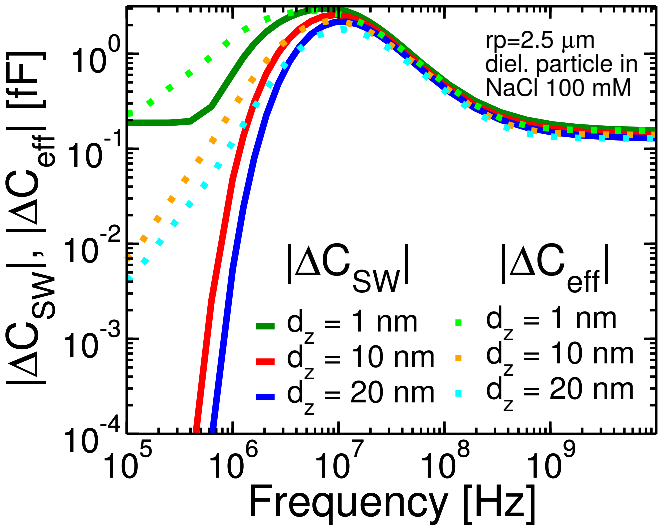

Figure 3.15: *Theoretical switching and effective capacitance spectra of a bare nanoelectrode in 100 mM NaCl electrolyte, due to inserting a 2.5 µm radius dielectric microparticle (permittivity $\varepsilon_p = 2.6\varepsilon_0$) at a vertical distance of 1, 10, or 20 nm from the surface of the (central) nanoelectrode.*

fashion as for the AC capacitance, we call:

$$\Delta C_{SW} = C_{SW\,w/\ analyte} - C_{SW\,w/o\ analyte} \tag{3.15}$$

the switching capacitance variation, induced by the presence of the analyte, i.e. the difference between the switching capacitance response with and without analyte. As has been already demonstrated in [215], the *effective capacitance* is also a good approximation of the response of the platform when it comes to inspecting capacitance variations, i.e.

$$\Delta C_{eff} = C_{eff\,w/\ analyte} - C_{eff\,w/o\ analyte} \tag{3.16}$$

This is also shown in Fig. 3.15, where we compare ΔC_{SW} and ΔC_{eff} due to the insertion of a 5 µm dielectric particle in a NaCl 100 mM electrolyte, at different vertical distances from the surface of the array. The capacitance variation spectra have a peak of the response around 10 MHz (which is a function of the salt concentration of the electrolyte, see also Sect. 3.5). Differences between the capacitance variation spectra of the two models are especially evident for frequencies lower than 2 MHz (very close to the lower frequency limit of the platform). This is consistent with the results of Fig. 3.12, in which C_{SW} and C_{eff} differed in particular close to the first cut-off frequency. Fig. 3.15 also serves as a further demonstration that detecting analytes beyond the Debye screening length requires high frequencies, because $\Delta C_{\square}$ becomes very small at low frequency.

It is worth to point out that the switching capacitance model is of even more general applicability. In fact, if the system under study (the ambient in contact with the nanoelectrode) is modeled with more elaborated lumped element networks, calculations of a switching capacitance can be performed in the same fashion (see for instance Sect. 4.5 and Appendix A.2). However, a main limitation of this approach is given by the fact that we require an equivalent lumped-element circuit model of the system on top of the nanoelectrode. While the C-RC model of Fig. 3.11 nicely captures the Physics of nanoelectrodes in contact with electrolyte, for more complex ambient conditions (like, for instance, electrolytes in the presence of analytes) it may not always be possible to derive (Physics-based) equivalent circuits. Hence, in the following of this work we will rely on C_{SW} (or on its extended version C_F, see Sect. 3.4) whenever possible, using instead C_{eff} for the other cases.

3.4 Simulation with arbitrary input voltage waveforms

ENBIOS simulates the DC and small-signal AC response of electronic biosensors. An AC voltage stimulus is applied at different (user-defined) frequencies, and the current at the electrodes is obtained, thus deriving information about the AC behavior of the system (e.g. in terms of admittance values). However, the actual chip does not operate in AC small-signal regime, nor with ideal square waveforms as assumed by C_{SW} calculations. In order to improve the accuracy of the ΔC calculations for comparison with C_M, here we expand the analysis capabilities of the simulator by deriving the response of the working electrode to an arbitrary input voltage waveform. The methodology is quite general and can be applied to determine the response of different systems (the nanoelectrodes discussed in this thesis, but also other devices like ISFETs). Fourier analysis is used for this purpose.

Let's consider an arbitrary periodic input voltage waveform $v(t)$, with repetition period $T = 1/f$ (f being the frequency). We can approximate it in Fourier series as:

$$v(t) \simeq \frac{a_0}{2} + \sum_{n=1}^{N_{harm}} \left[a_n \cos(2\pi nft) + b_n \sin(2\pi nft)\right] = \sum_{n=-N_{harm}}^{N_{harm}} c_n e^{j2\pi nft} \tag{3.17}$$

where a_n and b_n are real numbers, c_n are complex numbers, j is the imaginary unit, and N_{harm} represents the number of harmonics that we take into account. The coefficients are (in general) frequency dependent and take the following form:

$$\begin{aligned} a_n &= \frac{2}{T}\int_{t_0}^{t_0+T} v(t)\cos(2\pi nft)dt \\ b_n &= \frac{2}{T}\int_{t_0}^{t_0+T} v(t)\sin(2\pi nft)dt \\ c_n &= \begin{cases} \frac{1}{2}(a_n - jb_n) & \text{for } n > 0 \\ \frac{1}{2}a_0 & \text{for } n = 0 \\ c^*_{|n|} & \text{for } n < 0 \end{cases} \end{aligned} \tag{3.18}$$

We set the goal of computing (by means of ENBIOS simulations) the (output) electrode's current of a generic biosensor system resulting from the application of this arbitrary voltage waveform. One relevant example is given by trapezoidal voltage waveforms (analytical expressions for the coefficients of trapezoidal waveforms, as well as for the limiting case of square and triangular waveforms, are provided in Appendix B). In general, input waveforms at different frequencies (different repetition periods) may not maintain a constant DC bias.[1] For this reason, the most general approach requires to account for the possibility of having different DC bias values at different frequencies. Fig. 3.16 shows the flowchart of the most general approach to the problem.

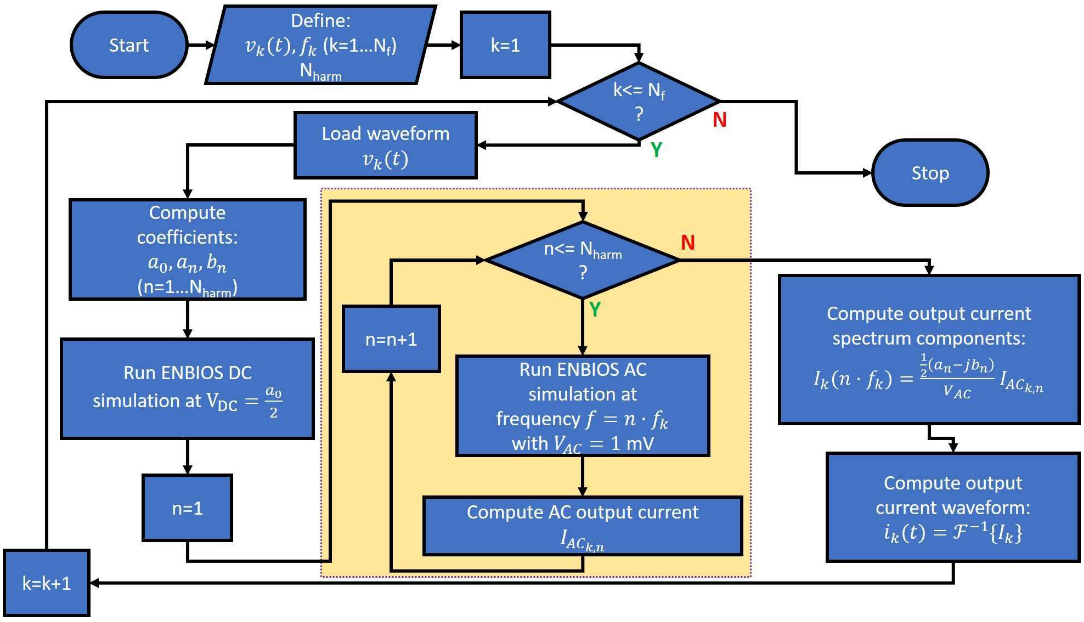

Figure 3.16: *Flowchart of a general ENBIOS-based Fourier analysis. The calculations included in the yellow-box are directly and efficiently implemented by ENBIOS, performing a parallel simulation over a* $(1{:}n{:}N_{harm})f_k$ *frequency vector of the system with fixed simulation parameters.*

The algorithm starts with the definition of the system (e.g. the nanoelectrode platform, the 1D system of Fig. 3.1, ISFET devices, ...), the definition of the fundamental frequencies to be analyzed (f_k) and, for each f_k, the definition of an input voltage waveforms ($v_k(t)$, e.g. extracted from Spice simulations). N_F represents the number of fundamental frequencies to be analyzed. The user also pre-defines the total number of harmonics (N_{harm}) that will be considered for the Fourier analysis (a fixed value of harmonics, for all the fundamental frequencies f_k). From this point, each fundamental frequency (scanned by the index parameter k) is processed separately (hence, this *for* loop could be implemented enabling parallelism). The specific waveform $v_k(t)$ is loaded, and the Fourier coefficients are computed. At this point, a DC ENBIOS simulation is run. The DC solution is the starting point for the AC analyses. For each (n-th) harmonic, an AC ENBIOS simulation is run at frequency

---

[1] As an example, trapezoidal waveforms may have a duration of the high/low voltage level that scales with frequency and rise/fall times that remain constant; another example is given by the possible presence of physical phenomena that introduce non-idealities at different operating frequencies, e.g. $1/f$ noise

equal to the n-th multiple of the fundamental tone f_k. The amplitude of the AC signal is set to 1 mV: this is an arbitrary choice, given the linearity of the ENBIOS solution (the simulator solves AC equations linearized around the DC solution). The corresponding output AC current $I_{AC_{k,n}}$ is collected. After all the harmonics are computed, the frequency spectrum of the output current (I_k) is easily constructed exploiting the linearity of ENBIOS, i.e. “correcting” for the arbitrary input voltage amplitude V_{AC}: $I_k\left(nf_k\right) = I_{AC_{k,n}} c_n V_{AC} = I_{AC_{k,n}} \left(a_n - jb_n\right)/2V_{AC}\ \forall n \in [1, N_{harm}]$. This procedure is chosen (instead of directly simulating the different harmonics with the proper AC amplitudes) because ENBIOS already implements efficient parallel calculations (of a system with fixed simulation parameters) over different frequencies: re-normalizing by the correct AC amplitude at the end of the AC calculations is therefore the fastest solution. Finally, starting from the current spectra, the current time waveform can be reconstructed (as per Eq. 3.17):

$$i(t) = \sum_{n=1}^{N_{harm}} \left[2\Re\{I_k\left(nf_k\right)\}\cos\left(2\pi nft\right) - 2\Im\{I_k\left(nf_k\right)\}\sin\left(2\pi nft\right)\right] \tag{3.19}$$

While this approach appears as a general solution, it presents a few drawbacks. First, a different DC simulation has to be run for each fundamental frequency of the input. This could be a problem, since the DC solution may take quite some time to be computed (e.g. for systems with complex charge distributions, as for viruses, see Sect. 3.5). On top of that, for each fundamental tone, the vector of frequencies to be simulated for the AC problem is different. The combination of these two factors can make the total simulation time very high. Finally, conventional ENBIOS DC and AC simulations are run at each iteration: this means that the hypotheses for the validity of the small-signal approximation have to be satisfied as well. As a consequence, the signals (i.e. every single harmonic component, in particular the fundamental tone) have to be small enough compared to the thermal voltage k_BT/q (≈25 mV at room temperature), therefore the analysis can be applied only to small-amplitude signals. For the biosensor platform of Sect. 2.1 this is not always the case since $V_T - V_D$ can be up to 200 mV in real experiments.

For practical applications where the input DC bias is known not to change at different input fundamental frequencies (or at least not to change significantly, as is the case for the nanoelectrodes array platform where frequency-compensation is implemented, see Chapter 2), and considering systems for which a model is available (as is the case for both the 1D system, see Fig. 3.1 bottom, and for the nanoelectrode array platform, see the right branch of the circuit in Fig. 3.11), the Fourier analysis can be simplified and performed as a simple post-processing of conventional ENBIOS AC simulations.

Let’s then assume that the system verifies these hypotheses and a model M describes the relation between the AC input of the system (V_{AC}) and the desired AC output. In our case, the model is simply given by the admittance (or impedance) of the system (i.e. $I_{AC} = MV_{AC}$, with $M = Y_{a.m.}$ as per Eq. 3.8 for the 1D system, or with $M = Y_{el}$ as per Eq. 3.11 for the nanoelectrodes). The flowchart of the (now much easier and faster) calculations is shown in Fig. 3.17.

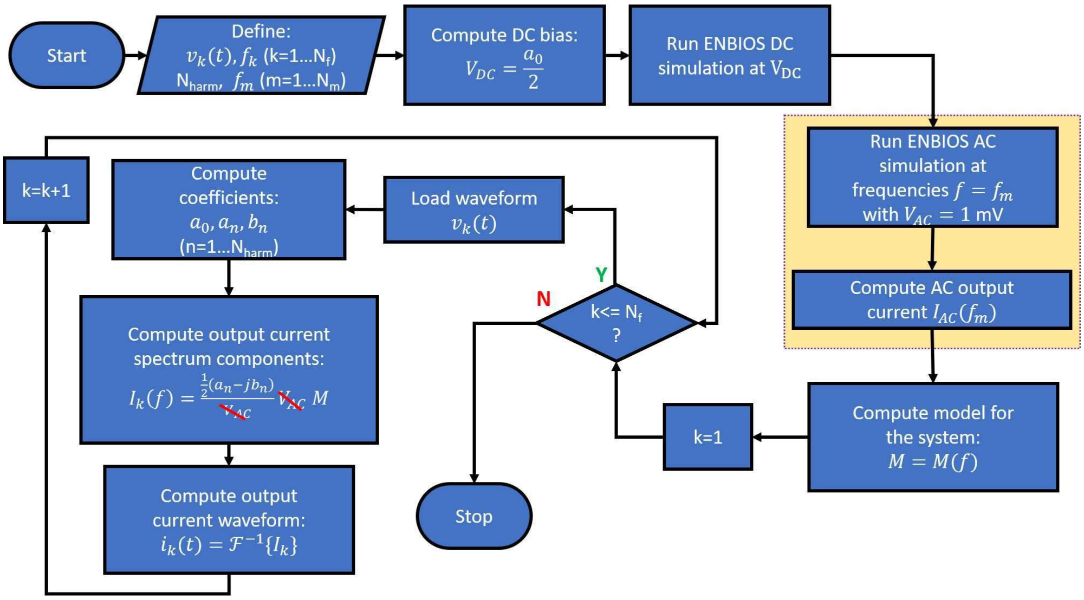

Figure 3.17: *Flowchart of a simpler Fourier analysis performed as a post-processing on a system model obtained from a single conventional ENBIOS simulation. The calculations included in the yellow-box are efficiently made by ENBIOS with a parallelized simulation over a f_m frequency vector of the system with fixed simulation parameters.*

We start from the definition of the system to be simulated (e.g. the nanoelectrode array, the 1D system of Fig. 3.1, an ISFET device, ...) and the knowledge of the input voltage waveforms ($v_k(t)$) for different fundamental frequency values f_k (given, for instance, by circuit simulations). A vector of frequencies f_m is also defined and will be used to run the ENBIOS simulations (f_m should be sufficiently broad-band to capture the low- and high-frequency limit response of the system). The DC bias of the waveform(s) is computed and the DC ENBIOS simulation is run; then, also the AC simulation is performed at frequencies f_m. After the ENBIOS simulation is completed, we can generate a model M for the system (e.g. a lumped element equivalent circuit as in Fig. 3.11 from which we can derive an expression for the admittance). The real Fourier analysis will now be applied to this model M and each frequency point f_k is processed separately. The waveform $v_k(t)$ is loaded, and the Fourier coefficients are computed. The frequency spectrum of the output current (I_k) is easily constructed exploiting the known model (the admittance in this example). Finally, starting from the current spectra, the current waveform can be reconstructed.

With this approach, a single ENBIOS simulation is required to compute the model for the system. If the model is already available (e.g. the analytical model for the 1D system), then ENBIOS simulations can be skipped.

3.4.1 Application to the nanoelectrodes

The methodology based on Fourier analysis can be used to convert ΔC calculations into an accurate estimate of the response of the nanoelectrodes, expressed as a

Fourier capacitance (C_F) alternative to the *switching* or *effective* capacitance models explained in Sect. 3.3. We remind from the discussion of Chapter 2 that the sensor yields a capacitance measurement C_M by integrating the current over time to obtain the charge transferred through the sensor cell per charge/discharge cycle (Eq. 2.1). Since the Fourier analysis allows us to reconstruct the current waveform at the nanoelectrode, the charge can be easily computed with a similar procedure as in the biosensor platform. The steps to achieve this goal are the following:

1. Define the nanoelectrode's input voltage waveform $v(t)$ (e.g. a square wave, a trapezoidal wave, or more realistic non-ideal waveforms obtained for instance by means of Spice simulations of the circuit);

2. Apply the Fourier analysis and compute the output current waveform $i(t)$ (Eq. 3.19);

3. Integrate the current waveform to obtain the charge transferred to/from the nanoelectrode $q(t)$ (this indefinite integral can be calculated analytically, without introducing numerical errors, simply by integrating the expression of Eq. 3.19);

4. Extract from $q(t)$ the charge *transferred* to the nanoelectrode in one cycle (i.e. move from the *indefinite* integral to a *definite* integral; this is the term Q_S of Eq. 2.1);

5. Divide by $\Delta V = V_T - V_D$ (see Eq. 2.1), i.e. the difference between the drive voltages during the charge and discharge phases.

This is repeated for all the fundamental tones of interest (the shape of $v(t)$ may change with frequency). Finally, a capacitance spectrum (at the different fundamental frequencies of the input waveforms) is obtained. In the following, we refer to this model as *Fourier capacitance*, C_F. We will make use of the Fourier capacitance in Sect. 4.4.

3.4.2 Model validation

In order to validate the methodology, we make use of the switching capacitance model described in Sect. 3.3. The switching model inherently accounts for all harmonics and it is valid exactly provided the voltage waveform is indeed a square wave. As we will see, significant deviations can arise in the actual circuit. Calculating C_F due to a square-wave input on the same circuit should in principle result in an identical capacitance spectrum.

We start by considering the switching model of Fig. 3.11 and computing C_{SW} with duty cycle δ =50%. The resulting capacitance spectra are reported in Fig. 3.18 (blue curves). Then, we consider a square wave with 50% duty cycle and high/low voltage levels V_T=365 mV and V_D=120 mV, respectively. We start by calculating the Fourier coefficients, considering $N_{harm} = 5000$ harmonics. Then, we calculate the current time waveform, we derive the charge transferred/removed to/from the nanoelectrode during one period, and we compute $C_F = Q_S/\left(V_T - V_D\right)$. The final result is shown in Fig. 3.18 (dashed orange). A good agreement is found between

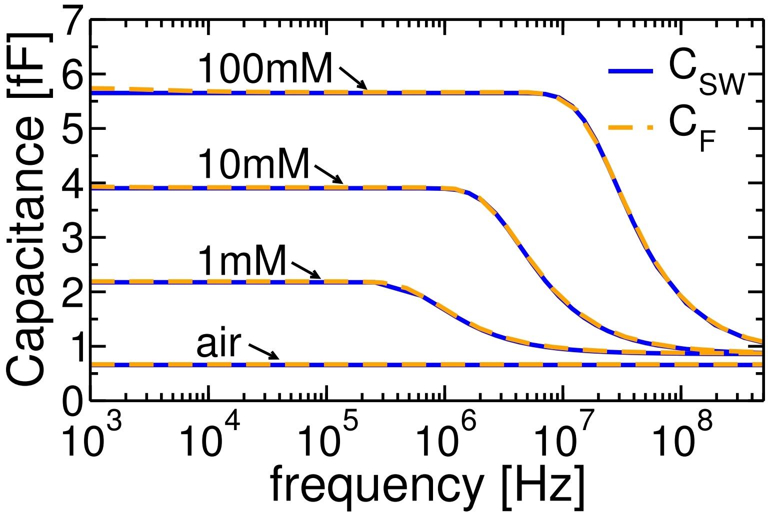

Figure 3.18: *Comparison between switching capacitance (C_{SW}) and Fourier capacitance (C_F) spectra for nanoelectrodes with radius r_{el} =90 nm in dry or in NaCl electrolytes at different salt concentrations. The parasitic capacitance used for the calculation of C_{SW} and C_F is C_P =0.65 fF. The duty cycle for C_{SW} is $\delta = 50\%$. The input signal for C_F is a square wave with the same duty cycle. The number of harmonics considered is $N_{harm} = 5000$.*

C_{SW} and C_F over the whole spectrum. The validity of the methodology is verified over a broad frequency range, in particular in the frequency range of operation of the biosensor platform.

3.4.3 Analysis of voltage and current waveforms

Here we report in details about the output waveforms for a relevant test case, namely trapezoidal waveforms. More realistic waveforms (comprising non-idealities) will be considered for the analyses of HFIS experiments in Sect. 4.4. We consider trapezoidal waveforms with amplitude spanning from a low-voltage level V_D=-60 mV to a high-voltage level V_T=60 mV, and rise/fall times of $t_r = t_f$=1 ns. We test different wave frequencies, scaling down the duration of the high/low level phases while keeping the rise/fall times constant. This poses a limit to the maximum frequency, that is given by $f_{max} = 1/(t_r + t_f)$. In Appendix B we report the calculations for the Fourier expansion of trapezoidal, square and triangular waveforms. The latter ones are of interest since they correspond to the low-frequency and high-frequency limit of the trapezoidal waveform.

Figures 3.19-3.20-3.21-3.22 show the results of the analysis on the lumped element circuit of Fig. 3.11 for fundamental frequencies f = 1 kHz, 500 kHz, 10 MHz and 500 MHz input trapezoidal waveform, respectively. Results are shown for air and KCl 10mM electrolyte. The total number of harmonics is N_{harm}=5000.

At low frequency (1 kHz) the trapezoidal input waveform resembles a square wave, since $t_r = t_f = 1$ ns are much smaller than $1/f$. The Fourier series exhibits the well-known Gibbs oscillations [292] (exceeding by 10 mV the nominal high/low-levels). The output current in air is essentially given by a spike during $v(t)$ transitions. This is consistent with the behavior of an ideal capacitor of ~ 3 aF with $dV/dt = (V_T - V_D)/t_r = 120$mV/ns. The response in electrolyte is also given by a a narrow pulse, induced by the high-frequency spectral components of the abrupt transition of the voltage level (again, consistent with the behavior of a capacitor: in fact, we remember that the electrolyte at low frequency is essentially defined by the Stern/EDL capacitance in parallel to C_P; therefore, for a square wave input at 1 kHz, the shape of the current is no different from that in air). The charge transferred to the nanoelectrode's node has a square-wave-like shape, both in air and in electrolyte, consistently with expectations (for a capacitive load, since the current is computed as the derivative of the voltage trace, and to obtain the charge we perform an integration, we re-obtain the input waveform shape).

At 500 kHz and 10 MHz, air still behaves as an ideal capacitor and the charge waveform resembles again that of the voltage. For the 10mM electrolyte, instead, the resistive component of the equivalent circuit starts to play a role. The current waveform increase/decrease more smoothly than a spike. As can be noticed from the charge plot, RC-exponential-like behaviors appear in the waveform. The exponential decay starts immediately after the end of one transition, due to charge repartition in the elements of the circuit sustained by the resistor, but due to the exponential time dependency it grows to a visible level only before the next transition.

Finally, at the maximum frequency $f = 1/(t_r + t_f) = 500$ MHz the voltage waveform is a triangular waveform, well reproduced by the large number of harmonics. Also in this case, the output charge in air has the same shape as the voltage waveform due to the capacitive behavior. We can say the same also for the electrolyte: in fact, 500 MHz is way beyond the cut-off frequency of a 10mM electrolyte and it behaves as a capacitor (given by the series of C_S and C_E, in parallel to C_P).

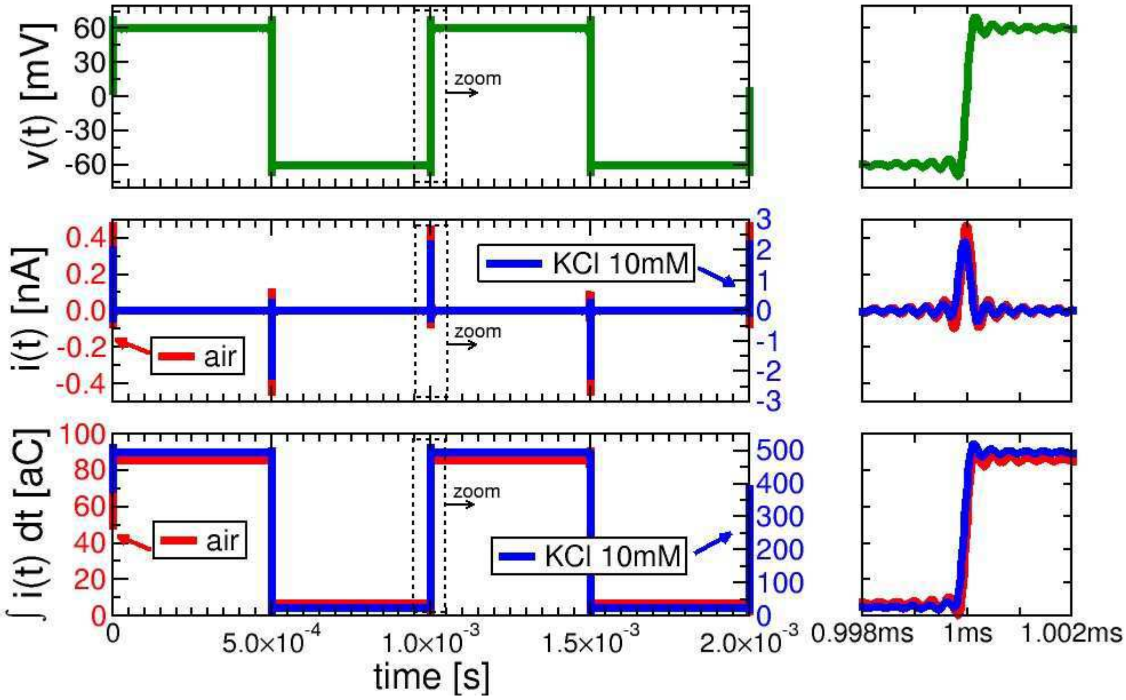

Figure 3.19: *Voltage, current and charge waveforms of the system of Fig. 3.11 due to a trapezoidal wave excitation at frequency 1 kHz. The values of the lumped elements are as listed in Tab. 3.2.* C_P*=0.65 fF,* $t_r = t_f$*=1 ns.*

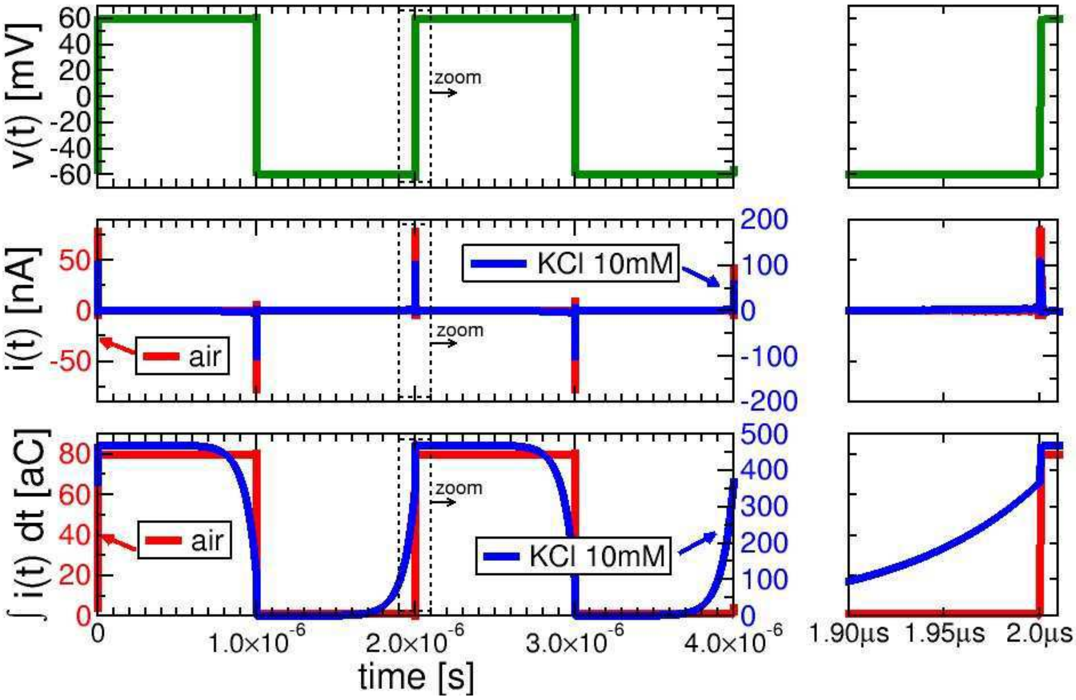

Figure 3.20: *Same as Fig. 3.19 at 500 kHz frequency.*

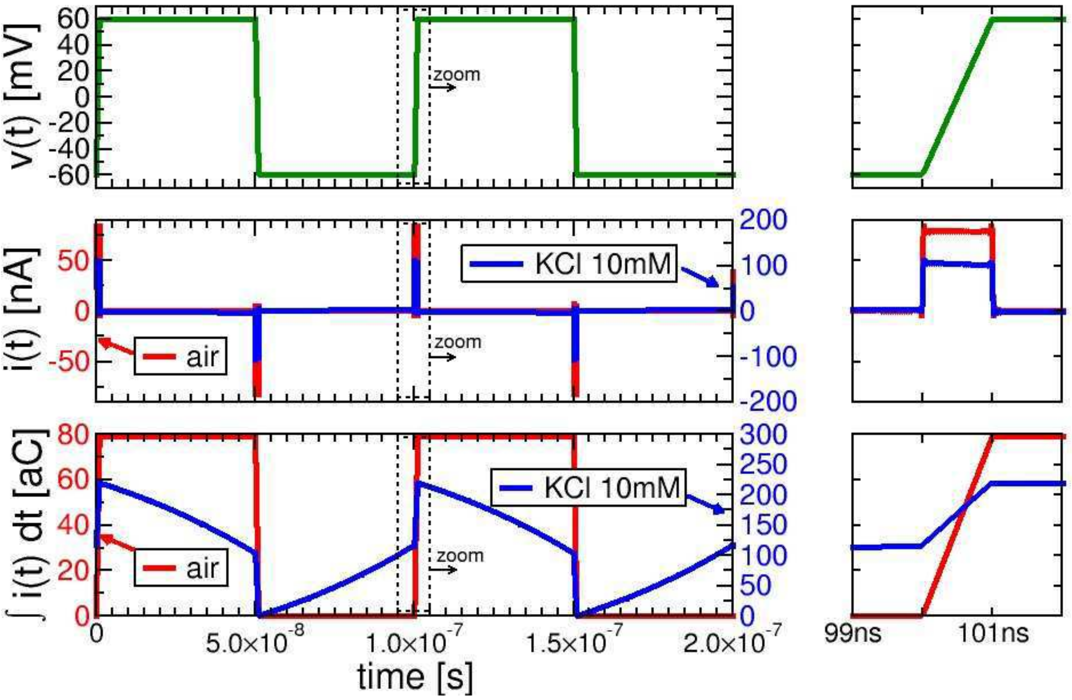

Figure 3.21: *Same as Fig. 3.19 at 10 MHz frequency.*

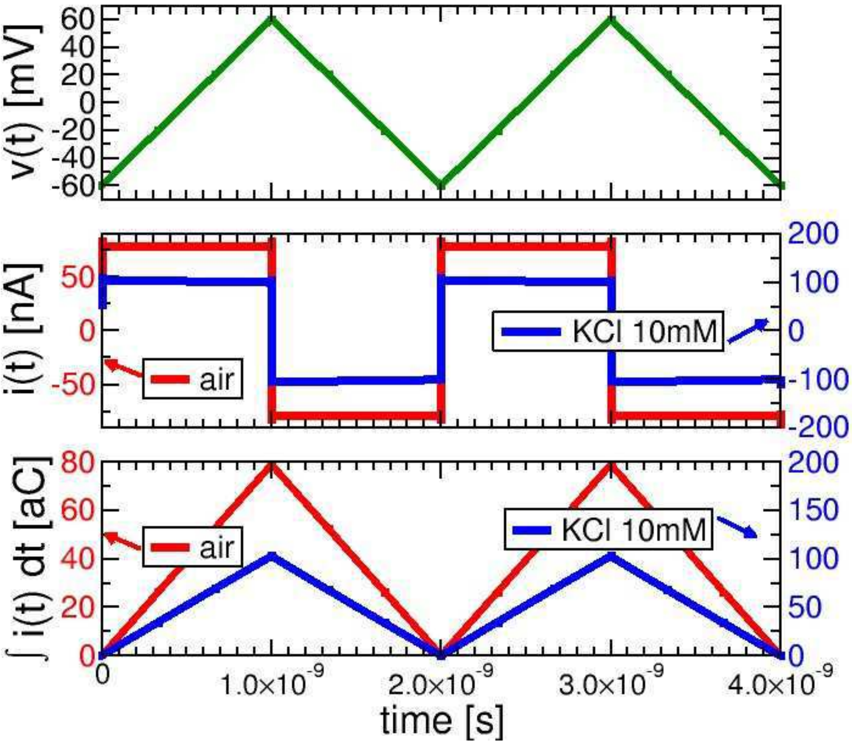

Figure 3.22: *Same as Fig. 3.19 at 500 MHz frequency.*

3.5 Models for viruses

In this section we present models to study the theoretical HFIS response of the nanoelectrode biosensor platform described in Chapter 2 to individual biomolecules of different viruses. This material is based on [247,248]. Examples of virus impedance/-capacitance spectra recordings are given, for instance, in [293, 294] (for FIV, HIV, AV5, HSV1, SV40, MVA and CPMV viruses), showing that the viruses possess distinguishable capacitances and that dielectric properties of capsid proteins and glycoproteins (which are different for every viral type) significantly influence the observed response. However, these measurements do not rely on CMOS technology (thus losing the opportunities offered by technology scaling) and the maximum frequency of analysis is still below the electrolyte relaxation frequency at physiological salt concentrations.

The structure and the morphology of isolated viruses is usually inspected by means of complex atomistic models, obtained e.g. from X-ray diffraction and cryo-electron microscopy [295, 296]. Rather than aiming at detailed and accurate virus descriptions, we use the atomistic data as the starting point to develop a compact and spatially averaged virus model, representative of the main geometrical and electrostatic properties of the viruses. In particular, here we consider three viruses whose structure is similar to truncated-icosahedrons: a plant virus (the *Cowpea Chlorotic Mottle Virus*, CCMV), an animal virus (the *Rabbit Haemorrhagic Disease Virus*, RHDV), and a human virus (the *Hepatitis A Virus*, HAV).

The proposed methodology is applicable to other viruses as well (provided the atoms' positions and charges are available) and it would thus be useful to build a library of HFIS spectra profiles for different virus families. The results reveal aspects of relevance for modeling and of practical importance (the role of virus charge, the role of pH, the influence of ionic strength on the expected signal), possibly steering the design of successful experiments with ultra-sensitive CMOS biosensors as the one considered in this work.

3.5.1 T=3 viruses

Viruses are made up by an infective agent, either a deoxyribonucleic acid (DNA) or a ribonucleic acid (RNA), which can be double-stranded (ds) or single-stranded (ss). The infective agent is enclosed in a protective package (a *capsid*, typically made of proteins) [297], and some viruses also have an external coating around this capsid. A possible classification of viruses is based on the structure of the capsid, and helical and icosahedral symmetries are the most common patterns. Icosahedrons can be constructed as a combination of pentamers and hexamers, and icosahedral capsids are typically classified according to their *triangulation number* T (i.e. the number of equilateral triangles that can fit on one face). Viruses with T=3 triangulation number can be modeled as a truncated icosahedron and will be consider for this work.

The first virus we consider is the *Cowpea Chlorotic Mottle Virus* (CCMV), which belongs to the *Bromoviridae* virus family. We select this virus as a plant virus example, and because it is common and well studied. CCMV is a positive-sense single stranded RNA (ssRNA+) virus with no external coating, made up only by the proteic capsid ($\approx$ 24 nm diameter) and a nucleic acid (RNA) within it [296].

Fig. 3.23 (left) shows the truncated-icosahedral shape on top of a detailed atomistic contour map of the CCMV virus. Fig. 3.23 (center) shows a cross-section of the capsid. Part of the capsid proteins protrude into the inner core, generating proteic tails (red lines in Fig. 3.23, center). The negatively charged nucleic acid contained in the capsid is located next to the capsid's inner surface, with very low density at the center [295] (Fig. 3.23, right), and interacts with the (typically positively) charged proteic tails.

The CCMV genome is composed of three distinct RNA molecules (RNA1, RNA2, RNA3) [299]. The longest sequence (RNA1) has 3174 nucleotides. The CCMV native form is stable for pH values between 3 and 6 and ionic strengths lower than 100 mM. Increasing the pH level results in an increase of the virus size (*swollen state*) [300], along with the formation of openings in the capsid's structure which allow the exchange of ions between the inner core of the virus and the outer electrolyte. On top of that, for large ionic strengths ($\approx$ 1 M) the complete disgregation of the capsid can also occur [296]. In the following, we will first consider a pH of 5 and concentrations much smaller than 1 M, corresponding to the virus stable state, inspecting the capacitance spectra of empty capsids and full viruses (i.e., capsid + RNA) in electrolytes of different salt concentration. Then, we will also consider a higher pH value (7), taking into account the swelling process of the capsid [301].

As a second case study, we consider the *Rabbit Haemorrhagic Disease Virus* (RHDV) [302], from the *Caliciviridae* family. We select this virus as an animal virus example, and because of its economic and ecological importance [303]. As the CCMV, the RHDV has a non-enveloped capsid (i.e., it has no external coating). On top of that, as reported in Sect. 3.5.2, it is also an interesting test case due to its mass distribution. The capsid of the RHDV is of about 27-40 nm in diameter, and its ssRNA(+) genome is 7437 nucleotides long. As for the CCMV, we investigate

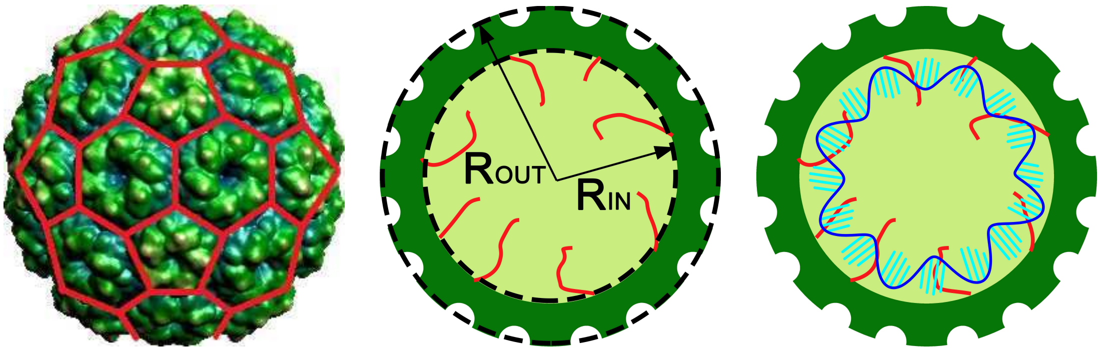

Figure 3.23: *Left: representation of the T=3 CCMV virus, highlighting its truncated icosahedral symmetry (image taken from VIPERdb web portal [298]). Center: 2D sketch of the capsid cross section. The dark-green region corresponds to the capsid, and the light-green region corresponds to the electrolyte which fills the core of the virus. Red lines represent proteic tails of the capsid, which protrude in the core of the virus and are not resolved by X-ray crystallography. Right: same as the central graph with the RNA enclosed by the capsid. Published in [247, 248].*

the capacitance spectra of the capsid and the full virus. Given its pH stability range ($4.5 < \text{pH} < 10.5$), we will consider physiological values of pH (7) and electrolyte salt concentration (NaCl 150 mM).

Finally, we analyze the *Hepatitis A virus* (HAV) [304,305], from the *Picornaviridae* family. We select this non-enveloped virus as a human virus example. It is a nice test case because it is still an enigmatic virus, since it has proved to be quite difficult to study. Its ssRNA(+) genome is about 7480 nucleotides long [305]. HAV remains stable up to 80 degrees and at pH levels down to 2. Thus, we will inspect its structure and capacitance spectra in 150 mM NaCl in water at different pH levels.

3.5.2 Model of the capsid

A continuum model suitable to describe the virus–nanoelectrode interactions is desirable for the analysis of the electrical response. To this end, we extend the *double-shell* modeling approach of [306], where the capsid (which is composed by a combination of amino acids) is actually represented as a spherical shell with finite (non-zero) thickness. We instead build a truncated icosahedral shape, inscribed within two spheres of radii R_{IN} and R_{OUT}, as also sketched in Fig. 3.23 (center). In order to build the capsid of the viruses, we follow these steps:

1. **Atoms' positions**
   The spatial position of the atoms (as obtained by X-ray crystallography) is taken from the VIPERdb database [298], as a *.vdb file. In this file, a list of atoms is provided. Each atom entry of the database has some labels, used to identify its location and the amino acid which it belongs to. Hydrogen atoms and some mobile proteic tails not resolved by X-ray crystallography are not included in the list of atoms.

2. **Atoms missing $\mathbf{H^+}$ and fractional charge**
   We use the online tool *PDB2PQR* [307] to process the list of atoms in the downloaded *.vdb file. The tool includes the missing hydrogen atoms. Furthermore, a charge value is attributed to each atom, accounting for the pH-dependent atoms' fractional charge [308,309].

3. **Amino acids position**
   The position of each amino acid $\mathbf{R}_i$ is computed as the center of mass of the corresponding atoms: $\mathbf{R}_i = \sum_j m_{ij}\mathbf{r}_{ij}$, where m_{ij} and $\mathbf{r}_{ij}$ are the mass and the position of the j-th atom of the i-th amino acid, respectively. Due to their small mass, hydrogen atoms have a negligible impact on the estimation of the position. As an example, Fig. 3.24 (left) shows a 3D map of the location of the atoms for the CCMV, as extracted with the described methodology.

4. **Amino acids mass and charge**
   The mass of each amino acid (M_i, which is the sum of the masses of its atoms $M_i = \sum_j m_{ij}$) is computed according to [310] (hydrogen masses are included). A charge (Q_i) is assigned to the center of mass of each amino acid, and it is given by the sum of the fractional charges of the atoms belonging to the amino acid itself ($Q_i = \sum_j q_{ij}$, where q_{ij} is the charge of the j-th atom of the i-th

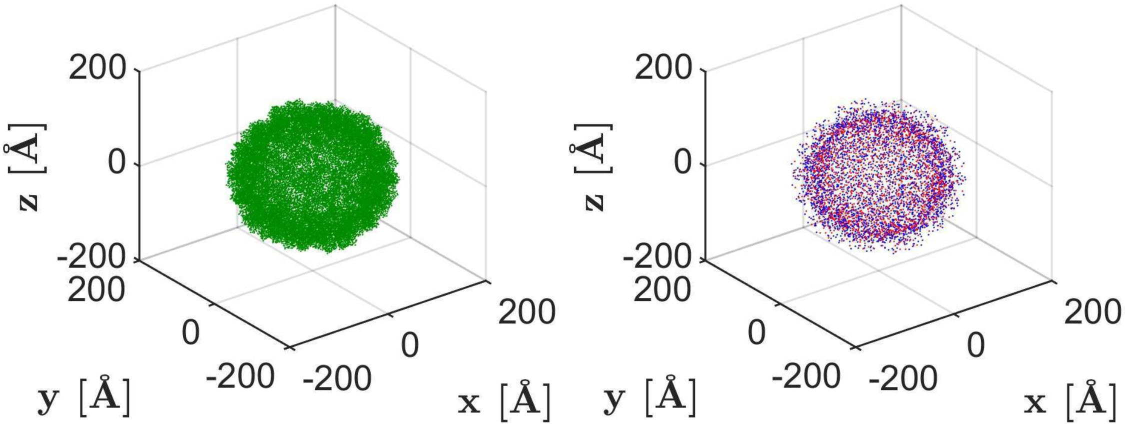

Figure 3.24: *Left: 3D scatter plot representing the location of the amino acids of the capsid of the CCMV. Right: 3D scatter plot representing the charge (red: positive, blue: negative) corresponding to each amino acid of the CCMV. Published in [248].*

amino acid). In Fig. 3.24 (right) we show a 3D map of the charge distribution (of individual amino acids) for the CCMV capsid.

5. **Capsid mass and charge densities**
The volume mass density and the volume charge density distributions are computed as a function of radial distance by averaging the local values over polar and azimuthal angles. We used a bin width of 2 Å(it does not have major impact on the results [306]). Fig. 3.25 (top row) shows the averaged mass distributions for the three viruses under study. Fig. 3.25 (central row) shows the averaged charge distributions (at pH=5 for the CCMV, pH=7 for the RHDV, pH=7 for the HAV).

6. **Capsid dimension**
Full Width Half Maximum (FWHM) limits of the mass distribution are extracted to identify R_{IN} and R_{OUT} (Fig. 3.25, top), following the approach of [306]. As anticipated, the mass distribution of the RHDV is peculiar, due to the presence of a density peak near the inner surface. As a consequence, the FWHM extraction does not properly represent the mass profile, since a large part of the distribution at large radial distances is excluded (Fig. 3.25, top center). To overcome this limitation, we extract Full Width Half Mean values instead. This approach entails a difference in the radii estimation of merely 2 Å for the HAV, and an increase of R_{OUT} by 1 nm for the CCMV. Table 3.4 reports the radial parameters for the different capsids under study.

7. **Capsid charges**
The charges beyond the inner and outer surfaces of the capsid, Q_{IN} and Q_{OUT}, are computed summing the charges of the amino acids at distance $r < R_{IN}$ and $r > R_{OUT}$, respectively. As for the body of the capsid, i.e. $R_{IN} < r < R_{OUT}$, Ref. [311] concludes that the charges therein (Q_{BODY}) are essentially zero because the energy which is required to dissociate them is very high. Instead,

Refs. [312–314] consider the amino acids in the body of the capsid as charged. We will first discuss both cases for the CCMV; then, we will rely on the latter assumption for the other viruses.

8. **Mobile proteic tails in the capsid**
   The charge of the unresolved amino acids of the mobile proteic tails is computed based on the database [315] and the online calculator [316], and it is added to Q_{IN}. Table 3.4 reports the final electrical parameters for the different capsids under study.

The above methodology was first validated by generating the *cucumber mosaic virus* (CMV) model as a test case. The extracted model parameters are consistent with those reported in [306], thus proving the accuracy of the methodology. The truncated icosahedron model is inscribed into the spheres of radii R_{IN} and R_{OUT}. We assign Q_{IN} and Q_{OUT} as volume charges to δ=0.5 nm thick shells located at $[R_{IN} - \delta, R_{IN}]$ and $[R_{OUT} - \delta, R_{OUT}]$, respectively. We assign Q_{BODY}, when considered, to the remaining part of the capsid (i.e., in $[R_{IN}, R_{OUT} - \delta]$). As an example, Fig. 3.25 (bottom) reports the volume charge profiles (Q_{IN}, Q_{BODY}, and Q_{OUT}) as assigned for the numerical simulations of CCMV, RHDV and HAV capsids.

All the relevant geometrical and electrical parameters are summarized in Tab. 3.4. Finally, the dielectric permittivity of the capsid body and shells ($r \in [R_{IN} - \delta, R_{OUT}]$) is set to ε_r=5, as in [317], whereas the core of the virus ($r \in [0, R_{IN} - \delta]$) is filled with electrolyte.

3.5.3 Model of the RNA

The nucleic acid possibly enclosed in the capsids contributes as well to the charge of the virus. We model the RNA as:
1) either an additional charge contributing to Q_{IN} (thus, with no change in volume of the shell at low dielectric constant),
2) or also partially filling the core of the virus (replacing the electrolyte with a low dielectric constant material in another 0.5 nm shell).

These alternative models are sketched in Fig. 3.26. Regarding the CCMV, it can be filled by three possible RNA sequences [299], and we show results for the longest one, which is 3174 nucleotides long. For the RHDV and the HAV, 7500 and 7480 nucleotides are considered, respectively [302,305]. Since the RNA is partly immersed in electrolyte, we assign an effective charge of $-0.8q$ per nucleotide (instead of the theoretical $-1q$) to account for screening effects, as also reported in [317,318].

The RNA carries a negative charge, that for the CCMV compensates the positive charge of the proteic tails. The full CCMV virus presents a negative Q_{IN} value, compared to the positive charge of the empty capsid (see Fig. 3.25 bottom left).

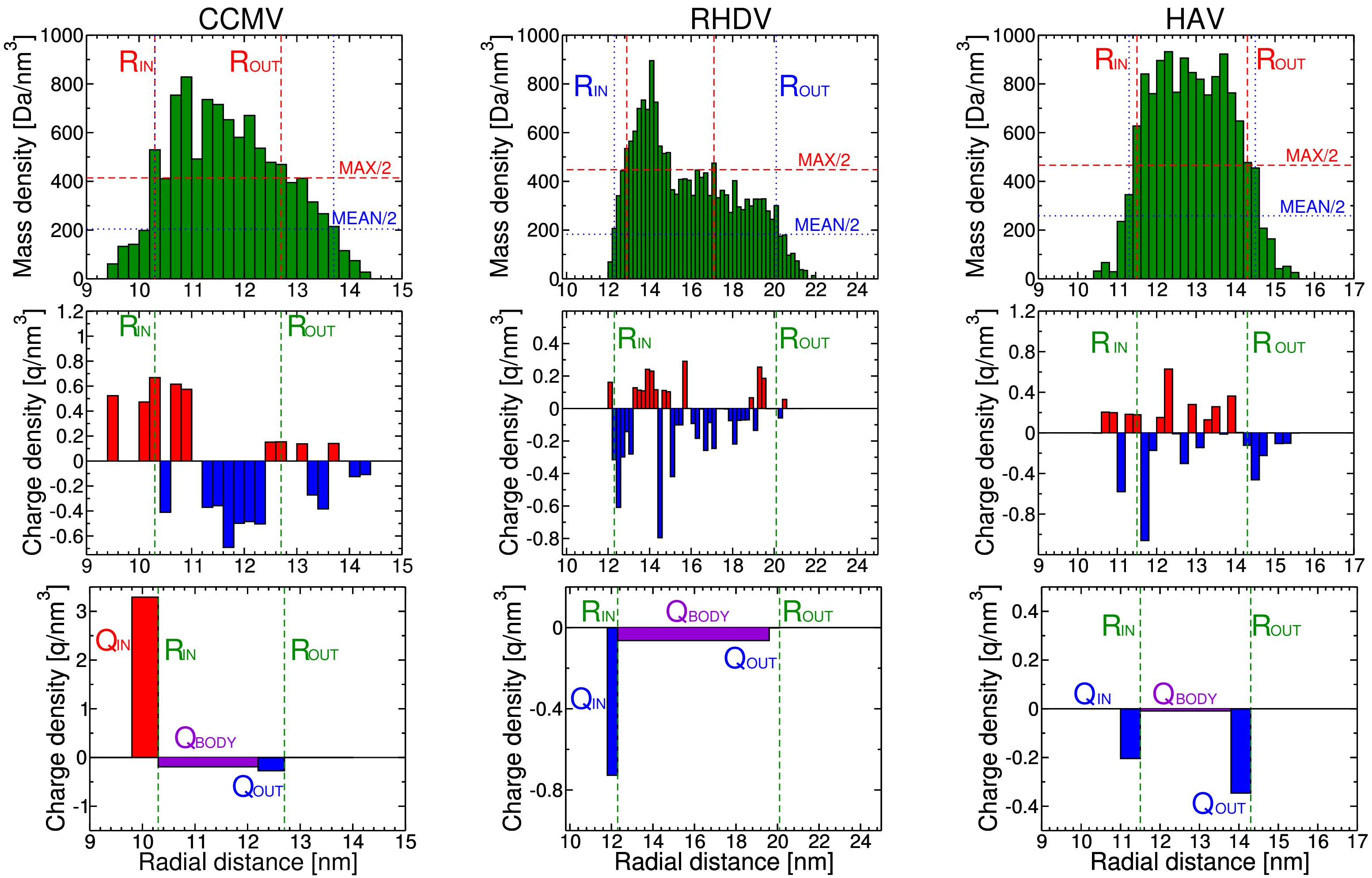

Figure 3.25: *Geometrical and electrical models of the stable CCMV capsid (left column), RHDV capsid (center column), and HAV complete capsid (right column). Top row: density of mass radial distributions, highlighting* R_{IN} *and* R_{OUT} *and Full Width Half Max/Mean values. Central row: charge radial distributions, obtained at pH=5 for the CCMV, and pH=7 for the RHDV and the HAV. Bottom row: compact charge distributions assigned in the simulator. Published in [248].*

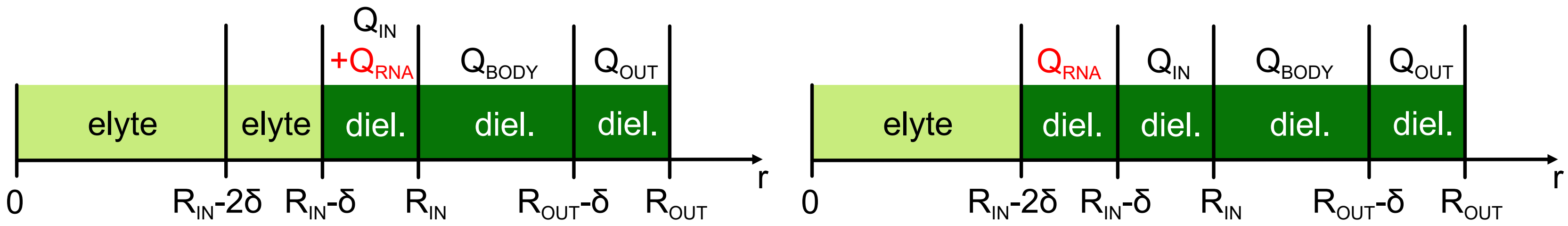

Figure 3.26: *1D cross-section representation of the virus model, with definition of the material properties and volume charges assigned to the different regions. Light-green regions correspond to electrolyte, dark-green regions correspond to dielectric material.* Q_{IN} *and* Q_{OUT} *are assigned to* δ=0.5 *nm thick shells located at* $[R_{IN}-\delta, R_{IN}]$ *and* $[R_{OUT}-\delta, R_{OUT}]$*, respectively.* Q_{BODY} *is assigned in* $[R_{IN}, R_{OUT}-\delta]$*). The RNA is either an additional charge contributing to* Q_{IN} *(left), or it also partially fills the core of the virus, thus partially replacing the electrolyte with dielectric material in another* δ=0.5 *nm shell (right).*

Parameter	**CCMV Capsid** (neutral)	**CCMV Capsid** (charged)	**CCMV Capsid Swollen 1** (charged)	**CCMV Capsid Swollen 2** (charged)	**RHDV Capsid** (charged)	**HAV Capsid** (charged)	**HAV Capsid Empty** (charged)
R_{IN}	10.3 nm	10.3 nm	12.7 nm	12.5 nm	*12.3 nm	11.5 nm	11.7 nm
R_{OUT}	12.7 nm	12.7 nm	15.5 nm	15.3 nm	*20.1 nm	14.3 nm	14.3 nm
Q_{IN}	+1812 q	+1812 q	+1962 q	+1842 q	-576 q	-141 q	238.8 q
Q_{BODY}	0	-550 q	-720 q	-660 q	-1320.6 q	-36.6 q	381 q
Q_{OUT}	-230 q	-230 q	-359 q	-300 q	-4.2 q	-372.6 q	-549.6 q

* Full Width Half Mean calculation

Table 3.4: *CCMV, RHDV and HAV capsids model parameters. The labels "neutral" and "charged" refer to the assumption of Ref. [311] and that of Refs. [312]– [314] for the charge in the body of the capsid, respectively. CCMV values correspond to pH=5. CCMV (swollen), RHDV, and HAV correspond to pH=7. [248]*

3.5.4 Model for the body of the capsid

As discussed in section 3.5.2, the body of the capsid might not be completely neutral. To investigate this scenario, we take into account also the charge located in $R_{IN} < r < R_{OUT}$, and we set Q_{BODY} to this value.

The first and second columns of Table 3.4 report the model parameters for the CCMV following these two assumptions regarding the charge of the body. We will compare these two options for the CCMV case only (and, in this case only, for the sake of a worst-case estimation a charge of $-1q$ per nucleotide is assumed for the "charged" capsid body), then relying on the "charged" model for RHDV and HAV viruses.

3.5.5 Simulation setup and metrics

The simulation setup consists in an array of 5x5 electrodes. In practical experiments, including an analyte capture layer is fundamental to immobilize small entities like viruses. Bovine serum albumin (BSA [319]) is often used as a capture layer [320], hence we include a h_{BSA} =3 nm thin BSA layer (24% water content) covering the array surface.

Unless otherwise stated, we place the analyte at a distance of 0.5 nm from the BSA surface (here we indicate as d_z the distance between the bottom edge of the virus and the surface of the BSA). The typical mesh has $\approx$ 10k elements for the virus ($\approx$ 200k total) and the DC simulation runs in about 2.5 hours, with an approximately 2× increment if the virus body is discretized in three regions instead of just one.

3.5.6 Simulation of CCMV

Since it is practical to manipulate the CCMV with sodium acetate buffers [321], we first simulate the virus in a 100 mM $C_2H_3NaO_2$ electrolyte, and the capsid in 300 mM NaCl water electrolyte.

The left and right plots of Fig. 3.27 show the ΔC_{eff} spectra considering both the "neutral" and the "charged" model for the body of the capsid. We do also consider the cases in which the RNA is either an additional charge (with no inner electrolyte volume substitution), or it partially fills the core of the virus (thus replacing the electrolyte with a low permittivity region). ΔC_{eff} at 50 MHz (i.e. within the frequency range of operation of the nanoelectrodes biosensor platform) is in the order of a few hundred zF. The difference between the capsid and virus responses is of the same order of magnitude. As expected [211], the charge of the RNA in the CCMV has no impact on the high frequency response, affecting mainly the low frequency part of the curves. Q_{BODY} has a small impact on the capsid's spectrum, also due to the relatively high electrolyte salt concentration; conversely, it has a larger impact on the CCMV's, which is immersed in an electrolyte with lower salt concentration. The partial replacement of electrolyte with low dielectric constant RNA is visible mostly at low frequency; however, if Q_{BODY} is considered this impact is smaller (the response being mainly determined by the extra charge).

Since different electrolyte salt concentrations shift the spectrum of ΔC_{eff} and amplify differences between the curves at 50 MHz, it would be of interest to compare the response of empty capsid and full CCMV in the same ambient conditions. In Fig. 3.28, we make this comparison using a 150 mM NaCl electrolyte. The corresponding change of ΔC_{eff} between the empty capsid and full virus is reduced to only $\approx$ 50 zF at 50 MHz (unless the change of ε in the capsid core is considered): sensitivity should be improved to $\approx$ 10 zF to safely detect the difference.

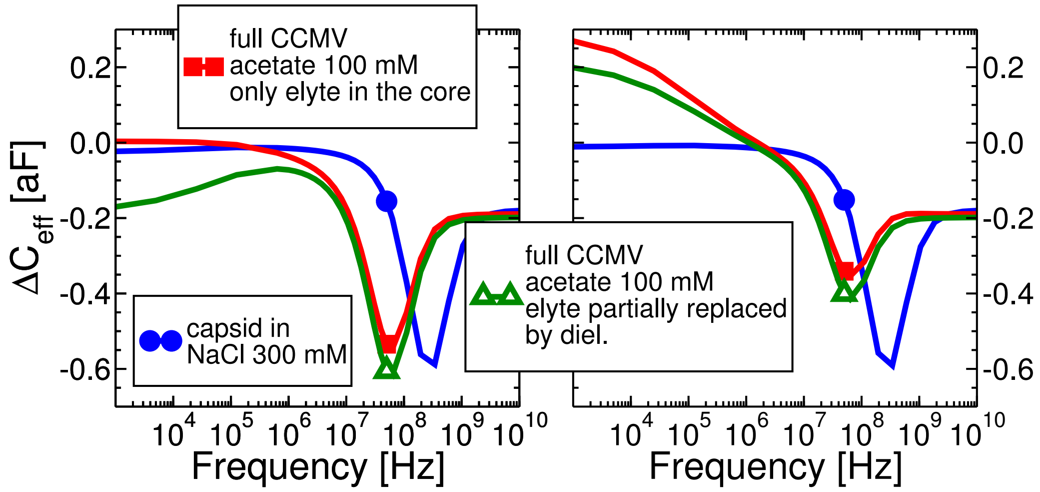

Figure 3.27: *ENBIOS simulations of CCMV capsids in 300 mM NaCl water electrolyte and CCMV full viruses in 100 mM $C_2H_3NaO_2$ electrolyte. The symbols correspond to the 50 MHz point. The analyte is located 1 nm from the BSA surface. The capsid body is assumed without (left) and with (right) charge between R_{IN} and R_{OUT}. Published in [247, 248].*

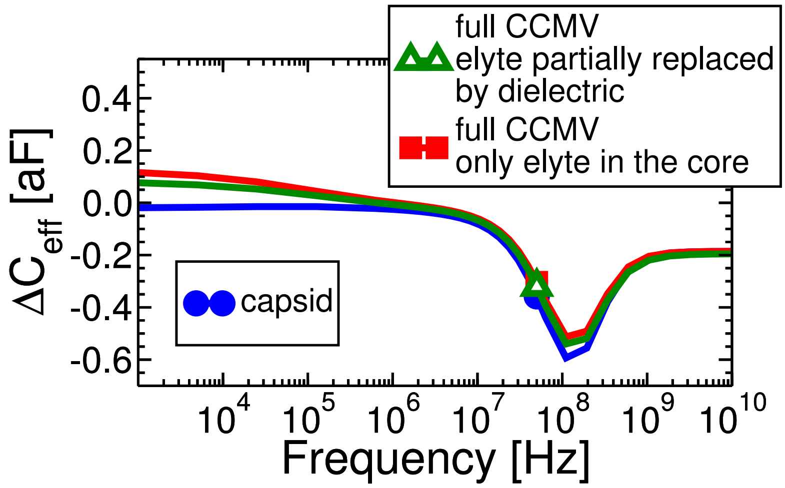

Figure 3.28: *Same as Fig. 3.27 (right) with NaCl 150 mM electrolyte for all the curves, both for capsids and for full CCMVs. Published in [247, 248].*

These preliminary results suggest that while detection of one virus requires 0.1 aF sensitivity and resolution (a value demonstrated in [227] but only up to 1 MHz), discriminating the full virus from the capsid requires approximately 10 zF sensitivity and resolution. We conclude that even with a high-sensitivity CMOS nanoelectrode sensor platform as the one of this work, discrimination between the capsid and the infectious virus remains very challenging, because the differences in response are mostly due to the electrolyte environment required by experiments.

At sufficiently high frequency, we can infer from Fig. 3.28 that the response to empty capsids is always larger (in absolute value) than the response to full CCMVs. However, the deposited BSA layer would inevitably be affected by surface roughness, and even more critically, the nanoelectrode coverage cannot be expected to be perfectly uniform over the whole array. For these reasons, the conclusion that the response to empty capsids is always larger than the response to full CCMVs at 50 MHz may not always hold. To investigate this scenario, we run ENBIOS simulations of CCMV capsids and full viruses for different values of the BSA layer thickness. The results are shown in Fig. 3.29 (top), with the two insets highlighting how the capacitance variation changes with the BSA thickness at 1 kHz and at 50 MHz. The curve at 50 MHz (top-right inset) shows that less than 1 nm difference in BSA thickness can lead to a larger response for the CCMV. Fig. 3.29 (bottom) shows how the capacitance variation at low and high frequency changes according to the analyte vertical elevation above the BSA (d_z); due to the screening induced by the EDL, the low frequency response essentially vanishes above a few Debye lengths, whereas at high frequency the discrimination between CCMV and capsid is possible also at larger d_z.

As discussed at the beginning of Sect. 3.5.1, an increase of the pH of the solution *swells* the capsid. In the following we investigate this scenario. A mechanism for the pH-induced swelling process of the CCMV is described in [301], where the details of the loss of the interactions at the quasi-3-fold interfaces[2] (occurring especially in the initial stages of the swelling process) are provided. The protein-protein association energies at the interfaces [322, 323] are progressively reduced during the swelling, possibly resulting in a complete loss of protein-protein interactions at some interfaces [301]. Models of two intermediate states ("Swollen Form Model 1" and "Swollen Form Model 2") are available from [298] to characterize the progressive change of the structure. We analyze these models assuming pH=7 in the calculation of the charges. The third and fourth columns of Table 3.4 report the extracted values (radii and charges) for these two models. It must be noted that the differences with respect to the stable capsid arise not only due to different protein-protein interactions and amino acids spatial locations, but also due to the different pH of the environment. In particular, the charge of the unresolved amino acids of the mobile proteic tails (which is computed with [316] and is added to Q_{IN}) differs as well between the stable and swollen model.

---

[2] "3-fold interfaces" identify the interfaces of an object (in this example, the truncated icosahedron) where a rotational symmetry of order n =3 (*3-fold*) applies, i.e. the interfaces where a rotation by an angle 360°/n (120° in this case) does not change the object. Thus, referring to Fig. 3.23 (left), where the truncated icosahedral symmetry is highlighted in red, the *quasi* (since the truncated icosahedral symmetry is a good but not perfect representation of the virus) 3-fold symmetry axes correspond to the center of the hexagonal faces.

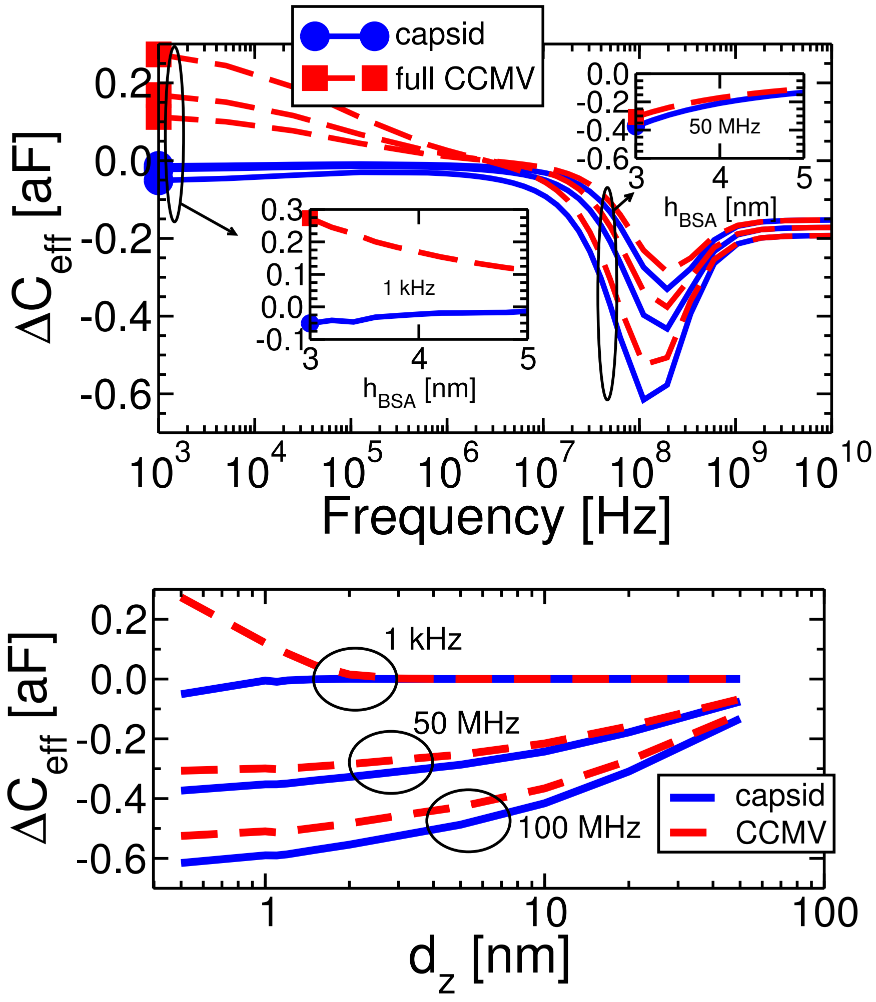

Figure 3.29: *Families of ENBIOS simulations of CCMV capsid (blue curves) and full virus (red curves) for different BSA thickness values (h_{BSA}) or vertical elevation (d_z) above the BSA. For the full CCMV, the RNA is modeled as an additional charge (as for the red curve in Fig. 3.28). The electrolyte is NaCl 150 mM. Top: capacitance spectra for different h_{BSA} (3, 4, or 5 nm) with the analyte located at d_z = 0.5 nm. Bottom: capacitance variation response at three different frequencies as a function of d_z. Published in [248].*

Fig. 3.30 shows ENBIOS simulations for the stable capsid (at pH=5) and for the two intermediate swollen structures (at pH=7) in 150 mM NaCl electrolyte. At high frequency, the response is larger for the swollen capsids. A peak of 1 aF is obtained around 100 MHz, and the high frequency limit is at 0.33 aF (compared to the 0.2 aF for the stable CCMV). This behavior is explained mostly by the difference in volume (∼4023 nm^3 for the stable CCMV and ∼6735-6932 nm^3 for the two swollen models, numbers obtained calculating the volumes of truncated icosahedral shells in $[R_{IN} - \delta, R_{OUT}]$), as also predicted by Eq. 10 and Fig. 5 in [211], since the charge plays a marginal role at very high frequencies. In fact, the response of the two swollen capsid models is essentially the same, since the volume difference is minimal.

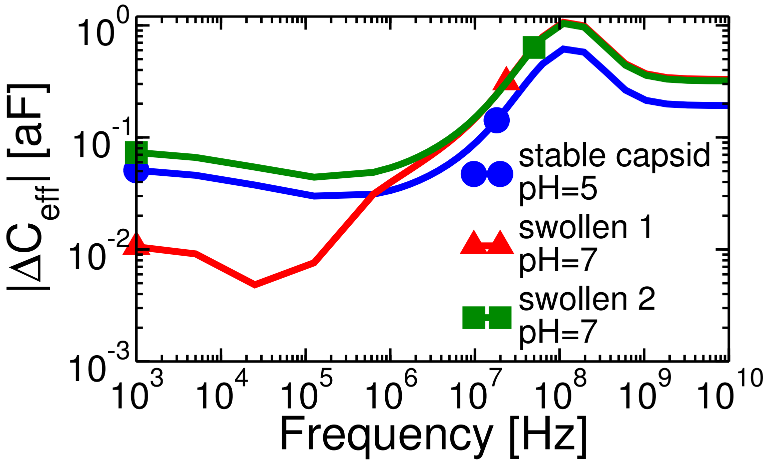

Figure 3.30: *Comparison between ΔC_{eff} spectra of stable CCMV capsid and two models of swollen CCMV capsid. The analyte is located at d_z =0.5 nm from the BSA surface. The electrolyte is NaCl 150 mM. Published in [248].*

Differently, at low frequency the response of the two swollen capsid models differs: due to the very close distance to the BSA surface, part of the capsid interacts with the EDL (more precisely, d_z is larger than λ_D; however, since the virus is charged it also possesses its own EDL which interacts with the EDL on the array surface). As a consequence, small variations in volume and charge can lead to larger variations of the capacitance profile.

The best detection conditions (maximizing $|\Delta C_{eff}|$) are found increasing the detection frequency above 100 MHz where ΔC_{eff} has a peak response. For the same electrolyte environment, the frequency of optimum sensitivity changes only slightly for the different states of the CCMV virus. This is consistent with the results reported in [211], in which the frequency corresponding to the peaks in the ΔC_{eff} spectrum depends only on the electrolyte salt concentration (via its relaxation frequency and Debye length) and the mean unperturbed electric field in the region occupied by the analyte. The same conclusion can be applied to the viruses presented in the following.

3.5.7 Simulation of RHDV

As discussed in Sect. 3.5.2, we rely on a Full Width Half Mean estimation of the capsid size to avoid losing a significant part of the mass distribution, located beyond R_{OUT}. The RNA sequence enclosed by the capsid is approx. 7500 nucleotides long, corresponding to a partially screened charge of approximately -6000q [317, 318].

Fig. 3.31 compares the capacitance spectra of the empty capsid and the full virus, considering both approaches to extract the radii. As for the CCMV virus, the difference between empty capsids and full viruses is very small at high frequency. In fact, they differ essentially for the charge profiles, and spectra at high frequency are weakly sensitive to charges. Regarding the two approaches for the radii estimation,

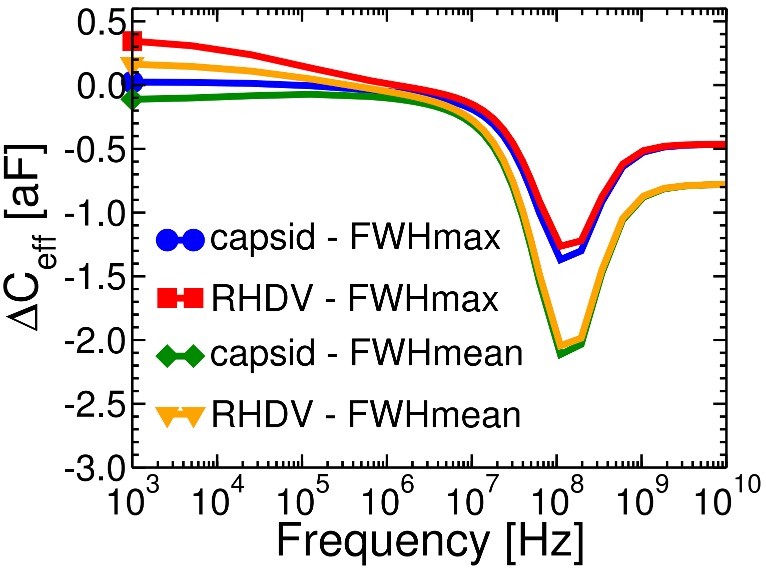

Figure 3.31: *ΔC_{eff} spectra of RHDV capsid and full virus, considering the two models for the radii estimation. The analyte is located 0.5 nm from the BSA surface. The electrolyte is NaCl 150 mM. Published in [248].*

as expected the Full Width Half Mean approach leads to estimate larger ΔC_{eff} (in absolute value), since the estimated volume of the analyte is larger [211]. Due to the larger dimension, compared to the CCMV, a peak of about 2 aF can be noticed, whereas the high frequency limit leads to a capacitance variation of -0.8 aF.

3.5.8 Simulation of HAV

As anticipated in Sect. 3.5.1, HAV remains stable down to pH=2. Hence, we investigate the charge distribution and the capacitance spectra at different pH levels.

Two models are available for the capsid of HAV [298]: the complete capsid and an "empty" capsid version (roughly 400 atoms are missing, compared to the complete model). As a first step, we compare the charge values (Q_{IN}, Q_{BODY}, Q_{OUT}) over different pH levels. Figure 3.32 (bottom) shows how the charges vary with the pH. For progressively lower pH values, the charge distribution within the capsid becomes more positive, as can also be noticed by inspecting the data at pH=3, pH=5, pH=7 in Fig. 3.32, top.

Fig. 3.33 reports capacitance spectra of complete and empty HAV capsids, at different pH levels. For the complete capsid, we do also show the spectra including the RNA charge. As expected, since the volume difference is minimal, the response to the two capsid models at high frequency is almost indistinguishable. At low frequency, due to the significant differences in volume charge density, the two capsids can be easily discriminated. On top of that it must be noticed that the response at different pH levels also changes remarkably, due to the different charge distributions (Fig. 3.32). This is in particular true at low frequency (Fig. 3.33 bottom)

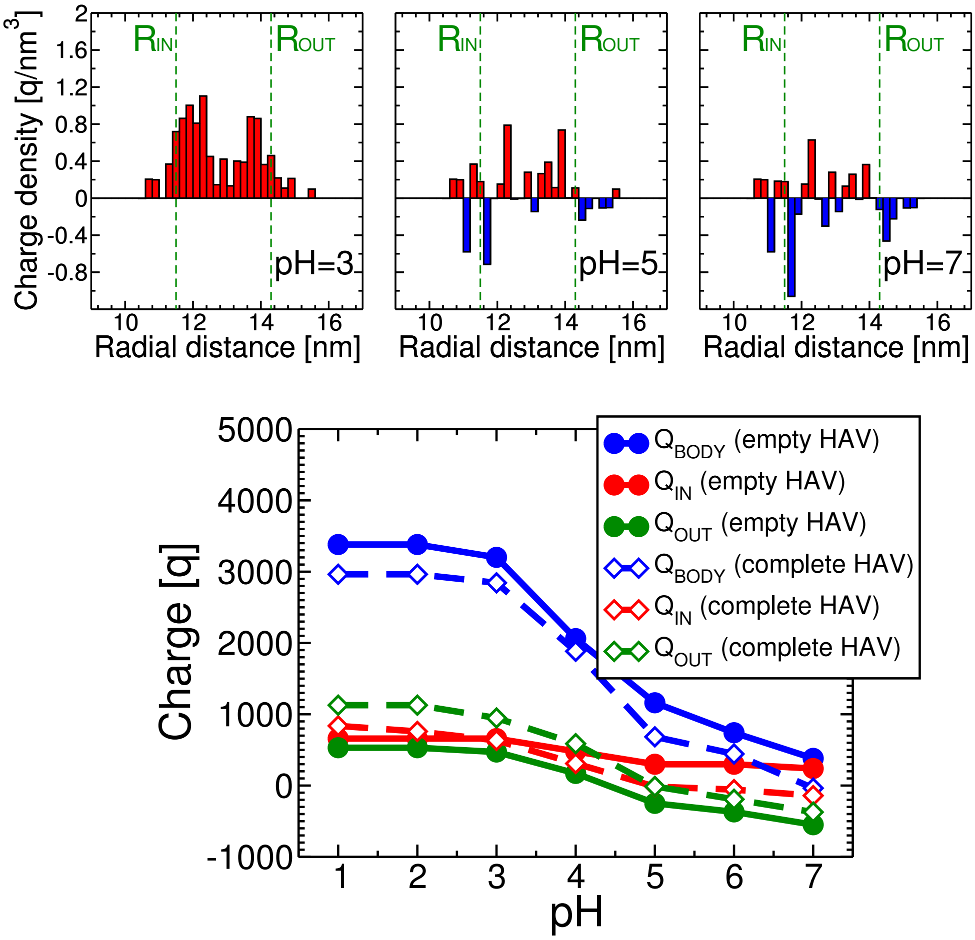

Figure 3.32: *Top: HAV complete capsid charge distributions at pH=3, pH=5, pH=7 [248]. Bottom: HAV capsid charge values (Q_{IN}, Q_{BODY}, Q_{OUT}) as extracted with the described methodology at different pH levels. Two models for the HAV capsid are considered. Published in [248].*

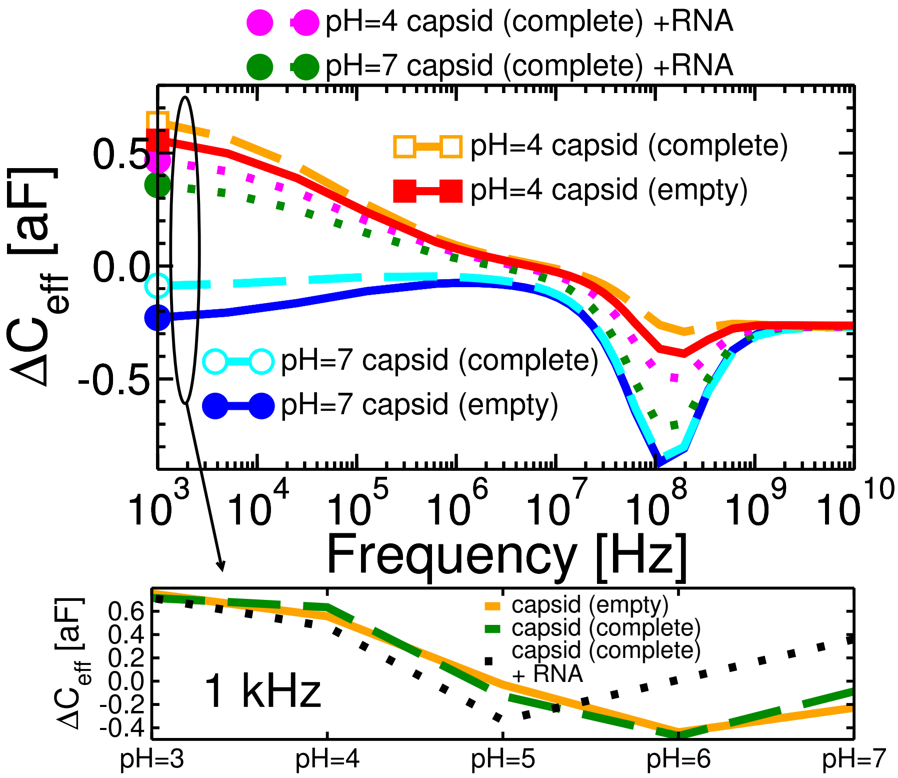

Figure 3.33: *Top: ΔC_{eff} spectra of HAV capsid and full virus, considering the two models for the capsid [248]. The analyte is located 0.5 nm from the BSA surface. The electrolyte is NaCl 150 mM. Bottom: low frequency capacitance variation for varying pH. Published in [248].*

3.6 Bayesian Statistical Techniques

In this thesis we make use of the nanoelectrode array biosensor platform presented in Chapter 2 with the aim to characterize its response to electrolytes and analytes not merely qualitatively, but also providing dependable quantitative indications. Quantitative analyses are possible if an accurate estimation of system parameters is performed, together with the quantification of the related uncertainties. Application of advanced statistical techniques to estimate parameters and quantify uncertainty thus appear as fundamental.

A number of geometrical and physical parameters have an influence on C_{post}, each with its own random variability. For instance, the radius (r_{el}), protrusion and roughness of the electrodes, the concentration of ions in the electrolyte, the polarization of water molecules in a thin layer between the nanoelectrode surface and the bulk of the electrolyte (which affects the dielectric permittivity $\varepsilon_{r,Stern}$). As regards characterization of analytes, while the in-plane analyte geometry can be extracted with conventional image processing algorithms [324], simultaneous extraction of the out-of-plane elevation and electrical properties of the analyte and the environment remains challenging at the micro- and nanoscale. In fact, a reliable electrical model of the physical transduction mechanism is necessary, while noise and fluctuations limit the precision. In this section and in the following chapters we will exemplify the analysis of a few of these problems.

Uncertainty Quantification (UQ) identifies which variables are uncertain in the system to be studied and their effect on the observables of the system. UQ is becoming increasingly important in nanoelectronics and all its applications due to non-negligible sources of fluctuations and variability which affect nanoscale devices [325,326], and in turn constrain the design of functional electronics. UQ is even more important for nanoelectronic biosensors, where biological noise adds to traditional electrical noise sources and contributes to determine the limit of detection (LoD).

A popular UQ method is Bayesian Estimation (BE) [327–329], where prior knowledge is updated after new information of the system is obtained, for instance by means of measurements, and included in the posterior knowledge by means of the Bayes' Theorem from Probability Theory [330]. BE not only provides a solution but also an estimate of its expected statistical distribution. Parameter extraction by means of classical inverse-modeling techniques [331, 332], instead, suffers serious limitations, because the solution comes without any estimate of its uncertainty. Furthermore, ill-posed nonlinear inverse problems may not have unique solutions, requiring a separate verification of the correctness of the result. The advantage of the presented approach is that we obtain probability distributions for the parameters, which inform us how reliable the results are. If a probability distribution is close to a uniform distribution, the parameter cannot be identified reliably. If the probability distribution has a well-localized maximum, the parameter can be found with great confidence. Thus, it becomes possible to determine if and how well a parameter can be identified, and confidence intervals are also obtained, which are precious information to achieve in the field of biosensors.

3.6.1 Essentials of Bayesian inference

To set the stage for the description of the method we start reminding that errors η due to measurement and modeling can be represented by means of random variables. For a given random variable $\mathcal{M}$ representing the information provided by measurements, for which we have a model $g(Q)$ dependent on a random variable Q representing parameters, we have that

$$\mathcal{M} - g(Q) = \eta\,. \tag{3.20}$$

For vector quantities $\mathcal{M}$, η, which represent different measurements $\mathcal{M}_i$, we assume that the errors η_i are independent, identically distributed (IID) and unbiased. We will assume in general that the errors are additive and mutually independent from Q, which can be a vector of parameters (q_i) as well [327].

In the Bayesian framework, the parameters Q are random variables, with realizations $q = Q(w)$, and with an associated probability density function (PDF) giving information about them (here, w is an element of a probability space Ω_w). A prior PDF π_0 reflects our knowledge of the parameters prior to measurements of observations. The final goal is to obtain a posterior PDF that incorporates the new knowledge of the acquired observations. This posterior is the solution to the inverse problem of parameter estimation via Bayesian techniques.

Bayes' Theorem [328]:
The following relation among conditional probabilities is satisfied,

$$P(\mathcal{I}_Q|\mathcal{M}) = \frac{P(\mathcal{M}|\mathcal{I}_Q)}{P(\mathcal{M})}P(\mathcal{I}_Q)\,, \tag{3.21}$$

where $\mathcal{I}_Q$ is a subset of possible uncertain parameters Q, and $\mathcal{M}$ is the information provided by the measurement.

Assuming the probability measures above have PDF's, we can reformulate the theorem in terms of the PDFs:

Bayes' Theorem in PDF form for Inverse Problems [327, 328]:
Let $\pi_0(q)$ be the prior probability density function for the realizations q of the random parameters Q. Let m be a realization of measurement $\mathcal{M}$. Then the posterior density of Q, given the measurements m, is

$$\pi(q|m) = \frac{\pi(m|q)}{\pi(m)}\pi_0(q) = \frac{\pi(m|q)\pi_0(q)}{\int_{\Omega_q}\pi(m|q)\pi_0(q)dq}\,. \tag{3.22}$$

where Ω_q is the space of parameters q. The Bayesian approach to inverse problems is then to find the posterior probability density function $\pi(q|m)$ given the measurements m.

3.6.2 Markov-Chain Monte Carlo and Metropolis-Hastings algorithm

In principle, it would seem that, in order to use the formula in Eq. 3.22 as it is, it would be required to compute the high dimensional integral $\int_{\Omega_q} \pi(m|q)\pi_0(q)dq$, which is costly to evaluate. Furthermore, for a large dimension of the integration space, resorting to integration techniques such as Monte Carlo (MC) methods would be required. Even so, an efficient sampling of the integration space is required, but there is no knowledge, beforehand, of where exactly the support of the probability density is (since that is exactly the information to be found).

However, there are numerical methods such as Markov Chain Monte Carlo (MCMC)[3], which do not require to compute this high dimensional integral: they only require the ratios of the probabilities in Eq. 3.22, and explore the right regions of the distributions, making the application of Bayes' formula feasible [328].

In the following we will consider one particular type of random walk MCMC method (MCMC uses correlated random samples for integration), known as Metropolis-Hastings (MH) algorithm.

The original Metropolis algorithm has been presented in [333] to compute equations of state for interacting molecules, by performing modified Monte Carlo integrations over the configuration space representing the state of all the particles. In this algorithm, proposal/jump distributions (J, which will be defined more precisely in the following) must be symmetric and, typically, are Gaussians: this is an important limitation. The MH generalization of this algorithm has been presented in [334], and allows to use asymmetric and non-Gaussian proposal/jump distribution (as will be shown in the following, this have an impact in the acceptance criteria of the algorithm, which will be defined in Eq. 3.23). This is an important advantage for the application of the method to numerical problems in statistics.

Let's then consider the use the MH algorithm to solve the inverse problem of determining an uncertain parameter (q) for a given physical problem. A measurement (m) is performed, obtaining information on one specific observable quantity of the system. Let's also assume that a model (g) is available to describe the system (e.g. an analytical or a numerical model), and that the the model response is $G = g(q)$ (where G is the solution provided by the model prescribing a given parameter q). The error between the experiment and the model can be calculated via Eq. 3.20. The MH algorithm to solve this (general) Bayesian inverse problem is now described.

Metropolis-Hastings MCMC Algorithm

- **Required data and definitions:**
    - *Prior Distribution*: $\pi_0(q)$.

      This is a distribution of the unknown parameter q, constructed based on

---

[3] A Markov Chain is a sequence of random variables with the property that the $n+1$ term depends only on the n term and not on any other past terms. Monte Carlo methods perform numerical integrations by means of a random discretization of the space under consideration. The Markov Chain Monte Carlo method constructs Markov chains whose stationary distribution is the posterior density we are looking for, adequately exploring the geometry of the distribution [327].

possible prior knowledge. It can be, for example, a Gaussian centered in $\hat{q}$ with standard deviation σ_0: $\pi_0(q) = \frac{1}{\sqrt{2\pi}\sigma_0} \exp\left(-(q-\hat{q})^2/2\sigma_0^2\right)$.

- *Likelihood Function* of G given q: $L(G|q)$.
  The measurement information m is hidden in this likelihood function. L is a commonly-used symbolic way to represent data likelihood, which can be expressed in terms of probability density as $\pi(m|q)$. It represents the likelihood of observing a certain output quantity for a given value of the parameter. For scalar quantities, this can be, for example, a Gaussian with standard deviation σ_L: $L(G|q) = \pi(m|q) = \frac{1}{\sqrt{2\pi}\sigma_L} \exp\left(-(m-g(q))^2/2\sigma_L^2\right)$. For vector quantities (N_m measurements), this can be, for example, a product of the Gaussians for the different variables: $L(G|q) = \pi(m|q) = (2\pi\sigma_L^2)^{-N_m/2} \exp\left(\sum_{i=1}^{N_m} \frac{(m_i-g(q))^2}{2\sigma_L^2}\right)$. The standard deviation σ_L represents the level of confidence on the measurements: a low value of σ_L means that the experimental data m are extremely trustworthy, whereas higher values mean that the uncertainty on m is larger.
- Initial value q_0.
  This is the first guess on the unknown parameter. It is chosen such that $\pi_0(q_0) > 0$.
- *Proposal Distribution* $J(q \to q')$.
  The algorithm starts from prior knowledge on the unknown parameter, as defined by the prior distribution. By means of the Likelihood, at each iteration the algorithm inspects if it is getting or not closer to the solution, adding some new knowledge. This new knowledge can be used to correct the estimation of the parameter. The proposal distribution thus represents the proposed variation of the value of the parameter (q) into a new estimation (q'). J can be any meaningful (not necessarily symmetrical) function.

- **Iterate:**

  for $k = 1 : N_{samples}$ **do**

  - Propose next sample q^* according to Proposal Distribution $J(q_{k-1} \to q^*)$;
  - Compute acceptance ratio α:

  $$\alpha = \min\left\{1, \frac{L(G|q^*)\pi_0(q^*)J(q* \to q_{k-1})}{L(G|q_{k-1})\pi_0(q_{k-1})J(q_{k-1} \to q^*)}\right\}; \tag{3.23}$$

  - Cast a random number $\chi \sim U(0,1)$, and accept proposal ($q_k := q^*$) if $\chi \leq \alpha$, else $q_k := q_{k-1}$.

  end

- **Output results**
  Mean value (of the estimated parameter) $\langle q \rangle$ – It is the mean value of the

(histogram of) the ($N_{samples}$) estimations q_k obtained during the algorithm: $\langle q\rangle = \sum_{k=1}^{N_{samples}} q_k/N_{samples}$

Posterior distribution (of the estimated parameter) $\pi(q)$ – It is found, starting from the histogram of the ($N_{samples}$) estimations q_k, by means of Kernel Density Estimation (KDE, [335]).

It can be noticed that this MCMC algorithm uses only the ratios of the needed probabilities, so the integral in the denominator of Eq. 3.22 cancels out, with remarkable reduction of computational cost. If the chosen proposal distribution is symmetric, $J(q_{k-1} \to q*) = J(q* \to q_{k-1})$ and they cancel out in Eq. 3.23.

The algorithm converges asymptotically to the equilibrium distribution. Hence, we must wait until k is big enough before using the values to sample. The duration of this *burn-in period* is estimated by testing if the sequence is close to stationary [328]. Assuming that the number of samples $N_{samples}$ is sufficiently high to overcome the *burn-in period*, larger values of $N_{samples}$ do not significantly alter the estimated mean value: the main effect of using more samples is on the shape of the posterior distribution [249].

It is worth to mention that the original idea of this algorithm is inspired from the physical problem in [333] of finding the configuration that minimizes the energy for a system of particles. If the proposed new configuration for the particles decreases its energy, it is accepted with probability one. In case the proposed new configuration actually increases its energy, it is accepted with a probability equal to the exponential of the normalized energy difference term [333]. The equivalent form of this latter term for our problem is the second term inside the brackets in Eq. 3.23.

More details of MCMC methods and the Metropolis-Hastings algorithm, such as the proof that the stationary distribution for this method is exactly the posterior density we look for, can be found in [327].

The MCMC algorithm, on which we rely in the following of this thesis for estimation of parameters, has implemented (in Julia programming language [336]) by the research group of C. Heitzinger (TU–Wien).

3.6.3 Validation for a 1D system without analytes

Estimation of 1 parameter

As a first test to prove the effectiveness of the algorithm, we consider the 1D system of Fig. 3.1 and we set the goal to estimate the value of one individual system parameter: the Stern layer relative permittivity ($\varepsilon_{r,Stern}$).

As discussed in Sect. 3.6.2, MCMC exploits a model (g) to estimate parameters (Q) from a measurement (m). In this validation example, the vector of parameters Q is one–dimensional and is given by $q = \varepsilon_{r,Stern}$. The 1D system has an analytical solution for its capacitance ($C_{a.m.}$), as given in Eq. 3.9. We make use of this analytical solution in place of experiments: we prescribe a specific value to the Stern layer permittivity, $\varepsilon_{r,Stern} = 7$, and consider as a “measurement” $m = C_{a.m.}(\varepsilon_{r,Stern} = 7)$. Finally, regarding the model $g(q)$, we run ENBIOS simulations of the system for different values of $q = \varepsilon_{r,Stern}$ and compute its small-signal AC capacitance $C_A(\varepsilon_{r,Stern})$: $g(q) = C_A(\varepsilon_{r,Stern})$.

To summarize, the model $g\left(q\right) = C_A\left(\varepsilon_{r,Stern}\right)$ will be fitted via MCMC Bayesian estimation to the “measurement” $m = C_{a.m.}\left(\varepsilon_{r,Stern} = 7\right)$ with the goal to estimate the parameter $q = \varepsilon_{r,Stern}$. Since the exact parameter value for the experiment is known *a-priori* in this case (the “experiment” is an analytical expression computed prescribing a specific value for the parameter), this test case serves as a validation step for the methodology. The opposite approach, i.e. using ENBIOS to generate a “measurement” and using the analytical model of Eq. 3.9 as a model $g(q)$ for the calculations, is also considered.

The electrolyte we consider is 100 mM NaCl in water, and the analysis is performed at two frequencies of the AC signal: f=100 kHz and f=1 GHz, corresponding to two distinct values of $m = C_{a.m.}$ and $g = C_A$. As a prior distribution, we consider a Gaussian (centered in $q_0 = 7.2$). At f=100 kHz, considering the nominal value of the parameter ($\varepsilon_{r,Stern} = 7$), the output of the analytical model of Eq. 3.9 and of ENBIOS are $C_{a.m.}(\varepsilon_{r,Stern} = 7) = 0.091819$ F/m^2 and $C_A(\varepsilon_{r,Stern} = 7) = 0.091921$ F/m^2, respectively.

Table 3.5 shows the outcome of the estimation at f=100 kHz for different number of samples (either using ENBIOS as measurement and Eq. 3.9 as a model, or vice versa) for $\sigma_L = 10^-3$ F/m^2 (i.e. uncertainty on the second significant digit of measurements, see above).

m	**g (q)**	$\mathbf{N_{samples}}$	**q (MCMC mean)**
$C_{a.m.}$	C_A	10^4	7.037510048995102
$C_{a.m.}$	C_A	10^5	7.015862797372027
C_A	$C_{a.m.}$	10^4	7.026537199094944
C_A	$C_{a.m.}$	10^5	7.022535434153356
C_A	$C_{a.m.}$	10^6	7.018336872583550

Table 3.5: *Output of the MCMC estimation of the $\varepsilon_{r,Stern} = 7$ parameter of the 1D system shown in Fig. 3.1, in 100 mM NaCl electrolyte at 100 kHz. ENBIOS simulations (C_A) and the analytical model of Eq. 3.9 are considered as “measurement” or model for the algorithm. Different number of samples are tested. MCMC output data kindly provided by TU–Wien.*

The estimation of the mean by MCMC does not change too much from 7.0d.... (with d a decimal), using different powers of j for $N_{samples} = 10^j$. The true value of $\varepsilon_{r,Stern}$ is thus correctly identified.

If a larger value of σ_L is used, e.g. $\sigma_L = 10^{-2}$ F/m^2 (i.e. uncertainty on the first significant digit of measurements, see above), the estimated value changes to $q = 7.2$ (for any choice of $N_{samples}$). This is consistently found for both kinds of run, either using ($m = C_{a.m.},\ g = C_A$) or using ($m = C_A,\ g = C_{a.m.}$). This make sense in the light of the following interpretation: since the likelihood function is a distribution of the measurement error centered at zero, having a smaller standard deviation for that function corresponds to assuming that the measurements are more accurate, therefore more weight is given to the closeness of the model ($g(q)$) to the value of m; consequently, in the MCMC runs, the permittivity converges to the true value of $\varepsilon_{r,Stern} = 7$. It is worth highlighting that in this example the wrong estimation of the parameter for large σ_L equals the center of the prior distribution.

Estimations at f=1 GHz provide consistent results.

Estimation of 2 parameters

Having verified the method and its implementation on single parameter extraction problems, here we use the MCMC technique to do simultaneous Bayesian estimation of two parameters – the relative permittivity of the Stern layer ($\varepsilon_{r,Stern}$, nominally equal to 7) and the ionic strength of the NaCl electrolyte (Na$^+$ and Cl$^-$ molarity $n^{\infty}_{0,Na^+} = n^{\infty}_{0,Cl^-} = n^{\infty}_0$, nominally equal to 0.1 M), i.e. we consider a vector of unknown parameters $q = [q_1, q_2] = [\varepsilon_{r,Stern},\ n^{\infty}_0]$. As before, we perform analyses considering two distinct frequencies (f_{low}=100 kHz and f_{high}=1 GHz). Compared to the previous cases, here we also introduce interpolations of existing data, proving that a previously-generated set of model data (g) can also be used to compute the MCMC analyses. Furthermore, we will use more than just a single measurement.

To this end, we run ENBIOS simulations to generate a non-regular grid of observables (C_A) on the $(q_1, q_2) = (\varepsilon_{r,Stern},\ n^{\infty}_0)$ plane. A total of 10^5 grid points have been generated, each one with its associated low (100 kHz) and high frequency (1 GHz) capacitance values, namely $C^{low}_A = C_A\,(f = 100\text{ kHz})$ or $C^{high}_A = C_A\,(f = 1\text{ GHz})$. The sample points are generated randomly, centered at $(\varepsilon_{r,Stern}, n^{\infty}_0) = (7.2, 0.1\text{M})$. The two frequencies are considered separately. This grid of data is interpolated by means of polynomial approximation of degree 10, constructed through minimizing the sum of the squared errors between the grid points and the polynomial. As a result, two models $g\,(q) = C^{low}_A\,(\varepsilon_{r,Stern}, n^{\infty}_0) : \mathbb{R}^2 \mapsto \mathbb{R}$ or $g\,(q) = C^{high}_A\,(\varepsilon_{r,Stern}, n^{\infty}_0) : \mathbb{R}^2 \mapsto \mathbb{R}$ are obtained for the low and high frequency data, respectively.

As artificial measurements, for each frequency of analysis, we rely again on the analytical model of Eq. 3.9, namely $m = C^{low}_{a.m.} = C_{a.m.}\,(f = 100\text{ kHz})$ or $m = C^{high}_{a.m.} = C_{a.m.}\,(f = 1\text{ GHz})$. Differently from the previous sections, here we do not consider only a single measurement. Instead, N_m =10 distinct artificial measurements are generated for both the low and the high frequency case by taking 10 samples from a normal distribution centered around the nominal values of the parameters, namely $m \sim \text{N}(\mu_m, \sigma_m)$ where the mean values are $\mu_m = C^{low}_{a.m.}\,(7.2, 0.1) = 0.0938\text{ F/m}^2$ or $\mu_m = C^{high}_{a.m.}\,(7.2, 0.1) = 0.0064\text{ F/m}^2$, and the standard deviations are $\sigma_{low} = 0.0007\text{ F/m}^2$ or $\sigma_{high} = 4.735 \cdot 10^{-5}\text{ F/m}^2$, for the low and high frequency case, respectively.

The likelihood function takes the following form (the product of the Gaussians for the different measurements):

$$L(m|q) = (2\pi\sigma_L^2)^{-N_m/2} \exp\left(\sum_{i=1}^{N_m} \frac{(m_i - g(q))^2}{2\sigma_L^2}\right) \tag{3.24}$$

where the corresponding standard deviation is set to $\sigma_L = \sigma_{low}$ or $\sigma_L = \sigma_{high}$, for the low and high frequency case, respectively. As a prior, we use a uniform distribution in the domain $q_1 \times q_2 = \varepsilon_{r,Stern} \times n^{\infty}_0 = [6, 8.5] \times [0.02\text{M}, 0.4\text{M}]$. The proposal distribution follows a normal distribution.

Fig. 3.34 shows the 2-dimensional histograms of the posterior distributions based on $N_{samples}$=10^6. The shapes of the distributions suggest remarkably different behaviors at the two different frequencies, $g = C_A^{low}$ and $g = C_A^{high}$. This is consistent with expectations from the Physics of the system. In fact, at high frequency the Stern and the diffusion layer capacitances are next to short circuits for the AC signal, and the $\varepsilon_{r,Stern}$ has a modest influence on the observable, regardless of the electrolyte ionic strength. To extract single values, alternative solutions would be to select either the mean value or the mode, based on the 2-dimensional histogram of the posterior distribution. Both of these values are highlighted in Fig.3.34.

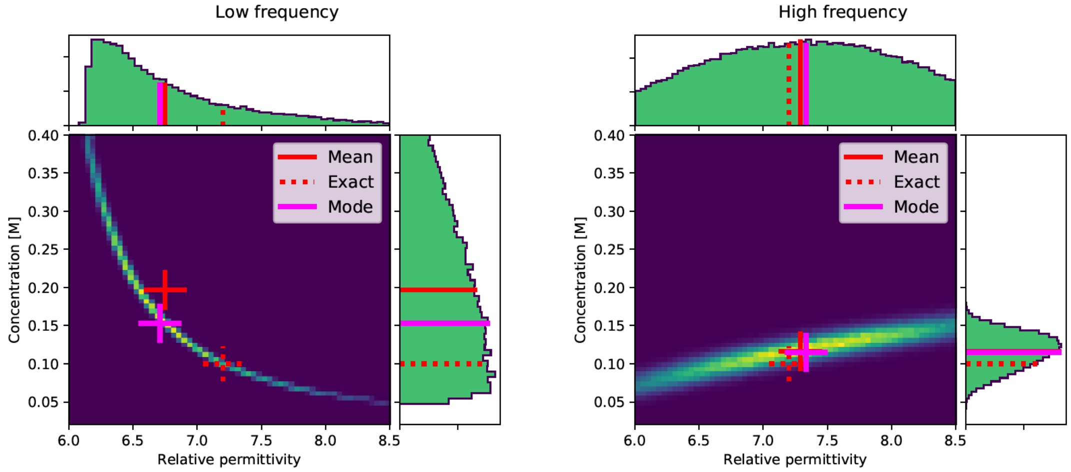

Figure 3.34: *Two-dimensional histograms of posterior distribution based on* $N_{samples}$=10^6 *and histograms of the marginal posterior distributions for* f=*100 kHz (left) and* f=*1 GHz (right). The mean value and the mode of the estimated posterior, as well as the exact value* $q = (\varepsilon_{r,Stern}, n_0^\infty) = (7.2, 0.1M)$*, are shown. The range of the colored map coincides with the support of the prior distribution. Figures generated with the MCMC code by TU–Wien.*

Fig. 3.34 demonstrates that a correct determination of the parameters is more difficult at low frequency, where the range of capacitance variation is larger and the sensitivity is also stronger. This proves the advantage of being able to perform parameters extractions at different frequencies: different parameters can be easier to be estimated at different frequencies, thus a multi-frequency multi-parameter extraction technique can be advantageous in reducing the uncertainty of estimation. In Sect. 3.6.4-4.4.3-5.2, estimations by means of MCMC will be performed also considering different frequencies together (i.e., using all the information at different frequencies in one single estimation).

3.6.4 Validation for a 3D system with analytes

Here we consider the Bayesian estimation of parameters in the presence of analytes using ENBIOS and analytical models. While the validation of the ENBIOS-based MCMC methodology has already been presented for the 1D system in Sect. 3.6.3, showing results of idealized test-cases, with a fictitious "measurement" obtained by means of analytical models with parameters known *a-priori*, is also of great interest to anticipate the analyses performed on analytes in real experiments.

For this study, we consider the 3D domain depicted in Fig. 3.2, with a matrix of nanoelectrodes and a spherical particle (of radius r_p) at a certain vertical elevation (d_z) and lateral displacement (d_x and d_y).

We set the goal of estimating 2 parameters together: the radius and the vertical elevation of the particle. Thus, we have $q = [r_p, d_z]$. To compute a fictitious measurement, we rely on ENBIOS simulations, i.e. $m = \Delta C_A(r_p, d_z)$. Regarding the model ($g(q)$) for the MCMC algorithm, also in this case we make use of an analytical model.

An analytical model of the frequency response of one nanoelectrode to a particle can be derived from the solution of the PB-PNP equations for a constant AC field $\tilde{E}_0$ in the absence of analytes. The model, extensively validated in [211], allows to compute the admittance variation due to inserting a particle of volume Ω_p in a region of constant AC electric field $\tilde{E}_0$ of an electrolyte with conductivity σ_{el} and permittivity ε_{el} as[4]:

$$\begin{aligned}\Delta Y_{a.m.,p} =& f\left(\omega, \varepsilon_p, \Omega_p, \sigma_{el}, \varepsilon_{el}\right)\left(\sigma_{el} + j\omega\varepsilon_{el}\right)\Omega_p\left(\frac{\tilde{E}_0}{\tilde{V}_0}\right)^2 \\ \Delta C_{a.m.,p} =& \frac{1}{\omega}\Im\left[\Delta Y_{a.m.,p}\right]\end{aligned} \tag{3.25}$$

where $\tilde{V}_0$ is the AC voltage applied to nanoelectrodes and $f\left(\omega, \varepsilon_p, \Omega_p, \sigma_{el}, \varepsilon_{el}\right)$ is a complex function which depends on frequency and particle/electrolyte parameters (ε_p is the particle's permittivity). For non-uniform electric field configurations (as is the case of the nanoelectrode array), using the mean value of the electric field in the volume later occupied by the particle is a good approximation [211]. The model for MCMC estimation is then $g(q) = \Delta C_{a.m.,p}(r_p, d_z)$ (where the dependency on d_z is hidden in the $\tilde{E}_0$ term). Unless otherwise stated, hereafter we consider $N_{samples} = 10^5$ and likelihood factors $\sigma_L = 5 \cdot 10^{-5}$. Furthermore, we perform the estimation by considering multiple frequencies together (32 frequency points, log-spaced between 1 kHz and 1 GHz), i.e. m and $g(q)$ are not scalar values, but vectors of 32 elements.

This model is used to determine the response of the nanoelectrode array to particles of different size and position. The information required to compute the model is the electric field configuration in the "unperturbed" system, i.e. in the system without the particle. The big advantage of this model is that the unperturbed configuration needs to be computed only once (by means of ENBIOS simulations), thus a significant reduction of the computational burden is obtained compared to running full simulations for many particle positions. Hereafter we consider a 100 mM NaCl electrolyte. Fig. 3.35 shows the AC voltage and electric field profiles as extracted from ENBIOS simulations.

The analytical model is in fairly good agreement with ENBIOS in the limit of a small Ω_p, as shown in Fig. 3.36 for varying the particle radius, r_p, and elevation,

---

[4] We include the subscript "p" to discriminate between the analytical model for the 1D system of Eq. 3.9 and this model in the presence of a particle

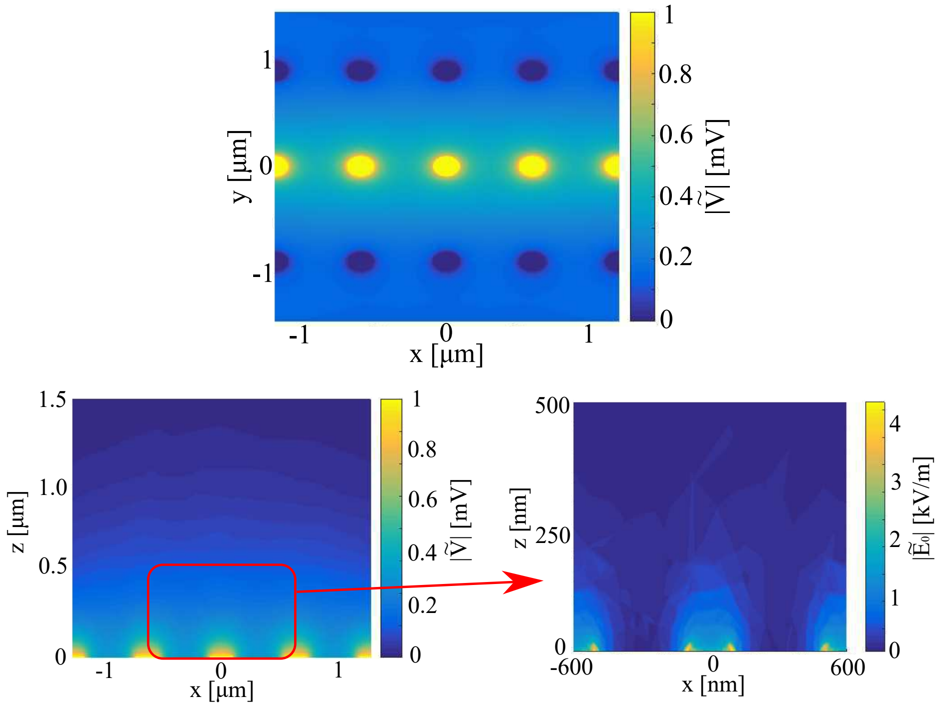

Figure 3.35: *AC voltage and electric field profiles on the xy and xz planes resulting from the application of a 50 MHz small-signal excitation with amplitude 1 mV to the central row of nanoelectrodes, in contact with NaCl 100 mM electrolyte.*

d_z, and in [211]. Considering a particle with r_p=50 nm at d_z=100 nm (Fig. 3.36, left), a small discrepancy between the model (red curves) and ENBIOS simulations (green curves) is expected due to the non perfectly uniform electric field distribution at the location of the particle). The agreement between the model and ENBIOS simulations is remarkably improved (Fig. 3.36, right) considering a smaller particle (r_p=10 nm) much closer (d_z=10 nm) to bigger electrodes (r_{el}=200 nm). In this configuration, in fact, the electric field in the region occupied by the particle is nearly uniform. Both these configurations will be inspected.

We start by considering a particle of radius r_p=50 nm suspended above the center of one electrode (r_{el}=90 nm, $d_x = d_y = 0$, d_z= 100 nm) and we use the analytical model of Eq. 3.25 to compute the likelihood function. Fig. 3.37 (left) shows color maps and marginal distributions of the posterior distribution for the simultaneous estimation of r_p and vertical position ($d_z + r_p$) with $\sigma_L = 5 \cdot 10^{-5}$ (yellow corresponds to high probability). The extracted mean values (r_p =48 nm, $d_z + r_p$=171 nm) are in good agreement with the exact ones (r_p =50 nm, $d_z + r_p$=150 nm). The residual difference is partly due to the slight error of the analytical model compared to the reference ENBIOS solution used to calculate $\tilde{E}_0$, consistently with Fig. 3.36, partly due to using a non-negligible value for σ_L (i.e., the measurement is considered not much reliable). If $\tilde{E}_0$ becomes more uniform (as assumed be the analytical model, e.g. by considering a larger electrode, r_{el} = 200 nm, a smaller r_p = 10 nm and d_z=10 nm), and an almost ideal measurements accuracy is considered ($\sigma_L = 10^{-17}$), then the estimate coincides with the true value without uncertainty (Fig. 3.37, right).

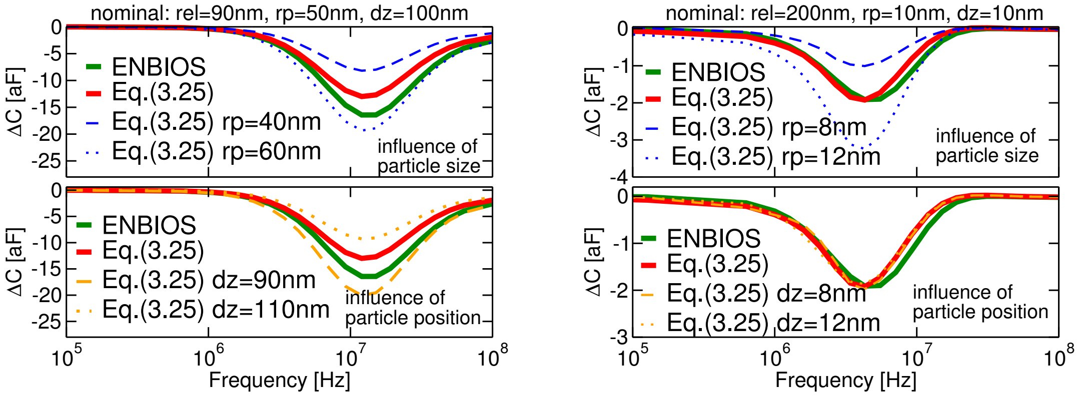

Figure 3.36: *ΔC spectra computed with ENBIOS and with Eq. 3.25 for a 100mM NaCl electrolyte with parameter variations. Left: r_{el}=90 nm, r_p=50 nm, d_z=100 nm; the model inaccuracy w.r.t. ENBIOS entails $\approx$ 10 nm uncertainty. Right: r_{el}=200 nm, r_p=10 nm, d_z=10 nm; uncertainty $\approx$1 nm (a smaller r_p and larger r_{el} entail a more uniform $\tilde{E}_0$, as assumed by the model).*

These results demonstrate the ability of the method to reliably estimate the size and vertical position of the nanoparticle.

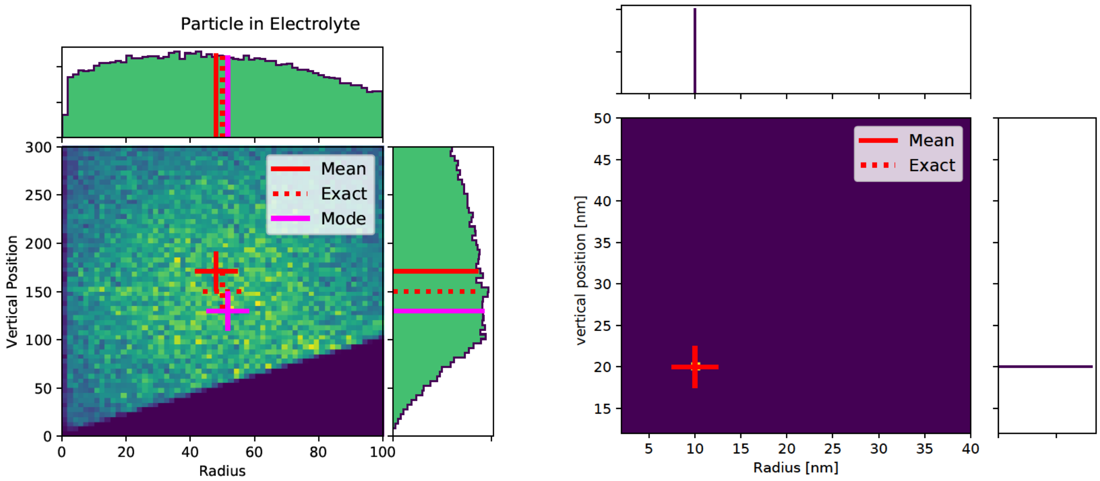

Figure 3.37: *2D color map of posterior distribution for the simultaneous estimation of radius (r_p) and vertical position ($d_z + r_p$) of a particle floating in NaCl 100 mM electrolyte above the center of an electrode using 32 frequency points in the f=1 kHz–1 GHz range. Yellow means high probability. Left: r_{el}= 90 nm, r_p=50 nm, $d_z + r_p$=150 nm, $\sigma_L = 5 \cdot 10^{-5}$. The extracted values are r_{el}=48 nm, $d_z + r_p$=171 nm. The residual difference is partly due to the slight error of the analytical model. Right: r_{el}=200 nm, r_p=10 nm, d_z=10 nm, $\sigma_L = 10^{-17}$. The estimates coincide with the true values. These results validate the ability of the method to quantify the extraction uncertainty via the posterior distribution and to converge to the exact values in the absence of measure uncertainty and model errors. Figures generated with the MCMC code by TU–Wien.*

To validate further the methodology, we investigate multi-parameters estimations of geometrical and electrical properties, using not only the information at the central electrode but, instead, taking into account the response at the electrodes e_{00} , e_{01} and e_{10} (as identified in Fig. 3.2). Again, we consider 32 frequencies together. 5-parameters (radius, permittivity and position of the particle) are estimated together. The nominal values are: d_x= 0 nm, d_y= 0 nm, d_z = 0nm, r_p = 50 nm, $\varepsilon_p = 2.6\varepsilon_0$. To summarize the problem,

- the vector of parameters has 5 elements: $q = [d_x, d_y, d_z, r_p, \varepsilon_p]$;
- the fictitious measurement $m = \Delta C_A$ is obtained from ENBIOS simulations performed at 32 different frequencies at 3 different electrodes, therefore m is a vector of $32 \times 3 = 96$ observables of a single measurement;
- the model for MCMC $g(q) = \Delta C_{a.m.,p}(d_x, d_y, d_z, r_p, \varepsilon_p)$ is given by Eq. 3.25 and maps the 5 parameters into 32 frequency values at 3 electrodes: $g(q) : \mathbb{R}^5 \mapsto \mathbb{R}^{96}$. This high-dimensional estimation problem is a great demonstration of the potential of Bayesian estimation via MCMC.

A very good agreement is obtained between estimated and nominal values, as shown in Tab. 3.6. Interestingly, using the information at more electrodes, the accuracy of estimation is much improved compared to Fig. 3.37 (left), using the same $\sigma_L = 10^{-5}$.

These results confirm the ability of the methodology to support nanoparticle metrology.

Vector of parameters (q)	**q (nominal)**	**q (MCMC mean)**
d_x	0 nm	0.28 nm
d_y	0 nm	0.01 nm
d_z	150 nm	151 nm
r_p	50 nm	50.5 nm
ε_p	$2.6\varepsilon_0$	$2.5\varepsilon_0$

Table 3.6: *Output of the MCMC estimation of the d_x, d_y, d_z, r_p, ε_p particle's parameters of the 3D system shown in Fig. 3.2, in 100 mM NaCl electrolyte at 32 frequencies (log-spaced from 1 kHz to 1 GHz) and at three electrodes. Using the information at three electrodes, the accuracy of estimation is much improved compared to Fig. 3.37 (left), for the same $\sigma_L = 10^{-5}$. MCMC output data kindly provided by TU–Wien.*

3.7 Summary

This chapter presented numerical, analytical and statistical models, as well as simulation tools, for nanoelectronic biosensors and analytes.

We started by presenting the PB-PNP mathematical framework, which is at the basis of ENBIOS. ENBIOS is the electronic nanobiosensor simulator extensively used in this thesis, which solves self-consistently the PB and PNP equations in DC and linearized small-signal AC regimes. We make use of ENBIOS by mimicking the operating principle of the nanoelectrode biosensor platform of Chapter 2, simulating arrays of nanoelectrodes activated row-wise, and computing the small-signal admittance (capacitance) at the electrodes. Two simulation tools (powered by ENBIOS) have also been developed for the simulation of simple 1D (semiconductor-dielectric-electrolyte) and 2D (ISFET) structures, which have been made available to the scientific community on nanoHUB.org.

Since the biosensor platform described in the previous chapter operates according to a CBCM measurement principle, its output is not directly comparable to the small-signal AC capacitance obtained from ENBIOS. To account for the switching activity of the nanoelectrodes, a *switching capacitance* model (C_{SW}) is used. This requires to first define an equivalent circuit to model the system under study (the nanoelectrode-electrolyte), whose elements can be estimated via (ENBIOS) simulations. Then, conventional charge-pump analyses allow to estimate the capacitance of this system due to a square-wave voltage input (thus mimicking the switching operating principle of the platform).

Then, to further generalize the switching capacitance concept, we implemented a procedure to simulate (with ENBIOS) the response of a biosensing system (e.g. the nanoelectrode array) to arbitrary input waveforms. This allows to overcome the limitation of assuming square-wave inputs and to inspect the influence of the harmonic content of the input signals.

A modeling methodology was proposed to study the response of the HFIS platform to small viruses. The case study of three plant, animal and human viruses are discussed, where compact geometrical and electrical models are derived from their atomistic descriptions. Simulation of these compact models in ENBIOS allow to derive a number of qualitative and quantitative indications on the properties of these analytes, and to identify the sensitivity and resolution requirements for the optimal detection of small viruses (possibly discriminating the presence/absence of nucleic acids in their capsids). Due to the fact that different portions of the capacitance spectra are sensitive to different factors (the charge affects the response especially at low frequency, the volume at high frequency), expanding the covered spectrum both at high frequency (facing the issue of parasitic capacitance) and low frequency (facing the issue of $1/f$ noise) would also be of interest. The proposed methodology is applicable to other viruses as well (provided the atoms' positions and partial charges are available) and it would thus be useful to build a library of HFIS spectra profiles for different virus families.

Finally, a Bayesian statistical approach to estimate parameters and quantify uncertainties was discussed. Markov-Chain Monte Carlo analyses were described in detail and validated on reference model systems exploiting analytical models and

ENBIOS simulations (of a simple 1D structure and of the nanoelectrodes in presence of particles).

While ENBIOS had been developed previously, the author partly contributed to the development of the nanoHUB tools. The author's contributions to this chapter further include the analyses with the switching capacitance model, the development of ENBIOS simulation methodologies with arbitrary waveforms, the development of models for viruses, and the analytical model/ENBIOS simulations for the subsequent Bayesian estimation analyses (performed by TU-Wien).

4 High Frequency Impedance Spectroscopy Calibration Strategies

In this chapter we analyze the response of the nanoelectrode biosensor platform to uniform environments (i.e. continuous media in the absence of analytes), we describe the calibration procedures, compare experiments to theoretical predictions and perform parameters estimations.

Chapter 2 introduced the platform and its main features, from the original concept to the implementation of a complete system. With the goal to perform not only qualitative but also accurate quantitative analyses, this system (as any other measurement instrument) requires calibrations and identification/compensation of possible sources of systematic errors. This is the specific focus of Chapter 4.

In particular, Sect. 4.1 describes the procedure to extract model parameters for the transistor of the column read-out circuits. Sect. 4.2 presents the calibration procedures used to keep the transfer voltage V_T (see Fig. 2.3 and Eq. 2.1) at a fixed and controlled level, or to *a-posteriori* compensate measurement for its deviations from expectations. In Sect. 4.3 we present results of frequency spectra measurements in electrolyte. Sect. 4.4 is devoted to analyzing the possible causes of residual disagreement between simulations and measurements, including the application of MCMC parameter estimation procedures to determine the radius of nanoelectrodes. Finally, Sect. 4.5 presents concluding remarks on the fitting of experimental data.

We acknowledge F. Widdershoven (NXP Semiconductors) for developing the calibration technique, S. G. Lemay and C. Laborde (University of Twente) for performing part of the experiments reported in this chapter, M. Anese and M. C. Nicoli (University of Udine) for support with experiments in liquid, F. Andreatta (University of Udine) for the support with SEM/AFM measurements (at the Advanced Materials Laboratory – Parco Scientifico e Tecnologico L. Danieli), and C. Heitzinger's group (TU–Wien) for running the MCMC calculations. The content of this chapter is partly published in [190, 251].

4.1 Extraction of calibration model parameters

Following the discussion of Chapter 2, for convenience we show again the basic sensor cell in Fig. 4.1. We also recall that the average column current I_M can be expressed

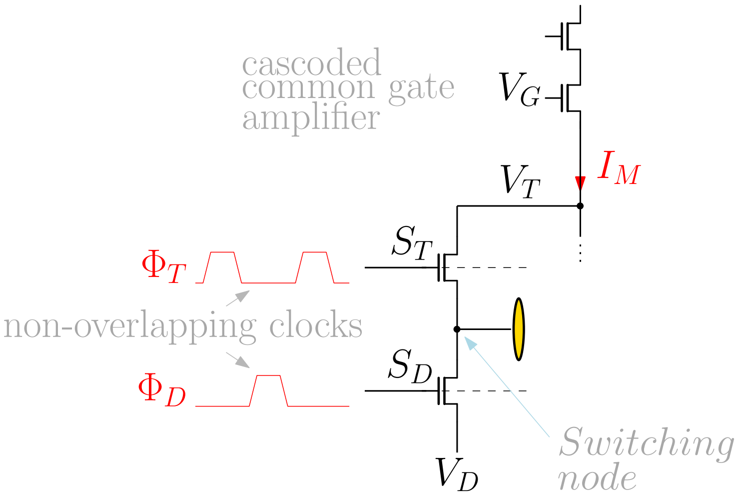

Figure 4.1: *Zoom over the schematic of a selected sensor cell (see Fig. 2.3).*

in terms of the measurement capacitance C_M provided by the board as:

$$I_M = C_M f_s \Delta V \tag{4.1}$$

where f_s is the switching frequency and $\Delta V = V_{T,E} - V_D$ is the estimated charge/discharge modulation peak-to-peak amplitude, which is defined by setting an estimate for the transfer voltage V_T. In fact, we recall that, differently from the discharge voltage V_D, V_T is not directly controllable (see also Sect. 2.1). As will be discussed in Sect. 4.2, a possibly wrong estimation of V_T is easily corrected after the measurement and does not result in measurement errors. The estimated transfer voltage value is hereafter considered as $V_{T,E}$=0.365 V.

As a starting point before performing any target experiments, we run measurements in dry in order to estimate parameters which will be subsequently used to calibrate the experiments (see the following sections).

Figure 4.2 (top) shows a measurement capacitance (C_M) map of the array in air at 50 MHz switching frequency. Striped patterns are visible, which can be attributed partly to lithography effects, which make even and odd rows systematically slightly different from each other, partly to statistical variations and Random Telegraph Noise (RTN) in the column readout circuitry, and partly to the fact that odd and even columns are processed by different ADCs, in groups of 32 columns per ADC (see Sect. 2.1). In Fig. 4.2 (middle) the capacitance distribution of the nanoelectrodes processed by different ADCs are shown. They have nearly Gaussian behavior, but some of them exhibit non-negligible deviations at low percentile. Fig. 4.2 (bottom) shows the corresponding normal probability plots, which confirm some deviation from the normal plot. Many distributions are close to ideal but, for each A/D converter ($k \in [1, 8]$), the distribution has a different mean value ($C_M^{ADC_k}$). These offsets from the full matrix mean value (C_M =0.37 fF for this chip) can easily be corrected. Considering the measurement capacitance $C_M^{(i,j)}$ of the electrode in (row,column)=(i, j), the correction we apply is:

$$C_M^{(i,j)} = C_M^{(i,j)} - C_M^{ADC_k} + C_M, \;\; k = \left\lceil \frac{j}{32} \right\rceil + [1 - (j \bmod 2)] \tag{4.2}$$

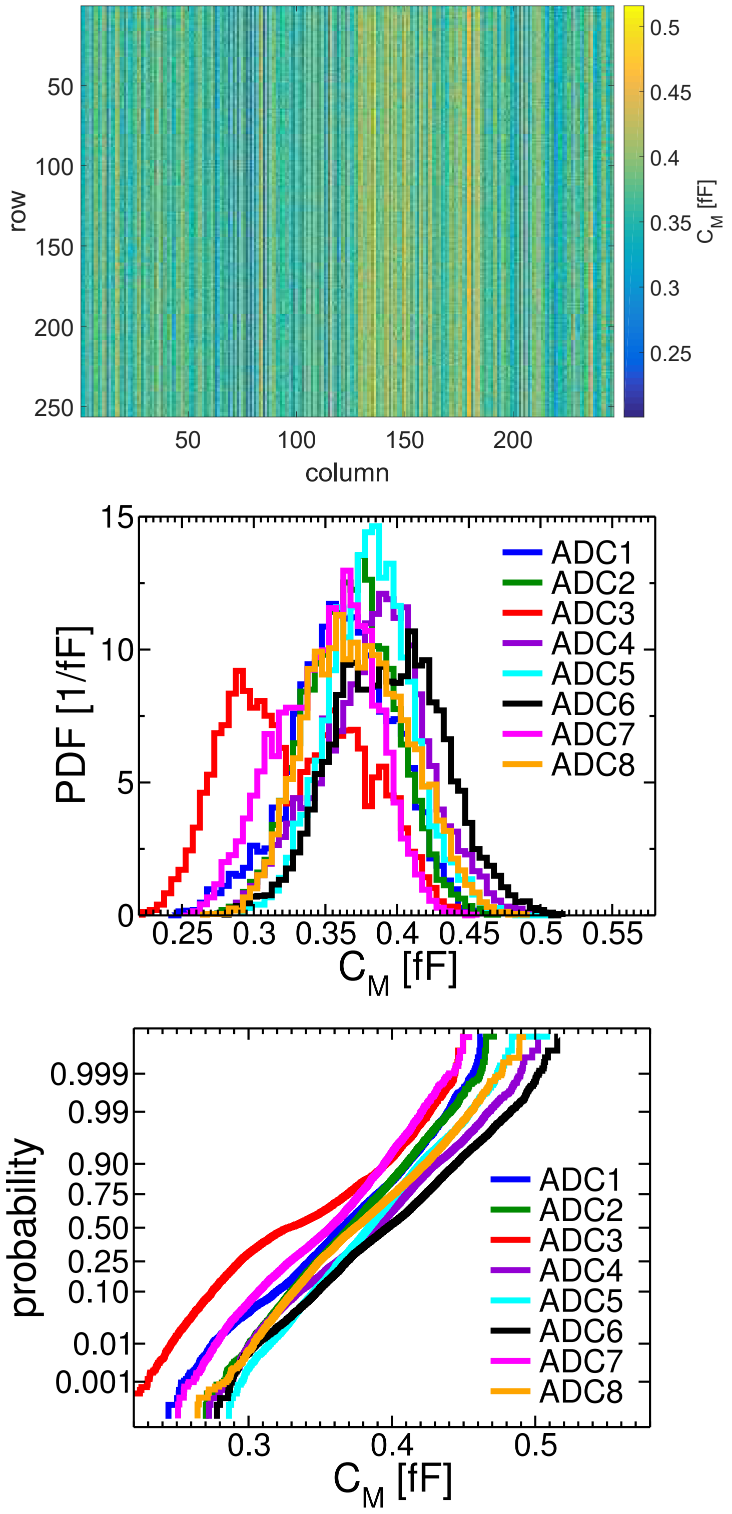

Figure 4.2: *Measurement capacitance in air at 50 MHz. Top: array map. Middle: histograms of the measurement capacitances, obtained from the 8 ADCs (each one showing a different mean value). Bottom: normal probability plots. Published in [190].*

where the *ceil* operator $\lceil\cdot\rceil$ rounds up to the nearest integer. The correction thus consists in shifting the nanoelectrode capacitance by the difference between the full matrix average and the single ADC (that processes that specific column) average. Possible non-working electrodes are neglected in the calculation of the averages.

With the typical voltage levels described in Sect. 2.1, the two transistors of the cascoded common gate amplifier are biased in sub-threshold (in fact, for typical values of C_M in the range 0.6–4 fF, the maximum column current at f_s=70 MHz is 56 nA). The non-linear relation between the cascode current, I_M, and the source (V_T) and gate (V_G) voltages of the lower transistor can be expressed as:

$$I_M = I_0 \exp\left(\frac{q\,(p_G V_G - p_T V_T)}{k_B T}\right) \tag{4.3}$$

where V_G and V_T are the transistor's gate and source voltages, respectively, T is the absolute temperature, q is the elementary charge unit, k_B is Boltzmann's constant, and I_0, p_G and p_T are transistor model parameters. The transistor model parameters I_0, p_G and p_T can be estimated by fitting Eq. 4.3 to a set of C_M (that is, I_M) measurements, for variable frequency and applied voltages (V_G and V_D, with V_T being indirectly controlled via V_G). Note that p_G is in general different from p_T because of body effect. As a first step in our calibration procedure, these three parameters are computed for all columns of the array. Fig 4.3 shows an example of extracted parameters sets. Varying frequency and/or applied voltages may yield outlier C_M values at some columns, if the properties of the corresponding column-readout transistors differ significantly from the average or in the presence of Random Telegraph Noise (RTN). These outlier columns can be identified (see for example the spikes in the p_G and p_T plots at column 102) and neglected during subsequent analyses.

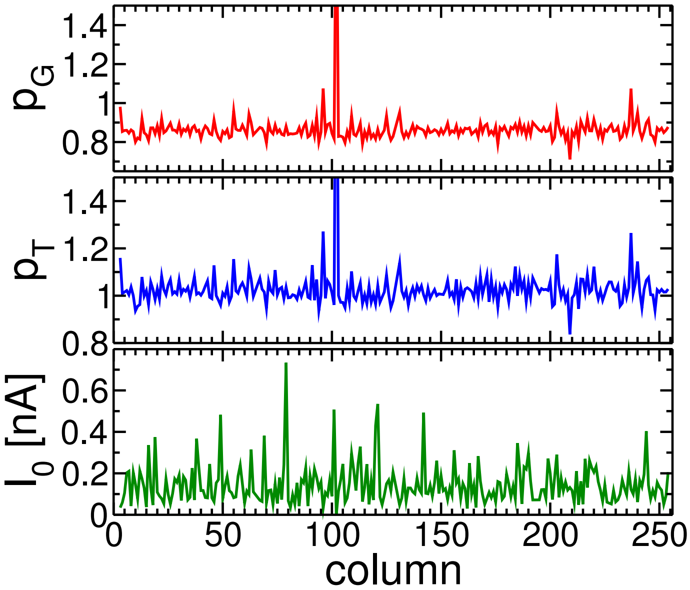

Figure 4.3: *Column transistor parameters as extracted by fitting Eq. 4.3 to a set of C_M measurements for variable frequency and applied voltages.*

4.2 Pre- and post-measurement calibration methods

Since the two transistors of the cascoded common gate amplifier are biased in subthreshold, their gate-source voltages (and consequently, V_T) depend logarithmically on the average column current I_M, which, in turn, depends on the switching frequency f_s and the capacitance C_M. Without further measures, this would cause frequency- and capacitance-dependent deviations of ΔV (due to deviations of V_T, since the discharge node of the sensor's cell is directly accessible and is kept at voltage V_D). As a consequence, the average nanoelectrodes DC potentials would shift from their setpoints (nominally at V_{FL}). Shifts of the DC potential, in turn, can cause unintended electrochemical disturbances at the nanoelectrode surface, and/or of the nanoelectrode admittance (via the voltage-dependence of the EDL capacitance). Furthermore, a gain error would be generated prior to A/D conversion.

We focus firstly on the frequency dependence of V_T. From Eq. 4.1 it follows that, at constant ΔV and C_M (air and non-electrolytic environments, such as IPA or silicone oils, are examples of constant and frequency-independent capacitance mediums), I_M should depend linearly on f_s. Under these conditions, we can keep V_T constant by correcting V_G:

$$V_G = V_{G,r} + \frac{k_B T}{q p_E} \ln\left(\frac{I_M}{I_{M,r}}\right) = V_{G,r} + \frac{k_B T}{q p_E} \ln\left(\frac{f_s}{f_{s,r}}\right) \tag{4.4}$$

where $V_{G,r}$ and $I_{M,r}$ are values at a reference frequency $f_{s,r}$ (e.g., 50 MHz), k_B, T and q have their usual meaning, and p_E is a non-ideality factor.

p_E is calibrated on frequency sweeps with dry nanoelectrodes, as discussed in Sect. 4.1 (i.e., in principle $p_E = \bar{p}_G$, where $\bar{p}_G$ is the mean value of p_G computed on all columns). The parameter p_E is thus set to the value that makes C_M, calculated from the measured $I_M\left(f_s\right)$ response, frequency-independent. The same correction is applied to the gate voltage of the upper cascoded common gate transistor, such that the difference between the gate voltages of the two transistors of the cascode remains constant. Fig. 4.4 shows that this "pre-calibration" indeed yields a frequency independent capacitance C_M for dry nanoelectrodes, as expected over the extended 1 MHz – 70 MHz range.

This correction is calculated from measurements in air but is then applied also during subsequent frequency sweeps with nanoelectrodes exposed to electrolyte.

Pre-calibration works fine for constant-capacitance cases. However, dielectric properties of electrolytes in general deviate from purely capacitive behavior. This introduces additional sources of frequency-dependent variations of V_T that are not compensated for. Pre-calibration compensates for the dominant source of variation, which is the frequency shift (up to 2 decades for the longest sweeps); the remaining systematic sources of gain error and DC offsets are significantly smaller. Therefore, frequency pre-calibration is quite effective in keeping the nanoelectrodes biased close to the intended DC setpoint (zero voltage w.r.t the fluid). After the measurement, once I_M is known (calculated via Eq. 4.1, where C_M is the measurement capacitance

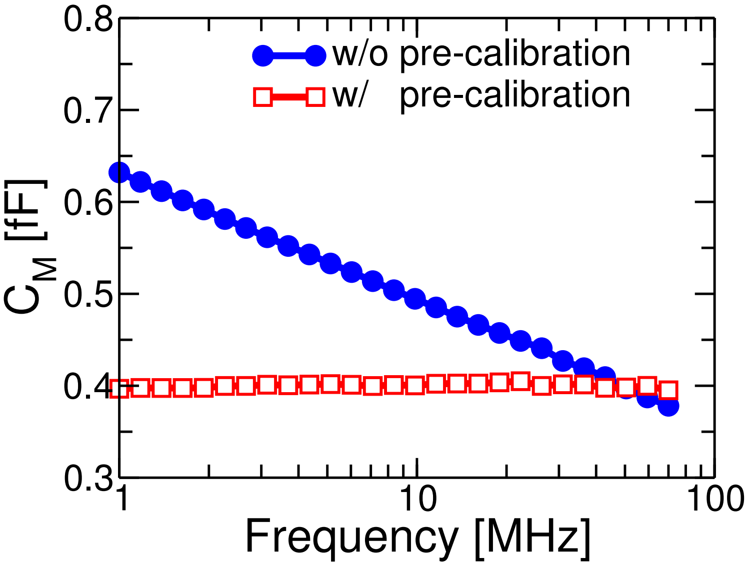

Figure 4.4: *Uncalibrated and pre-calibrated capacitance spectra (average over all nanoelectrodes) for dry nanoelectrodes at 1-70 MHz (the capacitance of dry nanoelectrodes is almost equal to the parasitic capacitance C_P in Fig. 3.11). Published in [190].*

provided by the platform), we calculate a post-measurement correction for V_T:

$$V_T = V_{T,r} - \frac{k_B T}{q p_T} \ln\left(\frac{I_M}{I_{M,r}} \frac{f_{s,r}}{f_s}\right) \tag{4.5}$$

This value is used in Eq. 2.1 to calculate (off-line) the final measurement capacitance, which we refer to as C_{post} in the following. The direct relation between C_{post} and C_M will now be derived [337].

As discussed in Chapter 2, we remind that the measurement current I_M is converted to a capacitance value C_M (on the board) by making an estimate of V_T ($V_{T,E}$), that differently from V_D is not directly controllable. On top of that, experiments performed with an empirical estimation of the parameter p_E (i.e. $p_E \neq \bar{p}_G$, for experiments performed before the extraction of the transistor parameters, see Sect. 4.1) would present deviations of V_T caused both by the capacitance of the medium and by a residual dependency on the frequency.

The current through the lower transistor of the cascode is described by Eq.4.3. Since a frequency-dependent gate voltage is applied, as per Eq. 4.4, inserting Eq. 4.3 in Eq. 4.4 gives:

$$I_M = \left(\frac{f_s}{f_{s,r}}\right)^{\frac{p_G}{p_E}} I_0 \exp\left(\frac{q\,(p_G V_{G,r} - p_T V_T)}{k_B T}\right) \tag{4.6}$$

Thus, we perform a current measurement ($I_{M,r}$) at a given gate voltage ($V_{G,r}$) and frequency ($f_{s,r}$) for a reference medium (air). We indicate as $V_{T,r}$ the source voltage corresponding to this measurement. $V_{T,e}$ can be explicitly obtained from Eq. 4.6 by setting $I_M = I_{M,r}$, $f_s = f_{s,r}$. We can then rewrite Eq. 4.6 as:

$$I_M = \left(\frac{f_s}{f_{s,r}}\right)^{\frac{p_G}{p_E}} I_{M,r} \exp\left(\frac{qp_T\left(V_{T,r} - V_T\right)}{k_B T}\right) \tag{4.7}$$

By assuming that the source voltage of the cascode is equal to $V_{T,E}$, the platform returns a measured capacitance C_M given by:

$$C_M = \frac{I_M}{f_s\left(V_{T,E} - V_D\right)} \tag{4.8}$$

For a reference measurement we have of course:

$$C_{M,r} = \frac{I_{M,r}}{f_{s,r}\left(V_{T,E} - V_D\right)} \tag{4.9}$$

where $C_{M,r}$ is the capacitance returned for the reference measurement. By substituting Eq. 4.9 in Eq. 4.7 and equating the resulting equation to Eq. 4.8 we obtain

$$V_T = V_{T,r} - \frac{k_B T}{qp_T}\left[\ln\left(\frac{C_M}{C_{M,r}}\right) + (1 - \frac{p_G}{p_E})\ln\left(\frac{f_s}{f_{s,r}}\right)\right] \tag{4.10}$$

It can be noted that $V_{T,E}$ does not appear in this identity, hence a wrong estimation of $V_{T,E}$ does not cause an error. Furthermore, we can notice that the second term within square brackets performs a correction of V_T due to frequency-dependence. If $p_E = p_G$, then Eq. 4.10 is essentially equal to Eq. 4.5. We should however consider that all columns share the same gate voltage signal V_G (hence the same p_E). Since different columns have a different p_G parameter, for a given p_E $(= \bar{p}_G)$ at individual columns there is always a difference between p_E and p_G. This further correction is thus fundamental to compensate these differences as well. Finally, considering that the actual capacitance derives from the "real" value of V_T, by using Eq. 4.1 and Eq. 4.10 we obtain the final form for the post-calibration correction:

$$C_{post} = \frac{C_M}{g(C_M)} \tag{4.11}$$

where the correction function $g(C_M)$ reads:

$$g(C_M) = 1 + \frac{V_{T,r} - V_{T,E}}{V_{T,E} - V_D} - \frac{k_B T}{qp_T\left(V_{T,E} - V_D\right)}\left[\ln\left(\frac{C_M}{C_{M,r}}\right) + (1 - \frac{p_G}{p_E})\ln\left(\frac{f_s}{f_{s,r}}\right)\right] \tag{4.12}$$

We implemented this correction separately for each nanoelectrode, that is using for each column the corresponding parameters; array-averages are computed only afterward if needed.

If more accurate models of the relation $I_M = I_M\left(f_s\right)$ are available, Eq. 4.5 can be adjusted accordingly.

If applied to each column independently, the post-calibration correction of Eq. 4.11 reduces significantly the column-striped pattern (Fig. 4.5, top) for both the current-generation chips with the nanoelectrode processing described in Chapter 2 (see Fig.

4.5 left) and for the previous-generation chips of [215] (see Fig. 4.5 right). In the latter case a few regions still can be seen (e.g., in the top left part of the array) where

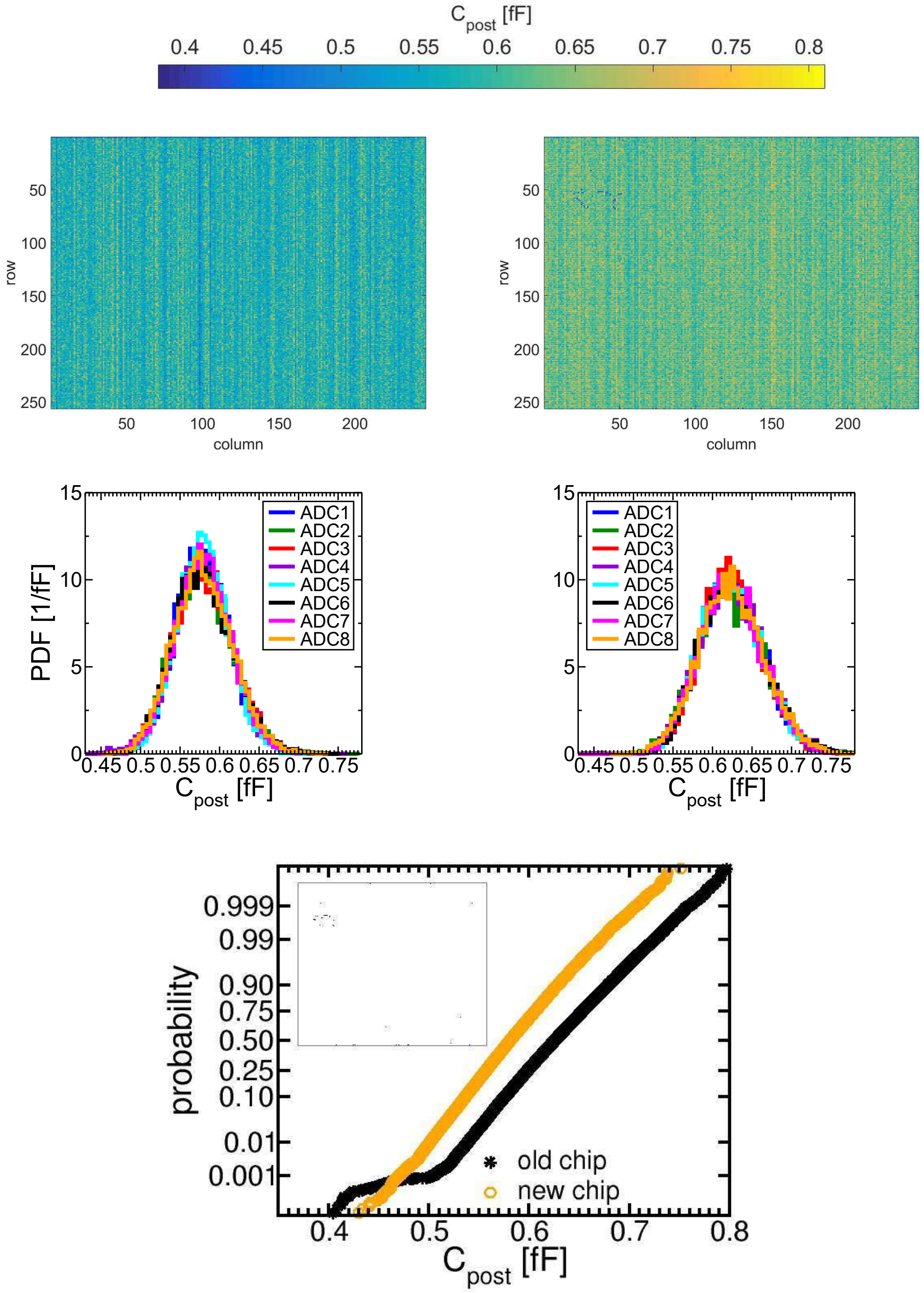

Figure 4.5: *Top and middle graphs: same as Fig. 4.2 for the post-calibrated capacitance* C_{post}*, also corrected for the ADC offsets, both for new (left, see Chapter 2) and old (right, [215]) nanoelectrode processing. The resulting standard deviation is 0.04 fF and 0.05 fF, respectively; the std/mean ratio is 6.5% for both. Bottom: normal probability plot of all the nanoelectrodes, for old (black) and new (orange) nanoelectrode processing. Inset: 2D binary map that identifies the location of the outliers for the old chip (black spots over white background). Published in [190].*

faulty or dirty electrodes can be identified. These few outliers can be easily identified and excluded from further analyses. The source of the residual column-striped patterns is instead still under investigation.

Fig. 4.5 (middle) shows the post-calibrated capacitance distributions for the 8 ADCs after offset compensation. The normal probability plot of the capacitance distribution of all the nanoelectrodes (Fig. 4.5, bottom) allows for easy identification of outliers, which cause a major deviation of the curve from the expected approximately straight-line trend. The numerous outliers of the old-generation chip (black line in Fig. 4.5, bottom) are easily located on a binary 2D map (inset), and require to be pruned before further analyses with that chip. They visually match the "bad nanoelectrodes", visible in the top-right color map of Fig. 4.5. Instead, chips realized with the improved new nanoelectrode process, described in Chapter 2, do not show outliers. The mean value of the black and orange plots of Fig. 4.5 (bottom) are slightly different. This is consistent with the fact that different chip versions (see Sect. 2.1) can yield different parasitics at the nanoelectrodes.

Compared to C_M, the C_{post} capacitance trace in air has increased to about 0.6 fF (see also Fig. 4.5, middle, and Fig. 4.8), which is close to the value of C_P obtained from parasitic extraction on the physical layout of the sensor cells. In fact, C_P is essentially equal to the sum of the gate-source and gate-drain overlap capacitances of the transistor junctions connected to the switching node (Fig. 2.2), and the parasitic capacitance of the metals involved in connecting the nanoelectrode. This increase of capacitance in air is the result of the V_T correction: in fact, for a given column current, compared to the estimation before measurement ($V_{T,E} = 365$ mV) a lower value for V_T (approx. 280 mV for the correction in air at 50 MHz) results in a smaller ΔV and hence a larger capacitance (see Eq. 4.1).

4.3 Calibration and verification of impedance spectra in electrolyte

Measurement protocols

All the measurement protocols in liquid include some preliminary steps to gradually fill the fluidic chamber with the appropriate electrolyte. The first step usually consists in flushing with high-purity isopropyl alcohol (IPA, 99.5%), followed by degassed milliQ water. Thanks to IPA's good wetting properties, compared to directly injecting milliQ, these steps help in filling the whole fluidic chamber with liquid, without stagnant air bubbles. As successive steps, appropriate electrolytes can be flushed to replace the milliQ in the chamber. During all these steps, avoiding accidentally injecting air bubbles is also of critical importance. In fact, introduction of air bubbles in the fluidic chamber can result in local depressions of the measurement capacitance, thus affecting the measurements. In the following of the work, we will always follow these preliminary steps when performing experiments in electrolyte.

The chips are cleaned at the end of each experiment (to enable their re-use[1]) wip-

---

[1] Chips have indeed been re-used many times in this work, after multiple measurement and cleaning sessions.

ing their surface with clean cleanroom cloth soaked with IPA (to guarantee removal of particles from the chip surface, in the case of experiments with analytes) and flushing acetone-IPA-milliQ in sequence. UV-cleaning can also be used to remove organic contamination.

Comparison between simulations and experiments

Fig. 4.6 compares the theoretical response (as computed with the switching capacitance model of Eq. 3.12), to experiments in air and in KCl electrolytes at different salt concentrations. The symbols are array-averages of pre-calibrated (C_M) capacitances (excluding outliers). The results of these experiments on which we perform the following analyses have been kindly provided by the University of Twente. These data have been obtained with the old-generation chip, whose response is well reproduced by using $r_{el} = 75$ nm in simulations, as demonstrated in [203,215]. Parameters for the calculation of C_{SW} are thus the ones listed in Tab. 3.3. Calculations of C_{SW} have been performed with a duty cycle $\delta = 35\%$ (corresponding to the typical parameters for the clocks as reported in Sect. 2.1, namely 7 ns high-time and 20 ns period at 50 MHz). The number of integration cycles is not constant over different salt concentrations: it is lowered for larger salt concentrations in order to guarantee the A/D converters to operate within their range of linearity (see Sect. 2.1). In particular, these measurements ranged from 512 to 384 charge/discharge cycles.

While the main qualitative features are essentially well reproduced, the quantitative agreement is very poor. The measured capacitance in electrolyte is smaller than the simulations, especially at low frequency and high salt concentration, thus proving that the pre-calibration procedure alone is inadequate to cover the whole range of measurement conditions. Furthermore, the capacitance in dry is too low compared to the expectations (as will be explained in the following), providing a hint that the value of $V_{T,E}$ used for the calculation of C_M was different from the actual one.

In Fig. 4.7, instead, we compare the theoretical response to post-calibrated (C_{post}) capacitances. A good quantitative agreement is obtained up to 50 mM concentrations and frequencies above 2 MHz. Compared to C_M, the C_{post} capacitance trace in air has increased to about 0.6 fF (see also Fig. 4.5, middle, and Fig. 4.8), which is close to the value of C_P obtained from parasitic extraction on the physical layout of the sensor cells. In fact, C_P is essentially equal to the sum of the gate-source and gate-drain overlap capacitances of the transistor junctions connected to the switching node (Fig. 2.2), and the parasitic capacitance of the metals involved in connecting the nanoelectrode. This increase of capacitance in air is the result of the V_T correction: in fact, for a given column current, compared to the estimation before measurement ($V_{T,E} = 365$ mV) a lower value for V_T (approx. 280 mV for the correction in air at 50 MHz) results in a smaller ΔV and hence a larger capacitance (see Eq. 4.1).

The frequency sweeps exceed the dielectric relaxation cut-off frequencies $f_E = (2\pi R_E C_E)^{-1}$ for the measured electrolyte concentrations up to 15 mM (51.7 MHz), and approach them for 50 mM and 100mM (174 MHz and 352 MHz, respectively).

Fig. 4.8 shows a direct comparison between pre-calibrated and post-calibrated capacitance for air and for a KCl 50 mM electrolyte. As discussed in the previous

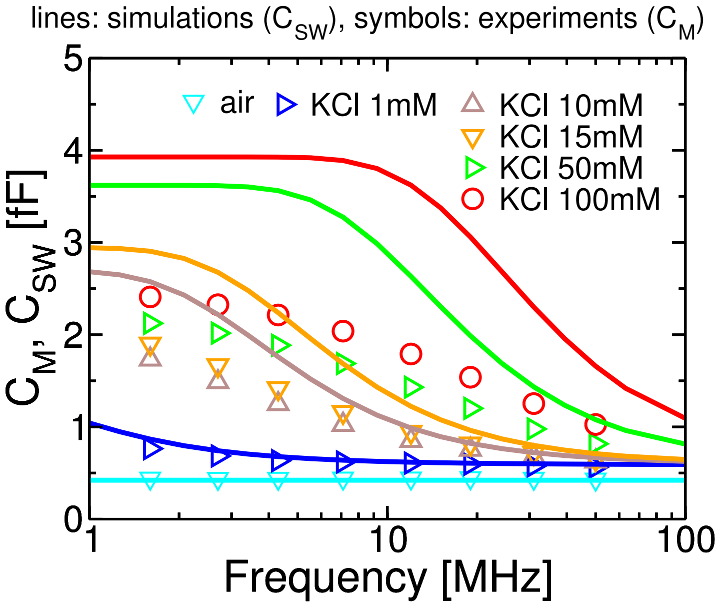

Figure 4.6: *Comparison of simulations (C_{SW}) and experimental pre-calibrated capacitance spectra (C_M) in air and KCl electrolytes of different salt concentrations. Pre-calibration was applied to the measurements. This set of experimental data (C_M) has been kindly provided by University of Twente.*

section, the C_{post} capacitance trace in air has increased w.r.t. C_M. The lower original estimation provided by C_M was due to the incorrect pre-measurement estimation of the transfer voltage $V_{T,E}$. A large variation of the capacitance is visible in electrolyte, especially at low frequency; this highlights the quantitative importance and impact of the post-calibration.

Finally, to highlight the increase of the response with the electrolyte salinity, Fig. 4.9 shows C_{SW} and C_{post} as a function of the electrolyte salt concentrations (at 1.6 MHz and 50 MHz switching frequencies).

Reproducibility and imaging

To show the consistency of measurements performed with different chips and in different laboratories (i.e. with slightly different measurement setups), Fig. 4.10 shows a comparison of (post-calibrated) experiments performed by the University of Twente (the original data are shown in Fig. 4.6) and performed in our lab, both in constant-permittivity ambient (IPA) and in electrolyte (10 mM). The qualitative and quantitative values are well reproduced, demonstrating the reproducibility of measurements. The experiments performed with the new chip have slightly lower values. This is consistent with the fact that, for this experiment, we used the chip corresponding to the orange curve in Fig. 4.5 (bottom), which have a slightly lower value of C_p.

Finally, to demonstrate the imaging capabilities of the platform, we performed measurements of a direct air-milliQ transition (here, intentionally without intermediate IPA flushing). Fig. 4.11 shows 2D capacitance maps of this experiment,

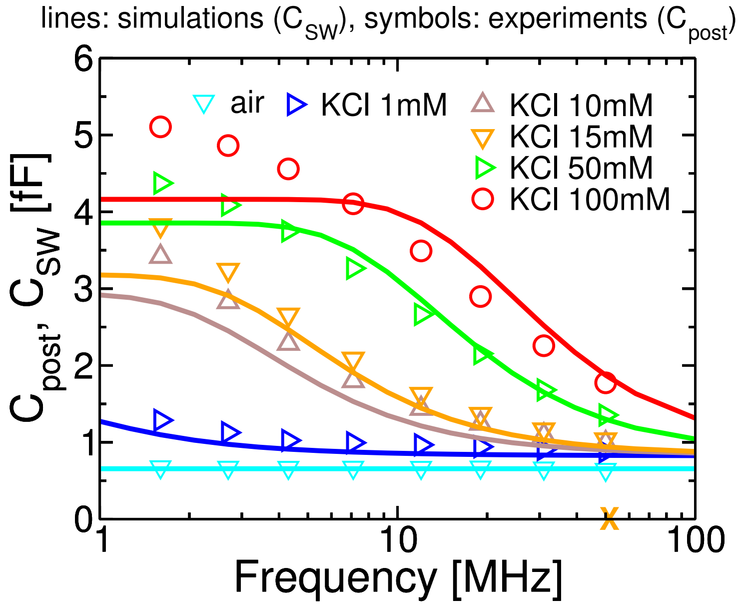

Figure 4.7: *Comparison of simulations (C_{SW}) and experimental post-calibrated capacitance spectra (C_{post}) in air and KCl electrolytes of different salt concentrations. Pre-calibration was applied to the measurements. Published in [190].*

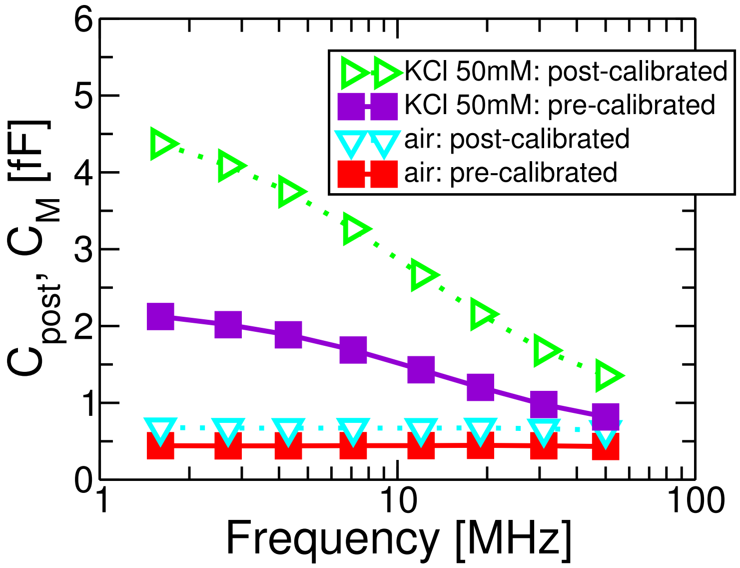

Figure 4.8: *Comparison between pre-calibrated (C_M) and post-calibrated (C_{post}) capacitance measurements in air and 50 mM electrolyte. The post-calibration increases the baseline value in air to about 0.6 fF. The impact on the spectrum in electrolyte is even more evident. Published in [190].*

recorded at 50 MHz. The 4 different time frames show the progressive displacement of the air in the fluidic chamber by milliQ. Three nanoelectrodes (A, B, C) are selected along the same column, and in Fig. 4.11 (bottom) their capacitance time

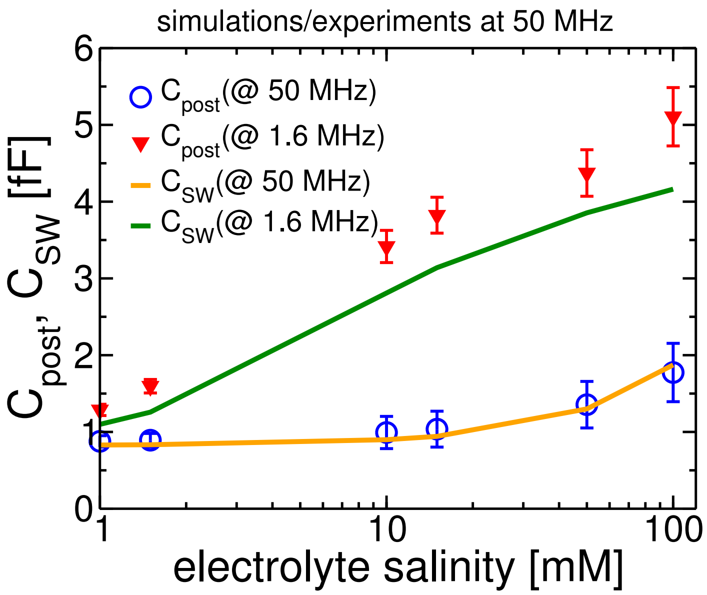

Figure 4.9: *Dependence on the electrolyte salinity of simulations (C_{SW}) and experiments (C_{post}), at 1.6 MHz and 50 MHz switching frequencies.*

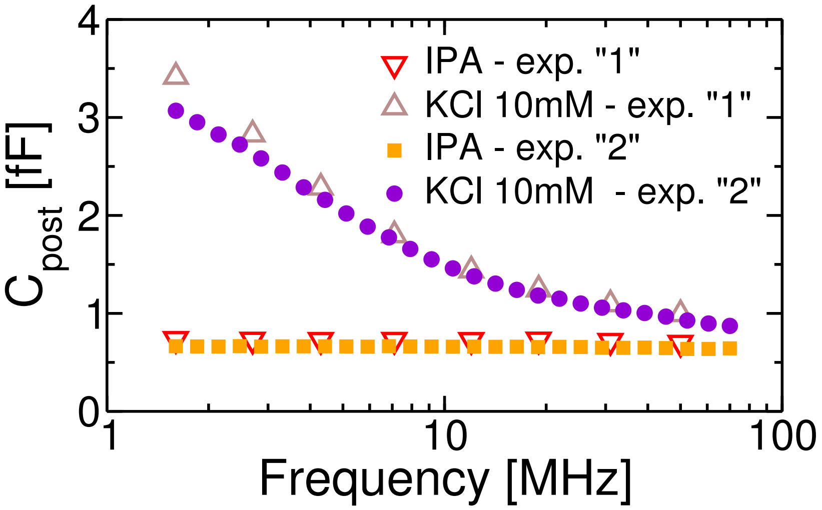

Figure 4.10: *Comparison between post-calibrated (C_{post}) capacitance measurements, in IPA and 10 mM electrolyte, performed with different chips in different laboratories, demonstrating the reproducibility of measurements. Blank symbols (exp. “1”): post-compensation of measurements performed by the University of Twente (Fig. 4.6). Filled symbols (exp. “2”): post-compensation of measurements performed in our lab.*

traces are shown, highlighting the steps in their responses upon wetting. Fractions of the surface not suited for analysis (e.g. electrode D, in the stained region near the right edge of the maps, probably due to surface contamination) can be identified *a-priori* and excluded from the analysis. Indeed, the much smaller capacitance increase upon wetting of nanoelectrode D indicates that its surface is not perfectly wetted by water.

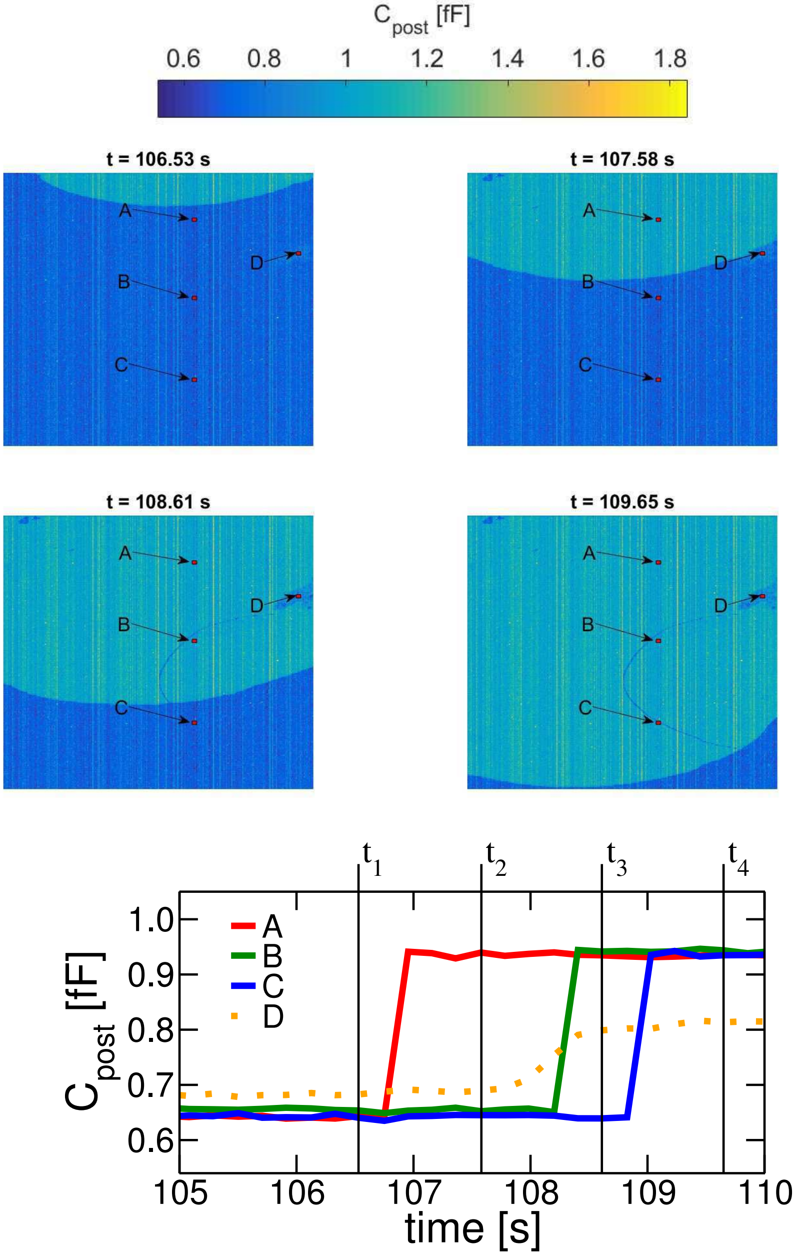

Figure 4.11: *Imaging sequence of direct air-milliQ transition at 50 MHz at four different time frames, showing the transient response of three nanoelectrodes along a column (A, B, C). The 2D maps are single frames, captured with* N_{cyc} *=512 charge/discharge cycles and 8 on-chip data accumulations. Skipping the intermediate IPA flushing step can result in an imperfect wetting. Contaminated areas (nanoelectrode D) are also evident. Published in [190].*

4.4 Sources of residual errors

To investigate the source of residual discrepancies between (post-measurement calibrated) experiments and numerical simulations (Fig. 4.7), we consider two possible mechanisms that may alter the experimental capacitance from the expected values, namely the presence of leakage currents and non-idealities of the voltage waveform at the nanoelectrodes. Then, we discuss about the influence of the size of nanoelectrodes.

4.4.1 Leakage currents

We speculate that four possible sources of leakage currents might be present:

- Leakage through the switches (due to subthreshold conduction) of the inactive cells (whose DC component is indicated as $I_{leak,C}$, where we use the subscript "C" to refer to the counter electrodes, i.e. the deactivated cells);
- Leakage through the deactivated switches (due to subthreshold conduction) of the selected sensor cell (whose DC component is indicated as $I_{leak,S}$, where we use the subscript "S" to refer to the switching cell);
- Leakage through the electrolyte (from the working electrode to the pool of counter electrodes, whose DC component is indicated as $I_{leak,E}$, where we use the subscript "E" to refer to the electrolyte);
- Leakage in the charge-integration circuit (see Fig. 2.3) through the calibration and reset switches (whose DC component is indicated as $I_{leak,I}$, where we use the subscript "I" to refer to the integrator).

Fig. 4.12 shows again the schematic of the sensor cell and read-out circuit highlighting the aforementioned possible sources of leakage currents.

As will be now demonstrated, we can modify the post-calibration procedure to account for these sources of leakage by defining a new post-calibrated capacitance C'_{post}:

$$C'_{post} = C_{post}\left(1 - \frac{I_{Leakage}}{C_M f\,(V_{T,E} - V_D)}\right) \tag{4.13}$$

where $I_{Leakage}$ can be any of the proposed leakage mechanisms, or combinations of them. The leakage through the switches describe the impact of one of their non-idealities: the subthreshold conduction. The impact of other non-idealities of the switches (namely, the presence of parasitic capacitances) will be discussed in Sect. 4.4.2.

Leakage in the inactive cells

We start by considering the possible presence of $I_{leak,C}$, neglecting the other leakage mechanisms. We expect $I_{leak,C}$ to be a constant value, since the transistors of the inactive cells are biased at a fixed voltage. In the presence of this leakage current

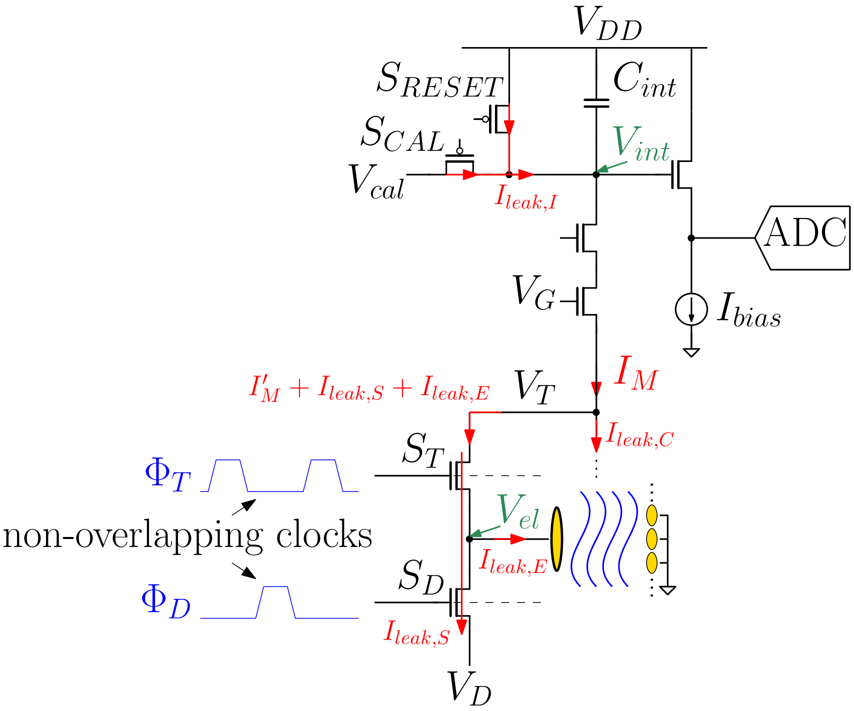

Figure 4.12: *Schematic representation of the selected sensor cell and read-out circuit highlighting the possible leakage currents.*

drawn from the column read-out circuit, the measurement current (as defined in Eq. 4.3) can be expressed as follows:

$$I_M = I'_M + I_{leak,C} \tag{4.14}$$

where I'_M represents the actual measurement current, i.e. the part of the total measurement current that is indeed caused by the switching of the sensor cell.

We follow the same steps presented in Sect. 4.2, applying the pre-calibration correction of the gate voltage (Eq. 4.4) and making a reference measurement (Eq. 4.9), which in this case is affected by leakage as well:

$$I_{M,r} = f_{s,r} C_{M,r} \left(V_{T,E} - V_D\right) = I'_{M,r} + I_{leak,C} \tag{4.15}$$

Since both “experimental” and “reference” measurements are affected by leakage, it is easy to see that the derivation of V_T takes the same form as for the case without leakage, i.e. Eq. 4.10.

The “real” capacitance of the system under study is given by the current component caused by the switching of the sensor cell. We can then write:

$$C'_{post} = \frac{I'_M}{f_s \left(V_T - V_D\right)} = \frac{I_M - I_{leak,C}}{f_s \left(V_T - V_D\right)} \tag{4.16}$$

which after straightforward calculations leads to Eq. 4.13.

As discussed in Chapter 2, the nanoelectrodes of the disabled cells are connected to a “fluid” potential V_{FL} via their S_D switches, while the corresponding S_T switches are disabled by passing logic low DC potential on their Φ_T terminals. The total leakage current $I_{leak,C}$ is thus the sum of the subthreshold leakage currents in the S_T switches of all the 255 deactivated cells of the same column, which reads:

$$I_{leak,C} \simeq 255 I_0 \exp\left(\frac{q\left(p_G\Phi_T - p_T V_{FL}\right)}{k_B T}\right) \tag{4.17}$$

where as a simplification we assumed all the transistor of the switching cells to be identical (i.e. having the same parameters p_G, p_T and I_0). In principle the parameters of these transistors differ from the ones of the cascoded common gate amplifier (the latter). To obtain a first-hand estimation of the leakage contribution, under the simplifying assumption of having $p_T = p_G = 1$, I_0 in the range 0.1–0.2 nA, Φ_T=0 V, V_{FL} in the range 200–230 mV, T =300 K, we get $I_{leak,C} \simeq 3 - 22$ pA.

Leakage in the switching cell

Now we consider the possible presence of $I_{leak,S}$, neglecting the other leakage mechanisms. In this case, $I_{leak,S}$ is not constant over time, since it derives from the subthreshold conduction of different transistors (namely, S_T and S_D) during the different phases of the switching activity. We will compute a mean value $I_{leak,S}$ and the same conclusions derived for the previous analysis apply, i.e. Eq. 4.13 holds also for this leakage mechanism.

In order to quantify this leakage contribution, we do consider the four different phases of the switching process separately (as in Appendix A):

- **Phase A: charging**
  S_T is ON and S_D is OFF. Out of the current flowing through the column read-out, a portion given by $I^A_{leak,S}$ is lost (and does not contribute to charging the nanoelectrode) due to leakage through S_D. This current can be quantified as:

  $$I^A_{leak,S} = I_0 \exp\left(\frac{q\left(p_G\Phi^A_D - p_T V_D\right)}{k_B T}\right)$$

  where Φ^A_D=0 V is the voltage applied to the gate of S_D during this phase. Assuming for simplicity $p_G = p_T = 1$, I_0 in the range 0.1–0.2 nA, T=300 K, V_D=120 mV, we get $I^A_{leak,S} \simeq$ 1–2 pA.

- **Phase B: floating**
  S_T is OFF and S_D is OFF. During this phase the current flowing through the column read-out, that in principle should be zero, is given by a contribution $I^B_{leak,S}$ that leaks through S_T and S_D. The leakage currents through the two switches read:

  $$I^{B,S_T}_{leak,S} = I_0 \exp\left(\frac{q\left(p_G\Phi^B_T - p_T V_{el}\right)}{k_B T}\right)$$

  $$I^{B,S_D}_{leak,S} = I_0 \exp\left(\frac{q\left(p_G\Phi^B_D - p_T V_D\right)}{k_B T}\right)$$

where V_{el} is the voltage level at the nanoelectrode (set by the previous charging phase), and $\Phi_T^B = \Phi_D^B$=0 V is the voltage applied to the gate of S_T and S_D during this phase. The voltage at the nanoelectrode is always greater than the discharge voltage ($V_{el} > V_D$), leading to $I_{leak,S}^{B,S_T} < I_{leak,S}^{B,S_D}$. Consequently, the amount of leakage current is set (and limited) by the switch S_T ($I_{leak,S}^{B} = I_{leak,S}^{B,S_T}$), while the extra current that leaks through S_D (i.e. $I_{leak,S}^{B,S_D} - I_{leak,S}^{B,S_T}$) contributes to (minimally) discharging the nanoelectrode's node. Assuming for simplicity $p_G = p_T = 1$, I_0=0.1–0.2 nA, T=300 K, V_D=120 mV, V_{el}=230–270 mV, we get $I_{leak,S}^{B} \simeq$ 3–27 fA. The current through S_D, which partly discharges the nanoelectrode, contributes to I'_M, hence it is already accounted for in the calculation of the capacitance.

- **Phase C: discharging**
  S_T is OFF and S_D is ON. During this phase the current flowing through the column read-out should in principle be zero, while the nanoelectrode is discharged to V_D. However, due to the leakage through S_T, a current $I_{leak,S}^{C}$ is drawn from the column read-out. This current can be quantified as:

$$I_{leak,S}^{C} = I_0 \exp\left(\frac{q\left(p_G \Phi_T^C - p_T V_{el}\right)}{k_B T}\right)$$

  where Φ_T^C=0 V is the voltage applied to the gate of S_T during this phase. During the discharge, the voltage at the nanoelectrode is not constant, spanning from V_T (minus a small contribution due to the leakage through S_D in the phase B) to V_D. Considering a worst case scenario (i.e. the greatest possible leakage current) by taking $V_{el} = V_D$, and assuming for simplicity $p_G = p_T = 1$, I_0=0.1–0.2 nA, T=300 K, V_D=120 mV, we get $I_{leak,S}^{C} \simeq$ 1–2 pA, just like in phase A (in practice slightly smaller since V_{el} takes some time to converge to V_D).

- **Phase D: floating**
  S_T is OFF and S_D is OFF. As for phase B, the leakage is given by a contribution $I_{leak,S}^{D}$ that flows through S_T and S_D. The leakage currents through the two switches are:

$$I_{leak,S}^{B,S_T} = I_0 \exp\left(\frac{q\left(p_G \Phi_T^B - p_T V_{el}\right)}{k_B T}\right)$$
$$I_{leak,S}^{B,S_D} = I_0 \exp\left(\frac{q\left(p_G \Phi_D^B - p_T V_D\right)}{k_B T}\right)$$

  where V_{el} is the voltage level at the nanoelectrode (set by the previous discharging phase), and $\Phi_T^D = \Phi_D^D$=0 V is the voltage applied to the gate of S_T and S_D during this phase. In principle $V_{el} = V_D$, leading to $I_{leak,S}^{B,S_T} = I_{leak,S}^{B,S_D}$. However, based on the analysis of Sect. 4.4.2, a lower value is also possible for a short amount of time (essentially due to capacitive-coupling between the gate of S_D and the the nanoelectrode, whose voltage can drop below V_D when Φ_D has a transition high-to-low). In that case, $I^{B,S_T}_{leak,S} > I^{B,S_D}_{leak,S}$ and the amount of leakage current is set (and limited) by the switch S_D ($I^{D}_{leak,S} = I^{D,S_D}_{leak,S}$), while the extra current that leaks through S_T (i.e. $I^{D,S_T}_{leak,S} - I^{D,S_D}_{leak,S}$) contributes to (minimally) charging the nanoelectrode's node. Assuming for simplicity $p_G = p_T = 1$, I_0=0.1–0.2 nA, T=300 K, V_D=120 mV, we get $I^{D}_{leak,S} \simeq$ 1–2 pA. The current through S_T, which partly charges the nanoelectrode, contributes to I'_M, hence it is already accounted for in the calculation of the capacitance.

Finally, we can average the leakage current values during the four different phases (assigning proper weights based on the duration of the phases). $I^{B}_{leak,S}$ and $I^{D}_{leak,S}$ contribute only for 1 ns each (the floating time between the charging and discharging phase), while $I^{A}_{leak,S}$ and $I^{C}_{leak,S}$ contribute for 6 ns to 500 ns (considering f_s in the range 1 MHz to 70 MHz). The final estimation of the leakage current through the sensor cell is $I_{leak,S}$=1–2 pA.

We expect $I_{leak,S}$ to be a constant value over frequency for constant capacitance mediums (since pre-calibration guarantees to have a constant V_T, hence a constant V_{el} during the charging phase). Differently, we expect it to be larger (approaching the upper limit of 2 pA of the previous estimation) at lower frequencies for electrolytes (since for non-constant capacitance mediums pre-calibration does not guarantee to have a constant V_T, which is compensated post-measurement and is larger for larger capacitance values). However, while in principle this would go in the correct direction (i.e. being more relevant at lower frequencies, where we have the larger discrepancies), this amount of leakage is negligible compared to $I_{leak,C}$, and is also too small to affect the results (see later in this section).

Leakage in the electrolyte

The existence of a DC current through the electrolyte would imply the presence of electrochemical red-ox reactions occurring at the electrodes (or it would imply that the electrodes are progressively dissolving in electrolyte). However, the electrodes are made of gold and no red-ox reaction should be present. Consequently, it is unlikely that a DC current is present in the electrolyte and we do not consider this leakage model.

Leakage in the charge integrator

Now we consider $I_{leak,I}$, neglecting the other leakage mechanisms.

As discussed in Chapter 2, at the beginning of the measurement the voltage on the integration node (V_{int}) is set to V_{DD} via S_{RESET}. Then, S_{RESET} is opened, and the non-overlapping clocks of the switching cell (Φ_T and Φ_D) run continuously: V_{int} gets progressively reduced. After a fixed number of charge/discharge cycles (N_{cyc}), V_{int} is set to V_{cal}, and CDS is performed. During each cycle, the current drawn from the column read-out circuit changes (as V_{int} changes); the measurement current I_M corresponds to the mean value of the current during the total number of N_{cyc} cycles. Differently from the previous leakage models, in this case the time evolution of the voltages/currents have to be taken into account.

Circuit simulations of the charge detector circuit allow to express the leakage current with the following compact expression [338]:

$$I_{leak,I}(t) = I_{L,0} - G_L\left(V_{int}(t) - V_{DD}\right) - I_{L,1}\exp\left(\beta_L\left(V_{int}(t) - V_{DD}\right)\right) \tag{4.18}$$

with $I_{L,0} = 28.5$ pA, $G_L = 76.3$ pS, $I_{L,1} = 106$ pA, $\beta_L = 34.3$ V^{-1}.

The waveform $V_{int}(t)$ can also be extracted from circuit simulations of the circuit in Fig 4.12, where we replace the nanoelectrode with the equivalent C-RC model described in Fig. 3.11. The extracted mean value of $I_{leak,I}$ is shown in Fig. 4.13.

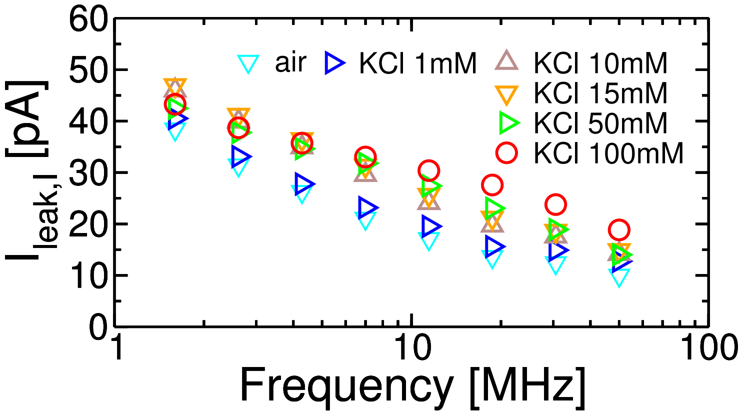

Figure 4.13: *Average values of the leakage current in the charge detector circuit ($I_{leak,I}$) at different frequencies and for different ambient conditions.*

The expected value of the leakage current is thus in the range 10–50 pA. The reason for having lower value at 50 mM and 100 mM compared to the 15 mM case at low frequency is easily explained. As discussed in Chapter 2, the number of switching cycles N_{cyc} is not kept constant for different measurements: it is reduced if larger values of C_M are expected (as is the case for the higher salt concentration electrolytes at low frequency). For the measurements of 50 mM and 100 mM, N_{cyc} was indeed reduced (from 576 to 448). Consequently, for $V_{int}(t)$ which decreases over time, hence $I_{leak,I}(t)$ that increases over time, the averaged leakage current of the charge detector is lower if a shorter period of time is considered.

Correcting the measurements

From the previous analyses, we deduce that the leakage in the switching or inactive cells contributes to *discharging* the integration node (the progressive decrease of V_{int}, from V_{DD} at the beginning of the measurement to the time CDS is performed, is accelerated by the leakage), with $I_{leak,C}$ and $I_{leak,S}$ that add up to I'_M. Therefore, the measurement (I_M) is an over-estimation of the actual I'_M due to the nanoelectrode only: correcting for the leakage would *reduce* the capacitance measurement. Based on the previous estimations, we can quantify $I_{leakage} = I_{leak,C} + I_{leak,S} = 4 - 24$ pA.

Differently, the leakage in the charge detector contributes to *charging* the integration node (in Fig. 4.12 we defined $I_{leak,I}$ as flowing into V_{int}, and Fig. 4.13 revealed that this current is always positive): the measurement (I_M) is an under-estimation of I'_M and correcting for the leakage would *increase* the capacitance measurement. From Fig. 4.13 we see that the leakage is not constant over frequency, and ranges from 10 pA to 50 pA. To use this leakage model in Eq. 4.13, taking into account the direction of $I_{leak,I}$, we have $I_{leakage} = -I_{leak,I} = 10 - 50$ pA.

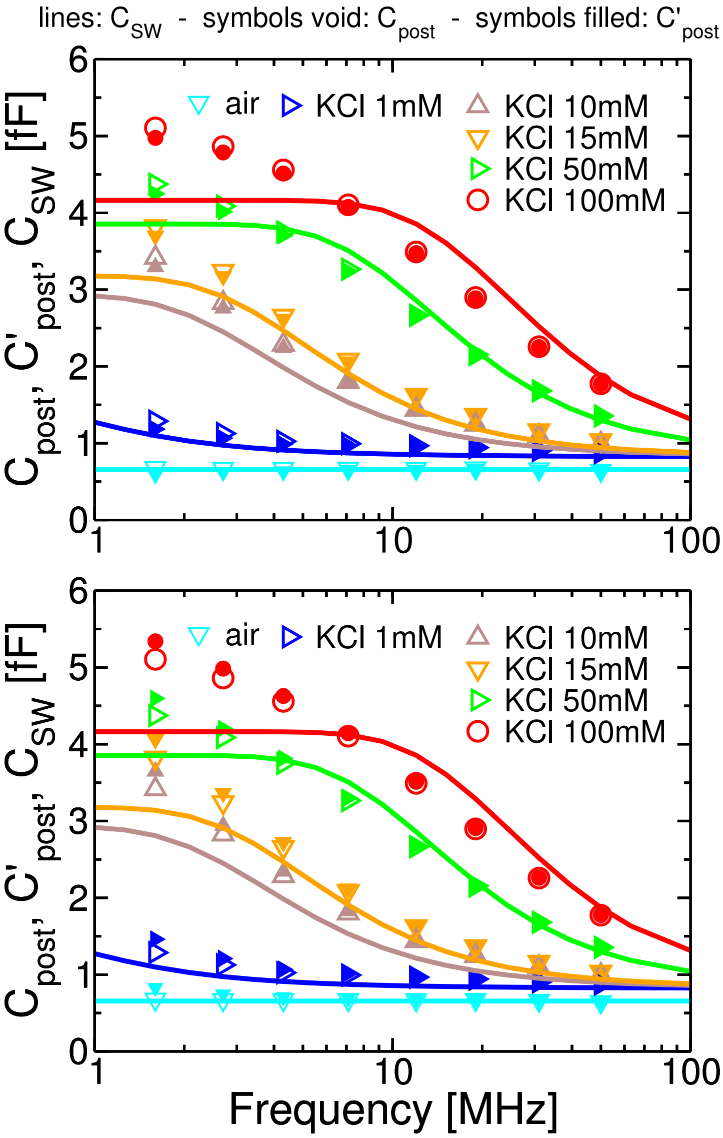

Figure 4.14: *Comparison between switching capacitance simulations (C_{SW}, lines), post-calibrated measurements (C_{post}, blank symbols), and post-calibrated measurements corrected for leakage currents (C'_{post}, filled symbols). Top: accounting for leakage currents in the array ($I_{leakage} = I_{leak,S} + I_{leak,C}$). Bottom: accounting for leakage currents in the charge detector ($I_{leakage} = -I_{leak,I}$).*

Fig.4.14 shows the corrected measurements (C'_{post}) accounting for the leakage in the active and inactive cells (top) or for the leakage in the charge detector (bottom). As anticipated, this figure proves that the different leakage models go in opposite directions and hence tend to cancel out.

Reasonable values for the transistor leakage current do not produce significant changes on the measurement data. As a consequence, we can safely conclude that leakage is not the cause of the residual discrepancy between experiments and simulations.

4.4.2 Non-ideal nanoelectrode voltage waveforms

The switching capacitance model (Sect. 3.3) computes the response of a circuit (in this case the C-RC lumped element model of Fig. 3.11) due to a charging/discharging process by means of a square-wave input voltage. Here we intend to verify the impact that non-idealities of the input voltage waveform would have on the capacitance. The approach we follow is to first derive the shape of the actual voltage waveforms at the nanoelectrodes from circuit simulations, and then use these waveforms with the Fourier-based methodology described in Sect. 3.4 to obtain the response of the system (C_F) to the different electrolytes.

In order to derive the voltage waveform at the nanoelectrode, we perform circuit simulations [339] of the basic sensor cell coupled to its column read-out and the other 255 cells connected to the same column, as shown in Fig. 4.15. We use the C-RC model of Fig. 3.11 to reproduce the electrolyte in contact with the electrode.

Since it was not possible to perform post-layout simulations of the actual chip design, we performed simulations using the BSIM4 Berkeley predictive technology models (PTM) [340, 341] for the 90 nm node (which is the same node used in the actual design). Even though the actual transistor model may differ from the one we use, the general features of the circuit can be reproduced, and will be successively corrected to account for the behavior of the real chip.

The first step of the analysis consisted in estimating the correct value of C_P to be used in the schematic (since the parasitic capacitance of our model may differ from the ~ 0.65 fF of the actual system, as can be extracted from measurements in air). Disconnecting the electrode-electrolyte circuit model, we run a "captab" analysis in Spectre [339] and we extract a value of roughly 120 aF for the parasitic capacitance at the nanoelectrode node. Consequently, we set $C_P = 650 - 120\text{aF} = 530$ aF, so that we reproduce the parasitic capacitance value extracted from experiments. In the following C_P will always be connected as shown in Fig. 4.15.

As a second step, we connect to the switching node the capacitor C_S set to model "air" environment (the value is set according to ENBIOS simulations in air, see Tab. 3.2), and we extract the voltage waveform at the nanoelectrode (V_{el}) when operating the system at 50 MHz. We remind from Chapter 2 that non-overlapping clocks Φ_T and Φ_D operated at 50 MHz (i.e. 20 ns period) have 7 ns high-time and 1 ns rise/fall times, and Φ_D is delayed by 10 ns w.r.t. Φ_T (i.e. it is phase shifted by 180°). This means that the nanoelectrode undergoes the following phases: gets connected to V_T during the 1 ns rise time of Φ_T, stays connected to V_T for 7 ns, gets disconnected from V_T during the 1 ns fall time of Φ_T, remains floating for 1 ns, gets connected to V_D during the 1 ns rise time of Φ_D, stays connected to V_D for 7 ns, gets disconnected from V_D during the 1 ns fall time of Φ_D, remains floating for 1 ns. Then repeat. Fig. 4.16 shows the extracted waveform.

The shape of the waveform is easily explained by considering that the nanoelec-

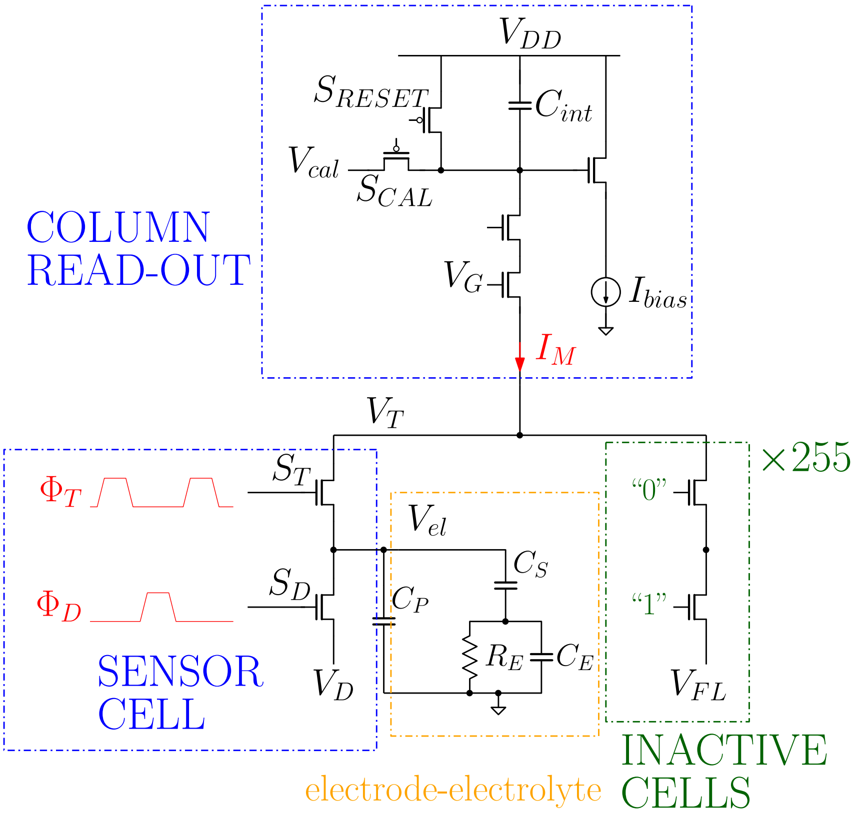

Figure 4.15: *Schematic of the circuit used to obtain the voltage waveform at the nanoelectrode ($V_{el}(t)$). The sensor cell is driven by the two non-overlapping clocks Φ_T and Φ_D. The inactive cells are connected to the "fluid" potential V_{FL} by setting a logic high voltage on their Φ_D terminals, deactivating their S_T switches with a logic low level on their Φ_T terminal. The nanoelectrode represented in Figs. 2.3-4.1-4.12 is replaced by the equivalent circuit of Fig. 3.11, with C_S, C_E and R_E extracted from ENBIOS simulations.*

trode is capacitively-coupled to the gates of S_T and S_D:

- During the interval A–B, Φ_T is high and V_{el} is connected to V_T. This phase is $T_{AB} = 7$ ns long.
- Then, S_T is switched off by lowering Φ_T. Due to capacitive coupling between V_{el} and Φ_T via the gate-source C_{GS} capacitance of S_T, the voltage at the nanoelectrode follows the drop of Φ_T and gets reduced as well (interval B–C, $T_{BC} = 1$ ns long).
- During the interval C–D, both Φ_T and Φ_D remain low and the nanoelectrode is floating ($T_{CD} = 1$ ns). Its voltage does not change.
- Then, S_D is switched on by making Φ_D high. Due to capacitive coupling between V_{el} and Φ_D via the gate-drain C_{GD} capacitance of S_D, the voltage at the nanoelectrode follows the rise of Φ_D and rises as well (interval D–E). However, as soon as Φ_D rises enough to turn S_D ON, V_{el} gets connected to V_D and the discharge process takes place (interval E–F). The sum of these two intervals (D–E and E–F) is $T_{DF} = 1$ ns long (the rise time of Φ_D).
- During the interval F–G, Φ_D is high and V_{el} is connected to V_D. This phase

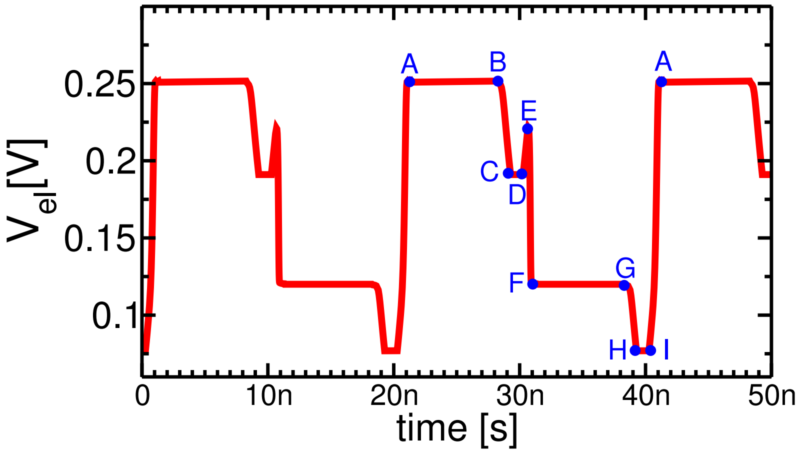

Figure 4.16: *Voltage waveform V_{el} profile as extracted from circuit simulations of Fig. 4.15 at 50 MHz in air. Relevant points of the waveform (at the main discontinuities) are highlighted and labeled. Published in [251].*

is $T_{FG} = 7$ ns long.

- Then, S_D is switched off by lowering Φ_D. Due to capacitive coupling between V_{el} and Φ_D via the gate-drain C_{GD} capacitance of S_D, the voltage at the nanoelectrode follows the drop of Φ_D and gets reduced as well (interval G–H, $T_{GH} = 1$ ns long).
- During the interval H–I, both Φ_T and Φ_D remain low and the nanoelectrode is floating ($T_{HI} = 1$ ns). Its voltage does not change.
- Finally, during the interval I–A S_D is switched on by making Φ_T high. Due to capacitive coupling between V_{el} and Φ_T via the gate-source C_{GS} capacitance of S_T, the voltage at the nanoelectrode follows the rise of Φ_T and rises as well. As soon as Φ_T rises enough to turn on S_T, V_{el} gets connected to V_T and the rise toward V_T continues. This phase is $T_{IA} = 1$ ns long. Then, the process cyclically repeats.

This analysis highlights the impact of another non-ideality of the switches: the presence of gate-source and gate-drain parasitic capacitances C_{GS} and C_{GD}.

When a new row is selected, stabilizing this voltage waveform (i.e. moving from the previously constant voltage value V_{FL} to this cyclic waveform) requires only a few cycles. Reminding that typical experiments can use a large number of cycles N_{cyc} (from ~ 1400 in air down to a few hundred cycles for larger capacitance loads), the initial transient can be neglected and we can focus on this stable V_{el} waveform.

As a third step, we vary the switching frequency f_s and we empirically tune the parameter p_E in order to guarantee that these circuit simulations yield a constant V_T (which means a constant high-level of the waveform during the A–B interval) when we perform the correction of V_G by means of Eq. 4.4. The extracted value is $p_E = 0.854$, in good agreement with the extraction of Fig. 4.3. Operating at different frequencies, for a constant-capacitance medium, only affects the high/low-level phases, namely the A–B and F–G intervals. In fact, independently of the frequency, the relations $T_{BC} = T_{CD} = T_{DF} = T_{GH} = T_{HI} = T_{IA} = 1$ ns always hold. T_{AB} and T_{FG}, instead, depend on the frequency according to $T_{AB} = T_{FG} = 7\text{ns} \cdot 50\text{MHz}/f_s$.

As a fourth step, we repeat these analyses in electrolyte, i.e. using different lumped elements for the electrode-electrolyte block of Fig. 4.15. Fig. 4.17 shows the extracted waveforms at 50 MHz for different electrolytes. For higher salt concentration electrolytes (i.e. higher load capacitance) the shape of the waveform tends to converge toward resembling a square wave, progressively reducing the non-idealities and glitches. This is a hint that regarding the previously discussed switching capacitance model, possible inaccuracies due to assuming a square wave input are progressively less relevant for high-salt concentration electrolytes, because the electrode capacitance dominates w.r.t. the parasitic coupling capacitance.

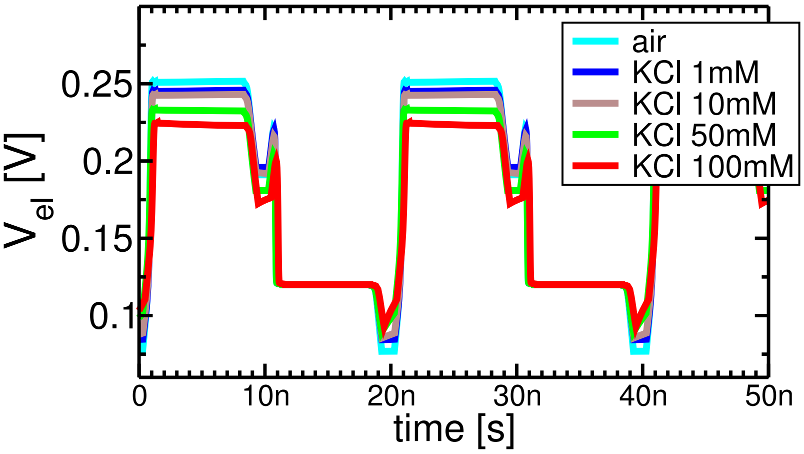

Figure 4.17: *Voltage waveform V_{el} profile as extracted from circuit simulations of Fig. 4.15 at 50 MHz in air (same as Fig. 4.16) and for different electrolyte salt concentrations. Larger load capacitance values (higher salt concentrations) affect the high-level voltage (since pre-calibration does not maintain V_T constant anymore) and the rise, fall, and floating time intervals.*

These waveforms can now be used to compute the Fourier capacitance C_F (Sect. 3.4). To speed up calculations, we approximate all the curves as simplified piecewise-linear waveforms, defined by the 9 points (A–I) highlighted in Fig. 4.16 (that identify the major phase transitions). Fig. 4.18 shows how the voltage level at these points vary with frequency and with the salt concentration of the electrolyte. Points F and G remain fixed at V_D. The voltage at points A to E gets reduced for higher salt concentrations and low frequencies (low frequencies and high salt concentrations result in a higher electrode capacitance), whereas points H and I go in the opposite direction, progressively making the glitches less and less important.

However, while using the predictive technology models lets us extract these qualitative shapes of the waveforms, the confidence on the quantitative values of the different voltage levels is poor. Hence, these waveforms should not be used as they are. To overcome this limitation, by investigating more in depth their properties, we extract the ratios between the voltage amplitude at all the major points of the waveforms and the mean high-level voltage during T_{AB} (V_{AB}) (which in turn is essentially given by the transfer voltage V_T). This is shown in Fig. 4.19, where differences

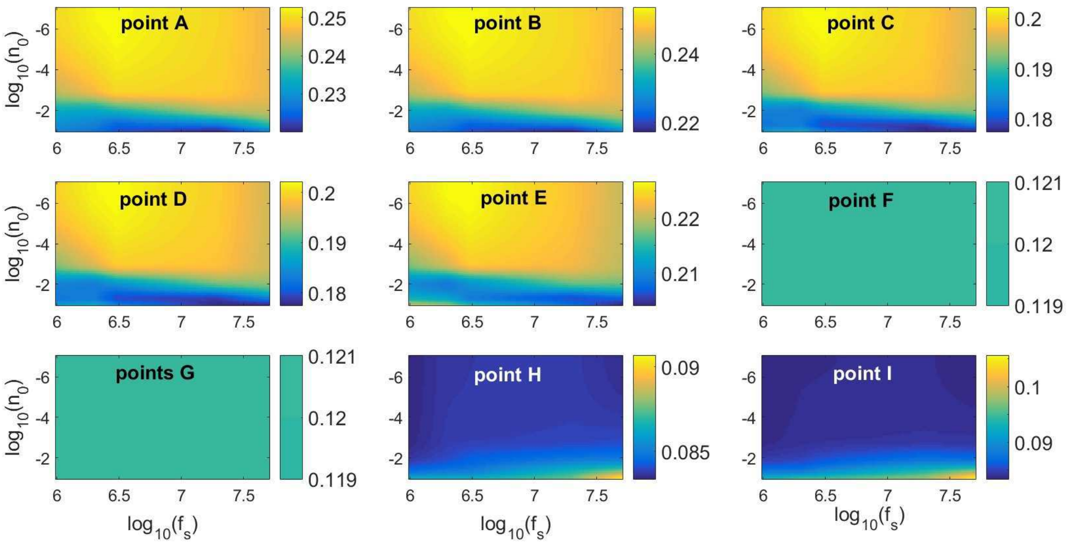

Figure 4.18: *2D maps representing the amplitude of the voltage levels at the main transition points (A–I, as defined in Fig. 4.16) for different frequencies (f_s) and electrolyte salt concentrations (n_0).*

between the ratios, over different frequencies and electrolytes, can be quantified to be at most 10%.

If the actual V_T is known, then all the other voltage values can be easily corrected and defined with greater confidence (provided that the estimation of V_T is correct). To this end, we can employ the post-measurement calibration methodology described in Sect. 4.2. In fact, V_T can be easily extracted from measurements by means of Eq. 4.5-4.10, as reported in Fig. 4.20 (values extracted from the measurements of Fig. 4.6-4.8).

Then, by extracting V_T as in Fig. 4.20, using this information together with the relative amplitudes of the major points in the waveform (Fig. 4.19) to generate the equivalent of Fig. 4.18 for the real experiments, building the corresponding waveforms, and running the algorithm of Sect. 3.4, we obtain the Fourier capacitance C_F that can be compared to experiments (C_{post}) and to the switching capacitance model (C_{SW}). It is worth mentioning that in order to compare the Fourier capacitance to experiments, two approaches are possible.

- One approach consists in calculating the Fourier capacitance in exactly the same way the biosensor platform computes the capacitance from the charge, i.e. $Q_s/(V_{T,E} - V_D)$. This approach entails using the estimated value for the transfer voltage ($V_{T,E}$) instead of the actual one (unknown during measurements). This capacitance can be directly compared to C_M, but not to C_{SW} (as shown in Fig. 4.6). As C_M requires the post-measurement correction to be compared with C_{SW}, the same can be said for the Fourier capacitance computed with the above approach. We can then post-compensate both C_M and C_F (with the same parameters), obtaining a corrected measurement and a corrected Fourier capacitance, which can all be compared to C_{SW}.
- A simpler way consists in calculating the Fourier capacitance employing the

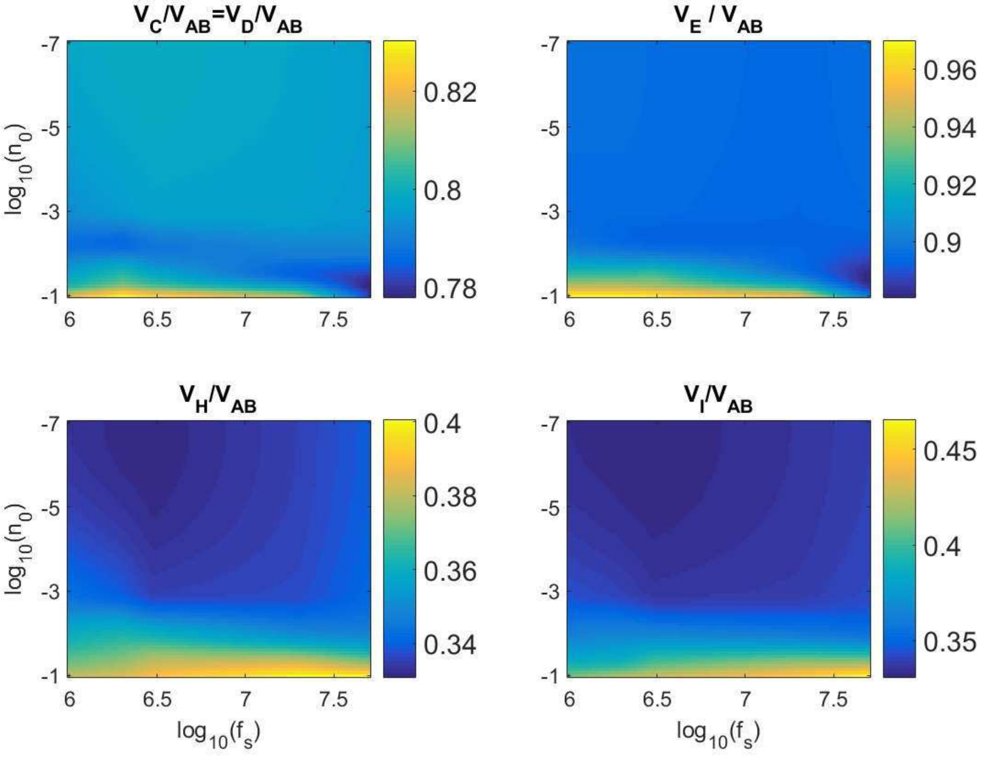

Figure 4.19: *2D maps representing the amplitude of the voltage levels at the main transition points, for different frequencies (f_s) and electrolyte salt concentrations (n_0), normalized by the mean value during the A–B interval (V_{AB}). The values vary by about 5–10% over frequency and for different electrolytes.*

actual value of V_T, instead of the estimated one (V_T is calculated by means of post-measurement calibration of experiments): $C_F = Q_s / (V_T - V_D)$. This capacitance is directly comparable to C_{post} and C_{SW}.

Hereafter, we indicate as C_F the Fourier capacitance computed using either of the above equivalent methodologies, i.e. the Fourier capacitance which is comparable to C_{post}. The result of the comparison between C_{post}, C_{SW} and C_F is finally shown in Fig. 4.21.

The agreement of C_F to measurements in low salt concentration electrolytes (15 mM, 10 mM and minimally also 1 mM) is improved. This is consistent with the fact that possible non-idealities of the input waveform (e.g. the glitches due to parasitic coupling and the finite rise/fall times that are not accounted for by the switching capacitance model) should play a role at low capacitance loads (see Fig. 4.17). Starting from the 15 mM electrolyte, the curves are non-monotonically decreasing, but a maximum and a slight downward bending is observed at lowest frequencies, which get even more evident at higher salt concentrations. This (physically unexpected) behavior reveals that the proposed methodology does not work properly for high load capacitance values (i.e. high-salt concentration electrolytes and at low frequency). We speculate that the reason for this behavior might be in the way V_T is extracted in Fig. 4.20 and due to the fact that estimated waveforms

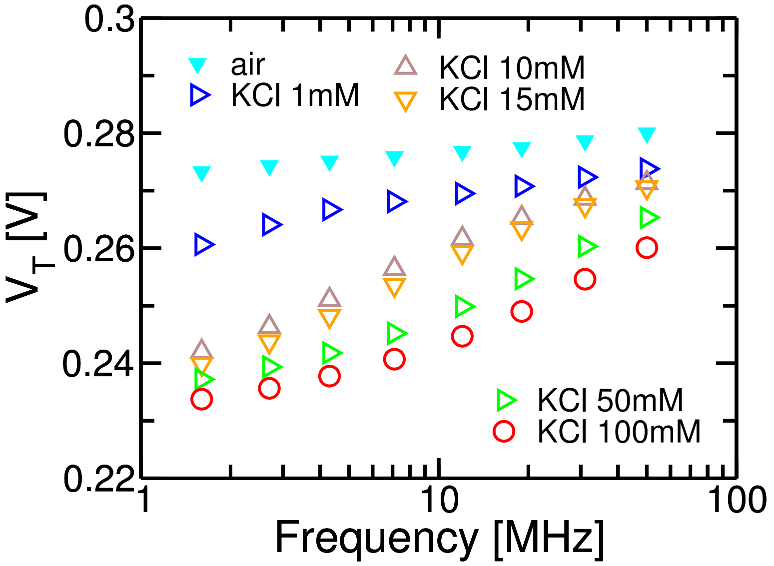

Figure 4.20: *Extraction of* V_T *from experiments by means of the post-measurement calibration technique of Sect. 4.2.*

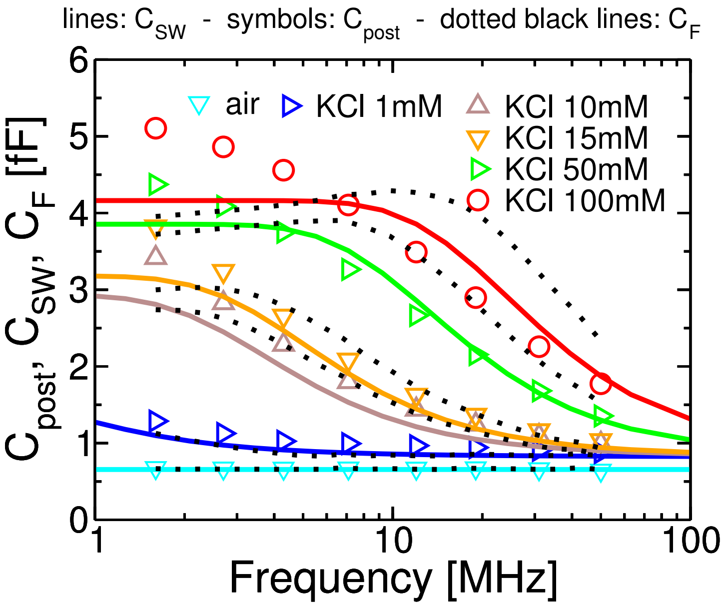

Figure 4.21: *Comparison between post-calibrated measurements* (C_{post}*, symbols), switching capacitance* (C_{SW}*, solid lines), and Fourier capacitance* (C_F*, black dotted lines) in air and 1/10/15/50/100 mM electrolytes.* C_F *slightly improves the matching between simulations and experiments at low salt concentrations, while the agreement gets poorer for the electrolytes at higher salt concentration.*

have been obtained with PTM instead of using the actual circuit. More accurate post-layout circuit simulations of the real system could help in revealing the true impact of the harmonic content of the voltage waveforms at the nanoelectrodes. The discrepancy between experiments and numerical simulations at low frequency and high salt concentrations, then, is not justified by the proposed C_F model either.

4.4.3 Size of nanoelectrodes

The simulations reported in this chapter have been performed using r_{el}=75 nm (and resulted in the parameters of Tab. 3.3), following the early demonstrations of [203, 215]. The residual discrepancies between simulations and experiments are visible especially at low frequency.

To investigate the influence the size of nanoelectrodes has on the C_{SW} curves, we performed ENBIOS simulations at different values of r_{el}. Fig. 4.22 shows the comparison between experiments and families of C_{SW} obtained with different nanoelectrodes radii ($r_{el} = [75, 80, 85, 90]$ nm). For each family of simulations (solid lines), the uppermost curve corresponds to the largest value of simulated radii. While using larger values for r_{el} improves the agreement for the 10 mM and 15 mM electrolytes, the agreement for higher salt concentrations gets progressively poorer. The impact on the 1 mM electrolyte, instead, is minimal (since its dielectric relaxation frequency is overcome).

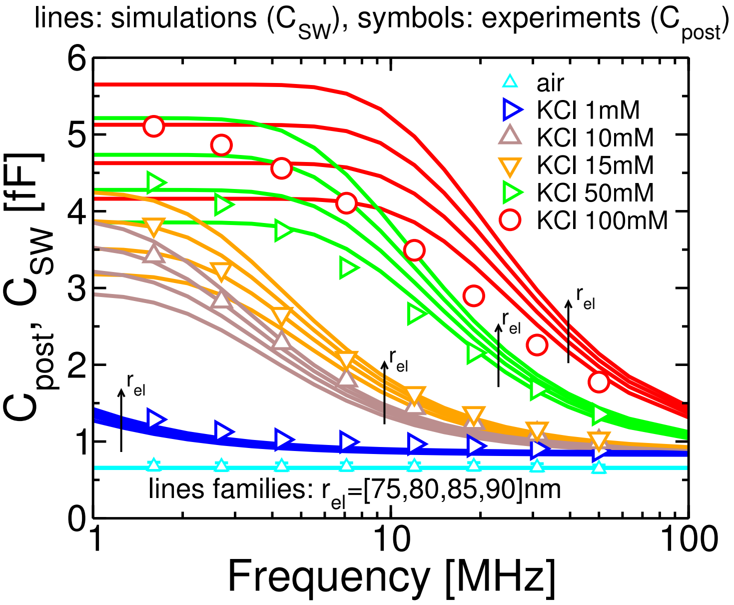

Figure 4.22: *Comparison between post-calibrated measurements (C_{post}, symbols) and switching capacitance (C_{SW}, solid lines) for different values of the radius of nanoelectrodes ($r_{el} = [75nm, 80nm, 85nm, 90nm]$).*

While an accurate estimation of the size of nanoelectrodes is of great importance, the discrepancy between experiments and simulations is not eliminated by changing the radius of nanoelectrodes in simulations.

Methodology to estimate the size of nanoelectrodes

Following the earlier demonstrations of Fig. 2.7, tentative extractions of the size of nanoelectrodes have been performed by means of SEM and AFM measurements, performed in Udine at the Advanced Materials Laboratory – Parco Scientifico e Tecnologico L. Danieli. Fig. 4.23 shows the nanoelectrode images obtained with these experiments.

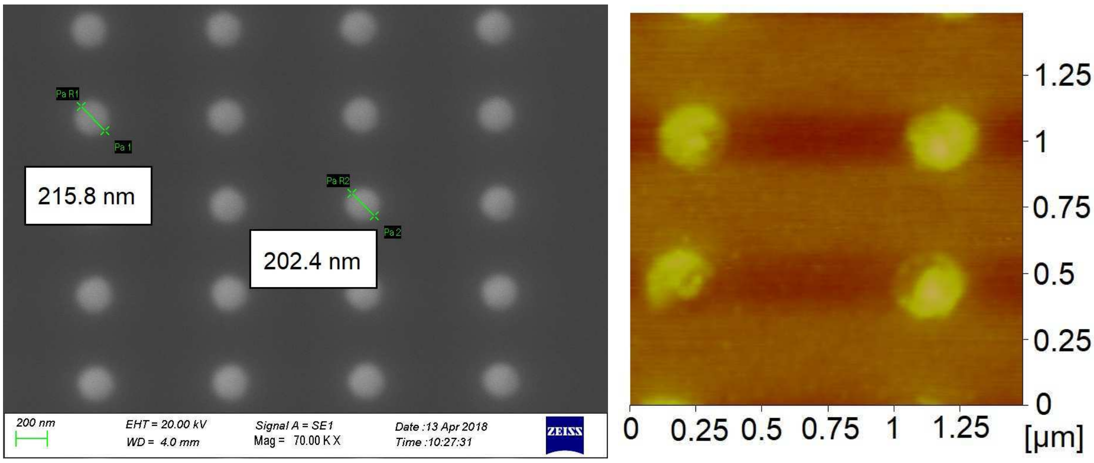

Figure 4.23: *Left: SEM measurement to extract the size of nanoelectrodes. The limited resolution of the microscope does not enable a precise estimation. Right: AFM measurement on the same chip. Horizontal line patterns are measurement artifacts.*

Fig. 4.23 (left) shows that the dimension of electrodes is fairly regular among different rows/columns; however a precise quantitative estimation of their radius was not possible with SEM measurements due to the limited resolution of the equipment. As an alternative approach, Fig. 4.23 (right) shows AFM measurements performed on the same chip (horizontal line patterns are measurement artifacts). While the quantitative accuracy of these last measurements is clearly superior to those in Fig. 4.23 (left), extracting the size of all electrodes of the array by means of AFM measurements is extremely time-demanding and was not a viable option. Therefore, to estimate the size of nanoelectrodes we follow a different approach based on the MCMC Bayesian estimation methodologies.

Sect. 3.6 presented the MCMC methodology to determine the values of physical parameters, together with validation examples on simple reference systems. Here we set the goal of using MCMC estimation procedures to determine the radii of the nanoelectrodes of a real sensor, possibly understanding the reason for variability in the capacitance measurements. The final output results of the subsequent MCMC analyses have been kindly provided by TU–Wien.

We remind that the Bayesian estimation procedure to estimate a vector of parameters q requires a measurement (m) and a model ($g(q)$, analytical or numerical). Experiments at controlled temperature (T=295 K) in IPA ($C_{post,IPA}$) and air ($C_{post,air}$) are considered for the purpose. Air and IPA environments can be described by frequency independent capacitance values, because in the absence of ions the spreading resistance ($1/G_E$) is very large. Since in the real biosensor array an (in principle) unknown parasitic capacitance C_P, essentially independent of nanoelectrode size, adds in parallel to the system (see Fig. 3.11), in the following we use as experimental value the difference between the sensor's response to IPA and air, namely $m = \Delta C_{post} = C_{post,IPA} - C_{post,air}$. By doing so, the dependency on the parasitic C_P is removed from the considered observable quantity. In the following, we restrict the analyses to a small sub-array of 71×31 nanoelectrodes.

Regarding the model for the MCMC estimation, the complex three-dimensional distribution of electric field flowlines in the array cannot be easily described in purely analytical forms; thus, using data from full-3D ENBIOS numerical simulations is mandatory. We use as model the Fourier capacitance model C_F described in Sect. 4.4.2 (which, as discussed, can be considered dependable for low capacitance values, as is the case in IPA and air). In the following, more details are provided to support this choice of using C_F (instead of C_{SW}). By analogy with the measurement quantity, the observable quantity for the model is again the capacitance difference between IPA and air, namely: $g = \Delta C_F = C_{F,IPA} - C_{F,air}$.

The estimation process is split into multiple consecutive steps.

One parameter estimation: average nanoelectrode radius

The first step aims at estimating the ensemble average of the nanoelectrodes radii in the array, i.e. the *mean* radius r_{av}.

From experiments in air and IPA at 50 MHz, a mean capacitance difference ΔC_{post}^{av}=32 aF has been obtained, with an uncertainty of 1 aF (one standard deviation). ENBIOS simulations have been run on a 7×7 array of electrodes at 50 MHz, extracting the capacitance difference (between IPA and air) of the central electrode. Hereafter, we indicate as $r_{enbios,el}^{(i,j)}$ the radius of the electrode in row i and column j of the simulated array ($i, j \in [-3, 3]$). To sample the model function, all the electrodes of every simulation are set to the same (common) size $r_{enbios,el}^{(i,j)} = r_{av}$ ($\forall i, j$), and we swept this (common) value r_{av} between 70 nm and 110 nm.

To motivate the choice of using the C_F model for simulations (instead of C_{SW}), Fig. 4.24 compares ΔC_F and ΔC_{SW} as a function of r_{av}. The corresponding value from experiments is also indicated as a horizontal dashed line. By using the C_{SW} model, a radius of $\approx$ 110 nm would be required to match the experiment. As already shown in Fig. 4.22, radius values greater than 90 nm would imply a great divergence between simulations and experiments. Hence, referring to Fig. 4.24, we consider replying on the red curve not dependable. Differently, the C_F model (green curve) intersects the experimental value for roughly 85 nm. This value is much closer to the nominal one given by the technology (90 nm). This ΔC_F curve has been obtained considering $N_{harm} = 1000$. Using a greater number of harmonics has been tested and yielded essentially identical results.

Based on the average experimental response of the array (m=ΔC_{post}^{av}) and on the ENBIOS model in which we vary the size of all the electrodes at the same time (q=r_{av}, $g\left(q\right)$=$\Delta C_F\left(r_{av}\right)$), the MCMC analysis is performed to determine the posterior PDF of r_{av}.

A uniform distribution on the interval [70nm, 110nm] (large enough to include the true average radius, which is expect to be close to 90 nm) is considered as a prior,

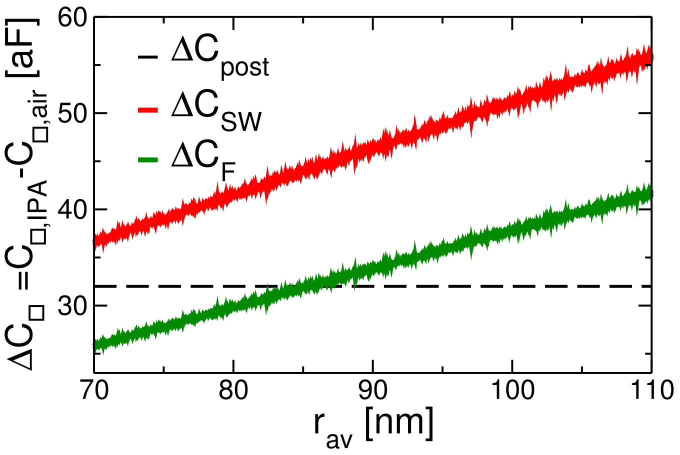

Figure 4.24: *Comparison between* $\Delta C_F = C_{F,IPA} - C_{F,air}$ *and* $\Delta C_{SW} = C_{SW,IPA} - C_{SW,air}$ *as a function of the average radius of the simulated array. All electrodes in simulations have the same size. The horizontal dashed line represents the value extracted from experiments.*

and the chosen number of samples for the MCMC algorithm is $N_{samples}$=10000. An estimation of $r_{av} = 86.6$ nm is obtained from this analysis.

This first step enabled to estimate the average size of nanoelectrodes in the array. The estimated $r_{av} = 86.6$ nm is used as an initial radius for all the following MCMC estimations. The simulated value corresponding to r_{av} is $\Delta C_F(r_{av}) = 32.42$ aF, which confirms the confidence in the estimation, since this value is very close to $\Delta C_{post}^{av} = 32 \pm 1$ aF.

One parameter estimation: individual electrodes radii

In the previous section, the mean radius of the electrodes has been determined, relying on one measurement ΔC_{post}^{av} at 50 MHz. In this section, the size of individual nanoelectrodes is estimated and maps of electrodes radii are generated. The purpose of the analysis is to verify if the assumption that radii fluctuations are the dominant source of variability in individual ΔC_{post} measurements is realistic.

One single parameter at a time is considered: the radius of an individual nanoelectrode of the 71×31 matrix, namely $r_{el}^{i,j}$ (where i and j identify the row and column in the array). The electrode's response ΔC_{post} at multiple frequencies (1-70 MHz) is used as a measurement (m) for the MCMC. Using multi-frequency data is an interesting application of MCMC estimation on real experiments using multi-dimensional measurements (m).

ENBIOS simulations are run by setting all the (7×7) nanoelectrodes radii at $r_{enbios,el}^{(i,j)} = r_{av} = 86.6\text{nm}\ \forall(i,j) \neq (0,0)$, i.e. except the central electrode, whose radius $r_{enbios,el}^{(0,0)}$ is swept from 70 nm to 110 nm (i.e., uniform prior distribution). The model response for MCMC is then the IPA-air capacitance variation at this central electrode of the simulated array, i.e. $g = \Delta C_F\left(r_{enbios,el}^{(0,0)}\right)$. As regards experiments,

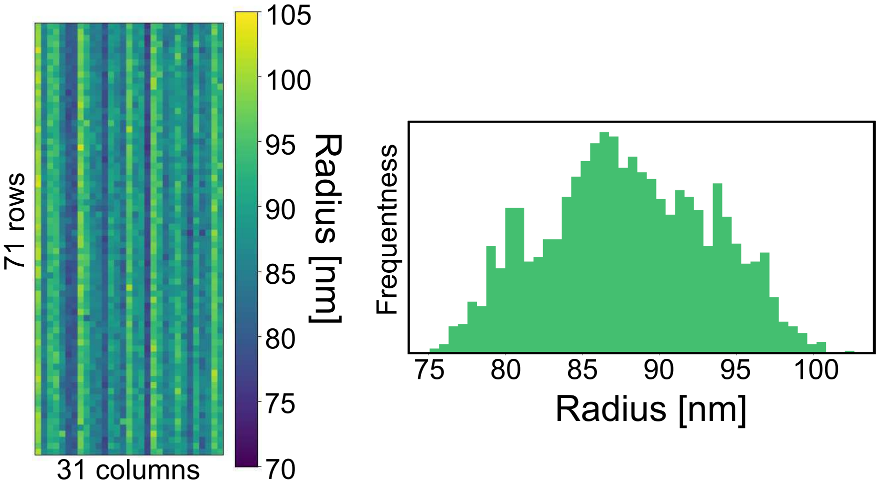

Figure 4.25: *Left: estimated radii* $r_{el}^{(i,j)}$ *for all the electrodes, considering multiple frequencies. ENBIOS simulations have been performed sweeping the size of the central electrode only, keeping all the others at the previously estimated* r_{av} *value. Right: Distribution of the extracted* $r_{el}^{(i,j)}$ *values. Output of MCMC analysis kindly provided by TU–Wien.*

the individual extraction of the radius of a single electrode is iterated for all the 71 × 31 electrodes, at each independent iteration using $m{=}\Delta C_{post}^{(i,j)}$, where $\Delta C_{post}^{(i,j)}$ is the experimental value recorded at the electrode in row i and column j of the 71 × 31 subarray.

By running the MCMC analysis with $N_{sample}{=}2000$ for each electrode, and extracting the mean values of the resulting posterior distributions, a matrix of 71 × 31 estimated radii values $r_{el}^{(i,j)}$ is obtained. The output of this MCMC estimation is reported in colormap form in Fig. 4.25. The results show column wise striped patterns and large spread of individual values (i.e., a broad posterior distribution). Both these features are however unexpected from the advanced fabrication process described in Sect. 2.1.2. A more in-depth analysis is thus performed in the following section.

Nine parameters estimation: radii of groups of electrodes

The estimation carried out in the previous section relied on a model that assumed that all nanoelectrodes except the central one have $r_{enbios,el}{=}r_{av}$. Thus, that estimation accounted for the *average* effect the array has on the response of an individual electrode. However, this approach does not take into account the influence that differently-sized neighbor electrodes might have on the capacitance of one electrode. This relation could be important in view of the asymmetry of the x- and y- pitch of the electrodes and the large spread of extracted values shown in Fig. 4.25.

To overcome this limitation at affordable computational cost, a 9-dimensional Bayesian extraction of the individual electrode radii is performed, extracting the size of the central electrode in small 3 × 3 subarrays. Considering the 71 × 31

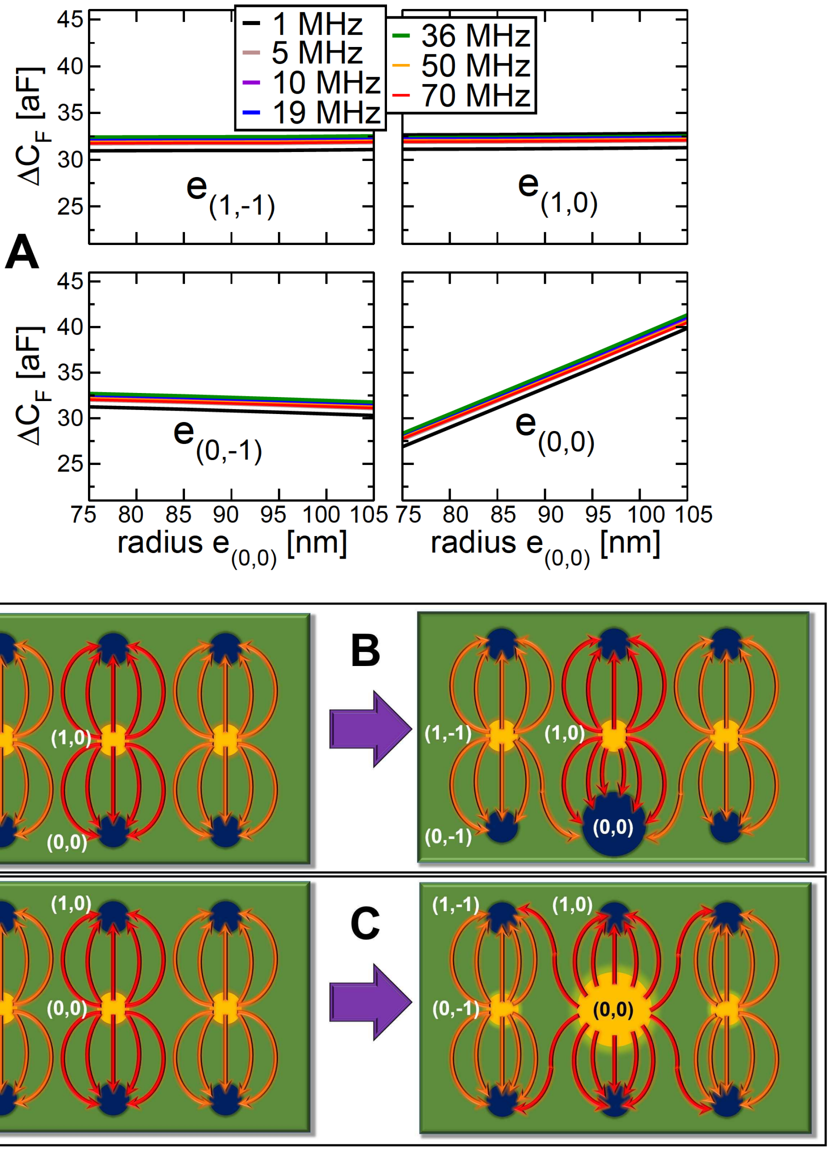

Figure 4.26: *(A): ΔC_F response at four neighboring electrodes at 8 different frequencies. The radius of electrode $e_{(0,0)}$ (lower right) varies between 70 nm and 110 nm, while the other radii stay fixed (at r_{av}). (B): sketch of the configuration of current-flux lines comparing a group of electrodes at nominal dimension (left) to a bigger electrode $e_{(0,0)}$ acting as counter-electrode (right). (C): same as (B), comparing a nominal configuration to a bigger electrode $e_{(0,0)}$ acting as working-electrode. When the row of electrodes $e_{(1,-1)}, e_{1,0}$ is active, the increase in the size of the electrode $e_{(0,0)}$ in the deactivated row (B) results in a small increase of the current flux lines from electrodes $e_{(1,-1)}, e_{1,0}$ to electrode $e_{(0,0)}$, which have a shorter path. When the row of electrodes $e_{(0,-1)}, e_{0,0}$ is active, the increase in the size of the electrode $e_{(0,0)}$ in the activated row (C) results in a great increase of current lines density at electrode $e_{(0,0)}$ itself and shorter current lines path toward the grounded electrodes; at the same time, it hampers the current flux from the neighbor active electrodes $e_{(0,-1)}$ of the same row.*

set of electrodes, the first estimation is performed on $q = r_{el}^{(2,2)}$ (row and column 1 are skipped, since these electrodes, being at the edge of the considered matrix, are not included in any 3×3 subarray) based on the corresponding measurements $m = \Delta C_{post}^{(i,j)}$, where $(1 \leq i \leq 3), (1 \leq j \leq 3)$. Then, to estimate the next adjacent electrode $q = r_{el}^{(2,3)}$, the next 3×3 subarray is considered $((1 \leq i \leq 3), (2 \leq j \leq 4))$, and so on, covering all the measured electrodes and generating a new map of radii which might differ from Fig. 4.25 (left). ENBIOS simulations are run sweeping independently the size of electrodes $r_{enbios,el}^{(i,j)}$ with $(-1 \leq i \leq 1), (-1 \leq j \leq 1)$, from 70 nm to 110 nm, while all other electrodes are kept at the nominal dimension r_{av}. By following this approach, the correlation between the size of one electrode and the response at first neighbor ones is taken into account.[2] Multiple frequencies are considered, as in the previous case.

To highlight the functional dependencies, Fig. 4.26 (A) shows the results of ENBIOS simulations (of the 7×7 array) for a $2{\times}2$ subarray as a function of the size of nanoelectrode number 1. Reminding that nanoelectrodes are excited row by row (see Chapter 2 and Fig. 2.6), the top row in Fig. 4.26 (A) shows the capacitance at electrodes $e_{(1,-1)}, e_{(1,0)}$ when the row of electrodes $e_{(1,-1)}, e_{(1,0)}$ is activated, for different dimensions of electrode $e_{(0,0)}$; the bottom row, instead, shows the capacitance at electrodes $e_{(0,-1)}, e_{(0,0)}$ when the row of electrodes $e_{(0,-1)}, e_{(0,0)}$ is activated, for different dimensions of electrode $e_{(0,0)}$. The capacitance of electrode $e_{(0,0)}$ increases linearly with the electrode radius. In fact, the larger the nanoelectrode, the less the spreading resistance to the current flow. The capacitance of the first neighbor on the same column (electrode $e_{(1,0)}$) has a barely visible increase as well: looking at Fig.4.26 (B), an increase of the size of electrode $e_{(0,0)}$ increases the current at electrode $e_{(1,0)}$ (when $e_{(1,0)}$ is active, and hence when we measure its capacitance), since the current flux lines have a shorter path. However, this increase is minimal, since other electrodes are present that, at the same time, contribute to the current sinking in the larger electrode $e_{(0,0)}$. The same discussion applies to electrode $e_{(1,-1)}$.

Differently, the capacitance of the first neighbor on the same row (electrode $e_{(-1,0)}$) decreases. This behavior can be understood looking at Fig.4.26 (C) and again reminding that nanoelectrodes are excited row by row. When electrode $e_{(0,0)}$ is active, electrode $e_{(0,-1)}$ is active as well. The increased size of electrode $e_{(0,0)}$ results in an increased density and broadening of its current flux lines, which partially obstruct the current flux lines originating from the neighbor electrode $e_{(0,-1)}$, thus reducing its AC current and capacitance. On top of that, the pitch of the nanoelectrodes array along the $x-$ and $y-$ directions is asymmetrical (600×720 nm); hence, electrodes on the same row affect each other more than neighbor electrode on the same column can do.

This analysis of the model function obtained by ENBIOS simulations confirms the correlation between the size of one nanoelectrode and the capacitance reading at neighbor electrodes, especially those along the same row. Hence, the simultane-

---

[2] It is worth pointing out that the hypothesis of having IID errors, as introduced with Eq. 3.20, still holds. While an error in the estimation of the size of one nanoelectrode could possibly affect the capacitance (and hence the size estimation) of a neighbor electrode (see Fig. 4.26), the errors η_i of Eq. 3.20 should be IID referring to successive measurements of the same quantities (e.g. successive measurements at the same electrode should yield IID errors).

ous estimation of electrodes dimensions taking into account the neighbor electrodes appears as mandatory. Using the measurements for the 71×31 subarrays described above and implementing an uniform prior distribution for the 3×3 subarray on $[70 \text{ nm}, 110 \text{ nm}]^9$, equivalent to the 1D uniform prior used previously, the results of the nine-parameter approach can be compared to those obtained with the 1D approach. Radii estimations are performed with $N_{samples} = 10^4$. Comparing this 9-dimensional approach with the one-dimensional approach of the previous section, the resulting map of radii With the 9-dimensional approach, the resulting map of radii is similar to Fig. 4.25 (left). Differences, induced by the cross-correlation between neighbor electrodes, are limited to ±2 nm, which is a small number compared to the huge spread in the data shown in Fig. 4.25. These results suggest that the inter-electrode correlation cannot justify the spread and, since the latter is large given the production-class technology used for the fabrication, we conclude that fluctuations of the r_{el} value cannot fully explain the variability of capacitance measures. The readout circuitry is thus identified as an important source of variability for this sensor implementation.

4.5 Final remarks

Fig. 4.27 shows the result of a numerical fitting of the *switching capacitance* model on the post-calibrated measurements. While fitting procedures allow to reduce the disagreement between the experiments and the model, and to extract the values of the model's lumped elements, these purely-numerical optimizations lack a physically-based understanding of the experiments. Furthermore, residual discrepancies are still present: this is especially true at high salt concentrations (green and red curves) where the slope of the capacitance drop is not well reproduced.

At the end of these analyses, we are convinced that the remaining discrepancy between the experiments and simulations most likely is not the consequence of an incorrect relation between the switching capacitance, as modeled by C_{SW} or C_F, and the actual measurement capacitance of the nanoelectrode, but of a real physical effects, such as electrode surface roughness.

At high frequencies and/or low salt concentrations, the EDL capacitance is less dominant, and the nanoelectrode capacitance is governed, via the much lower spreading capacitance C_E, by its geometrical shape. However, at low frequencies and/or high salt concentrations, the EDL capacitance becomes dominant (because C_E is short-circuited by the spreading resistance R_E). Then, the EDL capacitance, and therefore also the nanoelectrode capacitance, is governed by the effective electrode area (including nm-scale roughness on a scale larger than the Debye screening length). Because the effective area is larger than the geometrical area, the low-frequency capacitance is higher than expected for a perfectly flat electrode. This effect, which increases with decreasing frequency, explains the positive offset of measurements from simulations. However, because the chip was designed and optimized for sensing beyond the EDL at high-frequencies, larger discrepancies and spread at low frequencies are less relevant for the intended applications. Identifying the root cause of the discrepancies and larger variations at lower frequencies goes beyond the scope of the present work and will be the subject of further investigations.

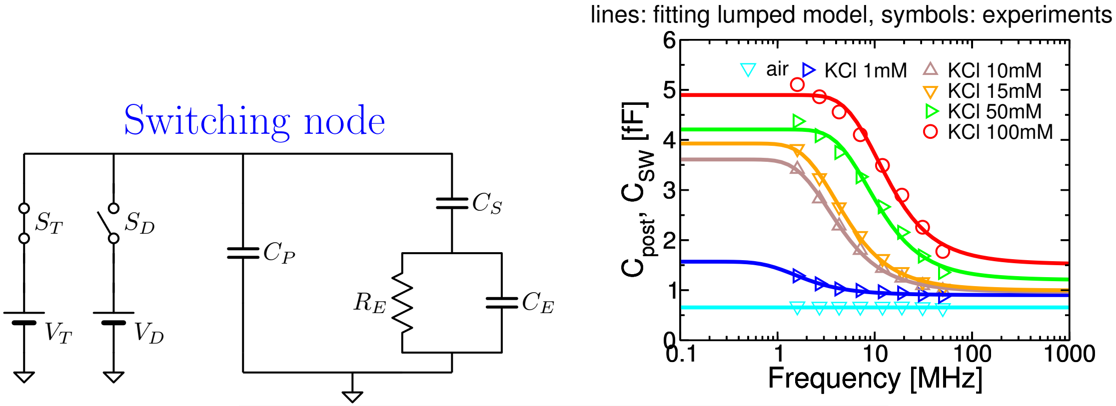

Electrolyte	C_S **[fF]**	C_E **[fF]**	R_E **[MΩ]**
1 mM	0.9194	0.3469	122.4268
10 mM	2.9598	0.3510	20.9158
15 mM	3.2786	0.3843	16.2456
50 mM	3.5593	0.6547	6.5513
100 mM	4.2465	1.0899	4.0688

Figure 4.27: *Fitting of post-calibrated measurements (C_{post}) with a switching capacitance model based on a C-RC circuit topology. Left: schematic representation of the switching cell for the lumped elements model. Right: comparison between post-calibrated (C_{post}) capacitance measurements and switching capacitance (C_{SW}) calculated on the C-RC circuit topology, fitting the values of the lumped elements to the experiments. Bottom: values of the lumped elements obtained by numerical fitting of the extended switching capacitance to experiments.*

The possible physical effects involved in the residual discrepancy between experiments and simulations can be modeled up to arbitrary accuracy with more complex and complete lumped element circuits. Indeed, if a more complex lumped element model is used to fit the data (e.g. a C-RC-RC circuit, as shown in Fig. 4.28 left, on which we can perform extended switching capacitance calculations as presented in Appendix A.2), that accounts for the possible coexistence of more than 2 time constants (e.g. because of surface-roughness-induced small local changes of capacitance and resistance), then the residual errors in Fig. 4.7 can be eliminated. In Fig. 4.28 (right) we compare C_{post} to the switching capacitance C_{SW} calculated on the C-RC-RC circuit, by fitting the lumped elements on the experimental data (the table in 4.28 reports the numerical values of the extracted parameters). This fitting was purely numerical, without including any physically-based constraint on the parameters (one example could have been to set $R_2 = R_E$ and $C_2 = C_E$, allowing only the other parameters to change). A perfect fitting is obtained, proving that three cells (C_S, $C_1//R_1$, $C_2//R_2$) are enough to reproduce the functional behavior of experiments, especially the decay profile from the low- to the high-frequency limit values which is much slower in the experiments than in the discussed simulation models.

The fitting methodology allows us to determine the lumped element parameter values for a given model (e.g., C-RC or C-RC-RC). Once these elements are

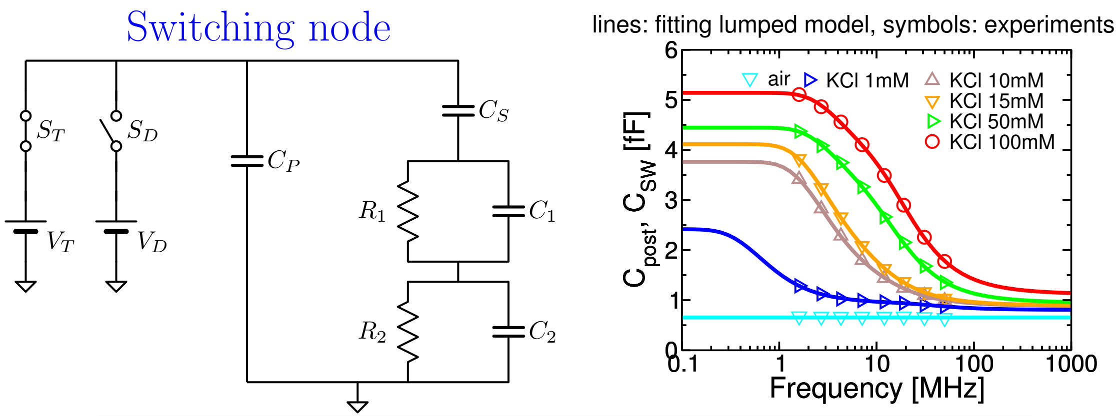

Electrolyte	C_S **[fF]**	C_1 **[fF]**	R_1 **[MΩ]**	C_2 **[fF]**	R_2 **[MΩ]**
1 mM	1.7669	0.3582	164.7515	0.3296	9.2442
10 mM	3.1127	3.4203	7.5730	0.2709	14.8712
15 mM	3.4648	5.6173	5.4565	0.2744	12.3889
50 mM	3.7956	0.3323	5.1970	11.8896	3.3453
100 mM	4.4900	0.5410	3.1758	15.5089	2.3562

Figure 4.28: *Fitting of post-calibrated measurements (C_{post}) with a switching capacitance model based on a C-RC-RC circuit topology. Left: schematic representation of the switching cell for the extended lumped elements model. Right: comparison between post-calibrated (C_{post}) capacitance measurements and switching capacitance (C_{SW}) calculated on the C-RC-RC circuit topology, fitting the values of the lumped elements to the experiments. Bottom: values of the lumped elements obtained by numerical fitting of the extended switching capacitance to experiments.*

extracted, the real and the imaginary part of the resulting admittance can also be computed, in an attempt to reconstruct information about the actual complex admittance of the system for the measurement of the real (scalar) values of the switching capacitance as a function of the frequency. The trustworthiness of the calculated real and imaginary parts of the admittance obtained from the lumped element circuit is strongly related to the confidence we have on the extracted parameters and, inherently, on the validity of the chosen equivalent circuit model. Lacking the possibility to run complete and accurate time dependent and small signal simulations of the actual physical system and to compare the AC and switching capacitance as possibly measured by a quadrature detector and by the CBCM detector, it is not possible to exactly determine the relation between C_{AC} and C_{SW}, nor the actual accuracy of the reconstructed real and imaginary parts of the nanoelectrode admittance as obtained from C_{SW} via the lumped element circuit model. Still we can attempt to get some clue about how sensitive the extraction of the real and imaginary part of the admittance is on the choice of the circuit model by comparing the real and imaginary parts of the admittance as obtained by the C-RC and the C-RC-RC models. Fig. 4.29 shows such a comparison. In particular, we consider the difference between the real (imaginary) part of the admittance extracted from the C-RC circuit and the real (imaginary) part of the admittance extracted from the C-RC-RC circuit, and we divide this difference by the latter quantity. The

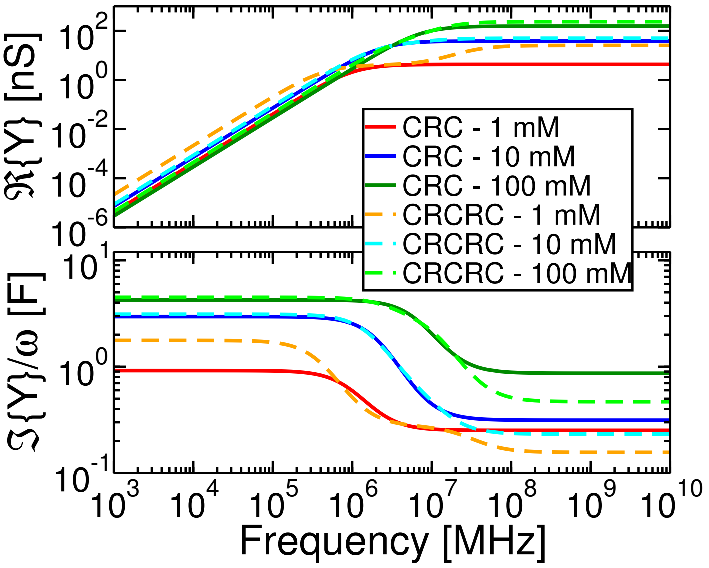

Electrolyte	$\left\lvert\frac{\Re\{\mathbf{Y}_{(\mathrm{CRC})}\}-\Re\{\mathbf{Y}_{(\mathrm{CRCRC})}\}}{\Re\{\mathbf{Y}_{(\mathrm{CRCRC})}\}}\right\rvert$	$\left\lvert\frac{\Im\{\mathbf{Y}_{(\mathrm{CRC})}\}-\Im\{\mathbf{Y}_{(\mathrm{CRCRC})}\}}{\Im\{\mathbf{Y}_{(\mathrm{CRCRC})}\}}\right\rvert$
1 mM	79%	36%
10 mM	23%	29%
15 mM	22%	34%
50 mM	28%	53%
100 mM	31%	47%

Figure 4.29: *Top: spectra of the real and imaginary parts of the admittance resulting from the fitting problem based on the C-RC model (Y_{C-RC}, see Fig. 4.27) and the fitting problem based on the C-RC-RC model ($Y_{C-RC-RC}$, see Fig. 4.28). Bottom: maximum relative difference, within the experimental frequency range (1-50 MHz), between the admittance resulting from the C-RC and the C-RC-RC models. The comparison is performed separately for the real and imaginary parts of the admittance.*

table reports the maximum value of these relative differences, for the different electrolytes, within the frequency range of the measurements (i.e. 1-50 MHz). The relative differences are lower than 100% for all electrolytes. A closer look at the real and imaginary part versus frequency as extracted above shows that even out of the band used for the extraction (up to 2 orders of magnitude below the minimum frequency and 2 orders of magnitude above the maximum frequency) the discrepancy is not enormous. While these results cannot be considered a definite proof of the possibility to determine the real and imaginary parts of the electrode admittance from the switching capacitance versus frequency via a suitable equivalent circuit (as would be possible via the Kramers-Kronig relations if $\Re\{Y\}$ or $\Im\{Y\}$ were known at all frequencies), they suggest a methodology to extract a plausible approximation to $\Re\{Y\}$ and $\Im\{Y\}$ corroborated by the resemblance of the switching to the AC capacitance of the system already shown in Fig. 3.12. Such resemblance is by itself grounded in the Physics-based topology of the equivalent circuit model adopted to translate the C_{SW} into a C_{AC}. The adoption of even more accurate and strongly physically-based lumped element circuits should provide even better results provided the corresponding measurements respect the small signal operating condition implicitly assumed by the methodology.

If parameters vary over time, the capability to fit experimental switching-capacitance spectra to estimate the model parameters depends on the time-scale of these variations. If the variations are slower than the time required to collect a full switching-capacitance frequency spectrum, then the fitting of the parameters can be performed for each electrode and for each subsequent frequency-scan.

Obviously, being able to fit the measurements with a more complex RC model is not equivalent to understanding the reason for the deviations at low frequencies unless each element of the new circuit has a solid Physics-based justification. Consequently, in the following we will not rely on the C-RC-RC model.

4.6 Summary

This chapter presented HFIS experiments and simulations in electrolytes, together with the calibration procedures required to improve the quantitative reliability of measurements.

As discussed in Chapter 2, the transfer voltage (V_T) of the nanoelectrodes is not directly controllable. Consequently, variations of operating conditions (namely, switching frequency and load capacitance) can shift its value from the intended set point, generating systematic errors in the calculation of capacitance. To account for this phenomenon, calibration procedures have been developed.

We first inspected the frequency dependence of V_T. Considering constant capacitance mediums (e.g. air), a *pre*-measurement calibration can be performed by correcting V_G (hence, indirectly, V_T) as a function of the switching frequency. This correction compensates for the most dominant source of variations of V_T and indeed yields flat frequency spectra for constant-capacitance mediums.

Then, we considered the dependence of V_T from the load capacitance. Electrolytes do not have flat capacitance spectra, and the pre-measurement calibration does not compensate for this further capacitance-dependent variations of V_T. Since, in general, the load ambient is not known *a-priori*, we developed a *post*-measurement compensation of the variations of V_T. Starting from the measurement capacitance, the actual value of V_T during measurement could thus be derived and the capacitance reading be corrected. We also demonstrated that a wrong estimation of V_T in the calculation of the original measurement capacitance does not have any influence.

Model parameters for this correction differ among different columns of the array, since different columns are connected to different column read-out circuits. Hence, the first step before any measurement consists in running experiments (in dry) to estimate these parameters for each column, so that the post-measurement compensation can be applied separately to each nanoelectrode of each column.

Comparing corrected experiments to numerical simulations (based on the switching capacitance model) resulted in an unprecedented agreement between measurements and simulations, over a broad range of switching frequencies and electrolyte salt concentrations.

Possible root causes for residual discrepancies (occurring especially at low frequency and high salinity) have been explored. In particular, we investigated the presence of leakage currents (due to sub-threshold conduction of deactivated transistors) and demonstrated that they indeed have an impact on the measurements, but of small amplitude. Then, we employed the methodology described in Sect. 3.4 to analyze the response of the platform to more realistic input waveforms. Circuit simulations using Predictive Technology Models allowed to estimate the actual shape of the waveform at the nanoelectrode. This analysis allowed to improve the agreement between simulations and experiments for low salt concentrations, while being inadequate for higher salinity values. Finally, the influence of the size of nanoelectrodes has been investigated, and MCMC analyses (as introduced in Sect. 3.6) have been employed to extract nanoelectrodes radii maps from experiments. The results suggested that variability of measured capacitance maps is not fully explained by fluctuations in the radius of electrodes, hence identifying the column readout circuitry as an important candidate for future parameter estimation analyses.

Remaining discrepancies between experiments and simulations are under investigation.

The author's contributions to this chapter include the calibration experiments and analyses in dry, the ENBIOS simulations in electrolyte, the application of post-measurement calibration procedures (on experiments performed by the University of Twente) and subsequent analyses/comparison with simulations, the analyses on residual sources of errors (together with the development of the extended C-RC-RC switching capacitance model), the new experiments demonstrating the reproducibility and imaging capabilities, and the simulations for parameter estimations.

5 High Frequency Impedance Spectroscopy and Imaging of Analytes

The previous chapter reported measurements in homogeneous media and showed how an increase of the permittivity of the medium in contact with the nanoelectrode surface during wetting of the array induces a capacitance change. This simple experiment is useful to develop quantitative calibration procedures, but it is of limited interest for applications. Additional experiments of detection and imaging of analytes have been reported in [190, 209] to demonstrate the ability of the chip to detect admittance changes originating from small entities located further from the surface (in particular beyond the electrical double layer) and to further show the imaging capabilities of the platform. In particular, the detection capabilities include dielectric characterization (e.g. droplets in milliQ water) and beyond, since the platform allows to identify also conductivity properties and charge states, as will be further discussed in the present Chapter.

The purpose of this chapter is firstly to report experimental results from our activity and carried out by partner groups in Europe (University of Twente) and then to perform in depth analyses of the measurements, providing methodologies to assist the design of experiments and to aid the interpretation of the results. In particular, Sect. 5.1 is devoted to discussing analyte size estimation problems, considering the test case of oil emulsions in milliQ water reported in [209], and generating correction curves to conveniently estimate the droplets dimensions from measurements at the nanoelectrodes. Sect 5.2 shows experiments and analyses with dielectric and conductive microparticles. Experiments with SiO_2 microparticles are performed to present evidence of the sedimentation process, the formation of agglomerates of particles, the possible unbinding of the analytes from the surface of the array, and the application of MCMC techniques to estimate particles geometry and dielectric properties. Then, extensive analyses based on numerical simulations provide new insights into the HFIS response to conductive particles. Finally, Sect. 5.3 presents analyses of nanoparticles, determining the spatial dependency of their response and the detection limits of the platform.

The discussion will focus on the single particle detection/characterization problem. Among the possible ways the target analytes can reach the sensor's surface, we focus on sedimentation (for the bigger analytes) and on the application of BSA as analyte capture layers (to immobilize the smallest analytes, which experience Brownian motion). While adding selectivity features is certainly possible with this sensor (e.g. by means of functionalizations of the sensor's surface [342]), these analyses are not addressed in the present work.

The investigations reported in this chapter benefited of fruitful discussions with F. Widdershoven (NXP Semiconductors) and S. G. Lemay (University of Twente). C. Laborde (University of Twente) performed part of the experiments reported in this chapter. We acknowledge also M. Anese and M. C. Nicoli (University of Udine) for support with in-house experiments in liquid, and C. Heitzinger's group (TU-Wien) for running the MCMC calculations. The contents of this chapter are partly published in [190, 209], partly included in journal papers under preparation.

5.1 Oil droplets

As a simple starting point to study the response of the biosensor platform of Chapter 2 to analytes, large (micrometer-sized) analytes in milliQ water, i.e. in the absence of ions and EDLs, are considered. These reference conditions are chosen because the absence of EDLs allows to image objects far from the electrodes while floating in the medium and, furthermore, makes the analyses simpler (because the system response can be modeled by a reduced circuit with essentially one capacitance and one resistance), and µm-sized analytes enable to highlight and exploit the imaging capabilities of the platform.

Oil emulsions in water are considered for the purpose. Experiments performed by the University of Twente with *ortho*–dichlorobenzene ($C_6H_4Cl_2$) droplets (1% v/v) proved the imaging capabilities of the platform [209], see Fig. 5.1. Oil droplets

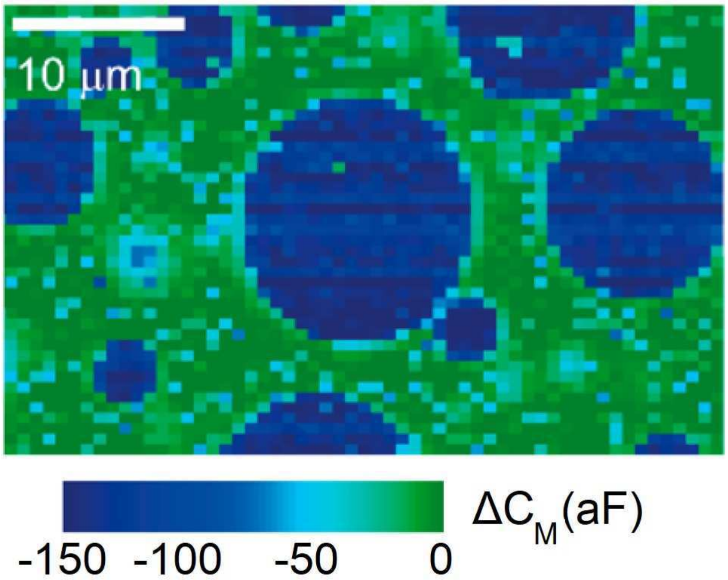

Figure 5.1: *ΔC_M maps of emulsions of inhomogeneous ortho-dichlorobenzene droplets (1% v/v) in milliQ, at 50 MHz. Measurements performed by University of Twente. Image taken from [209].*

suspended in water have an essentially spherical shape. Upon reaching the surface of the array, the shape changes: the droplet wets the surface and spreads on it, reaching a new equilibrium state with larger in–plane extension and lower thickness (along the z–direction), as determined by the surface tension and contact–angles between the droplet and the surface [343]. Also the spread along the x- and y-directions appears anisotropic, perhaps partly due to the uneven x and y spacing of the electrodes.

A potential application offered by the nanoelectrode array biosensor platform is the determination of contact angles between the array surface and droplets. This could be done by performing these subsequent operations [344]:

- A measurement before the wetting of the array surface: the droplet has a spherical/ellipsoidal shape, and the goal of this measurement is to determine the total volume of the droplet;

- A measurement after the wetting of the array surface: the droplet footprint (the projected area) can be determined from the response at the electrodes (see for instance the big blue circle at the center of Fig. 5.1).

- By volume conservation, the thickness/height of the droplet after the wetting are estimated and, consequently, the contact angle can be calculated [343].

From the description of the problem above, the correct estimation of the volume of the droplet before the wetting appears as a key enabling factor to perform the subsequent calculations and prove the micro/nano-scale metrology capabilities enabled by the platform. The goal of this section is thus to analyze and compare possible approaches to estimate the size of a (nearly) spherical *ortho*–dichlorobenzene droplet in water. The presented methodologies can be applied also to different objects. Size estimations based on the MCMC Bayesian approach of Sect. 3.6 will instead be used in the next section for dielectric microparticles in electrolyte (where the presence of more model parameters and uncertainties, such as the electrolyte salt concentration and the properties of the EDL, requires the use of more advanced approaches).

For the purpose, extensive analyses by means of ENBIOS simulations have been performed. Two approaches are discussed to estimate the radius of a spherical object (hereafter denoted as “apparent radius”, r_{app}) based on the response at multiple nanoelectrodes. By virtue of the knowledge of the “real radius” in simulations (r_p), *correction curves* are generated to map an estimated r_{app} on the real value r_p. Here it is implicitly assumed that the particle is spherical. This is reasonable given the images in [209]. Furthermore, the electrode response is to first order proportional to the particle volume, which is $\frac{4}{3}\pi r_p^3$ for a sphere and $\frac{4}{3}\pi abc$ for an ellipsoid (a, b, c being the length of the semi-axes along the three Cartesian directions). Therefore, the particle radius should be interpreted as an effective mean geometrical radius $r \approx \sqrt{abc}$.

Similarly to Fig. 3.2, Fig. 5.2 shows again a schematic layout of the nanoelectrodes in the simulation domain in the presence of a spherical particle, where (row,column) = (0,0) corresponds to the nanoelectrode nearest to the analyte under investigation, and (row,column) $\neq$ (0,0) correspond to adjacent nanoelectrodes.

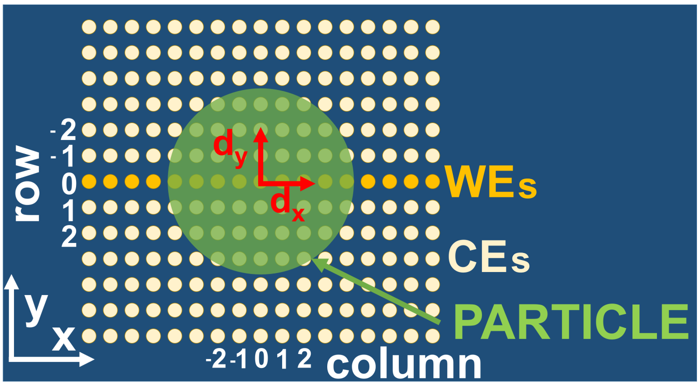

Figure 5.2: *Schematic layout of the nanoelectrodes in the simulation domain in presence of a spherical analyte. The AC signal is applied to an entire row of nanoelectrodes (row 0 in this sketch), and the AC currents of all individual nanoelectrodes of the active row (the working electrodes: WEs) are divided by the applied AC voltage to determine their AC admittances. All other nanoelectrodes are AC-grounded, effectively turning them into a single large counter electrode (CE). The response of a generic electrode* $e_{(i,j)}$ *is thus determined by activating the corresponding row* i*.*

Unless otherwise stated, the following simulations assume r_{el}=90 nm, p_x=600 nm, p_y=890 nm, n_{rows}=25, n_{cols}=35, $d_x = d_y$ =0 nm, d_z = 40 nm, r_p=2.5 µm, $\varepsilon_p = 9.9\varepsilon_0$ (i.e. the permittivity of *ortho*–dichlorobenzene). The quantitative results are thus specifically related to this sensor's version (pitch 600 × 890 nm) and to this specific analyte permittivity ($9.9\varepsilon_0$, i.e. *ortho*-dichlorobenzene). Adapting the parameters of the following simulations for different chips/analytes is possible. Due to the essentially flat frequency spectrum of milliQ (such as in other dielectric materials, as air or IPA), the results are presented for a single switching frequency of f_s=50 MHz.

5.1.1 Determination of droplet size: squared distance weighting

The first methodology to estimate r_{app} is expressed in Eq. 5.1, as originally used in [215]:

$$-r_{app}^2 = \frac{\sum_i \sum_j \left[(j \cdot p_x - d_x)^2 + (i \cdot p_y - d_y)^2\right] \Delta C_\square(i,j)}{\sum_i \sum_j \Delta C_\square(i,j)} \tag{5.1}$$

where the minus sign is introduced to make $r_{app}^2 > 0$, since capacitance variations $\Delta C_\square$ (hereafter ΔC_{eff}) for dielectric analytes in water are always negative (hence the overall right-hand side term is always negative). This is because by replacing a region originally occupied by water (high–permittivity) with a dielectric (lower permittivity) the current flow is reduced, and so is the measured capacitance.

In Eq. 5.1, the response at each nanoelectrode ($\Delta C_{eff}(i,j)$) is multiplied by the squared distance between the projected center of mass of the particle (d_x, d_y) and the electrode itself. The projected center of mass of the particle (d_x, d_y), known *a–priori* in simulations, can be easily extracted from experiments as:

$$(d_x, d_y) = \frac{\sum_i \sum_j \left[(j \cdot p_x \hat{x}) + (i \cdot p_y \hat{y})\right] \Delta C_M(i,j)}{\sum_i \sum_j \Delta C_M(i,j)} \tag{5.2}$$

The particle elevation, d_z, is in principle unknown. However, due to the fact that Eq. 5.1 includes a normalization by the total amount of ΔC_{eff} recorded at the considered electrodes and the absence of a strong d_z dependence (no EDL), the impact of small differences in d_z is expected to be small.

To address this point, Fig. 5.3 (left) shows the ΔC_{eff} values recorded at different electrodes on row $i = 0$ in the presence of a droplet at d_z=10 nm or d_z=40 nm. As expected, the configuration with smaller d_z yields the larger capacitance variation. Normalizing the response by the max value (i.e. $\Delta C_{eff}(0,0)$), as in Fig. 5.3 (right), yields essentially overlapping curves, with the d_z=10 nm curve (blue) being only slightly lower than the d_z=40 nm (red) one. Size estimation based on Eq. 5.1 should then yield similar results for these two configurations (possibly a slightly larger estimation for the d_z=40 nm case, since the response at the first neighbor is higher w.r.t. the central electrode compared to the d_z=10 nm case). In fact, estimation of a droplet with r_p=2.5 µm based on Eq. 5.1, considering a simulated array of 11 × 15 electrodes, yields r_{app}=1.93 µm for the d_z=10 nm case and r_{app}=2.01 µm for the d_z=40 nm case, i.e. only 4% relative difference among the two heights but ≈ 20% difference w.r.t. the real value.

Since Eq. 5.1 weights the response of each electrode by its squared distance from the particle, following the first analysis of Fig. 5.3 (left), it appears necessary to understand the functional dependence of the decay of the response in the electrodes'

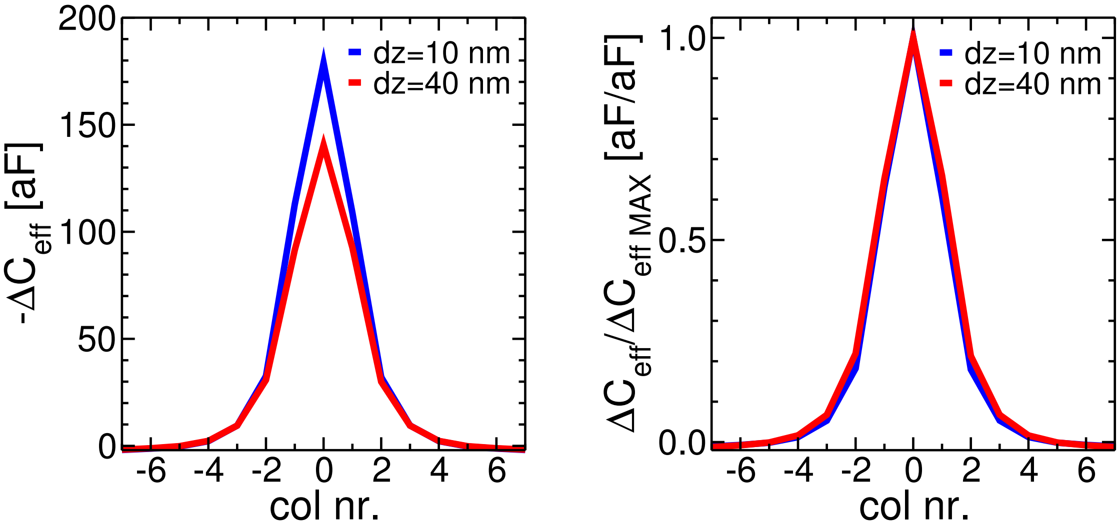

Figure 5.3: *Left: ΔC_{eff} recorded at different electrodes on the same row ($i = 0$), due to inserting an ortho-dichlorobenzene droplet with radius r_p=2.5 µm in milliQ on top of the central electrode $(d_x, d_y) = (0,0)$ at different vertical elevations. Right: same as left, normalized by the maximum (i.e. the response at the central electrode). Simulations performed on a $n_{rows} \times n_{cols} = 11 \times 15$ electrodes array.*

plane (i.e. at different electrodes for instance of the same row). In fact, the functional dependence of this decay on distance determines the appropriate weighting factor. Fig. 5.4 compares ΔC_{eff} at different electrodes (on the same row $i = 0$) to different extrapolated decay profiles of the response. Decay profiles with the following functional dependency are considered for this purpose:

$$\Delta C_{eff}(0, j) = \Delta C_{eff}(0, 0) \frac{k}{(j \cdot p_x)^{\alpha}} \tag{5.3}$$

thus, possible decays along the $x-$direction as $\sim 1/x$, $\sim 1/x^2$, $\sim 1/x^3$, ... are investigated. It should be noted as well that the lateral decay could be a function of d_z. Here we used:

$$k = \frac{\Delta C_{eff}(0, 1)}{\Delta C_{eff}(0, 0)} p_x^{\alpha} \tag{5.4}$$

i.e., the decay from the central electrode to the first neighbor is used to extrapolate the decay profiles.

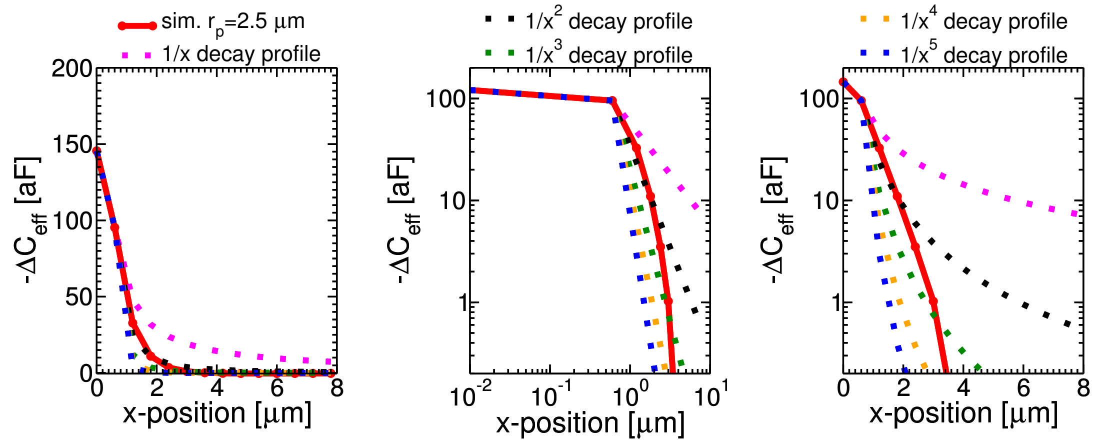

Figure 5.4: *Comparison between ΔC_{eff} at different electrodes along one row and different extrapolated decay profiles $\sim 1/x^{\alpha}$. Left: linear plot. Center: log-log plot. Right: semilog-y plot. The elevation is d_z=40 nm.*

From Fig. 5.4, it appears evident that the response does not simply decay as a power of the inverse of the distance from the particle. While on short distance is reasonable, at larger distance, instead, the decay is asymptotically faster than the fixed exponent power law. As an alternative extrapolation, Fig. 5.5 compares ΔC_{eff} at different electrodes (on the same row) to an exponential expression for the decay:

$$\Delta C_{eff}(0, j) = \Delta C_{eff}(0, 0) \exp\left(-k\left(j p_x\right)^{\alpha}\right) \tag{5.5}$$

where

$$k = -\frac{1}{p_x^{\alpha}} \log\left[\frac{\Delta C_{eff}(0, 1)}{\Delta C_{eff}(0, 0)}\right] \tag{5.6}$$

i.e., the decay from the central electrode to the first neighbor is used to extrapolate the decay profiles. Hence, possible decays along the $x-$direction as $\sim e^{-x}$, $\sim e^{-x^2}$ are investigated.

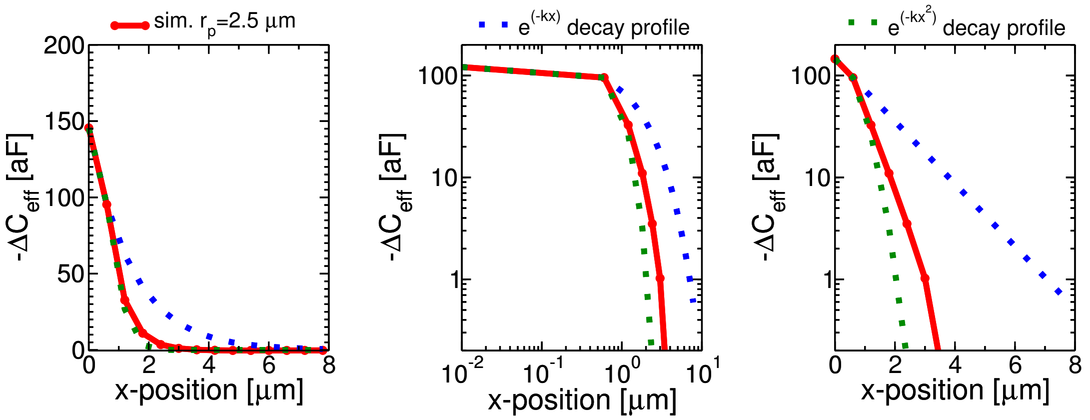

Figure 5.5: *Comparison between ΔC_{eff} at different electrodes along one row and different decay profiles $\sim e^{-x^{\alpha}}$. Left: linear plot. Center: log-log plot. Right: semilog-y plot.*

These analyses give a hint that the chosen estimation approach (i.e. weighting the electrodes by the squared distance) is not physically-based, since the response is instead more similar to a $\sim e^{-r^2}$ functional dependency for larger distances. Consequently, Eq. 5.1 gives more weight than it should to electrodes far away from the analyte: this implies that the size estimation is lower than the true value (as will be demonstrated in Fig. 5.8) and is also possibly be more susceptible to noise (as discussed in the following of this section).

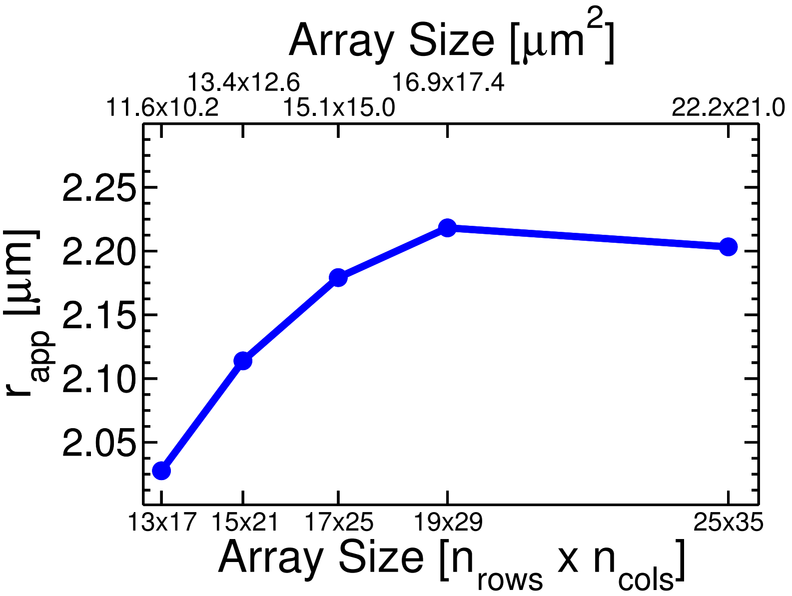

Figure 5.6: *Apparent size estimation (Eq. 5.1) of a r_p=2.5 μm o-dichlorobenzene droplet in milliQ as a function of the size of the simulated array. The simulation domain has to be sufficiently large.*

Choice of the array size

The discussed size estimations corresponding to Fig. 5.3 considered an array with $n_{rows} \times n_{cols} = 11 \times 15$ electrodes and r_p= 2.5 µm. To inspect what arrays are large enough for a given r_p, Fig. 5.6 shows the size estimation (r_{app}) as a function of the size of the simulated array (both the number of rows/columns and the physical x/y dimensions of the array are indicated). From this plot it appears mandatory to use a sufficiently large number of electrodes, such that the response reaches a sort of saturation for large array sizes.

The outermost rows/columns of the simulated array, however, should not be taken into account for the calculations of the apparent size. In fact, their response is affected by the proximity of the simulation boundaries.

To further inspect the dependency of the size estimation obtained with Eq. 5.1 from the number of electrodes used for the calculation, Fig. 5.7 shows how r_{app} changes as a function of the number of electrodes considered, both for r_p=2.5 µm (top) and for a r_p=4.4 µm (bottom). The plot is constructed as follows. Five different array sizes are considered (from 13×17 to 25×35). For each simulated array (for each curve), the estimation of r_{app} is performed using only the K electrodes which are closest to the particle (i.e. which are closest to the center of the array, $e_{(0,0)}$). This value, K, is the x–axis of the plot. Hence:

- For $K = 1$, the estimation is performed using only the central electrode $e_{(0,0)}$. A sub–array with size 1×1 is thus considered.
- For $K = 3$, the estimation is performed considering the central electrode ($e_{(0,0)}$) and the first two neighbor electrodes on the same row ($e_{(0,-1)}$ and $e_{(0,+1)}$; since $p_x < p_y$ these electrodes are closer to $e_{(0,0)}$ than the electrodes on the same column). Hence, a sub–array with size 1×3 is considered.
- For $K = 9$, the estimation is performed considering the central electrode and its surrounding eight electrodes ($e_{(i,j)}\ \forall i, j \in \{-1, 0, 1\}$). Thus, the considered subarray is 3×3.
- ... and so on, where at each step the previous subarray is extended along the rows or columns (depending on the distance from the center).[1]
- At the end, for $K = n_{rows} \times n_{cols}$, all the electrodes are taken into account.

The constraint of selecting only the K closest electrodes implies that, for instance, while both a 3×15 and a 5×9 sub–array yield a total number of 45 electrodes, only the latter is considered (which correspond to a more "squared" shape of the sub–array, whereas the former has a more distorted aspect ratio of the considered rows/columns). The size of the considered sub–arrays is explicitly indicated in Fig. 5.7.[2]

---

[1] As examples: after 3×3 it comes 3×5, because the intra-columns pitch is smaller than the intra-row pitch; after 3×5 it comes 3×7, and not 5×5, because the distance from the center to the outermost columns in the 3×7 array is smaller than the distance from the center to the outermost rows in the 5×5 one, due to the different intra-electrode pitch values.

[2] It is worth highlighting that configurations with an equal number of rows and columns (such as 5×5, 7×7, 9×9) never occur due to the asymmetry between the $x-$ and $y-$pitch.

As expected, considering the same sub-arrays yield the same estimation for all the simulation domains, provided that the outermost electrodes (the last two columns and two rows at each side) are neglected (each curve has tails, on the upper side of the plot, which deviate from the common trend). It can thus be inferred that the two outermost rows/columns induce deviations from the expectations and hence, for the calculations of Eq. 5.1, rows $\pm[(n_{rows}-1)/2,\ (n_{rows}-1)/2-1]$ and columns

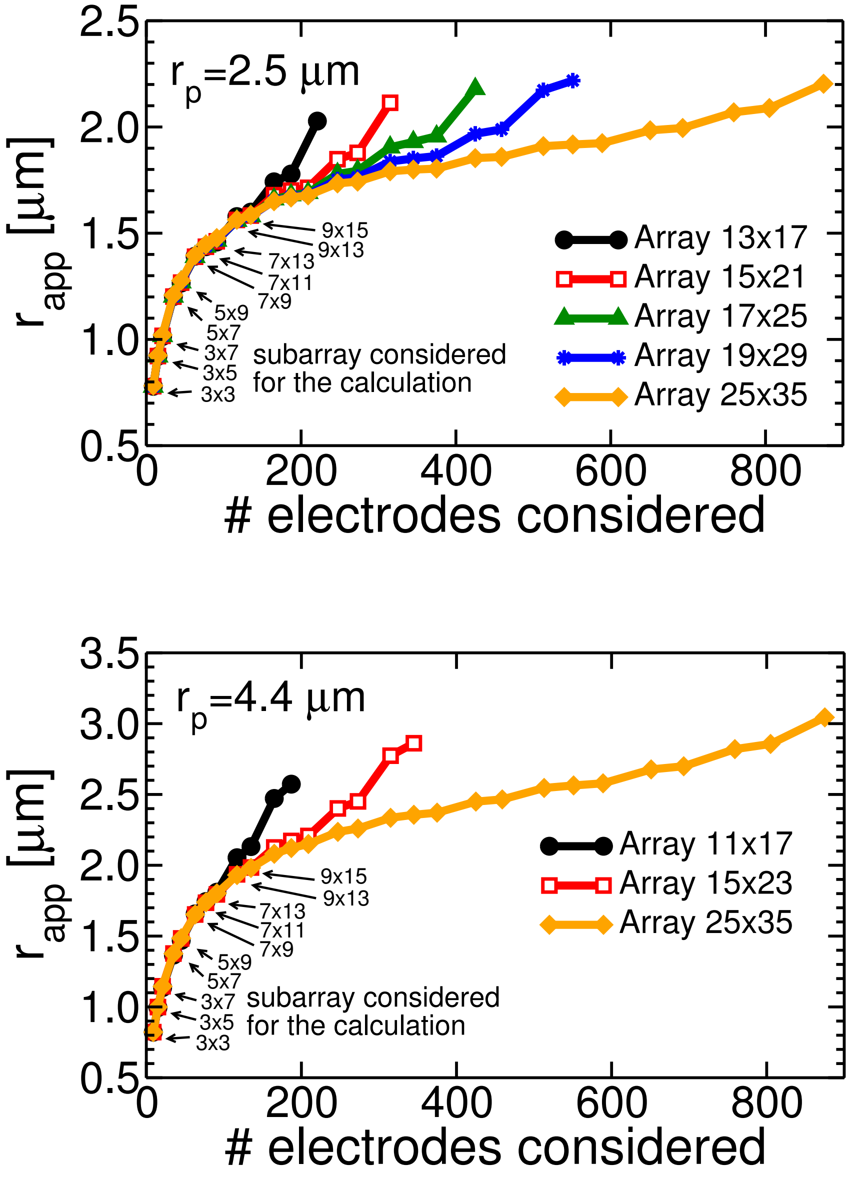

Figure 5.7: *Apparent size estimation (Eq. 5.1) of a r_p=2.5 µm (top) or r_p=4.4 µm (bottom) o-dichlorobenzene droplet in milliQ as a function of the total number of electrodes considered for the calculation of Eq. 5.1 (a number of k considered electrodes refers to the k electrodes closest to the particle, i.e. closest to the center of the simulation domain). Different size of the simulated array are shown.*

$\pm[(n_{cols}-1)/2,\ (n_{cols}-1)/2-1]$ have to be discarded. Consequently, to estimate the size of the analyte by taking into account the response of $N \times M$ electrodes, simulations have to be performed using an array large, at least, $(N+4)\times(M+4)$ electrodes. Unless otherwise stated, in the following calculations are reported considering 25×35 electrodes.

Generation of the correction curves

After these considerations, a dependable $r_{app} - r_p$ correction curve can finally be generated from Eq. 5.1 used in [215]. Fig. 5.8 shows the correction curve (black dashed line) obtained by means of Eq. 5.1, considering all electrodes (apart from the outermost rows/columns, as per above discussion), i.e. both the ones which are closest to the analyte and yield a large response, and the ones which are far away and yield a lower response. A nearly straight line is obtained, with a small deviation toward the lowest r_p values. As predicted in the above analysis, this curve stays below the ideal line $r_{app} = r_p$, i.e. Eq. 5.1 underestimates the size of the object. Considering the unavoidable presence of measurement noise, thresholds can be used to rule out those electrodes whose response is not sufficiently large compared to

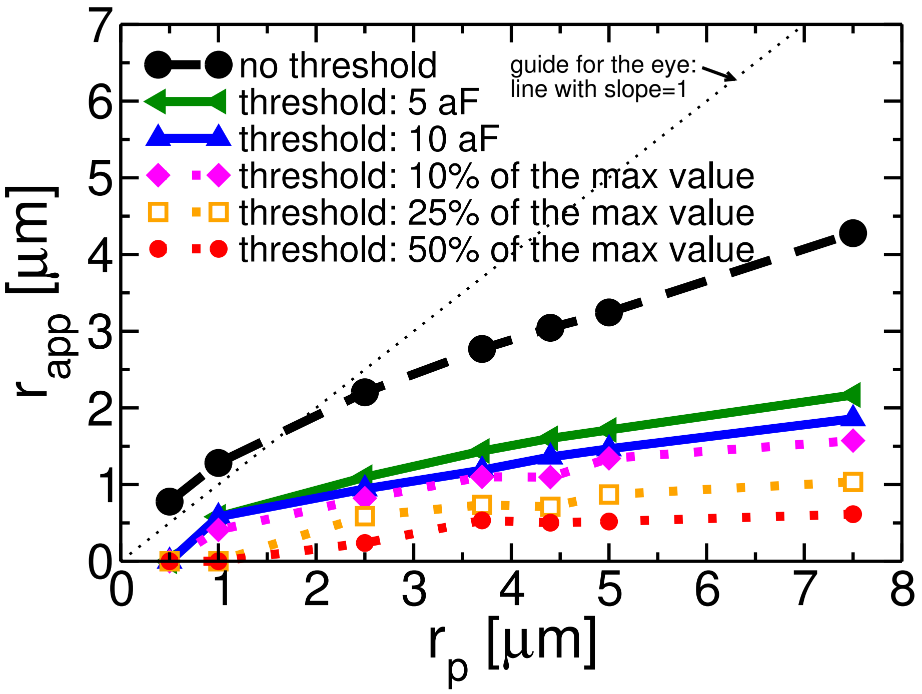

Figure 5.8: *Correction curve to derive the real size of a particle/droplet (r_p) based on its apparent size (r_{app}), computed with Eq. 5.1. Including thresholds (i.e. neglecting the electrodes whose response is lower than the threshold) the apparent size gets smaller (since a lower number of electrodes is considered). If the threshold cuts out all electrodes but the central one (e.g. for small particles), the apparent size drops to zero. Examples of corresponding fitting equations of these curves (1st order polynomial fitting, neglecting the first point in r_p=0.5 µm) are* $r_{app} = 0.9899 + 0.4514 \cdot r_p$ *for the black curve,* $r_{app} = 0.3446 + 0.1774 \cdot r_p$ *for the magenta curve.*

background noise.[3] Examples of the impact that the introduction of such thresholds (absolute and relative w.r.t. the maximum value of the response, i.e. the response at $e_{(0,0)}$) can have on the correction curve are shown in Fig. 5.8. As expected, for higher thresholds the number of discarded electrodes grows and hence r_{app} decreases for a given r_p. Thresholds higher than the response at the first neighbor electrodes ($e_{0,\pm1}$), as happens for the smallest analytes, result in considering only $e_{(0,0)}$ for the calculation, consequently obtaining $r_{app} = 0$ (Eq. 5.1 requires to use more than one single electrode).

Accounting for statistical noise

Due to the prominent relevance of noise in measurements of low capacitance changes, as those induced by nanoscale objects, we reconsidered the curves of Fig. 5.8 and how they are affected by randomness. To this end, an Additive White Gaussian Noise (AWGN), with standard deviation σ_N, is superimposed on the ΔC_{eff} response of the electrodes of the array (independent and uncorrelated noise at the different electrodes), and the calculation r_{app} is repeated in the presence of this noise for a total number of 10^4 iterations. The mean value and the standard deviation of the set of 10^4 estimations are then calculated and plotted in the form of correction curves. The resulting curves in the presence of noise are reported in Fig. 5.9, where the mean value of the r_{app} estimations are shown, together with the standard deviation (error bars). Given that the maximum value of ΔC_{eff}, at the central electrode, spans from 95 aF to 160 aF for the smallest r_p=0.5 µm and the largest r_p=7.5 µm, respectively, noise levels of $\sigma_N = 1/5/10/60$ aF are considered.

If the threshold is sufficiently larger than the noise level (e.g. blue and cyan curves) the correction curves are essentially the same as in Fig. 5.8 (in the absence of noise). For larger noise levels and using the same threshold value, the estimation is larger (see for instance blue, red and green curves). This is simply explained considering that, for a fixed threshold, the higher the noise, the higher the probability of having some pixels exceeding the threshold (thus contributing to the summation term of Eq. 5.1). A peculiar feature of the correction curves in the presence of large noise (w.r.t. the threshold) is the flattening for low r_p values which can even end up in a non-monotonic behavior.

Applying thresholds, however, is in general not enough. In the presence of noise, the outlier electrode capacitance values (i.e. those that are above threshold simply due to a large value of noise) have to be removed. This topic will be addressed in the next section, where a different technique to extract the size of the analytes is also proposed.

As a final remark, we remind that the approach of Eq. 5.1 requires multiplying the response of the electrodes by a factor of r^2 (r being the distance from the center of mass of the analyte) to compensate for the drop in the response at larger distances. However, this approach is not 100% physically-based, since the response does not

---

[3] We recall that ΔC_{eff} is negative for dielectric particles. Hence, for this specific problem, the threshold should to be defined as a negative number as well and the condition to be satisfied to consider an electrode is $\Delta C_{eff}(i,j) >$ threshold. For the generality of the algorithm, hereafter we indicate the thresholds as positive numbers, whose sign is adjusted according to the sign of the response of the analyte.

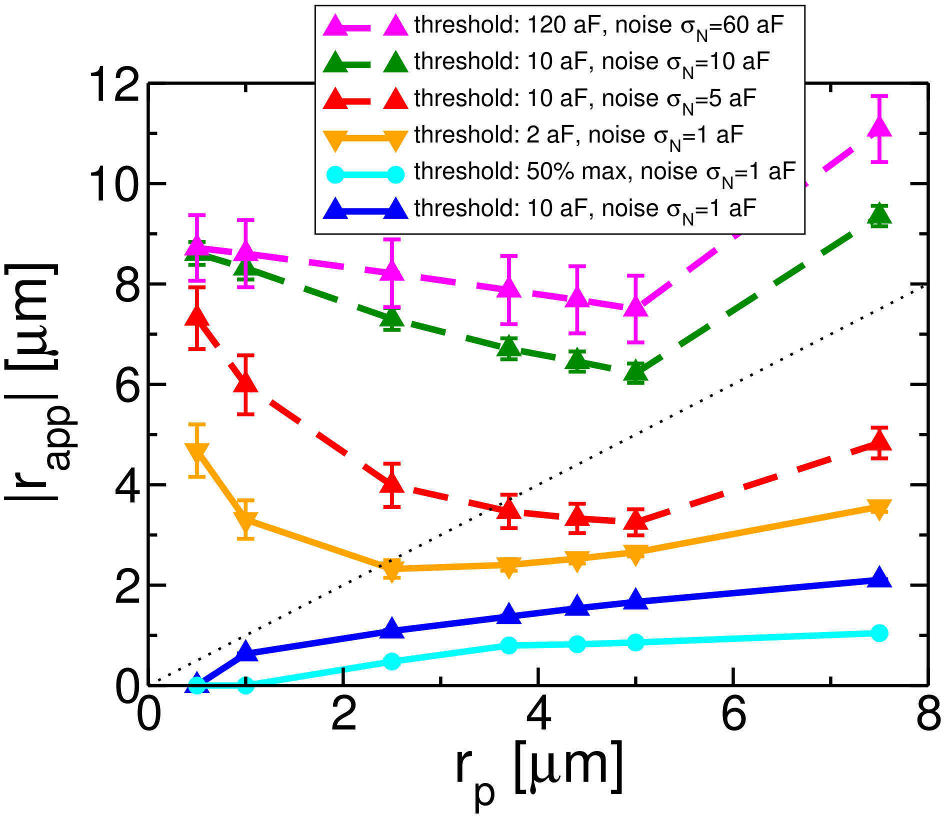

Figure 5.9: *Same as Fig. 5.8, including an AWGN of amplitude* $\sigma_N = [1, 5, 10]$ *aF.*

decay as $\sim 1/r^2$ up to arbitrary distances, but only in an approximate way and up to limited distance. For these reasons, a different approach is investigated in the following section.

5.1.2 Determination of droplet size: digitalized projected area

As an alternative approach, we consider a digitalization of the ΔC_{eff} spatial maps and an estimation of r_{app} based on the calculation of the in–plane projected area of the analyte. The algorithm works as follows:

1. Each electrode is a pixel, whose physical area can be calculated simply as $A_{pixel} = p_x \cdot p_y$.

2. A threshold $\Delta C_{eff,threshold}$ is defined.

3. The 2D map of the response at the electrodes is digitalized: pixels exceeding the threshold are set as ON, the others are set as OFF (in this case $\Delta C_{eff} < \Delta C_{eff,threshold}$, since ΔC_{eff} and $\Delta C_{eff,threshold}$ are negative values for dielectric particles).

4. A weight w_i is assigned to each pixel (both the ON and the OFF pixels).

5. The weights are used to convert, for each pixel (i), its physical area into an *effective* area $A^{eff}_{pixel,i} = w_i A_{pixel}$.

6. The projected area of the object is calculated as the sum of the effective areas of the pixels:

$$A_{object} = \sum_{i=1}^{N_{pixels}} A^{eff}_{pixel,i} \tag{5.7}$$

7. The radius is estimated from the projected area as $r_{app} = \sqrt{A_{object}/\pi}$.

The methodology to define the effective area of each pixel is based on analyzing the status (ON or OFF) of the other neighbor pixels [324, 345]. The approach is sketched in Fig. 5.10. Each pixel can be considered as being part of four possible 2-by-2 pixel sets. Each one of these four sets is given a weight, and the total weight of the pixel is calculated as the sum of the weights of the four 2-by-2 neighborhoods it belongs to. For a given 2-by-2 set of digitalized pixels, there are six possible scenarios, whose corresponding wrights are:

- All the pixels are OFF → weight=0;
- Only one pixel is ON → weight=1/4;
- Two adjacent pixels are ON → weight=1/2;
- Two diagonal pixels are ON → weight=3/4;
- Three pixels are ON → weight=7/8;
- All four pixels are ON → weight=1;

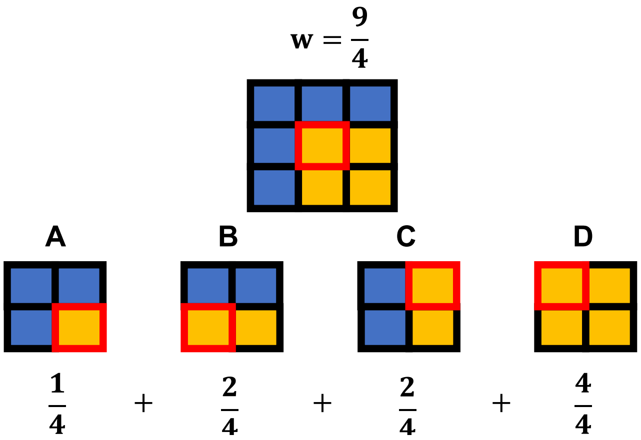

Figure 5.10: *Schematic example for the calculation of the weight of a pixel in the projected area algorithm. Blue pixels have* $-\Delta C_{eff} < -\Delta C_{eff,threshold}$ *and have been digitalized to "0"; yellow pixels have* $-\Delta C_{eff} > -\Delta C_{eff,threshold}$*, hence a digitalized value of "1" (remember that in this test case* ΔC_{eff} *are negative numbers). The central pixel in the top sketch (highlighted in red) can be considered as part of four different* 2×2 *sub-arrays (A-D, bottom). The sub-array A does have only 1 active pixel out of 4: its weight is* $1/4$*. The sub-arrays B and C do have 2 active pixels out of 4: their weight is* $1/2$*. The sub-array D has 4 active pixels out of 4: its weight is 1. The total weight of the central pixel of the top sketch is thus* $w = 1/4 + 1/2 + 1/2 + 1 = 9/4$.

An example of calculation is shown in Fig. 5.10 (examples of simulated capacitance maps will be shown later, e.g. in Fig. 5.12). Without weighting, every ON pixel would have the same importance. Differently, these weights assign more importance to the pixels belonging to clusters of ON patterns, likely belonging to the core of the in-plane projection of the analyte. A remarkable example of the impact of the weights is the following. In the absence of a weighting, an isolated OFF pixel within a cluster of ON pixel is neglected, while an isolated ON pixel within a cluster of OFF pixel is taken into account. However, isolated pixels in real experiments are likely due to local noise and should be considered as outliers. The weighting algorithm takes this into account and tries to dump its most obvious anomalies. In fact, according to the algorithm above, an OFF pixel within a cluster of ON pixels has a weight equal to $4 \cdot \frac{7}{8} = 7/2$ (since it belongs to four 2-by-2 neighborhoods with 3 ON pixels), i.e. nearly as high as an ON pixel surrounded by only ON pixels (which has the maximum possible weight, 4). This example suggests that the algorithm can be very robust to noise fluctuations and possibly yield better results than the previous correction curves for small values of r_p.

Fig. 5.11 shows the correction curves that are obtained by using this algorithm. Nearly straight lines are obtained, with a very small curvature. The slope is close to 1 whenever a sufficiently large number of pixels is retained in the digitalized image. As was done for the previous methodology, also in this case the impact of noise is investigated.

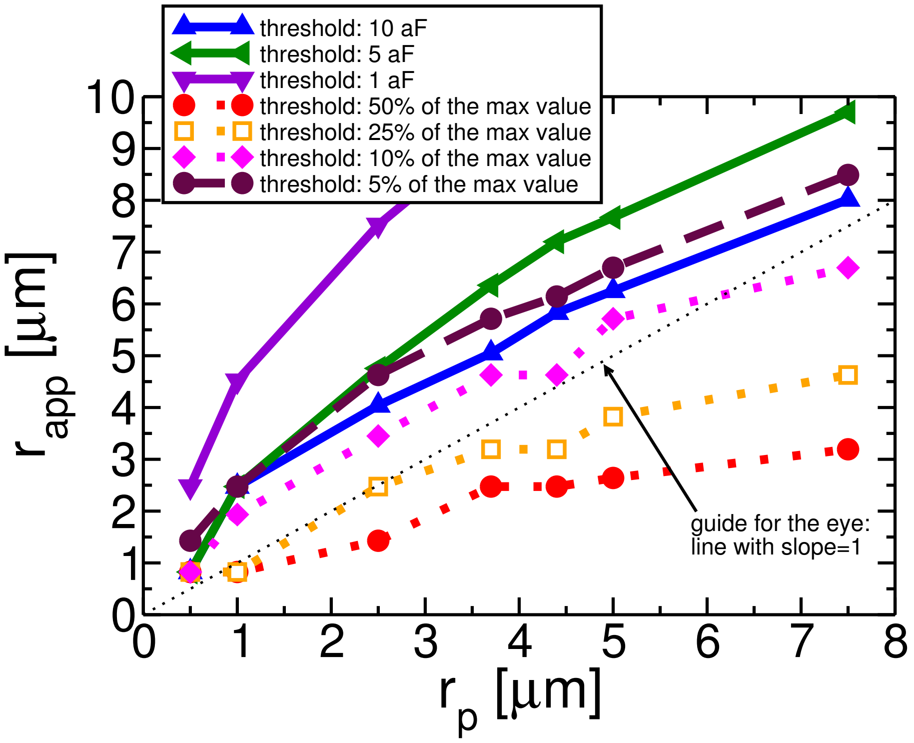

Figure 5.11: *Correction curve to derive the real size of a particle/droplet (r_p) based on its apparent size (r_{app}), computed with the algorithm of Sect. 5.1.2.*

Accounting for statistical noise

We use the same approach discussed above to investigate noise. In particular, AWGN is added to the simulated data and 10^4 Monte Carlo analyses are run. In addition, we test the effect of pruning outlier ON pixels. In particular, all the ON pixels which do not have a direct connection (by means of neighbor ON pixels, either adjacent or on the diagonal) to the central cluster are set OFF. An example of this filtering procedure applied on the map of a r_p=2.5 µm droplet is shown in Fig. 5.12. This is different from simply modifying the above weights to force zero weight on isolated ON pixels. In fact, due to noise fluctuations, adjacent ON pixels can appear far from the projected footprint of the analyte (see the green-circled pixels in Fig. 5.12, left).

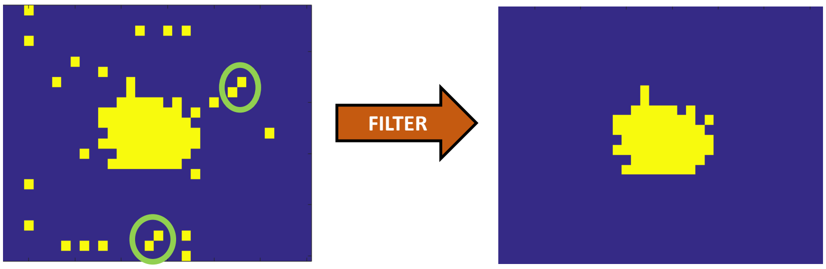

Figure 5.12: *Left: binary map of ENBIOS* ΔC_{eff} *in the presence of a 2.5 µm droplet with* σ_N*=1 aF AWGN with a threshold of 2 aF. Green circles highlight the presence of adjacent active pixels far from the bead. Right: filtered version in which isolated pixels are removed.*

Fig. 5.13 reports the correction curves in the presence of noise (σ_N=1 aF). Examples of corresponding digitalized images (before and after the filtering) are also shown. The standard deviation of the estimations (error bars), also with low thresholds, are very small, proving the robustness of the curves.

Fig. 5.14 compares the estimation performed by means of the digitalized maps to the estimation by means of Eq. 5.1. The standard deviation over mean ratio of r_{app} (i.e. the noise/signal ratio of the estimation) is reported, for a fixed noise level (σ_N=1 aF), as a function of the real size of the analyte. When using large thresholds, no significant differences are found between the two approaches; for of low thresholds (as those necessary for small objects, or for objects with large d_z displacements), instead, the calculation based on the digitalized estimation of the projected area appears definitely superior.

This benefit of the proposed algorithm is further corroborated by inspecting the standard deviation over mean ratio for a fixed r_p (2.5 µm) at different signal-to-noise ratio (SNR) levels. The outcome of this analysis is shown in Fig. 5.15. Again, for large thresholds the benefits of the projected area algorithm are minimal. Differently, using low thresholds (orange and green curves) the benefits are more evident.

In summary, this section presented two alternatives to generate correction curves to estimate the size of particles in simple reference conditions (milliQ ambient, in the absence of EDLs), which could possibly be embedded in the real-time software of the biosensor platform to perform real-time analyses of the size of droplets.

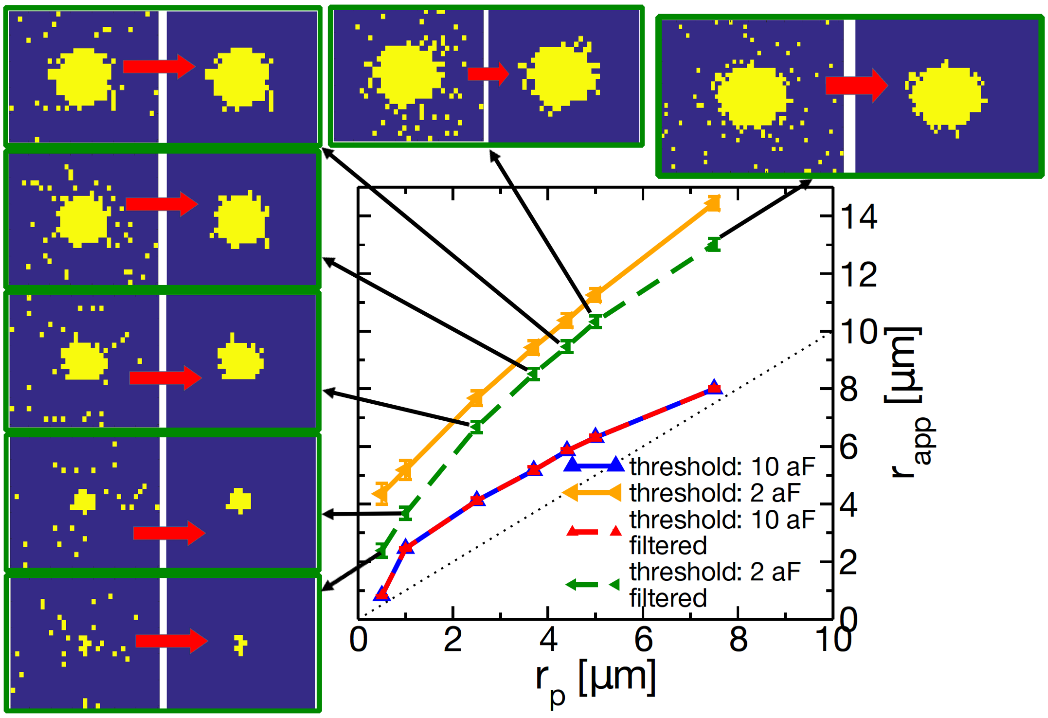

Figure 5.13: *Correction curves to derive the real size of a particle/droplet (r_p) based on its apparent size (r_{app}), computed with the digital estimation of projected area of Sect. 5.1.2. AWGN is added to ΔC_{eff} maps (σ_N=1 aF), 10,000 noisy images are considered. Examples of noisy maps, then filtered to remove the isolated pixels, are highlighted for the green curve.*

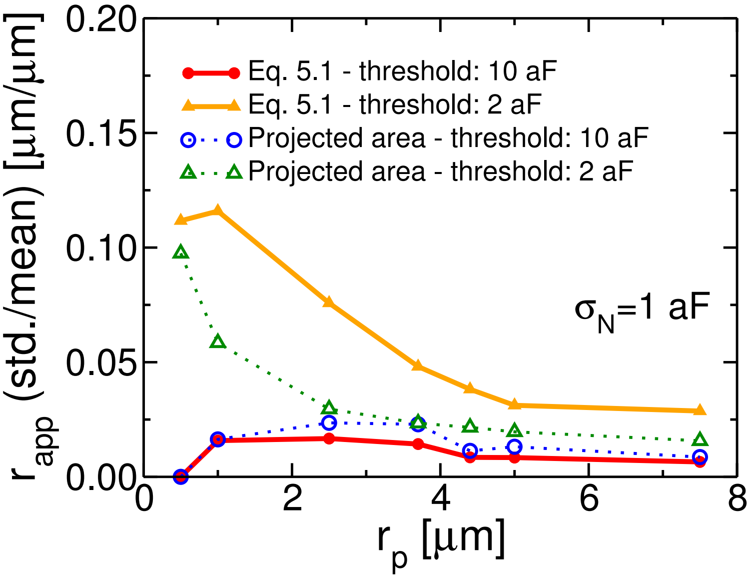

Figure 5.14: *Comparison between standard deviation over mean ratios of estimated r_{app} versus r_p for the two different approaches to generate correction curves: Eq. 5.1 and the projected-area algorithm. For low thresholds (necessary when noise approaches the amplitude of the relevant signals) the binary maps of the projected area algorithm are more robust (lower standard deviation/mean values).*

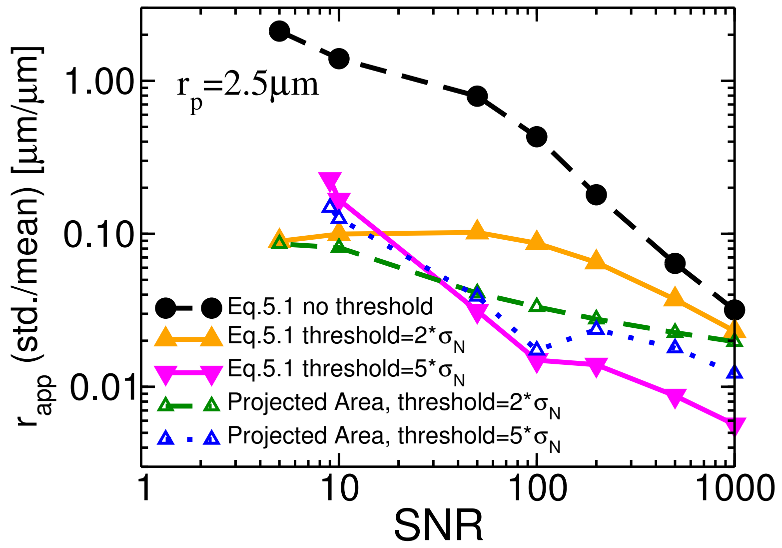

Figure 5.15: *Comparison between standard deviation over mean ratios of estimated r_{app} for a given r_p=2.5 µm at different SNR levels ($SNR = \Delta C_{eff}(0,0)/\sigma_N$, i.e. defined w.r.t. the maximum value of the response at the central electrode, see Fig. 5.3).*

5.2 Dielectric and conductive microparticles

Sedimentation experiments performed by the University of Twente, in which microspheres landed on the array while the capacitance was recorded at several frequencies, have been reported in [190]. Fig. 5.16 shows the outcome of such an experiment, in which a mixture of 5 µm radius insulating (latex) and conducting (gold-coated polystyrene) particles were immobilized on the chip surface. The surrounding solution consists of phosphate buffered saline with an ionic strength of 0.1 M, corresponding to a Debye length of approximately 1 nm. The resulting 2D capacitance maps for four different frequencies ranging from 1.6 MHz to 50 MHz are shown in the figure.

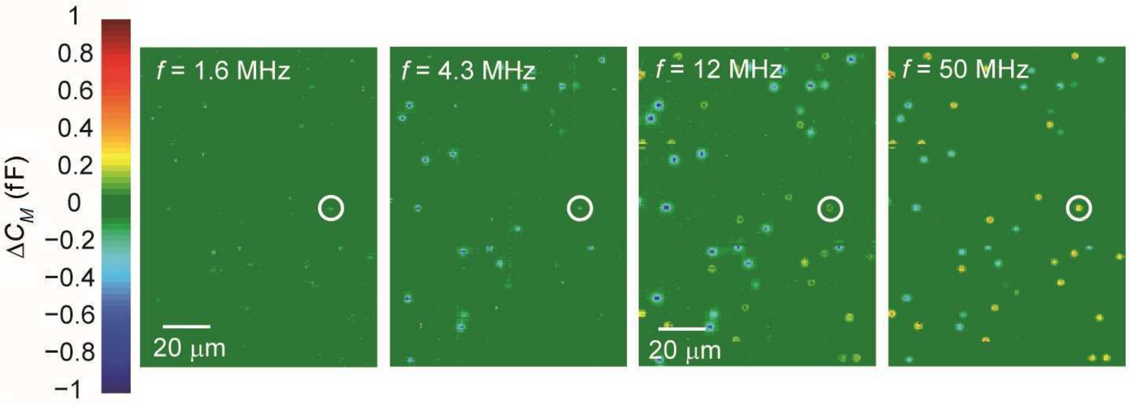

Figure 5.16: *ΔC_M 2D maps for 200×100 nanoelectrodes resulting from the sedimentation of dielectric and conducting microspheres at different frequencies. The capacitance before microparticle deposition has been subtracted from each pixel (green = no change). Dielectric particles exhibit a decrease in capacitance (cyan/blue) at all frequencies while metallic particles (e.g. in white circle) transition from a decrease to an increase (yellow/red) with increasing frequency. The 2D maps are single frames, captured with 512 charge/discharge cycles and 16 on-chip data accumulations. Measurements performed by University of Twente. Published in [190]*

By virtue of their radius being larger than the pitch of the array, the footprint of each microparticle spans a number of nanocapacitors, yet it can only be in near contact with a single one. Indeed, at the lowest measured frequency of 1.6 MHz, essentially only single nanocapacitors exhibit a significant response to microparticle sedimentation, corresponding to particles located in close vicinity to that electrode. As the frequency increases the signals become gradually stronger, however, and the spatial extent over which the particle is detected grows in size, such that above 10 MHz the particles exhibit a footprint on the array which can be related via simulations to the real size of the particles themselves.

A striking feature of the data of Fig. 5.16 is the qualitative difference in response between the two types of particles. While dielectric microspheres cause a decrease of the capacitance at all frequencies, conducting particles cause a decrease at low frequencies and an increase at high frequencies. Understanding the nanoelectrode response to dielectric and conductive particles is the scope of this section. In particular, Sect. 5.2.1 presents further experiments and analyses of dielectric particles, while in-depth analyses of the peculiar features of conductive particles are presented in Sect. 5.2.2.

Simulations are performed with the usual setup, as shown in Fig. 3.2 and Fig. 5.2, and, unless otherwise stated, are run with p_x=600 nm, p_y=890 nm, $n_{rows} = 13$, $n_{cols} = 17$.

5.2.1 Dielectric microparticles and particles-aggregates

As mentioned above, dielectric microparticles always yield $\Delta C_{eff} < 0$ over the whole frequency interval (1-70 MHz). This has been observed consistently in our experiments and is also in line with predictions based on the PB-PNP formalism discussed in Chapter 3. Fig. 5.17 (left, top) shows ΔC_{eff} spectra obtained from simulations of a polystyrene microparticle (r_p=2.5 µm, $\varepsilon_p = 2.6\varepsilon_0$, same as for the experiments in Fig. 5.16) at d_z=10 nm perfectly centered on $e_{(0,0,)}$ (i.e., $d_x = d_y = 0$) in NaCl 10 mM. The particle distance from the array is larger than a Debye length,

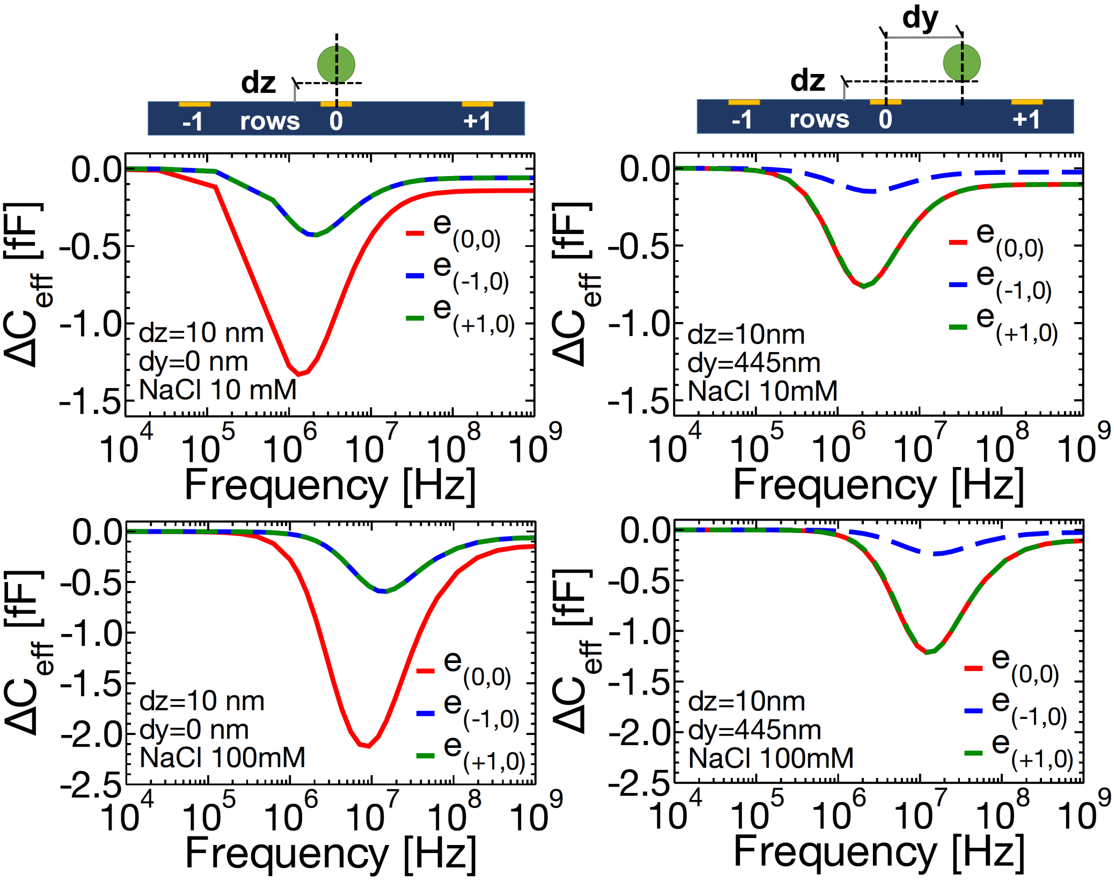

Figure 5.17: *Simulated ΔC_{eff} spectra for a dielectric polystyrene particle (r_p=2.5 µm, $\varepsilon_p = 2.6\varepsilon_0$) at vertical elevations d_z=10 nm ($\gg \lambda_D$) in NaCl 10 mM (top) or NaCl 100 mM (bottom) electrolyte. The response of both row 0 and rows ±1 are shown. Left: particle centered on the central electrode ($d_x = d_y = 0$). Right: particle laterally displaced (d_y=445 nm).*

hence the response at low frequency tends to zero due to EDL screening. A peak response can be observed around 1 MHz, which corresponds to the frequency of optimal detection [203]. The response at adjacent electrodes on the column ($e_{(\pm 1,0)}$) has the same qualitative features, with a reduction of the amplitude due to the larger distance from the particle to the electrodes. Electrodes $e_{(+1,0)}$ and $e_{(-1,0)}$ yield the same response since the distance from the bead is the same in this simple symmetric case. As a further example, Fig. 5.17 (right, top) shows the response to the same particle shifted at d_y=445 nm (i.e. halfway of the intra-electrode pitch) in NaCl 10 mM. As expected, in this case $e_{(0,0)}$ and $e_{(+1,0)}$ yield the same response, while the amplitude of ΔC_{eff} in $e_{(-1,0)}$ is further reduced because of the larger distance. Fig. 5.17 (bottom) shows the same results in NaCl 100 mM: the same qualitative features appear, and due to the higher electrolyte salinity (compared to the NaCl 10 mM electrolyte) the frequency of optimum sensitivity is increased to about 10 MHz.

Fig. 5.17 illustrates the typical features found in the spectra of dielectric microparticles. To further demonstrate the HFIS and imaging capabilities of the platform, the process of extracting key experimental parameters, and the predictive power of calibrated numerical simulations, we perform detection and imaging experiments with silicon dioxide (SiO_2) microparticles (r_p=2.5±0.1 µm, $\varepsilon_p = 3.9\varepsilon_0$), both in milliQ (as for the analyses of the oil droplets in Sect. 5.1) and in electrolyte (NaCl 10 mM). Liquids (NaCl solution) and analytes (SiO_2 microparticles) have been purchased from Sigma Aldrich [262]. SiO_2 microparticles are provided in aqueous suspension, with 5% concentration of solids. Samples for experiments in milliQ or NaCl electrolyte are prepared by diluting the suspension by a factor of 20×, so that the expected number of analytes in the fluidic chamber (which is a few nL in volume) is $\sim$ 100, large enough to guarantee detection events and possibly to record the formation of particle agglomerates, as reported in more detail in the following section. The following experiments are performed using a version of the chip with p_x=550 nm and p_y=720 nm, at a controlled temperature of 22°C (ambient temperature 25°C), and operating the syringe pumps at 50 µL/min pump rates in withdrawal mode.

Microparticles in milliQ

As a first test experiment, we consider silicon dioxide microparticles (r_p=2.5±0.1 µm) in milliQ. Given the nearly flat frequency spectrum of milliQ (at least in the frequency range of operation of the biosensor), measurements are performed at a single frequency (f_s=50 MHz, with 1344 charge/discharge cycles per measurement frame and 9 on-chip data accumulations, corresponding to a frame rate of 4.7 frames/s).

Fig. 5.18 (top) shows a 2D ΔC_{post} map recorded after the sedimentation of few particles (footprints of particles appeared on the real-time graphical interface of the platform a couple of minutes after the solution with particles was flushed in, and a large part of them remained stable during the experiment). Both small and large footprints can be observed, hinting that both individual particles and aggregates of multiple particles may be present in solution. A few selected footprints are labeled (P1-P5) for subsequent analyses.

Fig. 5.18 (bottom) shows time traces of the selected candidates, as recorded at the electrodes that yielded the highest ΔC_{post} for each footprint. Different particles reached the array at different times. It is interesting to note that a sharp decay of ΔC_{post} is sometimes followed by a slower tail in the response, hinting at a configuration adjustment or a slow final approach to the electrodes.

Fig. 5.19 shows, for each particle, a sequence of six subsequent measurement frames. A few particles (P1, P4) do not exhibit significant variations of the footprint over time, while others (P2, P3, P5) yield visible differences frame after frame, showing their evolution in terms of spatial location. At this regard, particle P2 is an interesting case. Its footprint initially occupies multiple electrodes; after some time, the response at a few electrodes is remarkably diminished and the footprint gets narrowed. This behavior suggests that P2 is likely an aggregate of more particles, and that a portion of this agglomerate gets detached from the surface over time. To further corroborate this point, Fig. 5.19 (bottom left) shows time traces of three selected electrodes (highlighted in red, the electrode which yields the maximum response $e_{(0,0)}$ and two neighbors $e_{(-1,0)}$ and $e_{(0,1)}$) in the P2 particle footprint. The response at the three electrodes is essentially equal in the first phase of the ΔC_{post} drop; then, the capacitance drop of $e_{(-1,0)}$ is reverted after some time. Since the response at the other electrodes ($e_{(0,0)}$ and $e_{(0,1)}$) remains constant and does not exhibit any further decrease (which would be expected if the particle simply moved farther from $e_{(-1,0)}$ and closer to the other electrodes), we speculate that this behavior is induced by a portion of an agglomerate that gets released or is removed from the sensor's surface by the flow of the liquid (which we remind being equal to 50 µL/min).

HFIS of particles in electrolyte

Following the first imaging examples in milliQ, detection experiments of silicon dioxide microparticles are repeated in NaCl 10 mM electrolyte. In this case, the measurement frequency is also swept from 1 MHz to 70 MHz, such that ΔC_{post} spectra can be recorded.

Fig. 5.20 reports color maps of the experimental ΔC_{post} measured by the sensor array . Each pixel represents one nanoelectrode. We observe spots where either individual particles or agglomerates are present, either suspended or attached to the surface. To gain better insight on their actual nature, the Bayesian estimation procedure of Sect. 3.6 is applied on the ΔC_{post} measurements, using again full 3D ENBIOS simulations as model $g(q)$ for the algorithm.

Parameters extraction for particle "A" yields r_p=2.5 µm, d_z=10 nm, d_y=300 nm. ENBIOS simulations corresponding to the extracted parameters are shown in Fig. 5.21 and compared to experimental ΔC_{post}. An unprecedented agreement between simulations and HFIS measurements at nanoelectrodes of particles in electrolyte is observed based on these Bayesian estimation methods. The residual discrepancies are under investigation.

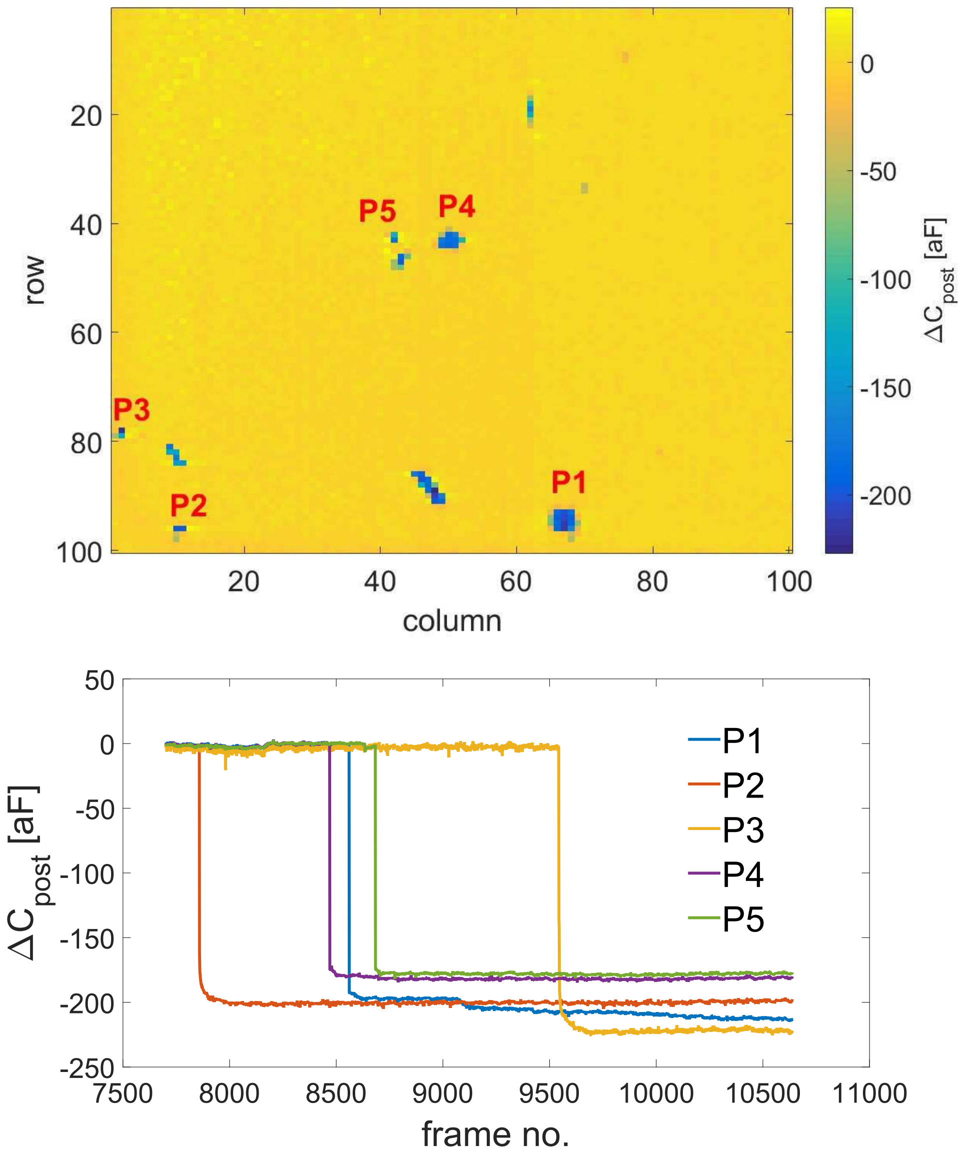

Figure 5.18: *Top: ΔC_{post} map of dielectric SiO_2 microparticles (r_p=2.5 μm) in milliQ at switching frequency f_s=50 MHz. The chip has p_x=550 nm and p_y=720 nm. Both individual particles and suspected particles aggregates can be identified. A few particles of interest are labeled (P1–P5). Bottom: electrodes time trace of ΔC_{post} for the selected particles (for each particle, the signal of the electrode that yields the highest response is plotted).*

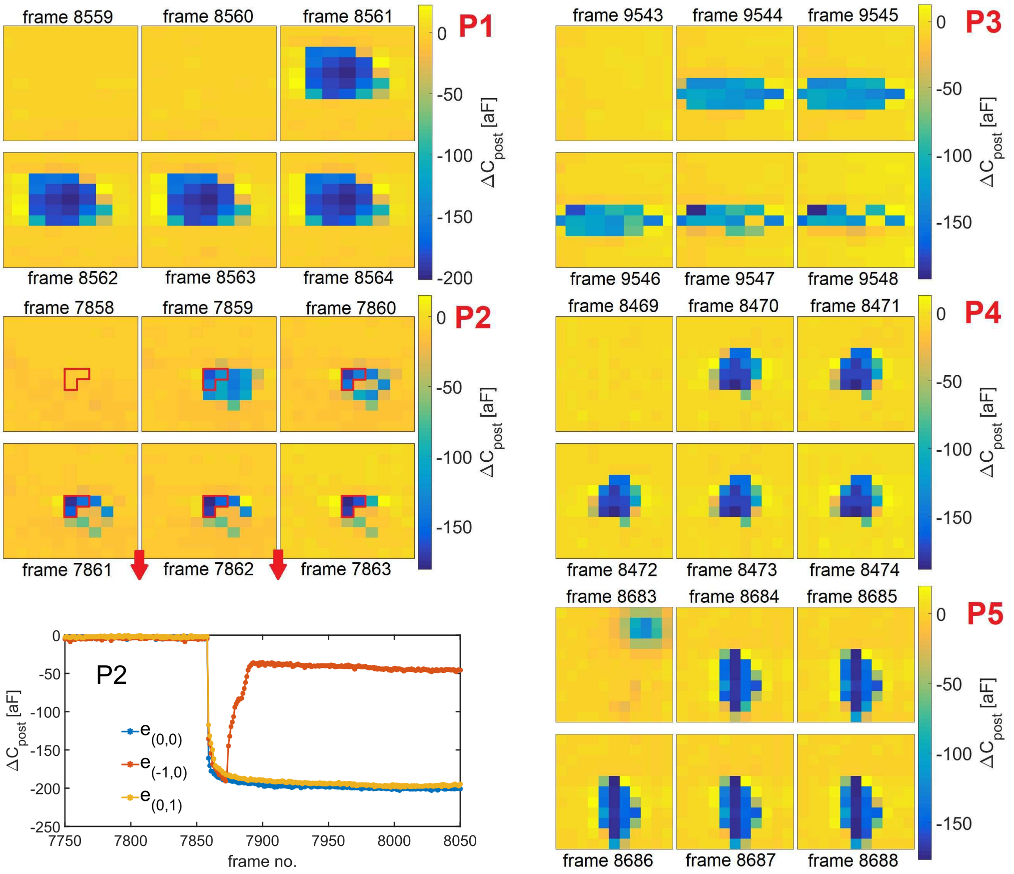

Figure 5.19: ΔC_{post} *maps of the selected particles in Fig. 5.18 (particles P1–P5). For each particle, a sequence of six subsequent frames is shown. A few particles (P2, P3, P5) show distinguishable evolutions of the footprints over time. For particle P2, a time trace of the response at three neighbor electrodes (highlighted in red in the P2 map sequence) is shown (bottom left): the electrode with the highest response* ($e_{(0,0)}$) *and the bottom/right neighbors* ($e_{(-1,0)}$, $e_{(0,1)}$) *are selected for this purpose. The wide footprint of P2 is progressively narrowed, suggesting that P2 is likely an agglomerate of particles and that a portion of this agglomerate gets detached over time. This is also highlighted by the red-curve time trace of* $e_{(-1,0)}$*: after an initial drop of the signal, the amplitude of the response is subsequently reduced.*

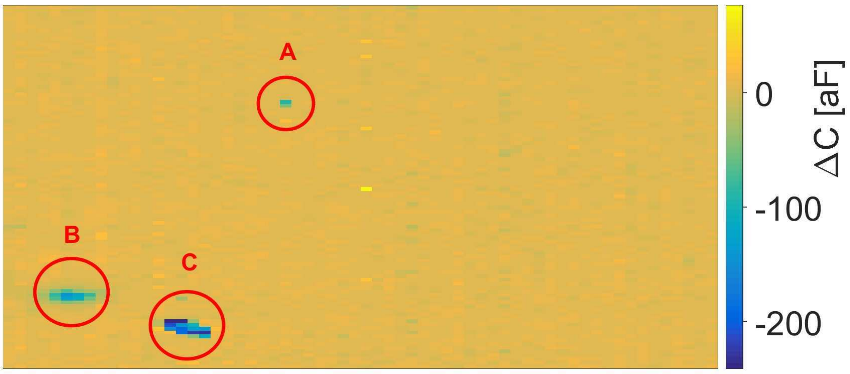

Figure 5.20: *ΔC_{post} map of dielectric SiO_2 microparticles (r_p=2.5 μm) in NaCl 10 mM at switching frequency f_s=70 MHz. The chip has p_x=550 nm and p_y=720 nm. Both individual particles and particles aggregates can be identified (red circles).*

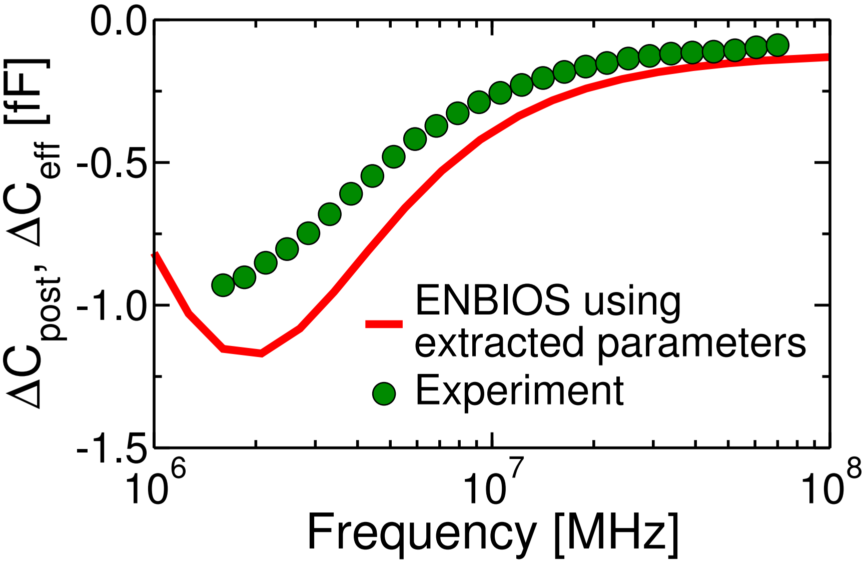

Figure 5.21: *Capacitance spectra at electrode $e_{(0,0)}$ of the experiments compared to the capacitance spectra simulated by ENBIOS for particle "A" (see Fig. 5.20).*

5.2.2 Conductive microparticles

As anticipated at the beginning of Sect. 5.2, while dielectric microspheres cause a decrease of the capacitance over the whole spectrum, the response to conducting particles cause a decrease at low frequencies and an increase at high frequencies (see Fig. 5.22).

Roughly speaking, dielectric beads (red open symbols in Fig. 5.22) increase the effective electrolyte impedance, blocking the access of the ionic and displacement currents to the electrode, lowering the cut–off frequencies f_1 and f_2, thus generating a negative ΔC_{eff} over the whole spectrum [211]. Fig. 5.22 also allows to better understand the features of the capacitance variation spectra. At low frequency, the capacitance in the presence of a dielectric bead is essentially similar to the case without bead, yielding a very small ΔC_{eff}. For increasing frequency, the C_{eff} spectrum in the presence of a dielectric bead (red curves in Fig. 5.22) drops to smaller values earlier than the C_{eff} spectrum without bead does (black curves in Fig. 5.22) due to the smaller value of the cut-off frequencies. Consequently, the ΔC_{eff} spectrum presents an initial decrease (increase in absolute value), later followed by an increase (decrease in absolute value) when the frequency is high-enough to have both the $C_{eff,w/\ bead}$ and the $C_{eff,w/o\ bead}$ curves reach their corresponding high frequency limit values.

Conducting particles, instead, provide a capacitor-like high-frequency short-circuit through the surrounding dissipative medium [346] ($C_{eff,w/\ bead} > C_{eff,w/o\ bead}$, thus leading to $\Delta C_{eff} > 0$, see Fig. 5.22 and Fig. 5.23). As predicted by the com-

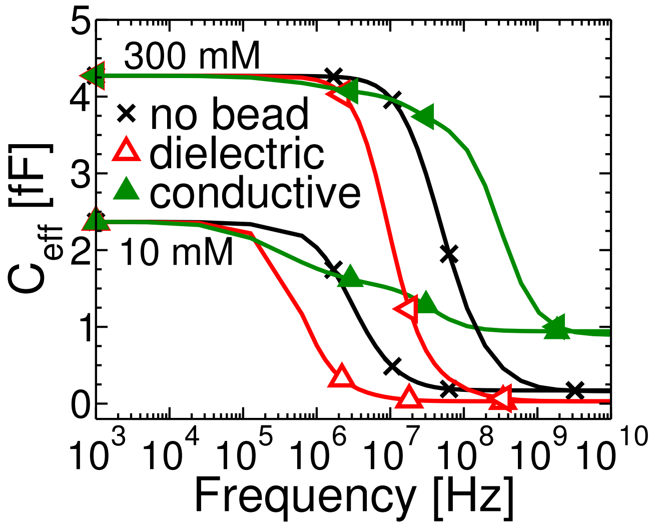

Figure 5.22: *C_{eff} spectra without particles and with dielectric (polystyrene) or conductive bead with radius $r_p = 2.5\ \mu m$, at lateral displacements (w.r.t. the central electrode) $d_x = d_y = 0$ and vertical elevation $d_z =\ 10 \gg \lambda_D$ nm. NaCl 10 mM and 300 mM electrolytes are considered. Curves with dielectric beads are almost rigidly shifted to lower frequency. Instead, curves with and without conductive beads cross each other, leading to opposite signs of ΔC_{eff} at low and high frequencies, due to capacitance drops and plateaus in the traces.*

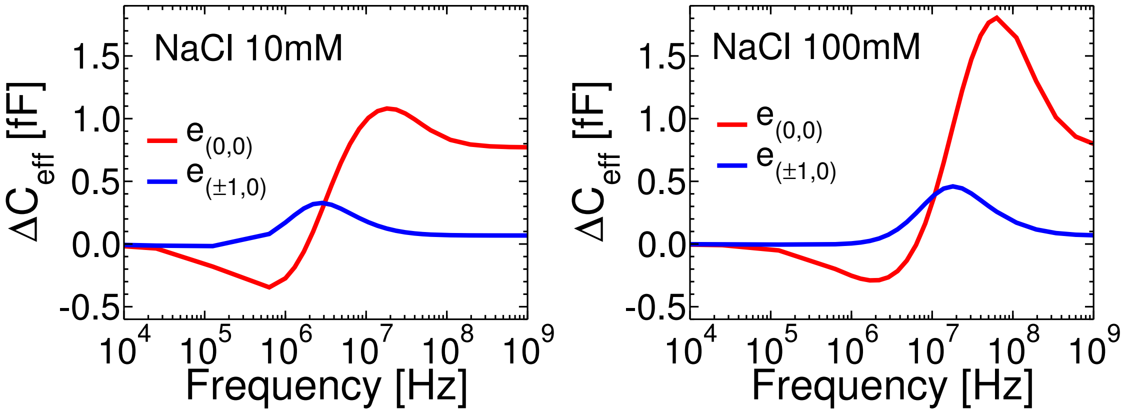

Figure 5.23: *Simulated ΔC_{eff} spectra for a conductive particle (r_p=2.5 μm) centered on $e_{(0,0)}$ ($d_x = d_y = 0$) at vertical elevation d_z=10 nm ($\gg \lambda_D$). The response of both row 0 and rows ±1 are shown. Left: NaCl 10 mM. Right: NaCl 100 mM.*

pact model in [211], at lower frequencies conducting particles also behave as high-impedance pathways and yield a suppression of the charging response, much like the dielectric particles ($C_{eff,w/\ bead} < C_{eff,w/o\ bead}$, thus leading to $\Delta C_{eff} < 0$, see Fig. 5.22 and Fig. 5.23). These different behaviors at low and high frequencies, to our knowledge observed experimentally for the first time in [190] (see highlighted particle in Fig. 5.16) has been verified and interpreted in detail by means numerical simulations, as reported in the present section.

As an example of typical behaviors, Fig. 5.23 shows ΔC_{eff} spectra in NaCl 10 mM and 100 mM due to a conductive microparticle at d_z =10 nm. Firstly, we remind that the capacitance response in the low-frequency limit is essentially determined by the series of the Stern and EDL capacitance, whereas in the limit of high-frequencies the input signals are fast enough to penetrate the EDL and the response is insensitive to (fixed or mobile) charges and is determined by the volume, position of and electrical properties the analyte [211]. As discussed regarding Fig. 5.17, the frequency of peak response is different for the different electrolytes. The response at $e_{(0,0)}$ clearly exhibits a sign change, occurring around 2 MHz for the 10 mM electrolyte and around 7 MHz for the 100 mM electrolyte. The response at the neighbor electrodes $e_{(\pm 1,0)}$, which has a much lower amplitude due to the larger distance from the particle, is positive at nearly all frequencies considered for the plots, decays at the low frequencies and eventually leads to a sign change at very low frequency (a few kHz). The reported behaviors entail the existence of a frequency $f = f_{zh}$ of zero–response[4], i.e. $\Delta C_{eff}(f_{zh}) = 0$.

The crossing of the C_{eff} traces with and without a conductive bead observed in Fig. 5.22, and hence the appearance of zeros of ΔC_{eff}, is due to sudden capacitance drops followed by plateaus. Depending on the salt concentration, particle size and position, and electrode properties (e.g. radius or surface roughness, which in turn influence the formation of the Stern compact layer and the EDL) and excitation patterns, these plateaus appear as distinct or gradually merged, but never disappear.

---

[4] we use the subscript "zh" to identify the highest (h) frequency of zero (z): in fact, as will be clear in the following, two frequencies of zero-response exist.

As an example, Fig. 5.24 shows the capacitance spectra, recorded at electrode $e_{(0,0)}$, resulting either from a row–wise excitation pattern (all electrodes $e_{(0,*)}$ are activated, red lines) or from a single electrode excitation (only $e_{(0,0)}$ acts as a WE, blue lines). The plateau on the conductive bead capacitance spectrum is more evident in the latter case.

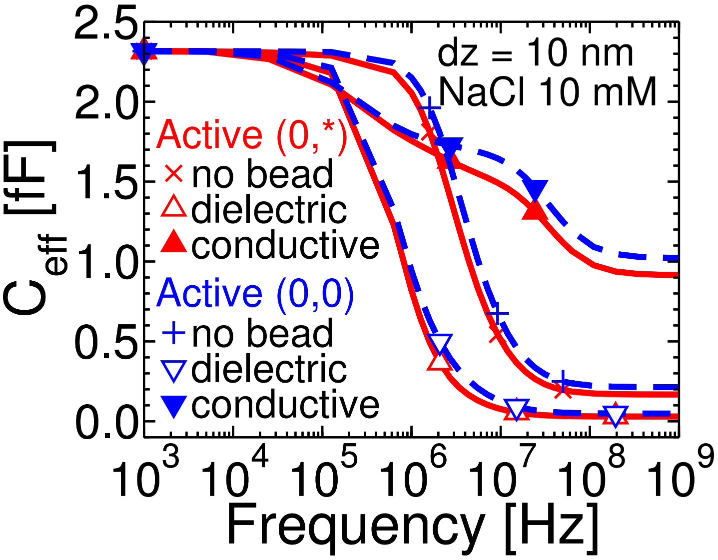

Figure 5.24: *C_{eff} spectra for r_p=2.5 μm dielectric and conductive particles immersed in a 10 mM NaCl electrolyte at $d_z \geq \lambda_D$. Either electrode $e_{(0,0)}$ (blue) or all the electrodes of the central row (row 0, $e_{(0,*)}$) (red) provide the AC excitation signal.*

In order to understand their origin, firstly we first notice that at low frequency all the voltage drop occurs in the EDL (Fig. 5.25a and 5.25b), and if a particle stands at $d_z \geq \lambda_D$, then it is essentially not reached by the excitation of the WE, and C_{eff} at low-frequency is given by the series of C_S and C_{EDL} both with and without particles.

As frequency increases, the AC current spreads in the essentially equipotential electrolyte. The introduction of a conductive particle does not per-se perturb the electrode capacitance, but the additional electrical double layer on the particle surface obstructs the AC current flow and thus reduces C_{eff}, similarly to what a dielectric particle would do. In fact, since conductive particles maintain a constant potential on their surface (see Fig. 5.25d and 5.25e), when they are immersed in an electric field (due to the excitation of the WE) they behave like a dipole, attracting charges of opposite sign on the side of the particle that faces the electrodes and on the opposite side [346], hence resulting in the formation of an EDL on their surface.

Then, at even higher frequencies, the EDLs (both the one on the electrodes and the one on the particle) do not respond anymore to the high-frequency signals and the short–circuit like behavior of the conductive particle yields an increase of C_{eff}.

For convenience, we temporarily focus on a smaller and more numerically manageable system (7 × 7 electrodes, r_p=500 nm or 1 μm). Unless otherwise stated, hereafter the Stern layer (permittivity $\varepsilon_{Stern} = 7\varepsilon_0$, thickness t_{Stern}=0.25 nm) is

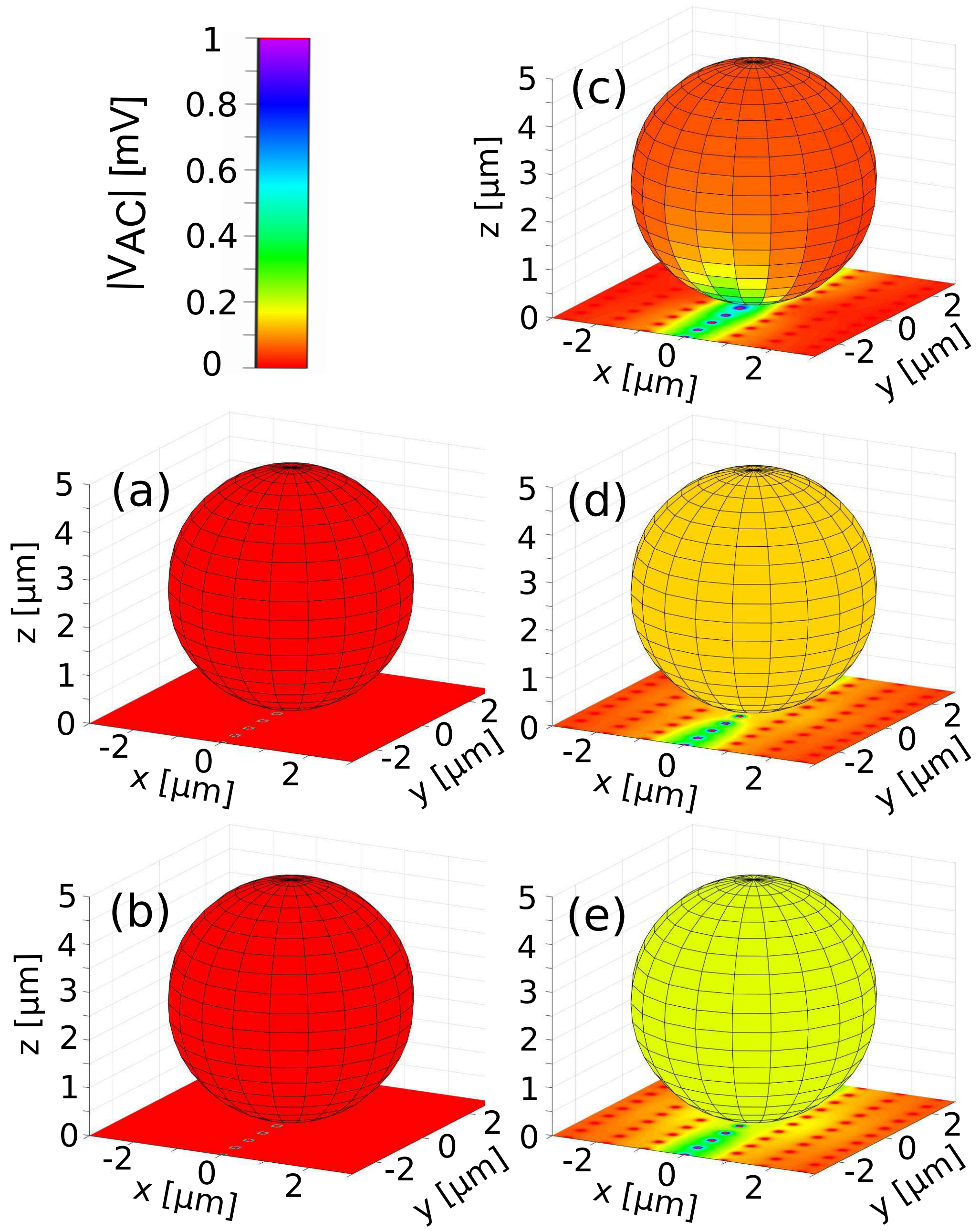

Figure 5.25: *Amplitude of the AC potential at the bead (r_p=2.5 µm) and at the array surfaces. (a) dielectric bead, 1 kHz, d_z=10 nm; (b) conductive bead, 1 kHz, d_z=10 nm; (c) dielectric bead, 50 MHz, d_z=10 nm; (d) conductive bead, 50 MHz, d_z=10 nm; (e) conductive bead, 50 MHz, d_z= 1 nm. Electrolyte: NaCl 10 mM. At low frequency all the voltage drop occurs in the WE's EDL and the bead/array surface is essentially not reached by the voltage signal (a-b). At high frequency the signal overcomes the EDL and reaches the beads (c-e). Dielectric beads obstruct the flow of current, enhancing the voltage drop and leaving the farther part of the bead's volume at much lower voltage level (c). Conductive beads keep a constant voltage level on their surface, enabling the signal to reach regions of the array far away from the electrode that were not reached before (d). This effect is further enhanced if the conductive bead is placed closer to the array (e).*

added only rows $-2 < i < 2$ and is not included on the other outer rows of the simulation domain. This is done to significantly reduce simulation time (t_{Stern}=0.25 Å, and the meshing of these very thin layers increases the number of nodes and tetrahedrons). The qualitative and quantitative impact of the Stern layer on the electrodes will also be addressed in the following of this section. It is worth to point out that the inclusion of a dielectric layer on top of some electrodes (which hampers their flux of current) can actually represent a variety of diverse physical conditions: it could represent, for instance, the presence of some extra undesired (disturbing) analytes on adjacent electrodes, or the use of functionalization layers on top of the electrodes.

The role of the particle EDL in the formation of the first capacitance drop is illustrated in Fig. 5.26, where we modulate its thickness and admittance by adding a charge surface density on the particle. Three capacitance drops can be observed, hence, two plateaus between the low-frequency and the high-frequency capacitance limit values, especially evident in the 300 mM curves. Modulating the EDL of the particle by adding a surface charge affects the first capacitance drop and plateau, i.e. exactly the one that originates the zero. Note that neutral dielectric particles, whose surface EDL is essentially negligible, do not exhibit such C_{eff} drop at low frequency (not shown). Furthermore, simulations of conductive particles that neglect the diffusive current component (hence, where electrical double layers cannot form) do not show zeros of ΔC_{eff} (not shown). This proves unambiguously that the particle EDL is the root cause of the first C_{eff} drop and of the corresponding zero in ΔC_{eff}.

Fig. 5.27 shows that by changing the configuration of electrodes next to the working electrode (e.g., eliminating the nearest neighbor rows or columns) only the second drop and the asymptotic C_{eff} value at high frequency are affected, not the first drop. Indeed, by removing rows of counter-electrodes next to the WE row, the current path between the WE and the CEs become longer, the series resistance increases and C_{eff} decreases. On the contrary, by removing adjacent columns, the current of the WE spreads out; consequently C_{eff} increases. These observations clearly suggest that the second drop depends on the geometry of the current distribution in the electrolyte and in particular on the working/counter-electrodes number and geometry. This is reasonable, since the frequency is large enough that the AC field appreciably penetrates the electrolyte. At this regard, Fig. 5.28 compares simulations of a 7×7 array with a conductive particle at d_z=1 nm in NaCl 300 mM (hence, beyond the EDL of the electrodes), either including a dielectric Stern compact layer (CL) on all electrodes or only on the working electrodes on the active row. In the range between the low-frequency and the high-frequency limit capacitance values, the absence of the Stern layer on the counter-electrodes makes visible a second intermediate plateau and dip, which is instead hidden in the other configuration (compare red to orange lines). To further corroborate this point, Fig. 5.29 shows simulations of a 5×5 array in which the CL is included on all electrodes, and its permittivity is changed for the outermost rows ($e_{(\pm 2,*)}$). In this figure, the capacitance spectra are normalized by their maximum value (i.e. the capacitance in the low-frequency limit) to facilitate a direct comparison of the curves. If all electrodes have the same Stern layer permittivity, a single plateau is visible. If differences in

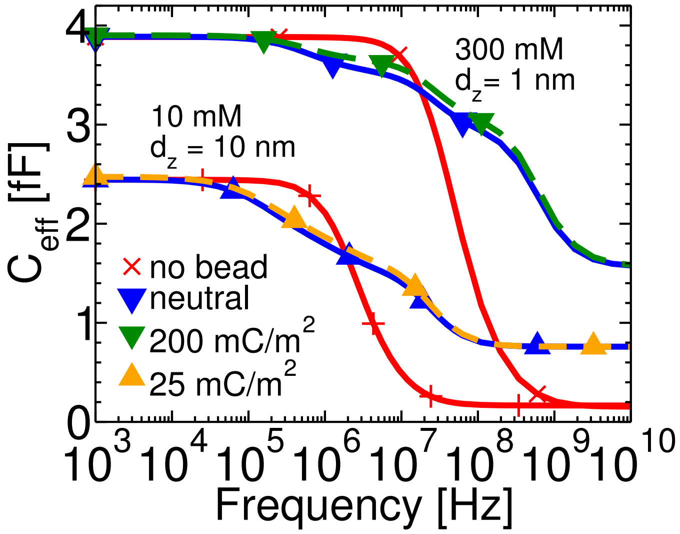

Figure 5.26: *C_{eff} spectra for neutral and charged conductive particles (r_p=1 μm) located at $d_z \geq \lambda_D$. Electrolyte: NaCl 10 mM and 300 mM. Smaller charge values are sufficient to perturb the response at the lower electrolyte salt concentration.*

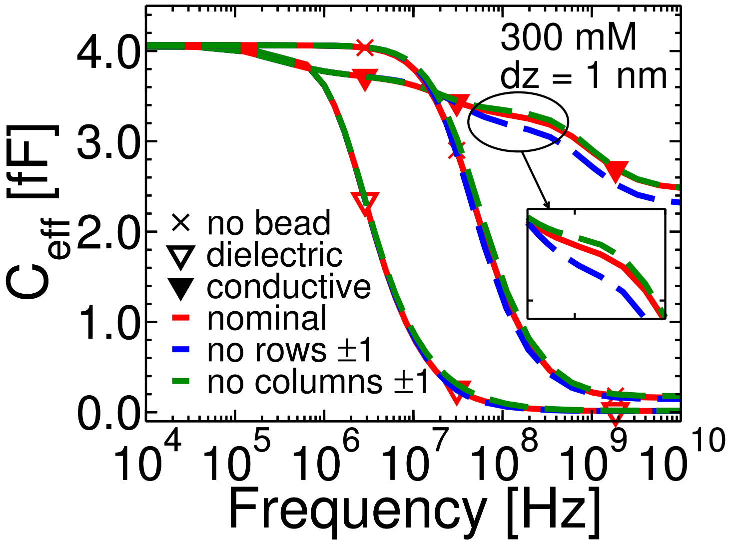

Figure 5.27: *C_{eff} spectra for r_p=2.5 μm dielectric and conductive particles at d_z=1 nm $\geq \lambda_D$ over the nanoelectrodes removing some electrode rows or columns from the simulated system. Electrolyte: NaCl 300mM. Removing the adjacent working electrodes ($e_{(0,\pm1)}$) current flux lines originating from $e_{(0,0)}$ can spread out and result in increased capacitance; removing the adjacent counter electrodes ($e_{(\pm1,0)}$), instead, the path for the current flux lines is longer and the capacitance is decreased (see the sketches of Fig. 4.26).*

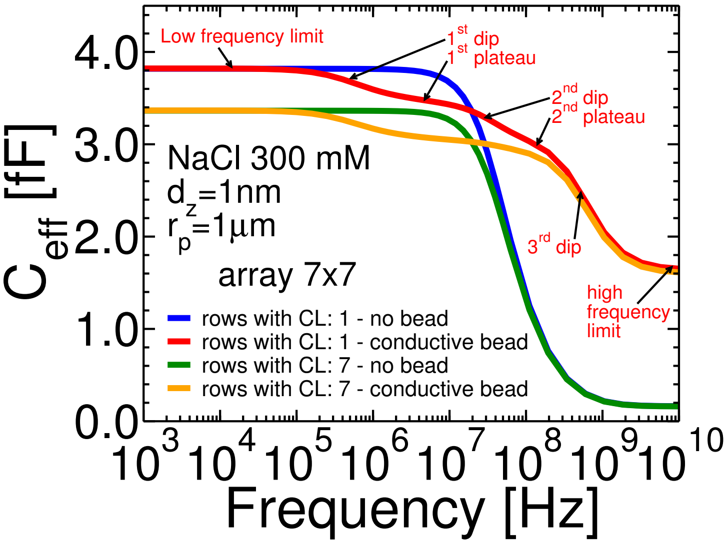

Figure 5.28: *C_{eff} spectra for conductive particles (r_p=1 µm) in NaCl 300 mM, located at d_z=1 nm $\geq \lambda_D$. An array of 7×7 electrodes is considered. A dielectric Stern compact layer (CL) is included either on all electrodes, or on only the electrodes of the active row. The low-frequency capacitance limit is smaller in the first case because of the CL capacitance of the $(7-1)\times 7$ CEs which adds in series to the current lines originating from the WEs. Furthermore, when present, this series capacitance hides the second dip/plateau. Thus, considering the frequency range between the low-frequency and the high-frequency limit capacitance values, either one or two intermediate dips and plateaus appear, depending on the electrode configuration.*

the properties of the Stern (compact) layers are included (e.g. changing the permittivity of the outermost CL from 7 to 21, or even outright removing the CL), then the second intermediate plateau reappears. These analyses prove that possible differences in the properties of the electrodes (as would be the case, for instance, in the presence of undesired disturbing analytes, or when using spatially-dishomogeneous functionalization layers) can result in the formation of more than just one intermediate plateau. This is consistent with the fact that, considering different current flux lines, if different values of series capacitance are included on these current paths, the time-constants (and hence the poles for the capacitance spectra) of the paths are shifted in different ways according to the corresponding path resistance values. In fact, simulations of a simple cylindrical simulation domain with a single WE and a single CE (as in Fig. 3.1) including a conductive particle between the electrodes always yield a single intermediate dip and plateau (not shown). Assuming that all the CEs are identical, and since it is reasonable to assume that the electrolyte properties above the WEs are (at least slightly) different compared to those above the CEs, a typical configuration of capacitance spectra for the nanoelectrode platform in the presence of conductive particles is expected to yield 3 capacitance drops, with 2 intermediate capacitance plateaus between the low-frequency and high-frequency limit of the response.

Until now, results have been discussed for $d_z > \lambda_D$. It is interesting to note

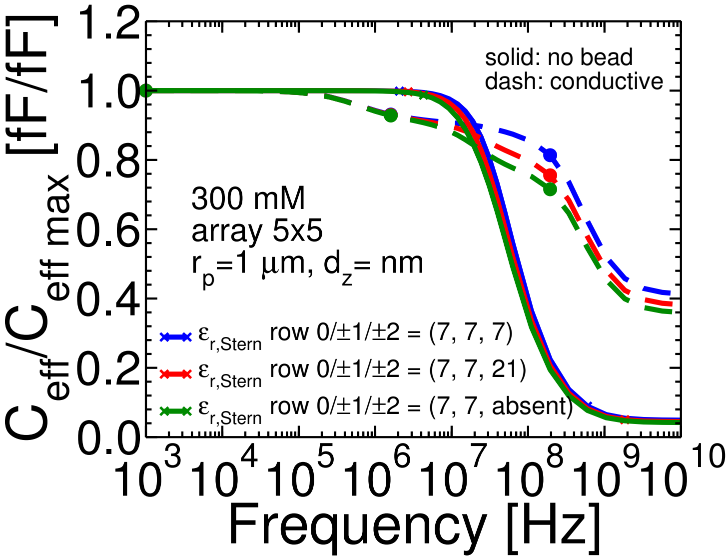

Figure 5.29: *C_{eff} spectra (normalized by the maximum value, to facilitate a direct comparison between the curves) of a r_p=1 µm bead in NaCl 300 mM at d_z=1 nm $\geq \lambda_D$. Array: 5 × 5 electrodes. Different values of the Stern compact layer (CL) permittivity are used for the outermost rows (either $\varepsilon_{r,Stern}$=7, or $\varepsilon_{r,Stern}$=21, or no CL at all). Including the CL on the central row of working electrodes and on the first neighbor rows (green curve), two intermediate plateaus are visible. By including the CL also on the outer rows, with progressively lower permittivity and hence lower and more relevant series capacitance (green to red, and red to blue curves), the CL gets more invasive and hides the second plateau.*

that if the particle comes closer to the electrode while still not interfering with its EDL, then the first drop and the value of f_{zh} become larger (see Fig. 5.30), likely because of the smaller electrolyte resistance in series with the EDL capacitance. If d_z increases, the resistance in series with the EDL capacitance increases as well, and therefore the capacitance curve detaches from the low-frequency limit capacitance value at a smaller frequency, eventually intercepting the capacitance curve in the absence of particle (black line) at a higher f_{zh}. As the particle and WE EDLs start to interact the low frequency limit of the capacitance curve is affected. Then, for metallic particles f_{zh} decreases and furthermore, an additional sign change of ΔC_{eff} appears at a low frequency (f_{zl}). This is because the potential of the metallic particle couples tightly to the electrode and the particle behaves as a protrusion of the electrode (compare Fig. 5.25e to Fig. 5.25d). The effective area of the electrode and consequently its capacitance increase at low frequency above the value without particle.

Fig. 5.31 illustrates how f_{zh} changes with the distance between the electrode and the analyte and the appearance of f_{zl}. Note that f_{zl} may fall outside the measurable range or be hidden by numerical noise in simulations as well as experiments. The curves are consistent with Fig. 5.31. Fig. 5.32 shows the simulated spectra of a r_p=2.5 µm conductive particle, centered on electrode $e_{(0,0)}$, as detected at different electrodes on the same row. Consistently with Fig. 5.31, we see that f_{zh} decreases for increasing column number that, for a spherical particle, entails a larger distance between the detection electrode and the particle, and consequently a larger resistance in series to the EDL capacitance.

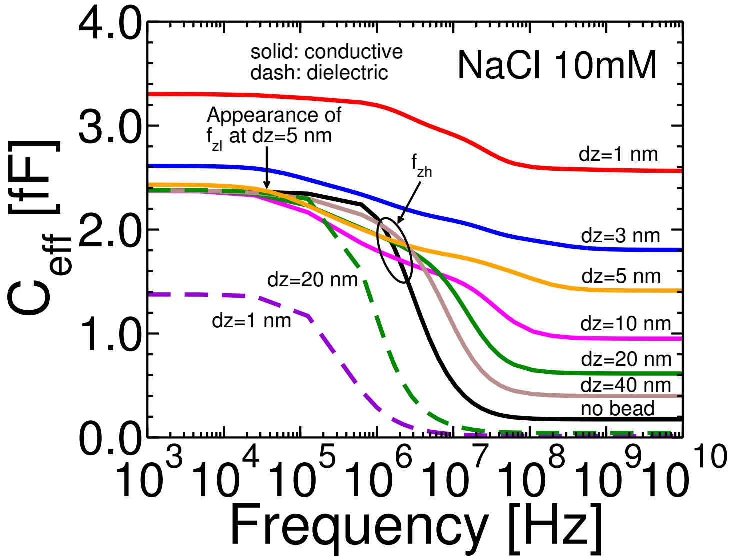

Figure 5.30: *C_{eff} spectra of a r_p=2.5 μm bead at different vertical displacements over the nanoelectrodes. Electrolyte: NaCl 10 mM.*

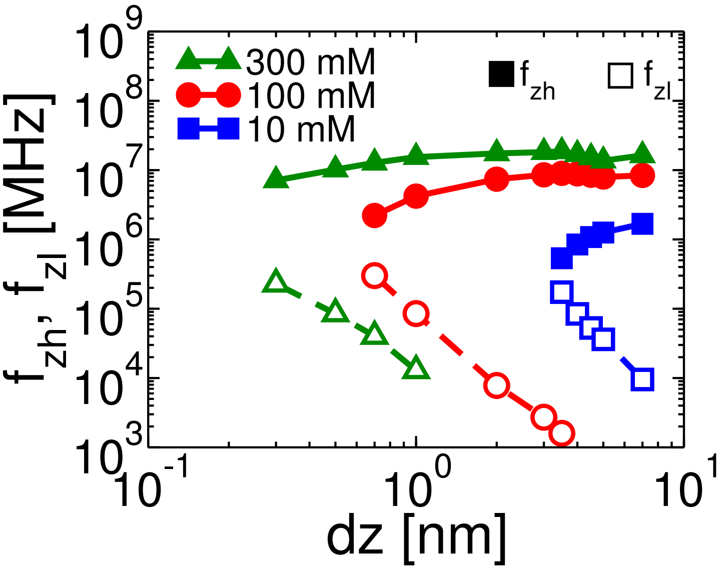

Figure 5.31: *Frequency of zero response as a function of the particle vertical displacement (d_z) and electrolyte salt concentration. The two distinct frequencies of zero response tend to diverge from each other as d_z increases.*

As further analyses, we inspected the intensity of the current at each counter-electrode of the array. At low frequency, the current is essentially the same on all these electrodes, no matter the distance between them and the active one(s). This is consistent with the fact that at low frequency essentially all the voltage drop occurs

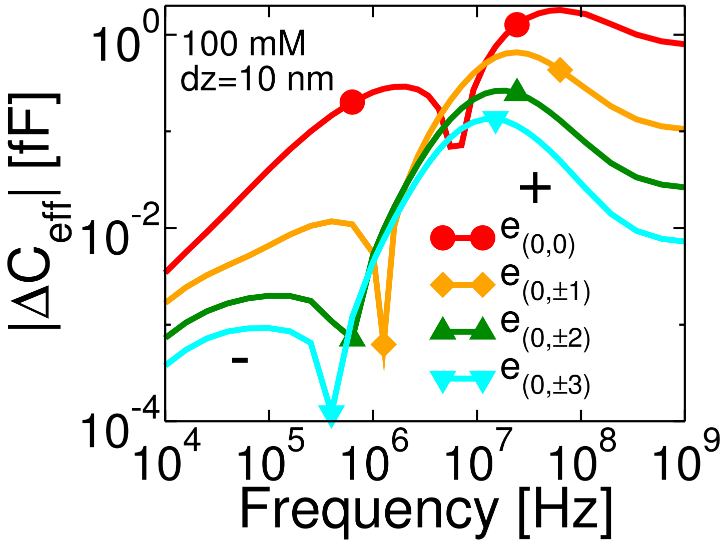

Figure 5.32: *Simulated ΔC_{eff} spectra as seen from different electrodes of the active row (r_p=2.5 μm).*

in the WE's EDL, therefore the current spreads uniformly on all electrodes. At high frequency (e.g., 50 MHz), the presence of the bead near the electrodes heavily affects the potential profile, and the current mostly flows from the active electrode(s) to the nearest counter electrodes.

Finally, Fig. 5.33 compares simulations of dielectric and conductive particles taken at different electrodes along the active row for a few frequency values. As expected, dielectric beads always yield a negative ΔC_{eff} and the peak response is centered, for each frequency, on the electrode which is nearest to the bead itself. The conductive beads instead exhibit electrodes $e_{(0,\pm i)}$ that can yield a larger response than the electrode nearest to the particle ($e_{(0,0)}$). This behavior is a consequence of the shift of the ΔC_{eff} spectrum and of the corresponding f_{zh} at different particle–electrode distance values, as reported in Fig. 5.32 and consistently with the results of Fig. 5.31.

These results nicely reproduce the measurements in [346], both qualitatively and quantitatively. They prove that the predictions and the insights provided by the PB-PNP modeling framework are accurate and effective in explaining experimental evidences.

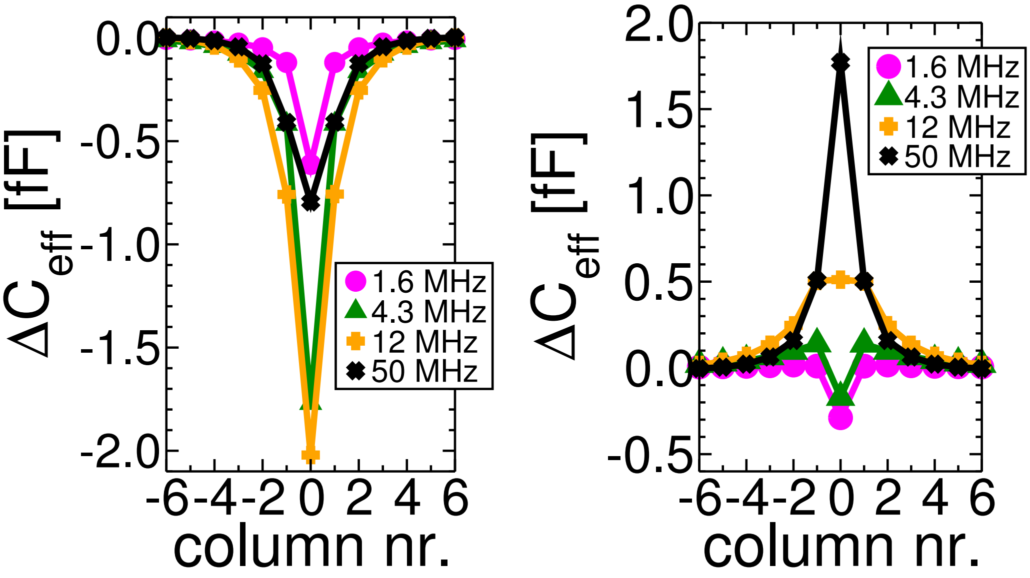

Figure 5.33: *Simulated* ΔC_{eff} *for a dielectric (left) or a conductive (right) particle, as detected at the electrodes of the active row,* $e_{(0,*)}$. *Particle dimension:* r_p*=2.5 μm. Electrolyte: NaCl 100 mM.* ΔC_{eff} *is always positive for the dielectric particle: consistently with Fig. 5.17, the amplitude of* ΔC_{eff} *gets larger with increasing frequency until about 10 MHz, and then gets smaller, for all electrodes. Differently, for conductive particles a* ΔC_{eff} *sign change appears, and it occurs at a larger frequency for electrode* $e_{(0,0)}$ *than for electrodes* $e_{(0,\pm1)}$ *due to the smaller electrode-particle distance, consistently with the* f_{zh} *in Fig. 5.31.*

5.3 Nanoparticles

As shown in Sect. 5.2, the high-frequency impedance response of nanocapacitors is largest to objects located in the region of greatest electric field strength [211], namely, the hemispherical volume located directly above the electrode. To exploit this capability, detection experiments using nanometer-scale spherical particles have been performed by the University of Twente [190, 346]. In this case the analyte is much smaller than the pitch of the array, and a response to a nanoparticle is only expected at a single electrode, even at high frequencies. Immobilization of the analyte to the surface of the array is absolutely necessary since the diffusion time of a nanoparticle past the electrode is much shorter than the inverse of the image capture rate of 4.5 frames/second. Bovine serum albumin (BSA, [319]) has been employed to immobilize polystyrene nanoparticles on the array.

Fig. 5.34 (a) shows an AFM image of a 40 nm diameter particle overlapping a nanoelectrode. The corresponding capacitance signal for the same electrode is shown in Fig. 5.34 (b), exhibiting a single step with a capacitance change <5 aF upon binding. The cyan curve is obtained applying the filtering method defined in [347] to the capacitance waveform. The time trace in Fig. 5.34 also shows the noise level of a single electrode: about 0.5 – 1 aF (1 standard deviation).

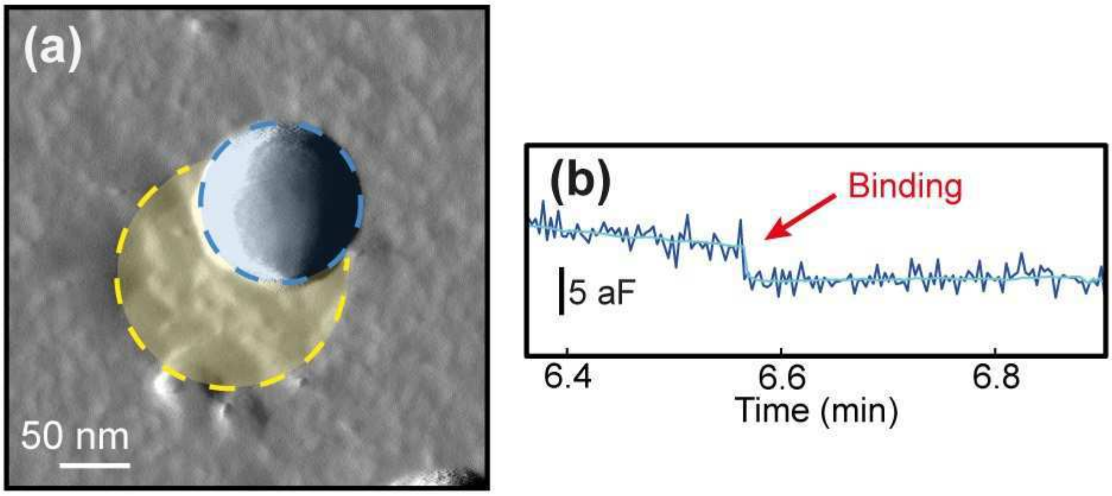

Figure 5.34: *(a) Tapping-mode AFM amplitude image of a nanocapacitor (yellow) with a single dielectric 40 nm diameter particle attached (blue). The particle diameter appears larger due to tip convolution. (b) Capacitive response of the same electrode exhibiting a single step attributed to binding of the nanoparticle. The measurement frequency is 50 MHz. Measurements performed by University of Twente. Published in [190].*

Triggered by these detection capabilities, we investigated more in detail the response of the platform to nanoparticles, with the goal to identify the detectability conditions and possibly the limit of detection of the system. In the following, in order to mimic the experimental conditions, a BSA layer is added on top of the nanoelectrodes. BSA is a serum albumin protein commonly used in lab experiments.

Fig. 5.35 shows a plot of its complex permittivity $\varepsilon_{BSA} = \varepsilon' - j\varepsilon''$ as a function of the hydration state. A model of the BSA permittivity is given in [319]. It was here adapted to simulate the BSA layer in ENBIOS. A water content between 20% and 40% yields a non-negligible contribution of the imaginary part of the permittivity. Fig. 5.36 shows $\Delta C_{eff,BSA} = C_{eff,w/\ BSA} - C_{eff,w/o\ BSA}$ as a function of the water content, for different values of the BSA layer thickness (h_{BSA}), at 50 MHz in NaCl 150 mM electrolyte (here we use r_{el}=90 nm). As expected, introducing a low permittivity material induces a negative capacitance variation (more negative for lower permittivity and larger volumes, i.e. for lower water content and higher thickness). The results reported hereafter are obtained considering a layer with h_{BSA}= 3 nm and 24% water content. The thickness is consistent with expectations based on the deposition rate and AFM scans. The water content was adjusted to better match experiments and is credible.

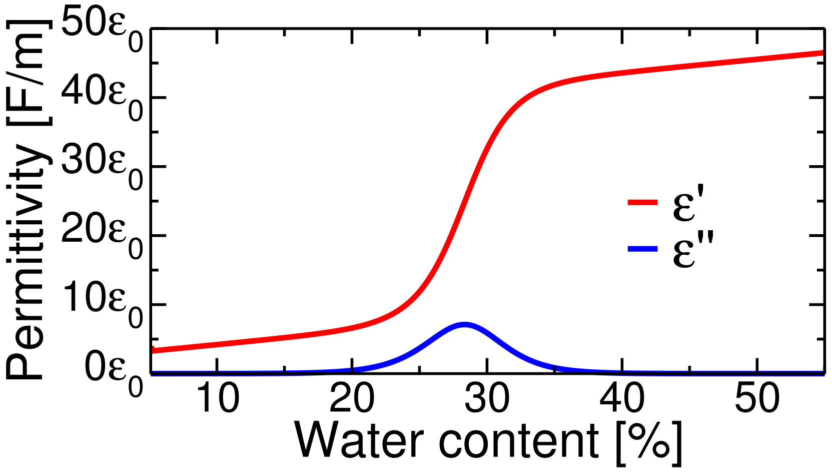

Figure 5.35: *Real (ε') and imaginary (ε'') part of the complex permittivity of BSA ($\varepsilon_{BSA} = \varepsilon' - j\varepsilon''$) as a function of the water content.*

Firstly, the response of a nanoelectrode to neutral polystyrene nanoparticles of different radii ($r_p = [14, 20, 30, 50]$ nm) at 50 MHz is considered. The electrolyte is NaCl 150 mM. The permittivity of polystyrene particles is set to $\varepsilon_p = 2.6\varepsilon_0$. Fig. 5.37 shows the decay profiles of the ΔC_{eff} response along the vertical and lateral direction.

Nanoparticles located in close proximity to the nanoelectrodes ($d_x = d_y = 0$ and $d_z = 0$, i.e. a nanoparticle in contact with the BSA layer added on top of the nanoelectrodes) yield capacitance variations in the range 0.5–10 aF. The signal of the smallest particles is comparable to the noise floor shown in Fig. 5.34, thus identifying $r_p = 14$ nm particles as the smallest sized particles the biosensor platform can detect. The response decays by one order of magnitude if the particles are vertically displaced by d_z=50 nm. Similarly, also the decay along the y-direction is fast. As long as the particles are located on top of the nanoelectrode (i.e. with lateral displacements d_y smaller than the nanoelectrode radius), the response is essentially constant. As soon as the particle moves over the edge of the electrode, a rapid drop of the response is observed: a particle located with a lateral displacement

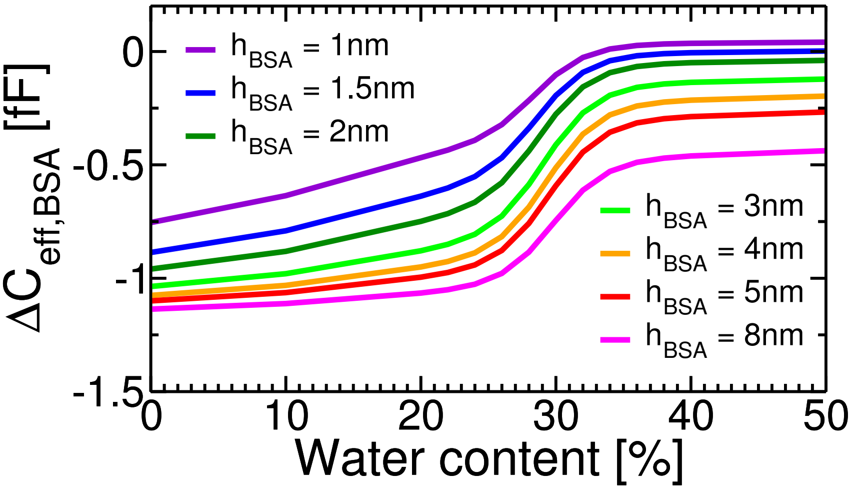

Figure 5.36: *$\Delta C_{eff,BSA} = C_{eff,w/\ BSA} - C_{eff,w/o\ BSA}$ profiles at 50 MHz in NaCl 150 mM, as a function of the hydration state of BSA, for different BSA layer thickness values (h_{BSA}).*

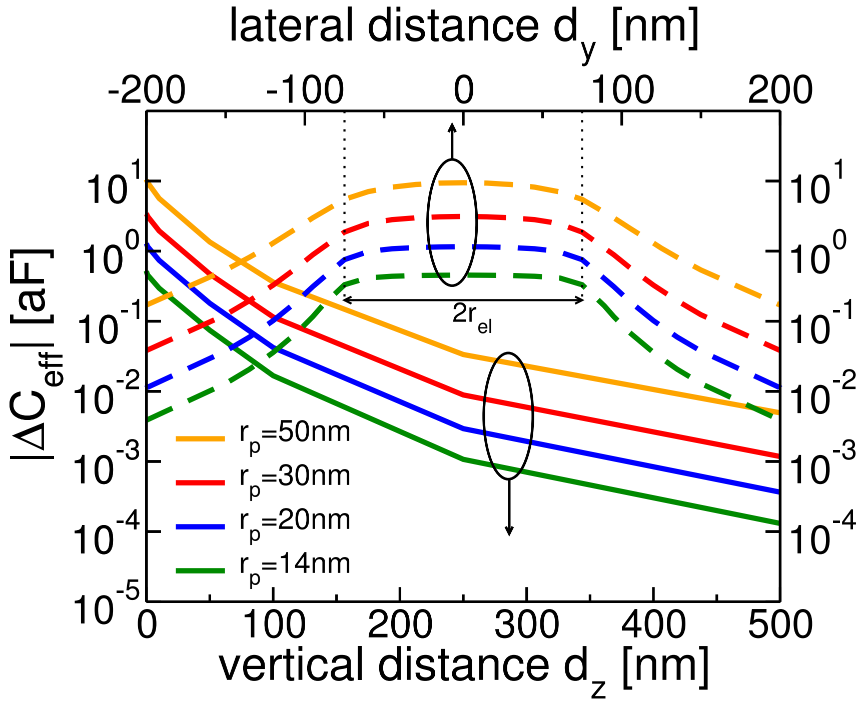

Figure 5.37: *ΔC_{eff} decay profiles for 14, 20, 30, and 50 nm radius polystyrene nanoparticles in 137 mM PBS solution as a function of their vertical elevation (d_z) or lateral displacement (d_y). A 3 nm BSA layer is added on top of the nanoelectrodes. The switching frequency is 50 MHz. Nanoparticles laterally-displaced over the edge of the nanoelectrode (indicated with dotted lines) present a significant drop of the response.*

of d_y= 200 nm from the center of the nanoelectrode yields a capacitance variation of roughly 2-orders of magnitude smaller than the response of the same particle perfectly centered (d_y=0).

Nanoparticles immersed in electrolyte may however have a surface charge, usually dependent on the electrolyte salt concentration.[5]. It would thus be of interest to inspect how surface charges affect the response of the system to nanoparticles. To this end, Fig. 5.38-5.39 show ΔC_{eff} capacitance spectra of the r_p=14 nm and r_p= 50 nm particles, neutral and charged.

From these plots an understanding of how different properties of the analyte affect the response can be derived.

In the high frequency limit, the response to neutral and charged particles is essentially the same. Here the system response is determined solely by the volume and permittivity of the analyte, and by the strength of the electric field in its location [211]. Due to the EDL screening, the low frequency part of the spectra is determined by the properties of the system within a Debye length from the sensor. Consequently, particles located far from the electrode (beyond the EDL) present capacitance spectra which are essentially unaffected by the presence of surface charges (red and orange curves), whereas for particles within the EDL (green and blue/cyan curves) the impact of surface charge is important, since it alters the ion distributions of the EDL. Clearly, the higher the surface charge is, the larger impact it has on the response (see the top plots to the bottom plots).

It can be shown by perturbation theory applied to the PB-PNP model that the capacitance spectra of charged particles are determined by two contributions: one proportional to the particle volume and one proportional to the charge [348]. For a fixed value of surface charge (e.g. -15 mC/m^2, top plots) and in the same experimental conditions (same d_z), the impact surface charge has on the capacitance spectra (w.r.t. the neutral particle case) is progressively smaller for bigger particles (since the charge-related term of ΔC_{eff} contribution remains constant whereas the volume related term increases).

The presence of a surface charge induces an accumulation of counter–ions at the nanoparticle–electrolyte interface, thus creating an EDL. While the physical origin of this EDL is different from the case of conductive particles, we know from Sect. 5.2.2 that the presence of an EDL on the particle can generate *zeros* in the ΔC_{eff} spectra. A zero is indeed visible on the low frequency side of the spectra, in particular for the configurations where the impact of surface charge is greater (i.e. for the smallest particles).

Fig. 5.40 shows again capacitance spectra due to a 14 nm charged particle, in double-log scale, to highlight the existence of the zeros in the ΔC_{eff} spectra. These zeros are induced by the interaction of the EDL on the charged particle with the EDL on the nanoelectrode. Their frequency f_{zl} is lower for higher values of d_z (consistently with the discussion for the conductive particles in Sect. 5.2.2).

---

[5] If knowledge of the surface–potential is available, the surface charge (σ) can be calculated by means of Gouy–Chapman theory as $\sigma = \sqrt{8k_BT\varepsilon_{el}n_0}\,\sinh\left(q\phi/2k_BT\right)$, where ϕ is the surface potential and the other parameters have the usual meaning

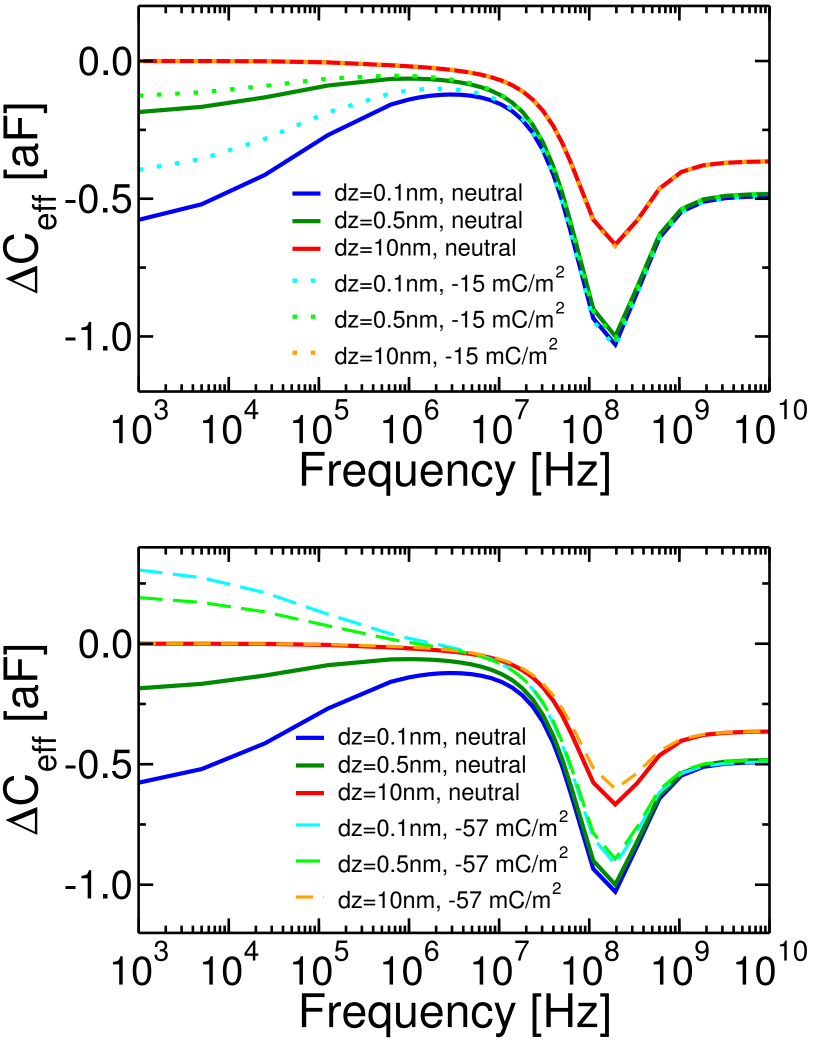

Figure 5.38: *ΔC_{eff} spectra profiles for r_p=14 nm polystyrene particles in 137 mM PBS solution at different values of vertical elevation (d_z) and charge state. Top: comparison between neutral and charged particles, with surface charge of -15 mC/m^2. Bottom: comparison between neutral and charged particles, with surface charge of -57 mC/m^2. Particles located beyond the EDL are essentially not visible at low frequency (d_z=10 nm), and hence their charge state cannot be discriminated. The charge plays a significant role at low frequency, due to the interaction of the EDL of the nanoelectrodes with the EDL on the surface of the charged particle (see also Sect. 5.2.2).*

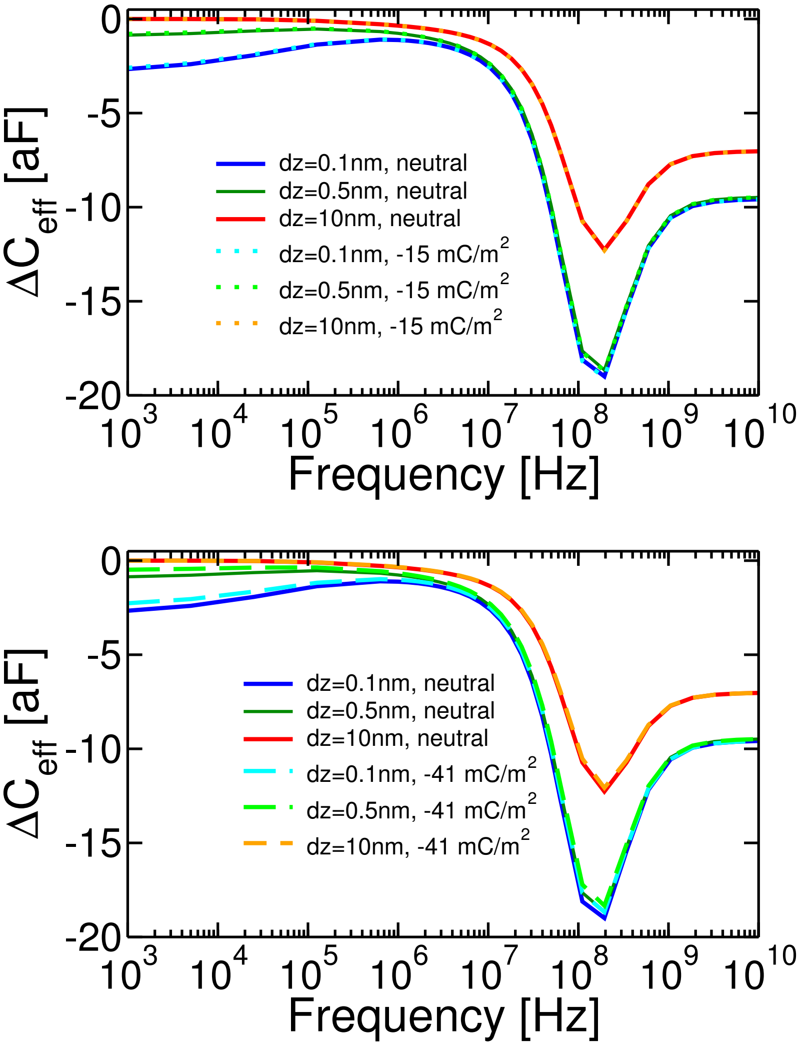

Figure 5.39: *Same as Fig. 5.38 for r_p=50 nm particles.*

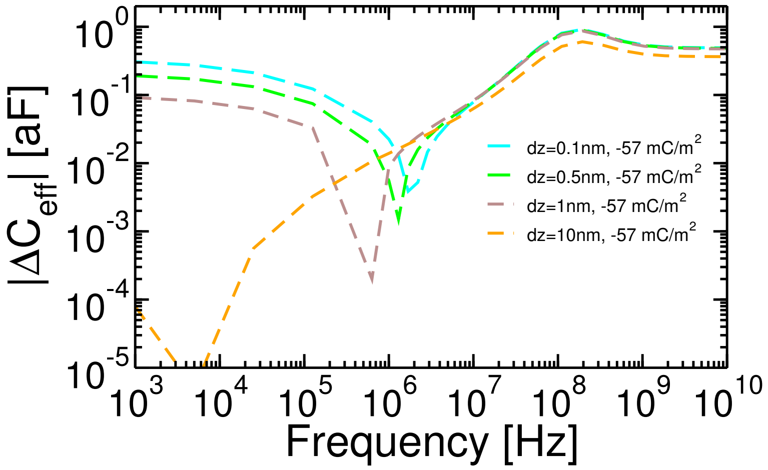

Figure 5.40: *Same as Fig. 5.38 for r_p=14 nm charged particles in double-log scale. Glitches represent sign-changes. LoD ≈ 1 aF.*

Finally, as regards the dependency of the response on the permittivity of the particle, Fig. 5.41 (left) shows ΔC_{eff} spectra of a 50 nm particle located at d_z=10 nm in NaCl 150 mM electrolyte (i.e., beyond the EDL) for varying particle permittivity ε_p. We observe that all curves lie on top of each other, except at frequency beyond the dielectric relaxation cutoff frequency; therefore, different permittivity values can be discriminated only when operating above this frequency. This result is consistent with the analytical model of particle response reported in [211], where the admittance variation due to the insertion of a dielectric particle can be expressed as:

$$\Delta Y = f\left(\omega, \varepsilon_p, \Omega_p, \sigma_{el}, \varepsilon_{el}\right)\left(\sigma_{el} + j\omega\varepsilon_{el}\right)\Omega_p\left(\tilde{E}_0/\tilde{V}_0\right)^2 \tag{5.8}$$

where σ_{el} and ε_{el} are the conductivity and permittivity of the electrolyte, Ω_p is the volume of the analyte, $\tilde{V}_0$ is the applied small-signal voltage, $\tilde{E}_0$ is the value of the unperturbed electric field in the location of the particle, and $f\left(\omega, \varepsilon_p, \Omega_p, \sigma_{el}, \varepsilon_{el}\right)$, the only term where the particle permittivity appears, is a complex function of the angular frequency ω, electrolyte conductivity and permittivity, particle size, and particle permittivity ε_p. This is well illustrated in Fig. 5.41 (right), where the real and imaginary part of the complex function f are shown versus the angular frequency and for different values of the particle permittivity, proving that a discrimination is possible especially at high frequencies.

Consistently with the analysis of Sect. 3.5 (about the influence of the charge on the nanoelectrode response to viruses), these analyses further demonstrate that different portions of the capacitance spectra are sensitive to different analyte parameters (the charge at low frequency, the volume at high frequency), and being able to expand the covered spectrum both at high frequency and low frequency would thus be of great interest.

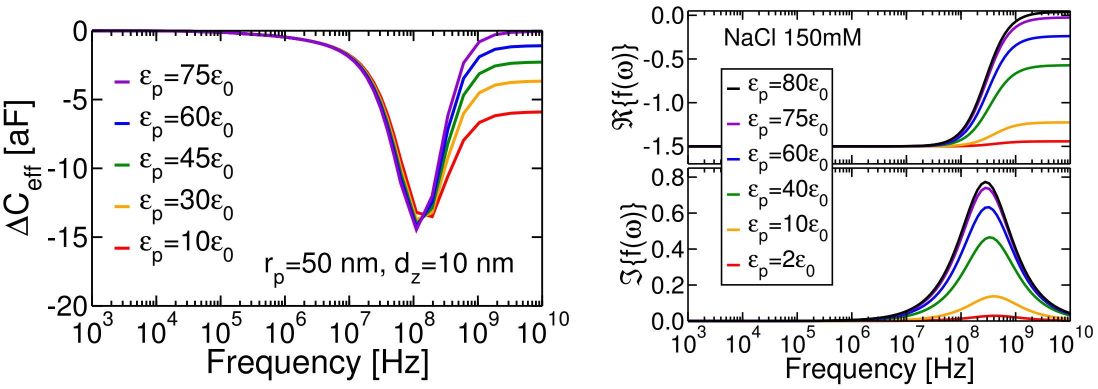

Figure 5.41: *Left: ΔC_{eff} spectra for r_p=50 nm dielectric particles at d_z=10 nm (above a 3 nm BSA layer), for different values of particle permittivity ε_p. The electrolyte is NaCl 150 mM. Right: real and imaginary part of the complex function f of the analytical model of [211], as a function of the frequency, for r_p=50 nm particles with different values of permittivity. The electrolyte is NaCl 150 mM.*

5.4 Summary

This chapter presented HFIS/imaging experiments and simulations of analytes in electrolyte, aimed at characterizing their properties, providing methodologies to support the design of successful experiments, aiding the interpretation of experimental results.

We started by considering the example of oil emulsions in milliQ water (i.e. in the absence of ions and EDL), serving as a meaningful test–case to discuss the problem of determining the size of analytes. Two approaches to map an “apparent size”, calculated according to specific models, to the geometrical size of the analyte were compared by means of ENBIOS simulations. The first approach consists in computing a weighted average of the response at different electrodes, where the weights at each electrode are chosen as the squared distance between the center of mass of the particle and the electrode itself. We showed this estimation method does not reflect so well the Physics. Furthermore, noise analyses revealed significant drawbacks in the presence of physically-random noise. As an alternative, digitalization of capacitance maps was considered. 2D maps of ΔC_{eff} were digitalized by selecting a proper threshold, and the size of the droplets was estimated from its in–plane projection as a weighted sum of the areas of the ON-pixels. The impact of noise was also investigated, proving the robustness of this alternative approach. This approach is simple enough to be embedded in the biosensor platform software, possibly enabling real-time size estimation.

Secondly, we considered dielectric and conductive microparticles in salty electrolytes. On one hand, we showed with silicon dioxide particles the sedimentation process, the formation of particle aggregates, and the possible unbinding of particles from the array surface. Parameters estimation based on the MCMC led to estimate the size and position of the particles and of multi-particle agglomerates. Capacitance spectra computed using the extracted parameter values yield an unprecedented agreement with measured HFIS spectra.

On the other hand, distinct signatures of the nanoelectrode response to conductive particles were examined and explained. While dielectric particles yield negative ΔC_{eff} over the whole spectrum (due to the replacement of part of the electrolyte volume with a lower permittivity material), conductive particles exhibit sign changes in the ΔC_{eff} spectra. They behave as dielectric particles at low frequencies, but cause an increase of capacitance ($\Delta C_{eff} > 0$) at high frequency. The physical mechanism at the basis of this phenomenon was unambiguously identified in the formation of an EDL on the particle, and the dependencies on a number of relevant parameters were studied.

Finally, stimulated by the outstanding detection capabilities of the nanoelectrode array platform, analyses of the functional dependencies of the response to small nanoparticles were reported. ΔC_{eff} spectra of dielectric and charged particles were shown, discussing the spatial decay profiles and the appearance of frequencies of “zero” response for charged particles, due to the interaction of the EDL of the particles with the EDL of the electrodes. The experimental noise of the platform and the simulations suggest that particles as small as r_p= 14 nm might be detected; this defines the size limit of detection. Detection of such a small capacitance with as good a time-resolution (Fig. 5.34) would be essentially impossible with a macro- or microelectrode.

The author's contributions to this chapter include the numerical simulations of oil droplets and the development of calibration curves for estimating their size, the experiments with SiO_2 microparticles and the corresponding ENBIOS simulations, the numerical simulations and analyses of dielectric and conductive particles, and the simulations of nanoparticles (experiments of the University of Twente).

Conclusions and Outlook

This thesis investigated new methods, models, characterizations and analyses techniques to expand the opportunities of electronic nanobiosensing offered by innovative high-frequency impedance spectroscopy CMOS platforms. A number of aspects have been addressed with the goal of improving the stability, reproducibility and accuracy of experimental conditions, highlighting new physical effects, understanding the quantitative details of measurements, predicting the system response to variety of analytes, and confirming predictions with experiments, all based on a 90 nm CMOS chip developed by NXP Semiconductors. Among these system developments: modeling, simulations, characterization, calibrations, experiments, statistical analyses. In summary, the main goal of this work has been to improve the measurement system and demonstrate its capabilities from the quantitative point of view (with the aid of analytical, numerical and statistical models), helping the understanding and characterization of the features that influence the outcome of experiments.

The main achievements reported in this thesis can be summarized as follows:

- Development and implementation of a temperature-controlled general-purpose test setup and of calibration and compensation procedures that enabled unprecedented quantitative agreement between HFIS experiments at nanoscale electrodes and simulations over a range of frequencies (1–70 MHz) extending well above those typical for EIS measurements (< 1 MHz) and a range of electrolyte salt concentrations up to physiological conditions. These include methodologies to account for non-idealities of the readout circuitry, such as the presence of leakage currents and the non-idealities of the voltage waveforms.

- Detailed modeling and simulation of the nanoelectrode experimental response to a variety of microscale analytes, including dielectric and conductive particles, which highlighted a new previously overlooked phenomenon of sign change in the frequency spectrum of ΔC. This includes quantitative understanding of all features of the measured spectra and the development of correction curves for a fast estimation of the size of nearly spherical analytes of known electrical properties, and identification of complex analyte behaviors such as motility, aggregation, disaggregation.

- Identification of the features of the nanoelectrode response to nanoscale analytes and understanding of the influence of the analyte charge; this includes the development of compact FEM models of the nanoelectrode response to complex virus biomolecules starting from atomistic descriptions and application to the identification of single virus detectability limits.

- Application of advanced Bayesian statistics to the estimation and uncertainty quantification for the parameters of the biosensor system and of the analytes.

All these achievements enable *quantitative* high-frequency impedance spectroscopy analyses with nanoelectrode biosensors. Furthermore, the experience gained in the use of existing FEM simulators contributed to the realization of two tools (powered by the in-house developed ENBIOS code) that have been made available to the scientific community for research and teaching purposes via the nanoHUB.org portal.

The CMOS pixelated nanocapacitor biosensor platform investigated in this thesis proved to be a unique system in the nanobiosensors scenario, thanks to the unprecedented high-frequency of operation with nanoscale electrodes, the real-time imaging capabilities, the massively parallel implementation, and the low power consumption. The extensive quantitative analyses, together with the corresponding lessons learned during the development, appear as fundamental ingredients to enable further progress of this nanobiosensing approach, possibly based on improved versions of the platform or new implementations optimized for specific applications. Our vision regarding possible future development includes:

- Scaling of the design, following Moore's law, while improving the noise floor. Smaller nanoelectrodes would enable the detection of even smaller analytes (see Fig. 1.9) [209], and smaller intra-electrodes pitch would result in improved imaging resolutions. For example, an implementation with the 40 nm node would yield a 3× shrink of the cell's area, enabling resolution comparable to those of optical microscopes in the visible range [210]. The latest CMOS technology nodes would go even further in this direction.
- Extension of the nanoelectrode addressing/readout approach (currently based on a row-wise nanoelectrode excitation pattern), to enable the readout and excitation of individual distinct nanoelectrodes. This requires an important re-design of the chip, but would enable interesting and different applications such as impedance tomography.
- Integration of the chip within stand-alone low-power IoT modules, enabling pervasive sensing also of non-*bio* analytes (e.g. gas/airborne particles detection), or integration of multiple (tens, hundreds, ...) chips running in parallel to support high-throughput applications at low cost and using small sample volumes (e.g. drug discovery, DNA sequencing, ...).

Finally, we propose a few more detailed key points of development we believe would be highly desirable, both from the hardware/experimental and from the modeling/simulations/signal processing point of view:

- *Hardware/Experimental*: extension of the maximum measurement frequency of the platform above the electrolyte dielectric relaxation frequency at physiological salt concentrations (this is possible with the existing chip, which can operate up to 320 MHz, but requires a redesign of the board and the connections); miniaturization and automatization of the microfluidic setup, together with an accurate temperature control of the incoming liquids (independent from the controller that regulates the operating temperature of the chip); development of nanoelectrode surface modification techniques to combine the high sensitivity with selectivity features.

- *Numerics*: development of large-signal non-linear simulation tools of the sensor array and electrolyte environment (e.g., by means of harmonic-balance techniques, to overcome the limitations induced by the small-signal hypothesis); development of automated procedures to assign charges and material properties to individual tetrahedrons of the mesh (e.g. starting from atomistic descriptions, in order to overcome the averaging procedures and enable more accurate molecule descriptions at reduced computational cost); investigation of more case studies for analytes (such as bacteria and cells) to build a library of the qualitative and quantitative features of the nanoelectrode response to different analytes suited to steer experiments in application areas of high impact.

We hope that the latest advancements and the quantitative developments reported in this thesis will attract the interest of researchers towards this platform or similar implementations, which demonstrated numerous benefits for large-scale and low-cost biosensing at the nanoscale in the context of Global Health and Internet-of-Things.

A Switching Capacitance: derivation

Here we derive analytical expressions of the *switching capacitance* for different circuit configurations under the following sequence of bias conditions:

- **Phase I**: charging ($0 < t < t_1$)
- **Phase II**: floating ($t_1 < t < t_2$)
- **Phase III**: discharging ($t_2 < t < t_3$)
- **Phase IV**: floating ($t_3 < t < t_4$)

repeating indefinitely over time ($\implies$ imposing $t_4 = 0$ and starting all over again).

The methodology of analysis is well known in the study of charge-pump circuits and will be first applied on a simple C-RC circuit, then on more elaborated R-C configurations.

A.1 C-RC circuit

We start the analysis with the C-RC circuit in Fig. A.1.

A.1.1 Phase I: charging

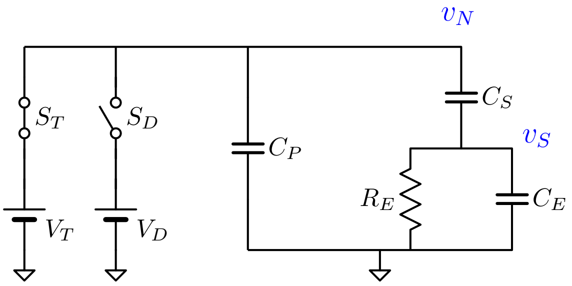

Figure A.1: *Equivalent circuit for the calculation of the switching capacitance according to the C-RC circuit during the charging phase.*

We consider at first the closing of switch S_T occurring at $t = 0^+$, and remaining closed until $t = t_1^-$. Kirchhoff's Current Law (KCL) leads to:

$$C_S \frac{dv_n}{dt} - C_S \frac{dv_S}{dt} = \frac{v_S}{R_E} + C_E \frac{dv_S}{dt} \tag{A.1}$$

Laplace Transform (LT) is applied. Closing the switch S_T results in a Heaviside step input $(V_T - v_N(0^-))\,\mathbf{1}(0)$ (where $\mathbf{1}(t)$ is the Heaviside step function), whose LT reads $(V_T - v_N(0^-))/s$. This leads to:

$$C_S \left(V_T - v_n\left(0^-\right)\right) - sC_S V_S + C_S v_S\left(0^-\right) = \frac{V_S}{R_E} + sC_E V_S - C_E v_S\left(0^-\right) \tag{A.2}$$

Hence, the voltage at the Stern layer interface takes the following form:

$$V_S \;=\; H^{\mathrm{I}}_{(V_S,v_N)} \left(V_T - v_N\left(0^-\right)\right) + H^{\mathrm{I}}_{(V_S,v_S)} v_S\left(0^-\right) \tag{A.3}$$

where we defined the transfer functions of phase I:

$$\begin{aligned} H^{\mathrm{I}}_{(V_S,v_N)} &= \frac{p_a}{s + 1/\tau_a} \\ H^{\mathrm{I}}_{(V_S,v_S)} &= \frac{1}{s + 1/\tau_a} \end{aligned} \tag{A.4}$$

where $\tau_a = R_E\left(C_S + C_E\right)$ is the time constant of the charging process, and $p_a = C_S/\left(C_S + C_E\right)$ is the capacitance-divider factor.

Inverse Laplace Transform (ILT) allows to express the voltage v_S at the end of the charging phase ($t = t_1$) as a function of the voltage values at the beginning of the charging phase. The voltage at the end of the charging phase thus becomes:

$$\begin{aligned} v_N\left(t_1\right) &= V_T \\ v_S\left(t_1\right) &= \left[v_S\left(0^-\right) + \left(V_T - v_N\left(0^-\right)\right) p_a\right] \exp\left(-\frac{t_1}{\tau_a}\right) \end{aligned} \tag{A.5}$$

A.1.2 Phase II: charge redistribution

At $t = t_1$ the switch S_T opens and charge redistribution occurs. KCL results in:

$$\begin{aligned} -C_P \frac{dv_N}{dt} &= C_S \frac{dv_N}{dt} - C_S \frac{dv_S}{dt} \\ -C_P \frac{dv_N}{dt} &= \frac{v_S}{R_E} + C_E \frac{dv_S}{dt} \end{aligned} \tag{A.6}$$

Isolating the dv_N/dt term in the first equation of (A.6) and substituting it in the second equation leads to:

$$C_S \frac{dv_S}{dt} = -\frac{C_S + C_P}{R_E C_P} v_S - \frac{\left(C_S + C_P\right) C_E}{C_P} \frac{dv_S}{dt} \tag{A.7}$$

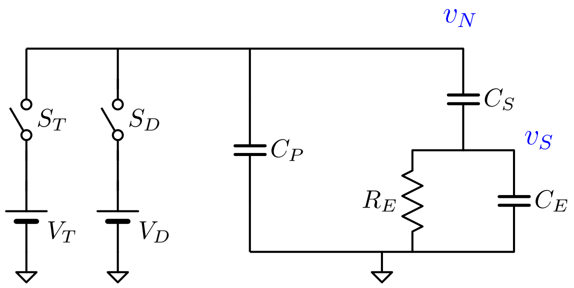

Figure A.2: *Equivalent circuit for the calculation of the switching capacitance according to the C-RC circuit during the charge redistribution phase.*

Application of LT and straightforward calculations let us express:

$$V_S = H^{\mathrm{II}}_{(V_S,v_S)} v_S\left(t_1^-\right) \tag{A.8}$$

where the transfer function of V_S of phase II is:

$$H^{\mathrm{II}}_{(V_S,v_S)} = \frac{1}{s + 1/\tau_b} \tag{A.9}$$

with $\tau_b = R_E\left(C_S C_P/\left(C_S + C_P\right) + C_E\right)$ being the time constant of the charge repartition.

As regards the voltage at the switching node, LT on the second equation of (A.6) and substitution of V_S allows to express:

$$V_N = H^{\mathrm{II}}_{(V_N,v_N)} v_N\left(t_1^-\right) + H^{\mathrm{II}}_{(V_N,v_S)} v_S\left(t_1^-\right) \tag{A.10}$$

where the transfer functions of V_N of phase II are:

$$\begin{aligned} H^{\mathrm{II}}_{(V_N,v_N)} &= \frac{1}{s} \\ H^{\mathrm{II}}_{(V_N,v_S)} &= \frac{C_S}{C_S + C_P}\left(\frac{1}{s + 1/\tau_b} - \frac{1}{s}\right) \end{aligned} \tag{A.11}$$

Finally, ILT allows us to express the voltage at the end of the charge-redistribution phase $(t = t_2)$ as:

$$\begin{aligned} v_N\left(t_2\right) &= V_T + \frac{C_S}{C_S + C_P}\left[\exp\left(-\frac{t_2 - t_1}{\tau_b}\right) - 1\right] v_S\left(t_1\right) \\ v_S\left(t_2\right) &= \exp\left(-\frac{t_2 - t_1}{\tau_b}\right) v_S\left(t_1\right) \end{aligned} \tag{A.12}$$

A.1.3 Phase III: discharging

Now we consider the discharging phase $(t_2 < t < t_3)$. Due to the symmetry of the configuration, the final result can be easily adapted from the discussion of Sect. A.1.1. Eq. (A.5) for this case becomes:

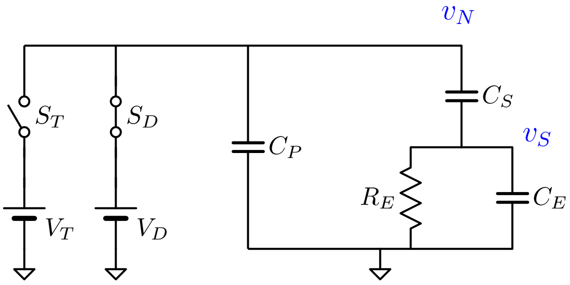

Figure A.3: *Equivalent circuit for the calculation of the switching capacitance according to the C-RC circuit during the discharging phase.*

$$\begin{aligned} v_N\left(t_3\right) &= V_D \\ v_S\left(t_3\right) &= \left[v_S\left(t_2^-\right) + \left(V_D - v_N\left(t_2^-\right)\right) p_a\right] \exp\left(-\frac{t_3 - t_2}{\tau_a}\right) \end{aligned} \tag{A.13}$$

A.1.4 Phase IV: charge redistribution

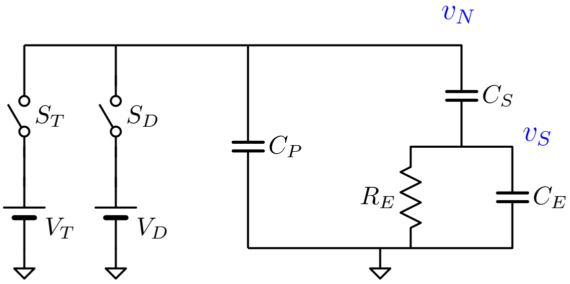

Figure A.4: *Equivalent circuit for the calculation of the switching capacitance according to the C-RC circuit during the charge redistribution phase.*

Finally, we consider the second charge-redistribution phase ($t_3 < t < t_4$). Again, the final configuration is easily obtained adapting Eq. (A.12):

$$\begin{aligned} v_N\left(t_4\right) &= V_D + \frac{C_S}{C_S + C_P}\left[\exp\left(-\frac{t_4 - t_3}{\tau_b}\right) - 1\right] v_S\left(t_3\right) \\ v_S\left(t_4\right) &= \exp\left(-\frac{t_4 - t_3}{\tau_b}\right) v_S\left(t_3\right) \end{aligned} \tag{A.14}$$

A.1.5 Calculation of the switching capacitance

The switching node (which is connected to capacitors C_S and C_P) is alternatively biased at V_T and V_D. We can compute the *switching capacitance* (C_{SW}) as:

$$C_{SW} = \frac{Q_{charge}}{V_T - V_D} = \frac{Q_{charge}\left(C_S + C_P\right)}{\left(C_S + C_P\right)\left(V_T - V_D\right)} = \gamma\left(C_S + C_P\right) \tag{A.15}$$

where we considered the charge pumped onto the switching node during each cycle (Q_{charge}) and we defined the *charge pump efficiency factor*

$$\gamma = \frac{Q_{charge}}{\left(C_S + C_P\right)\left(V_T - V_D\right)} \tag{A.16}$$

The charge transferred from the charging to the discharging node can be easily calculated as:

$$Q_{charge} = C_P\left[V_T - v_N\left(t_4\right)\right] + C_S\left[\left(V_T - v_S\left(t_1\right)\right) - \left(v_N\left(t_4\right) - v_S\left(t_4\right)\right)\right] \tag{A.17}$$

Because of the stationary repetitive cycling of the charging/discharging operations, the initial state of phase I is equal to the final state of phase IV. Then, setting $t_4 = 0$ and combining Equations (A.5)-(A.12)-(A.13)-(A.14) allows to obtain a closed-form expression of the voltage at the end of each individual phase.

Straightforward calculations lead to this final expression for the efficiency factor:

$$\gamma = 1 - p_a p_b \frac{e_1\left(1 - e_3\left(e_4 + \left(1 - e_4\right) p_b p_a\right)\right) + e_3\left(1 - e_1\left(e_2 + \left(1 - e_2\right) p_b p_a\right)\right)}{1 - e_1\left(e_2 + \left(1 - e_2\right) p_b p_a\right) e_3\left(e_4 + \left(1 - e_4\right) p_b p_a\right)} \tag{A.18}$$

where we defined $e_1 = \exp\left(-t_1/\tau_a\right)$, $e_2 = \exp\left(-\left(t_2 - t_1\right)/\tau_b\right)$, $e_3 = \exp\left(-\left(t_3 - t_2\right)/\tau_a\right)$, $e_4 = \exp\left(-\left(t_4 - t_3\right)/\tau_b\right)$.

A.2 C-RC-RC circuit

We now consider a C-RC-RC topology.

A.2.1 Phase I: charging

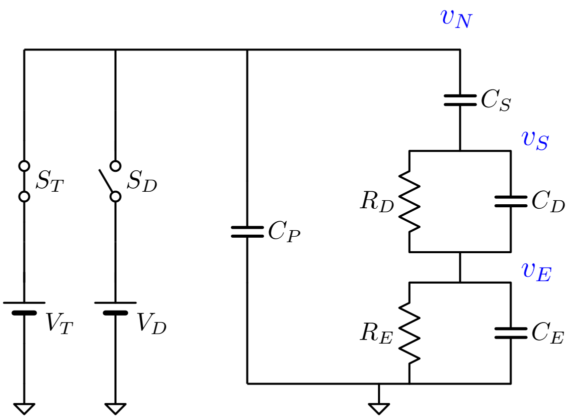

Figure A.5: *Equivalent circuit for the calculation of the switching capacitance according to the C-RC-RC circuit during the charging phase.*

We consider at first the closing of switch S_T (occurring at $t = 0^-$, and remaining closed until $t = t_1^-$). KCL leads to:

$$\begin{aligned} C_S \frac{dv_n}{dt} - C_S \frac{dv_S}{dt} &= \frac{v_S - v_E}{R_D} + C_D \frac{dv_S}{dt} - C_D \frac{dv_E}{dt} \\ C_S \frac{dv_n}{dt} - C_S \frac{dv_S}{dt} &= \frac{v_E}{R_E} + C_E \frac{dv_E}{dt} \end{aligned} \tag{A.19}$$

LT: determination of the transfer functions

The switching node gets connected to V_T. LT leads to:

$$\begin{aligned} C_S \left(V_T - v_n\left(0^-\right)\right) - sC_S V_S + C_S v_S\left(0^-\right) &= \\ \frac{V_S}{R_D} - \frac{V_E}{R_D} + sC_D V_S - C_D v_S\left(0^-\right) &- sC_D V_E + C_D v_E\left(0^-\right) \\ C_S \left(V_T - v_n\left(0^-\right)\right) - sC_S V_S + C_S v_S\left(0^-\right) &= \frac{V_E}{R_E} + sC_E V_E - C_E v_E\left(0^-\right) \end{aligned} \tag{A.20}$$

Calculations on this system of two equations in two unknowns (V_S and V_E) leads to:

$$\begin{aligned} V_S &= H^{\mathrm{I}}_{(V_S,v_N)} \left(V_T - v_N\left(0^-\right)\right) + H^{\mathrm{I}}_{(V_S,v_S)} v_S\left(0^-\right) + H^{\mathrm{I}}_{(V_S,v_E)} v_E\left(0^-\right) \\ V_E &= H^{\mathrm{I}}_{(V_E,v_N)} \left(V_T - v_N\left(0^-\right)\right) + H^{\mathrm{I}}_{(V_E,v_S)} v_S\left(0^-\right) + H^{\mathrm{I}}_{(V_E,v_E)} v_E\left(0^-\right) \end{aligned} \tag{A.21}$$

where the transfer functions at phase I (we indicate as $H^{\mathrm{i}}_{(V_X,v_Y)}$ the transfer function in phase i going from v_Y to V_X) are:

$$\begin{aligned}
H^{\mathrm{I}}_{(V_S,v_N)} &= \frac{n^{\mathrm{I},0}_{(S,N)} + s \cdot n^{\mathrm{I},1}_{(S,N)}}{1 + s \cdot d^{\mathrm{I},1}_{S} + s^2 \cdot d^{\mathrm{I},2}_{S}} \\
H^{\mathrm{I}}_{(V_S,v_S)} &= \frac{n^{\mathrm{I},0}_{(S,S)} + s \cdot n^{\mathrm{I},1}_{(S,S)}}{1 + s \cdot d^{\mathrm{I},1}_{S} + s^2 \cdot d^{\mathrm{I},2}_{S}} \\
H^{\mathrm{I}}_{(V_S,v_E)} &= \frac{n^{\mathrm{I},0}_{(S,E)}}{1 + s \cdot d^{\mathrm{I},1}_{S} + s^2 \cdot d^{\mathrm{I},2}_{S}} \\
H^{\mathrm{I}}_{(V_E,v_N)} &= \frac{n^{\mathrm{I},0}_{(E,N)} + s \cdot n^{\mathrm{I},1}_{(E,N)}}{1 + s \cdot d^{\mathrm{I},1}_{E} + s^2 \cdot d^{\mathrm{I},2}_{E}} \\
H^{\mathrm{I}}_{(V_E,v_S)} &= \frac{n^{\mathrm{I},0}_{(E,S)}}{1 + s \cdot d^{\mathrm{I},1}_{E} + s^2 \cdot d^{\mathrm{I},2}_{E}} \\
H^{\mathrm{I}}_{(V_E,v_E)} &= \frac{n^{\mathrm{I},0}_{(E,E)} + s \cdot n^{\mathrm{I},1}_{(E,E)}}{1 + s \cdot d^{\mathrm{I},1}_{E} + s^2 \cdot d^{\mathrm{I},2}_{E}}
\end{aligned} \tag{A.22}$$

Here we used a compact notation expressing with $n^{\mathrm{i,j}}_{(X,Y)}$ the j-th order polynomial coefficient of the complex variable s at the *numerator* of the transfer function $H^{\mathrm{i}}_{(V_X,v_Y)}$, and with $d^{\mathrm{i,j}}_{X}$ the j-th order polynomial coefficient of the complex variable s at the *denominator* of the transfer function $H^{\mathrm{i}}_{(V_X,v_\square)}$ (where there is no need to specify the source term $v_\square$ because in this case the denominator is the same for all the transfer functions going to V_X).

The values of the *denominator* coefficients for phase I are the following:

$d^{\mathrm{I},1}_{S} = d^{\mathrm{I},1}_{E} = R_D\left(C_S + C_D\right) + R_E\left(C_S + C_E\right)$

$d^{\mathrm{I},2}_{S} = d^{\mathrm{I},2}_{E} = R_D R_E\left(C_S C_D + C_S C_E + C_D C_E\right)$

The values of the *numerator* coefficients for phase I are the following:

$n^{\mathrm{I},0}_{(S,N)} = C_S\left(R_D + R_E\right)$

$n^{\mathrm{I},1}_{(S,N)} = R_D R_E C_S\left(C_D + C_E\right)$

$n^{\mathrm{I},0}_{(S,S)} = R_D C_D + C_S\left(R_D + R_E\right)$

$n^{\mathrm{I},1}_{(S,S)} = R_D R_E\left(C_S C_D + C_S C_E + C_D C_E\right)$

$n^{\mathrm{I},0}_{(S,E)} = R_E C_E - R_D C_D$

$n^{\mathrm{I},0}_{(E,N)} = R_E C_S$

$n^{\mathrm{I},1}_{(E,N)} = R_D R_E C_S C_D$

$n^{\mathrm{I},0}_{(E,S)} = R_E C_S$

$n^{\mathrm{I},0}_{(E,E)} = R_E C_E$

$n^{\mathrm{I},1}_{(E,E)} = R_D R_E\left(C_S C_D + C_S C_E + C_D C_E\right)$

ILT: determination of the waveforms

ILT applied to Equations (A.21) allows to express the node-voltages at $t = t_1$ as:

$$\begin{aligned}
v_N\left(t_1\right) =& V_T \\
v_S\left(t_1\right) =& \mathscr{E}^{\mathrm{I}}_{(v_S,v_N)}\left(V_T - v_N\left(0^-\right)\right) + \mathscr{E}^{\mathrm{I}}_{(v_S,v_S)} v_S\left(0^-\right) + \mathscr{E}^{\mathrm{I}}_{(v_S,v_E)} v_E\left(0^-\right) \\
v_E\left(t_1\right) =& \mathscr{E}^{\mathrm{I}}_{(v_E,v_N)}\left(V_T - v_N\left(0^-\right)\right) + \mathscr{E}^{\mathrm{I}}_{(v_E,v_S)} v_S\left(0^-\right) + \mathscr{E}^{\mathrm{I}}_{(v_E,v_E)} v_E\left(0^-\right)
\end{aligned} \tag{A.23}$$

where we introduced the symbols $\mathscr{E}^{\mathrm{i}}_{(v_X,v_Y)}$ representing exponential functions during phase i expressing the dependency of v_X from v_Y.

These functions take the following form:

$$\begin{aligned}
\mathscr{E}^{\mathrm{I}}_{(v_S,v_N)} =& \frac{\exp\left(-\frac{d_S^{\mathrm{I},1}+\sqrt{\left(d_S^{\mathrm{I},1}\right)^2-4d_S^{\mathrm{I},2}}}{2d_S^{\mathrm{I},2}}t_1\right)}{2d_S^{\mathrm{I},2}\sqrt{\left(d_S^{\mathrm{I},1}\right)^2-4d_S^{\mathrm{I},2}}}\left(2d_S^{\mathrm{I},2}n^{\mathrm{I},0}_{(S,N)}\left(-1+\exp\left(\frac{\sqrt{\left(d_S^{\mathrm{I},1}\right)^2-4d_S^{\mathrm{I},2}}}{d_S^{\mathrm{I},2}}t_1\right)\right)\right. \cdot \\
& n^{\mathrm{I},1}_{(S,N)}\left(d_S^{\mathrm{I},1}\left(1-\exp\left(\frac{\sqrt{\left(d_S^{\mathrm{I},1}\right)^2-4d_S^{\mathrm{I},2}}}{d_S^{\mathrm{I},2}}t_1\right)\right)\right. + \\
& \left.\left.\sqrt{\left(d_S^{\mathrm{I},1}\right)^2-4d_S^{\mathrm{I},2}}\left(1+\exp\left(\frac{\sqrt{\left(d_S^{\mathrm{I},1}\right)^2-4d_S^{\mathrm{I},2}}}{d_S^{\mathrm{I},2}}t_1\right)\right)\right)\right)
\end{aligned}$$

$$\begin{aligned}
\mathscr{E}^{\mathrm{I}}_{(v_S,v_S)} =& \frac{\exp\left(-\frac{d_S^{\mathrm{I},1}+\sqrt{\left(d_S^{\mathrm{I},1}\right)^2-4d_S^{\mathrm{I},2}}}{2d_S^{\mathrm{I},2}}t_1\right)}{2d_S^{\mathrm{I},2}\sqrt{\left(d_S^{\mathrm{I},1}\right)^2-4d_S^{\mathrm{I},2}}}\left(2d_S^{\mathrm{I},2}n^{\mathrm{I},0}_{(S,S)}\left(-1+\exp\left(\frac{\sqrt{\left(d_S^{\mathrm{I},1}\right)^2-4d_S^{\mathrm{I},2}}}{d_S^{\mathrm{I},2}}t_1\right)\right)\right. \cdot \\
& n^{\mathrm{I},1}_{(S,S)}\left(d_S^{\mathrm{I},1}\left(1-\exp\left(\frac{\sqrt{\left(d_S^{\mathrm{I},1}\right)^2-4d_S^{\mathrm{I},2}}}{d_S^{\mathrm{I},2}}t_1\right)\right)\right. + \\
& \left.\left.\sqrt{\left(d_S^{\mathrm{I},1}\right)^2-4d_S^{\mathrm{I},2}}\left(1+\exp\left(\frac{\sqrt{\left(d_S^{\mathrm{I},1}\right)^2-4d_S^{\mathrm{I},2}}}{d_S^{\mathrm{I},2}}t_1\right)\right)\right)\right)
\end{aligned}$$

$$\mathscr{E}^{\mathrm{I}}_{(v_S,v_E)} = \frac{\exp\left(-\frac{d_S^{\mathrm{I},1}+\sqrt{\left(d_S^{\mathrm{I},1}\right)^2-4d_S^{\mathrm{I},2}}}{2d_S^{\mathrm{I},2}}t_1\right)}{\sqrt{\left(d_S^{\mathrm{I},1}\right)^2-4d_S^{\mathrm{I},2}}}\left(n^{\mathrm{I},0}_{(S,E)}\left(-1+\exp\left(\frac{\sqrt{\left(d_S^{\mathrm{I},1}\right)^2-4d_S^{\mathrm{I},2}}}{d_S^{\mathrm{I},2}}t_1\right)\right)\right)$$

$$
\begin{aligned}
\mathscr{E}^{\mathrm{I}}_{(v_E,v_N)} = & \frac{\exp\left(-\frac{d_E^{\mathrm{I},1}+\sqrt{\left(d_E^{\mathrm{I},1}\right)^2-4d_E^{\mathrm{I},2}}}{2d_E^{\mathrm{I},2}}t_1\right)}{2d_E^{\mathrm{I},2}\sqrt{\left(d_E^{\mathrm{I},1}\right)^2-4d_E^{\mathrm{I},2}}} \Bigg(2d_E^{\mathrm{I},2} n^{\mathrm{I},0}_{(E,N)}\left(-1+\exp\left(\frac{\sqrt{\left(d_E^{\mathrm{I},1}\right)^2-4d_E^{\mathrm{I},2}}}{d_E^{\mathrm{I},2}}t_1\right)\right)\cdot \\
& n^{\mathrm{I},1}_{(E,N)}\Bigg(d_E^{\mathrm{I},1}\left(1-\exp\left(\frac{\sqrt{\left(d_E^{\mathrm{I},1}\right)^2-4d_E^{\mathrm{I},2}}}{d_E^{\mathrm{I},2}}t_1\right)\right)+ \\
& \sqrt{\left(d_E^{\mathrm{I},1}\right)^2-4d_E^{\mathrm{I},2}}\left(1+\exp\left(\frac{\sqrt{\left(d_E^{\mathrm{I},1}\right)^2-4d_E^{\mathrm{I},2}}}{d_E^{\mathrm{I},2}}t_1\right)\right)\Bigg)\Bigg)
\end{aligned}
$$

$$
\mathscr{E}^{\mathrm{I}}_{(v_E,v_S)} = \frac{\exp\left(-\frac{d_E^{\mathrm{I},1}+\sqrt{\left(d_E^{\mathrm{I},1}\right)^2-4d_E^{\mathrm{I},2}}}{2d_E^{\mathrm{I},2}}t_1\right)}{\sqrt{\left(d_E^{\mathrm{I},1}\right)^2-4d_E^{\mathrm{I},2}}} \left(n^{\mathrm{I},0}_{(E,S)}\left(-1+\exp\left(\frac{\sqrt{\left(d_E^{\mathrm{I},1}\right)^2-4d_E^{\mathrm{I},2}}}{d_E^{\mathrm{I},2}}t_1\right)\right)\right)
$$

$$
\begin{aligned}
\mathscr{E}^{\mathrm{I}}_{(v_E,v_E)} = & \frac{\exp\left(-\frac{d_E^{\mathrm{I},1}+\sqrt{\left(d_E^{\mathrm{I},1}\right)^2-4d_E^{\mathrm{I},2}}}{2d_E^{\mathrm{I},2}}t_1\right)}{2d_E^{\mathrm{I},2}\sqrt{\left(d_E^{\mathrm{I},1}\right)^2-4d_E^{\mathrm{I},2}}} \Bigg(2d_E^{\mathrm{I},2} n^{\mathrm{I},0}_{(E,E)}\left(-1+\exp\left(\frac{\sqrt{\left(d_E^{\mathrm{I},1}\right)^2-4d_E^{\mathrm{I},2}}}{d_E^{\mathrm{I},2}}t_1\right)\right)\cdot \\
& n^{\mathrm{I},1}_{(E,E)}\Bigg(d_E^{\mathrm{I},1}\left(1-\exp\left(\frac{\sqrt{\left(d_E^{\mathrm{I},1}\right)^2-4d_E^{\mathrm{I},2}}}{d_E^{\mathrm{I},2}}t_1\right)\right)+ \\
& \sqrt{\left(d_E^{\mathrm{I},1}\right)^2-4d_E^{\mathrm{I},2}}\left(1+\exp\left(\frac{\sqrt{\left(d_E^{\mathrm{I},1}\right)^2-4d_E^{\mathrm{I},2}}}{d_E^{\mathrm{I},2}}t_1\right)\right)\Bigg)\Bigg)
\end{aligned}
$$

A.2.2 Phase II: charge redistribution

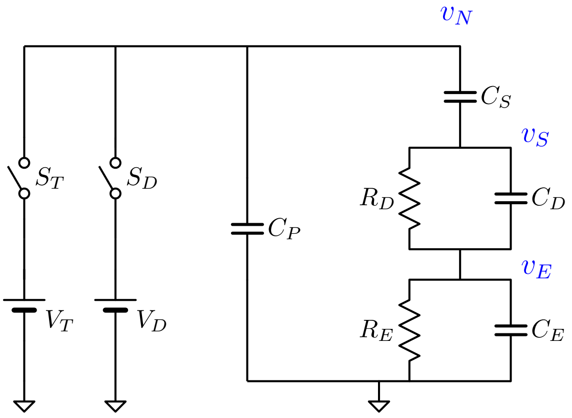

Figure A.6: *Equivalent circuit for the calculation of the switching capacitance according to the C-RC-RC circuit during the charge redistribution phase.*

At $t = t_1$ the switch S_T opens and charge redistribution occurs. KCL results in:

$$\begin{aligned}
-C_P\frac{dv_n}{dt} &= C_S\frac{dv_n}{dt} - C_S\frac{dv_S}{dt}\\
-C_P\frac{dv_n}{dt} &= \frac{v_S - v_E}{R_D} + C_D\frac{dv_S}{dt} - C_D\frac{dv_E}{dt}\\
-C_P\frac{dv_n}{dt} &= \frac{v_E}{R_E} + C_E\frac{dv_E}{dt}
\end{aligned} \tag{A.24}$$

LT: determination of the transfer functions

LT leads to:

$$\begin{aligned}
-sC_PV_N + C_Pv_N\left(t_1^-\right) &= sC_SV_N - C_Sv_N\left(t_1^-\right) - sC_SV_S + C_Sv_S\left(t_1^-\right)\\
-sC_PV_N + C_Pv_N\left(t_1^-\right) &= \frac{V_S}{R_D} - \frac{V_E}{R_D} + sC_DV_S - C_Dv_S\left(t_1^-\right) - sC_DV_E + C_Dv_E\left(t_1^-\right)\\
-sC_PV_N + C_Pv_N\left(t_1^-\right) &= \frac{V_E}{R_E} + sC_EV_E - C_Ev_E\left(t_1^-\right)
\end{aligned} \tag{A.25}$$

Calculations on this system of three equations in three unknowns (V_N, V_S, V_E) leads to:

$$\begin{aligned}
V_N &= H^{\text{II}}_{(V_N,v_N)}\left(V_T - v_N\left(0^-\right)\right) + H^{\text{II}}_{(V_N,v_S)}v_S\left(0^-\right) + H^{\text{II}}_{(V_N,v_E)}v_E\left(0^-\right)\\
V_S &= H^{\text{II}}_{(V_S,v_N)}\left(V_T - v_N\left(0^-\right)\right) + H^{\text{II}}_{(V_S,v_S)}v_S\left(0^-\right) + H^{\text{II}}_{(V_S,v_E)}v_E\left(0^-\right)\\
V_E &= H^{\text{II}}_{(V_E,v_N)}\left(V_T - v_N\left(0^-\right)\right) + H^{\text{II}}_{(V_E,v_S)}v_S\left(0^-\right) + H^{\text{II}}_{(V_E,v_E)}v_E\left(0^-\right)
\end{aligned} \tag{A.26}$$

where the transfer functions at phase II are:

$$\begin{aligned}
H^{\mathrm{II}}_{(V_N,v_N)} &= \frac{1}{s}\\
H^{\mathrm{II}}_{(V_N,v_S)} &= \frac{n^{\mathrm{II},0}_{(N,S)} + s\cdot n^{\mathrm{II},1}_{(N,S)}}{s\left(d^{\mathrm{II},0}_{N} + s\cdot d^{\mathrm{II},1}_{N} + s^2\cdot d^{\mathrm{II},2}_{N}\right)}\\
H^{\mathrm{II}}_{(V_N,v_E)} &= \frac{n^{\mathrm{II},0}_{(N,E)}}{d^{\mathrm{II},0}_{N} + s\cdot d^{\mathrm{II},1}_{N} + s^2\cdot d^{\mathrm{II},2}_{N}}\\
H^{\mathrm{II}}_{(V_S,v_N)} &= 0\\
H^{\mathrm{II}}_{(V_S,v_S)} &= \frac{n^{\mathrm{II},0}_{(S,S)} + s\cdot n^{\mathrm{II},1}_{(S,S)}}{d^{\mathrm{II},0}_{S} + s\cdot d^{\mathrm{II},1}_{S} + s^2\cdot d^{\mathrm{II},2}_{S}}\\
H^{\mathrm{II}}_{(V_S,v_E)} &= \frac{n^{\mathrm{II},0}_{(S,E)}}{d^{\mathrm{II},0}_{S} + s\cdot d^{\mathrm{II},1}_{S} + s^2\cdot d^{\mathrm{II},2}_{S}}\\
H^{\mathrm{II}}_{(V_E,v_N)} &= 0\\
H^{\mathrm{II}}_{(V_E,v_S)} &= \frac{n^{\mathrm{II},0}_{(E,S)}}{d^{\mathrm{II},0}_{E} + s\cdot d^{\mathrm{II},1}_{E} + s^2\cdot d^{\mathrm{II},2}_{E}}\\
H^{\mathrm{II}}_{(V_E,v_E)} &= \frac{n^{\mathrm{II},0}_{(E,E)} + s\cdot n^{\mathrm{II},1}_{(E,E)}}{d^{\mathrm{II},0}_{E} + s\cdot d^{\mathrm{II},1}_{E} + s^2\cdot d^{\mathrm{II},2}_{E}}
\end{aligned} \tag{A.27}$$

The values of the *denominator* coefficients for phase II are the following:

$d^{\mathrm{II},0}_{N} = d^{\mathrm{II},0}_{S} = d^{\mathrm{I},0}_{E} = C_S + C_P$

$d^{\mathrm{II},1}_{N} = d^{\mathrm{II},1}_{S} = d^{\mathrm{I},1}_{E} = R_D\left(C_SC_P + C_SC_D + C_PC_D\right) + R_E\left(C_SC_P + C_SC_E + C_PC_E\right)$

$d^{\mathrm{II},2}_{N} = d^{\mathrm{II},2}_{S} = d^{\mathrm{I},2}_{E} = R_DR_E\left(C_SC_PC_D + C_SC_PC_E + C_SC_DC_E + C_PC_DC_E\right)$

The values of the *numerator* coefficients for phase II are the following:

$n^{\mathrm{II},0}_{(N,S)} = -C_S$

$n^{\mathrm{II},1}_{(N,S)} = -C_SR_EC_E$

$n^{\mathrm{II},0}_{(N,E)} = C_S\left(-C_DR_D + C_ER_E\right)$

$n^{\mathrm{II},0}_{(S,S)} = C_SC_P\left(R_D + R_E\right) + C_SC_DR_D + C_PC_DR_D$

$n^{\mathrm{II},1}_{(S,S)} = R_DR_E\left(C_SC_PC_D + C_SC_PC_E + C_SC_DC_E + C_PC_DC_E\right)$

$n^{\mathrm{II},0}_{(S,E)} = \left(C_S + C_P\right)\left(-C_DR_D + C_ER_E\right)$

$n^{\mathrm{II},0}_{(E,S)} = C_SC_PR_E$

$n^{\mathrm{II},0}_{(E,E)} = \left(C_S + C_P\right)C_ER_E$

$n^{\mathrm{II},1}_{(E,E)} = R_DR_E\left(C_SC_PC_D + C_SC_PC_E + C_SC_DC_E + C_PC_DC_E\right)$

ILT: determination of the waveforms

ILT applied to Equations (A.26) allows to express the node-voltages at $t = t_2$ as:

$$\begin{aligned}
v_N\left(t_2\right) &= v_N\left(t_1^-\right) + \mathscr{E}^{\mathrm{II}}_{(v_N,v_S)}v_S\left(t_1^-\right) + \mathscr{E}^{\mathrm{II}}_{(v_N,v_E)}v_E\left(t_1^-\right)\\
v_S\left(t_2\right) &= + \mathscr{E}^{\mathrm{II}}_{(v_S,v_S)}v_S\left(t_1^-\right) + \mathscr{E}^{\mathrm{II}}_{(v_S,v_E)}v_E\left(t_1^-\right)\\
v_E\left(t_2\right) &= + \mathscr{E}^{\mathrm{II}}_{(v_E,v_S)}v_S\left(t_1^-\right) + \mathscr{E}^{\mathrm{II}}_{(v_E,v_E)}v_E\left(t_1^-\right)
\end{aligned} \tag{A.28}$$

The exponential functions take the following form:

$$\begin{aligned}\mathscr{E}^{\mathrm{II}}_{(v_N,v_S)} =& \frac{\exp\left(-\frac{d_N^{\mathrm{II},1}+\sqrt{\left(d_N^{\mathrm{II},1}\right)^2-4d_N^{\mathrm{II},0}d_N^{\mathrm{II},2}}}{2d_N^{\mathrm{II},2}}t_2\right)}{2d_N^{\mathrm{II},0}\sqrt{\left(d_N^{\mathrm{II},1}\right)^2-4d_N^{\mathrm{II},0}d_N^{\mathrm{II},2}}}\left(-d_N^{\mathrm{II},1}n_{(N,S)}^{\mathrm{II},0}\left(-1+\exp\left(\frac{\sqrt{\left(d_N^{\mathrm{II},1}\right)^2-4d_N^{\mathrm{II},0}d_N^{\mathrm{II},2}}}{d_N^{\mathrm{II},2}}t_2\right)\right)+\right.\\
&-n_{(N,S)}^{\mathrm{II},0}\sqrt{\left(d_N^{\mathrm{II},1}\right)^2-4d_N^{\mathrm{II},0}d_N^{\mathrm{II},2}}\left(1+\exp\left(\frac{\sqrt{\left(d_N^{\mathrm{II},1}\right)^2-4d_N^{\mathrm{II},0}d_N^{\mathrm{II},2}}}{d_N^{\mathrm{II},2}}t_2\right)+\right.\\
&\left.-2\exp\left(-\frac{d_N^{\mathrm{II},1}+\sqrt{\left(d_N^{\mathrm{II},1}\right)^2-4d_N^{\mathrm{II},0}d_N^{\mathrm{II},2}}}{2d_N^{\mathrm{II},2}}t_2\right)\right)+\\
&\left.2d_N^{\mathrm{II},0}n_{(N,S)}^{\mathrm{II},1}\left(-1+\exp\left(\frac{\sqrt{\left(d_N^{\mathrm{II},1}\right)^2-4d_N^{\mathrm{II},0}d_N^{\mathrm{II},2}}}{d_N^{\mathrm{II},2}}t_2\right)\right)\right)\end{aligned}$$

$$\mathscr{E}^{\mathrm{II}}_{(v_N,v_E)} = \frac{\exp\left(-\frac{d_N^{\mathrm{II},1}+\sqrt{\left(d_N^{\mathrm{II},1}\right)^2-4d_N^{\mathrm{II},0}d_N^{\mathrm{II},2}}}{2d_N^{\mathrm{II},2}}t_2\right)}{\sqrt{\left(d_N^{\mathrm{II},1}\right)^2-4d_N^{\mathrm{II},0}d_N^{\mathrm{II},2}}}\left(n_{(N,E)}^{\mathrm{II},0}\left(-1+\exp\left(\frac{\sqrt{\left(d_N^{\mathrm{II},1}\right)^2-4d_N^{\mathrm{II},0}d_N^{\mathrm{II},2}}}{d_N^{\mathrm{II},2}}t_2\right)\right)\right)$$

$$\begin{aligned}\mathscr{E}^{\mathrm{II}}_{(v_S,v_S)} =& \frac{\exp\left(-\frac{d_S^{\mathrm{II},1}+\sqrt{\left(d_S^{\mathrm{II},1}\right)^2-4d_S^{\mathrm{II},0}d_S^{\mathrm{II},2}}}{2d_S^{\mathrm{II},2}}t_2\right)}{2d_S^{\mathrm{II},2}\sqrt{\left(d_S^{\mathrm{II},1}\right)^2-4d_S^{\mathrm{II},0}d_S^{\mathrm{II},2}}}\left(2d_S^{\mathrm{II},2}n_{(S,S)}^{\mathrm{II},0}\left(-1+\exp\left(\frac{\sqrt{\left(d_S^{\mathrm{II},1}\right)^2-4d_S^{\mathrm{II},0}d_S^{\mathrm{II},2}}}{d_S^{\mathrm{II},2}}t_2\right)\right)+\right.\\
&n_{(S,S)}^{\mathrm{II},1}\left(d_S^{\mathrm{II},1}\left(1-\exp\left(\frac{\sqrt{\left(d_S^{\mathrm{II},1}\right)^2-4d_S^{\mathrm{II},0}d_S^{\mathrm{II},2}}}{d_S^{\mathrm{II},2}}t_2\right)\right)+\right.\\
&\left.\left.\sqrt{\left(d_S^{\mathrm{II},1}\right)^2-4d_S^{\mathrm{II},0}d_S^{\mathrm{II},2}}\left(1+\exp\left(\frac{\sqrt{\left(d_S^{\mathrm{II},1}\right)^2-4d_S^{\mathrm{II},0}d_S^{\mathrm{II},2}}}{d_S^{\mathrm{II},2}}t_2\right)\right)\right)\right)\end{aligned}$$

$$\mathscr{E}^{\mathrm{II}}_{(v_S,v_E)} = \frac{\exp\left(-\frac{d_S^{\mathrm{II},1}+\sqrt{\left(d_S^{\mathrm{II},1}\right)^2-4d_S^{\mathrm{II},0}d_S^{\mathrm{II},2}}}{2d_S^{\mathrm{II},2}}t_2\right)}{\sqrt{\left(d_S^{\mathrm{II},1}\right)^2-4d_S^{\mathrm{II},0}d_S^{\mathrm{II},2}}}\left(n_{(S,E)}^{\mathrm{II},0}\left(-1+\exp\left(\frac{\sqrt{\left(d_S^{\mathrm{II},1}\right)^2-4d_S^{\mathrm{II},0}d_S^{\mathrm{II},2}}}{d_S^{\mathrm{II},2}}t_2\right)\right)\right)$$

$$\mathscr{E}^{\mathrm{II}}_{(v_E,v_S)} = \frac{\exp\left(-\frac{d_E^{\mathrm{II},1}+\sqrt{\left(d_E^{\mathrm{II},1}\right)^2-4d_E^{\mathrm{II},0}d_E^{\mathrm{II},2}}}{2d_E^{\mathrm{II},2}}t_2\right)}{\sqrt{\left(d_E^{\mathrm{II},1}\right)^2-4d_E^{\mathrm{II},0}d_E^{\mathrm{II},2}}}\left(n^{\mathrm{II},0}_{(E,S)}\left(-1+\exp\left(\frac{\sqrt{\left(d_E^{\mathrm{II},1}\right)^2-4d_E^{\mathrm{II},0}d_E^{\mathrm{II},2}}}{d_E^{\mathrm{II},2}}t_2\right)\right)\right)$$

$$\begin{aligned}\mathscr{E}^{\mathrm{II}}_{(v_E,v_E)} = &\frac{\exp\left(-\frac{d_E^{\mathrm{II},1}+\sqrt{\left(d_E^{\mathrm{II},1}\right)^2-4d_E^{\mathrm{II},0}d_E^{\mathrm{II},2}}}{2d_E^{\mathrm{II},2}}t_2\right)}{2d_E^{\mathrm{II},2}\sqrt{\left(d_E^{\mathrm{II},1}\right)^2-4d_E^{\mathrm{II},0}d_E^{\mathrm{II},2}}}\Bigg(2d_E^{\mathrm{II},2}n^{\mathrm{II},0}_{(E,E)}\left(-1+\exp\left(\frac{\sqrt{\left(d_E^{\mathrm{II},1}\right)^2-4d_E^{\mathrm{II},0}d_E^{\mathrm{II},2}}}{d_E^{\mathrm{II},2}}t_2\right)\right)+\\ &n^{\mathrm{II},1}_{(E,E)}\Bigg(d_E^{\mathrm{II},1}\left(1-\exp\left(\frac{\sqrt{\left(d_E^{\mathrm{II},1}\right)^2-4d_E^{\mathrm{II},0}d_E^{\mathrm{II},2}}}{d_E^{\mathrm{II},2}}t_2\right)\right)+\\ &\sqrt{\left(d_E^{\mathrm{II},1}\right)^2-4d_E^{\mathrm{II},0}d_E^{\mathrm{II},2}}\left(1+\exp\left(\frac{\sqrt{\left(d_E^{\mathrm{II},1}\right)^2-4d_E^{\mathrm{II},0}d_E^{\mathrm{II},2}}}{d_E^{\mathrm{II},2}}t_2\right)\right)\Bigg)\Bigg)\end{aligned}$$

A.2.3 Phase III: discharging

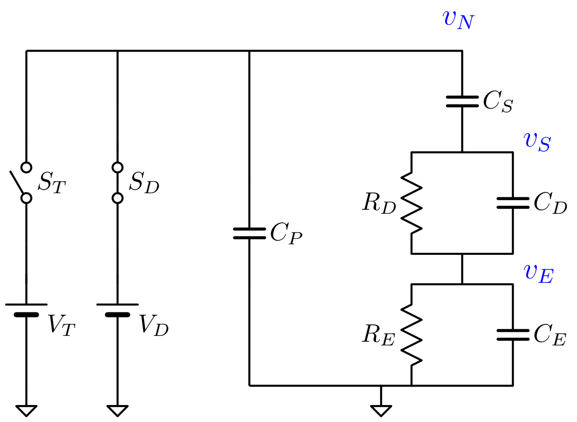

Figure A.7: *Equivalent circuit for the calculation of the switching capacitance according to the C-RC-RC circuit during the discharging phase.*

Now we consider the discharging phase ($t_2 < t < t_3$). Due to the symmetry of the configuration, the final result can be easily adapted from the discussion of Sect. A.2.1, with $v_N(t_3) = V_D$ and easily adapting Equations (A.23).

A.2.4 Phase IV: charge redistribution

Finally, we consider the second charge-redistribution phase ($t_3 < t < t_4$). Again, the final configuration is easily obtained adapting Eq. (A.28).

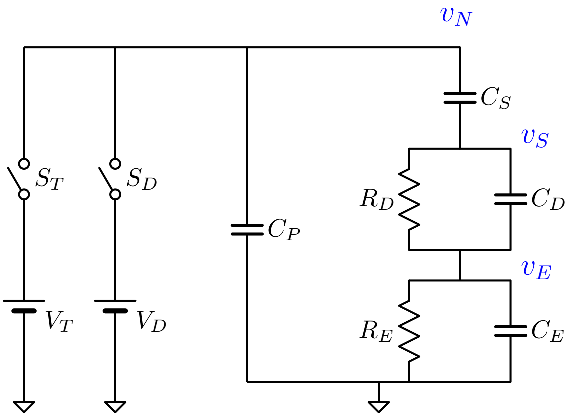

Figure A.8: *Equivalent circuit for the calculation of the switching capacitance according to the C-RC-RC circuit during the charge redistribution phase.*

A.2.5 Calculation of the switching capacitance

The switching node (which is connected to capacitors C_S and C_P) is alternatively biased at V_T and V_D. We can compute the *switching capacitance* (C_{SW}) as we did for the simpler C-RC case in Eq. (A.15).

Again, setting $t_4 = 0$ and combining the time-form equations allows to obtain a closed form of the voltage at each individual phase, and hence of the charge efficiency factor and the switching capacitance. The final result can be easily obtained with lengthy calculations, or with the aid of Mathematica [349].

B Fourier Analysis of Voltage Waveform

B.1 Fourier expansion of relevant waveforms

B.1.1 Trapezoidal waveform

Considering a trapezoidal waveform, with rise/fall times t_r and t_f, voltage level during the high phase V_H with duration T_H, and voltage level during the low phase V_L with duration T_L (the resulting total period is $T = T_H + T_L + t_r + t_f$), it can be demonstrated that the Fourier coefficients take the following form:

$$
\begin{aligned}
a_0 =& \frac{2}{T}\left[V_L T_L + V_H T_H + \frac{V_H + V_L}{2} t_r + \frac{V_H + V_L}{2} t_f\right] \\
a_n =& -\frac{(V_H - V_L)\,T}{2\pi^2 n^2 t_r} + \frac{(V_H - V_L)\,T}{2\pi^2 n^2 t_r}\cos\left(2\pi n \frac{t_r}{T}\right) + \frac{V_H}{\pi n}\sin\left(2\pi n \frac{t_r + T_H}{T}\right) + \\
& + \frac{V_H}{\pi n}\sin\left(2\pi n \frac{t_f + T_L}{T}\right) - \frac{(V_H - V_L)\,T}{2\pi^2 n^2 t_f}\cos\left(2\pi n \frac{T_L}{T}\right) + \\
& + \frac{(V_H - V_L)\,T}{2\pi^2 n^2 t_f}\cos\left(2\pi n \frac{t_f + T_L}{T}\right) \\
b_n =& \frac{(V_H - V_L)\,T}{2\pi^2 n^2 t_r}\sin\left(2\pi n \frac{t_r}{T}\right) + \frac{V_H}{\pi n}\cos\left(2\pi n \frac{t_r + T_H}{T}\right) + \\
& + \frac{V_H}{\pi n}\cos\left(2\pi n \frac{t_f + T_L}{T}\right) - \frac{(V_H - V_L)\,T}{2\pi^2 n^2 t_f}\sin\left(2\pi n \frac{T_L}{T}\right) + \\
& - \frac{(V_H - V_L)\,T}{2\pi^2 n^2 t_f}\sin\left(2\pi n \frac{t_f + T_L}{T}\right)
\end{aligned}
$$

B.1.2 Square waveform

This is the limit case of the trapezoidal waveform for $t_r, t_f \to 0$. Practically speaking, it corresponds to the limit case for a very-low frequency trapezoidal waveform (in which the high/low times scale with frequency and the rise/fall times remain constant).

Considering a square waveform, with voltage level during the high phase V_H of duration T_H, and voltage level during the low phase V_L of duration T_L (the resulting total period is $T = T_H + T_L$), it can be demonstrated that the Fourier coefficients take the following form:

$$\begin{aligned}
a_0 =& \frac{2}{T}\left[V_L T_L + V_H T_H\right] \\
a_n =& +\frac{V_L}{\pi n}\sin\left(2\pi n\frac{T_L}{T}\right) + \frac{V_H}{\pi n}\sin\left(2\pi n\frac{T_H}{T}\right) \\
b_n =& \frac{V_H - V_L}{\pi n} + \frac{V_L}{\pi n}\cos\left(2\pi n\frac{T_L}{T}\right) - \frac{V_H}{\pi n}\cos\left(2\pi n\frac{T_H}{T}\right)
\end{aligned}$$

B.1.3 Triangular waveform

This is the limit case of the trapezoidal waveform for $T_H, T_L \to 0$. Practically speaking, it corresponds to the maximum-frequency of a trapezoidal waveform (in which the high/low times scale with frequency and the rise/fall times remain constant).

Considering a triangular waveform, with rise and fall times t_r and t_f (the resulting total period is $T = t_r + t_f$), and high/low voltage levels V_H and V_L, it can be demonstrated that the Fourier coefficients take the following form:

$$\begin{aligned}
a_0 =& V_H + V_L \\
a_n =& -\frac{(V_H - V_L)\,T}{2\pi^2 n^2 t_r} + \frac{(V_H - V_L)\,T}{2\pi^2 n^2 t_r}\cos\left(2\pi n\frac{t_r}{T}\right) + \frac{V_H}{\pi n}\sin\left(2\pi n\frac{t_r}{T}\right) + \\
& + \frac{V_H}{\pi n}\sin\left(2\pi n\frac{t_f}{T}\right) - \frac{(V_H - V_L)\,T}{2\pi^2 n^2 t_f} + \frac{(V_H - V_L)\,T}{2\pi^2 n^2 t_f}\cos\left(2\pi n\frac{t_f}{T}\right) \\
b_n =& +\frac{(V_H - V_L)\,T}{2\pi^2 n^2 t_r}\sin\left(2\pi n\frac{t_r}{T}\right) + \frac{V_H}{\pi n}\cos\left(2\pi n\frac{t_r}{T}\right) + \\
& + \frac{V_H}{\pi n}\cos\left(2\pi n\frac{t_f}{T}\right) - \frac{(V_H - V_L)\,T}{2\pi^2 n^2 t_f}\sin\left(2\pi n\frac{t_f}{T}\right)
\end{aligned}$$

Publications of the Author

International Journals

S. G. Lemay, C. Laborde, C. Renault, A. Cossettini, L. Selmi, and F. P. Widdershoven, “High-frequency nanocapacitor arrays: concept, recent developments, and outlook,” *Accounts of Chemical Research*, vol. 49, no. 10, pp. 2355–2362, 2016.
DOI: 10.1021/acs.accounts.6b00349

A. Cossettini and L. Selmi, “On the Response of Nanoelectrode Impedance Spectroscopy Measures to Plant, Animal, and Human Viruses,” *IEEE Transactions on NanoBioscience*, vol. 17, no. 2, pp. 102–109, 2018.
DOI: 10.1109/TNB.2018.2826919

F. Widdershoven, A. Cossettini, C. Laborde, A. Bandiziol, P. P. van Swinderen, S. G. Lemay, and L. Selmi, “A CMOS Pixelated Nanocapacitor Biosensor Platform for High-Frequency Impedance Spectroscopy and Imaging,” *IEEE Transactions on Biomedical Circuits and Systems*, 2018.
DOI: 10.1109/TBCAS.2018.2861558

International Conferences

A. Cossettini, M. Dalla Longa, P. Scarbolo, and L. Selmi, “Modeling and simulation of small CCMV virus detection by means of high frequency impedance spectroscopy at nanoelectrodes,” in *Proc. IEEE 17th International Conference on Nanotechnology (IEEE-NANO)*, Pittsburgh, PA, USA, 25–28 July 2017, pp. 416–419.
DOI: 10.1109/NANO.2017.8117367

B. Stadlbauer, L. Taghizadeh, J. M. Escalante, C. Heitzinger, A. Cossettini, and L. Selmi, “Bayesian estimation for transport equations for nanocapacitors,” in *Proc. SIAM Conference on Uncertainty Quantification (UQ 2018)*, Garden Grove, CA, USA, 16–19 April 2018, pp. 69–70.

A. Cossettini, P. Scarbolo, J. M. Escalante, B. Stadlbauer, N. Muhammad, L. Taghizadeh, C. Heitzinger, and L. Selmi, “Calibration, compensation, parameter estimation, and uncertainty quantification for nanoelectrode array biosensors,” in *Proc. SIAM Conference on Uncertainty Quantification (UQ 2018)*, Garden Grove, CA, USA, 16–19 April 2018, p. 81.

A. Cossettini and L. Selmi, “Calibration of High-Frequency Impedance Spectroscopy Measurements with Nanocapacitor Arrays,” in *Proc. 2nd European Biosensor Symposium (EBS 2019)*, Florence, Italy, 18–21 February 2019.

Online Simulation Tools

P. Scarbolo, F. Pittino, M. Dalla Longa, A. Cossettini, and L. Selmi,
“ENBIOS-1D Lab”, version 3.0, April 2017 [Online].
Available: https://nanohub.org/resources/biolab
DOI: 10.4231/D3Z02Z963.

A. Hoxha, P. Scarbolo, A. Cossettini, F. Pittino, and L. Selmi,
“ENBIOS-2D Lab”, version 1.0, October 2016 [Online].
Available: https://nanohub.org/resources/biolabisfet
DOI: 10.4231/D3V11VM7D.

Journal Papers in preparation

- In collaboration with TU-Wien, on the topics of Sect. 3.6-4.4.3;
- In collaboration with NXP Semiconductors and University of Twente, on the topics of Sect. 5.2.2;

Bibliography

[1] Bill Gates, “2014 Gates Annual Letter - 3 myths that block progress for the poor,” 2014. https://www.gatesfoundation.org/Who-We-Are/Resources-and-Media/Annual-Letters-List/Annual-Letter-2014 (Accessed: Sept 2018).

[2] W. B. Group, “Global poverty,” in *Poverty and shared prosperity 2016 - Taking on inequality*, ch. 2, pp. 35–51, 2016.

[3] OurWorldInData, “World population living in extreme poverty, 1820-2015,” 2016. https://ourworldindata.org/extreme-poverty (Accessed: Sept 2018).

[4] P. Diamandis and S. Kotler, “Abundance - the Future is Better Than You Think,” 2012.

[5] D. T. Jamison *et al.*, “Global health 2035: a world converging within a generation,” *The Lancet*, vol. 382, no. 9908, pp. 1898–1955, 2013.

[6] J. Bryzek, “The Trillion Sensors (TSensors) Foundation for the IoT,” in *TSensors summit*, 2015.

[7] J. R. Stetter, E. F. Stetter, and M. T. Carter, “Abundant chemical sensors and the trillion sensor universe,” in *Meeting Abstracts*, no. 6, pp. 451–451, The Electrochemical Society, 2014.

[8] W. B. Group, “Reductions in inequality: A policy perspective,” in *Poverty and shared prosperity 2016 - Taking on inequality*, ch. 6, pp. 129–170, 2016.

[9] L. Pritchett and L. H. Summers, *Wealthier is healthier*, vol. 1150. World Bank Publications, 1993.

[10] K. Davis, “The amazing decline of mortality in underdeveloped areas,” *The American Economic Review*, vol. 46, no. 2, pp. 305–318, 1956.

[11] G. Pison, J.-F. Trape, M. Lefebvre, and C. Enel, “Rapid decline in child mortality in a rural area of Senegal,” *International journal of epidemiology*, vol. 22, no. 1, pp. 72–80, 1993.

[12] United Nations - Department of Economic and Social Affairs - Population Division, “World Population Ageing 2015,” tech. rep., United Nations, 2015.

[13] United Nations - Department of Economic and Social Affairs - Population Division, "World Population Prospects - The 2017 Revision," tech. rep., United Nations, 2017.

[14] European Commission, "Health, demographic change and wellbeing," in *Horizon 2020 - Work Programme 2018-2020*, ch. 8, pp. 1–134, 2018.

[15] European Commission, "Guardian Angels for a Smarter Life," 2012. https://www.ga-project.eu/ (Accessed: Sept 2018).

[16] Centers for Medicare and Medicaid Services - Office of the Actuary, "National Health Expenditure Projections 2017-26," tech. rep., Centers for Medicare and Medicaid Services, 14 February 2018.

[17] D. T. Jamison, M. Sandhu, and J. Wang, "Why has infant mortality decreased at such different rates in different countries?," *World Bank Disease Control Priorities Project, Washington DC*, 2004.

[18] European Commission, "Nanomedicine - the promise," 2018. http://ec.europa.eu/research/industrial_technologies/nmp-nanomedicine_en.html (Accessed: Sept 2018).

[19] IBM, "IBM Watson Health." https://www.ibm.com/watson/health/.

[20] M. A. Burns, B. N. Johnson, S. N. Brahmasandra, K. Handique, J. R. Webster, M. Krishnan, T. S. Sammarco, P. M. Man, D. Jones, D. Heldsinger, *et al.*, "An integrated nanoliter DNA analysis device," *Science*, vol. 282, no. 5388, pp. 484–487, 1998.

[21] A. K. Yetisen, M. S. Akram, and C. R. Lowe, "Paper-based microfluidic point-of-care diagnostic devices," *Lab on a Chip*, vol. 13, no. 12, pp. 2210–2251, 2013.

[22] Nanowerk, "Nanotechnology in healthcare," 2017. https://www.nanowerk.com/spotlight/spotid=47031_1.php (Accessed: Sept 2018).

[23] Y. Yuehong, Y. Zeng, X. Chen, and Y. Fan, "The internet of things in healthcare: an overview," *Journal of Industrial Information Integration*, vol. 1, pp. 3–13, 2016.

[24] W. Arden, M. Brillouët, P. Cogez, M. Graef, B. Huizing, and R. Mahnkopf, "More-than-Moore white paper," *Version*, vol. 2, p. 14, 2010.

[25] Beecham Research, "M2M Sector Map." http://www.beechamresearch.com/article.aspx?id=41.

[26] Sonnier, Paul, "Story of Digital Health." https://storyofdigitalhealth.com/.

[27] U.S. Food & Drug Administration, "Digital Health." https://www.fda.gov/medicaldevices/digitalhealth/.

[28] N. L. Bragazzi, “From P0 to P6 medicine, a model of highly participatory, narrative, interactive, and “augmented” medicine: some considerations on Salvatore Iaconesi’s clinical story,” *Patient preference and adherence*, vol. 7, p. 353, 2013.

[29] C. Nicolini, N. Bragazzi, and E. Pechkova, “Nanoproteomics enabling personalized nanomedicine,” *Advanced drug delivery reviews*, vol. 64, no. 13, pp. 1522–1531, 2012.

[30] A. Brand, “Public health genomics and personalized healthcare: a pipeline from cell to society,” 2012.

[31] S. Carrara, “Nano-bio-technology and sensing chips: new systems for detection in personalized therapies and cell biology,” *Sensors*, vol. 10, no. 1, pp. 526–543, 2010.

[32] D. L. Sackett, W. M. Rosenberg, J. M. Gray, R. B. Haynes, and W. S. Richardson, “Evidence based medicine: what it is and what it isn’t,” 1996.

[33] D. Gurwitz and J. E. Lunshof, “Personalized participatory medicine: sharing knowledge and uncertainty,” *Genome medicine*, vol. 3, no. 10, p. 69, 2011.

[34] M. F. Haward and J. M. Lorenz, “Communicating risk under conditions of uncertainty: not as simple as it may seem,” *Acta Paediatrica*, vol. 100, no. 5, pp. 651–652, 2011.

[35] G. Eysenbach, J. Powell, M. Englesakis, C. Rizo, and A. Stern, “Health related virtual communities and electronic support groups: systematic review of the effects of online peer to peer interactions,” *Bmj*, vol. 328, no. 7449, p. 1166, 2004.

[36] Liftware. https://www.liftware.com/.

[37] E. Rovini, C. Maremmani, and F. Cavallo, “How wearable sensors can support Parkinson’s disease diagnosis and treatment: A systematic review,” *Frontiers in neuroscience*, vol. 11, p. 555, 2017.

[38] D. R. Thévenot, K. Toth, R. A. Durst, and G. S. Wilson, “Electrochemical biosensors: recommended definitions and classification,” *Analytical Letters*, vol. 34, no. 5, pp. 635–659, 2001.

[39] M. A. Alam, “Principles of electronic nanobiosensors.” nanohub.org web course, 2013.

[40] C. M. Girardin, C. Huot, M. Gonthier, and E. Delvin, “Continuous glucose monitoring: A review of biochemical perspectives and clinical use in type 1 diabetes,” *Clinical biochemistry*, vol. 42, no. 3, pp. 136–142, 2009.

[41] J. M. Rothberg *et al.*, “An integrated semiconductor device enabling non-optical genome sequencing,” *Nature*, vol. 475, no. 7356, p. 348, 2011.

[42] N. Rusk, "Torrents of sequence," *Nature Methods*, vol. 8, 2011.

[43] J. Bustillo *et al.*, "Development of the ion torrent CMOS chip for DNA sequencing," in *Proc. IEDM*, pp. 196–199, 2013.

[44] C. I. Justino, T. A. Rocha-Santos, and A. C. Duarte, "Review of analytical figures of merit of sensors and biosensors in clinical applications," *TrAC Trends in Analytical Chemistry*, vol. 29, no. 10, pp. 1172–1183, 2010.

[45] N. Bhalla, P. Jolly, N. Formisano, and P. Estrela, "Introduction to biosensors," *Essays in biochemistry*, vol. 60, no. 1, pp. 1–8, 2016.

[46] Bureau international des poids et mesures (BIPM) - Joint Committee for Guides in Metrology (JCGM), *International vocabulary of metrology – Basic and general concepts and associated terms (VIM).* 2012.

[47] M. J. McGrath and C. N. Scanaill, "Sensing and sensor fundamentals," in *Sensor Technologies*, pp. 15–50, Springer, 2013.

[48] P. E. Sheehan and L. J. Whitman, "Detection limits for nanoscale biosensors," *Nano letters*, vol. 5, no. 4, pp. 803–807, 2005.

[49] P. Nair and M. Alam, "Performance limits of nanobiosensors," *Applied physics letters*, vol. 88, no. 23, p. 233120, 2006.

[50] T. M. Squires, R. J. Messinger, and S. R. Manalis, "Making it stick: convection, reaction and diffusion in surface-based biosensors," *Nature biotechnology*, vol. 26, no. 4, p. 417, 2008.

[51] P. R. Nair and M. A. Alam, "Screening-limited response of nanobiosensors," *Nano Letters*, vol. 8, no. 5, pp. 1281–1285, 2008.

[52] Y. Li, W. Xie, and G. Fang, "Fluorescence detection techniques for protein kinase assay," *Analytical and bioanalytical chemistry*, vol. 390, no. 8, pp. 2049–2057, 2008.

[53] C. P. Toseland and M. R. Webb, "Fluorescence tools to measure helicase activity in real time," *Methods*, vol. 51, no. 3, pp. 259–268, 2010.

[54] S. Harz, M. Schimmelpfennig, B. Tse Sum Bui, N. Marchyk, K. Haupt, and K.-H. Feller, "Fluorescence optical spectrally resolved sensor based on molecularly imprinted polymers and microfluidics," *Engineering in Life Sciences*, vol. 11, no. 6, pp. 559–565, 2011.

[55] H. Sahoo, "Fluorescent labeling techniques in biomolecules: a flashback," *Rsc Advances*, vol. 2, no. 18, pp. 7017–7029, 2012.

[56] S.-S. Liang, L. Qi, R.-L. Zhang, M. Jin, and Z.-Q. Zhang, "Ratiometric fluorescence biosensor based on CdTe quantum and carbon dots for double strand DNA detection," *Sensors and Actuators B: Chemical*, vol. 244, pp. 585–590, 2017.

[57] J. Yu, S. Wang, L. Ge, and S. Ge, “A novel chemiluminescence paper microfluidic biosensor based on enzymatic reaction for uric acid determination,” *Biosensors and Bioelectronics*, vol. 26, no. 7, pp. 3284–3289, 2011.

[58] U. S. Akshath, L. S. Selvakumar, and M. S. Thakur, “Detection of formaldehyde in food samples by enhanced chemiluminescence,” *Analytical Methods*, vol. 4, no. 3, pp. 699–704, 2012.

[59] C. Ma, E. S. Yeung, S. Qi, and R. Han, “Highly sensitive detection of microRNA by chemiluminescence based on enzymatic polymerization,” *Analytical and bioanalytical chemistry*, vol. 402, no. 6, pp. 2217–2220, 2012.

[60] X. Wang, C. Lau, M. Kai, and J. Lu, “Hybridization chain reaction-based instantaneous derivatization technology for chemiluminescence detection of specific DNA sequences,” *Analyst*, vol. 138, no. 9, pp. 2691–2697, 2013.

[61] N. Li, J. Chen, M. Luo, C. Chen, X. Ji, and Z. He, “Highly sensitive chemiluminescence biosensor for protein detection based on the functionalized magnetic microparticles and the hybridization chain reaction,” *Biosensors and Bioelectronics*, vol. 87, pp. 325–331, 2017.

[62] N. Gibson, U. Holzwarth, K. Abbas, F. Simonelli, J. Kozempel, I. Cydzik, G. Cotogno, A. Bulgheroni, D. Gilliland, J. Ponti, *et al.*, “Radiolabelling of engineered nanoparticles for in vitro and in vivo tracing applications using cyclotron accelerators,” *Archives of toxicology*, vol. 85, no. 7, p. 751, 2011.

[63] Y. Qi, N. Li, Q. Xu, X. Xia, J. Ge, and J. Lu, “A cancer-targetable copolymer containing tyrosine segments for labeling radioactive halogens,” *Reactive and Functional Polymers*, vol. 71, no. 4, pp. 390–394, 2011.

[64] R. S. Yalow and S. A. Berson, “Assay of plasma insulin in human subjects by immunological methods,” *Nature*, vol. 184, no. 4699, p. 1648, 1959.

[65] E. M. Bernstein, *Bioelectrochemistry research developments.* Nova Publishers, 2008.

[66] A. Syahir, K. Usui, K.-y. Tomizaki, K. Kajikawa, and H. Mihara, “Label and label-free detection techniques for protein microarrays,” *Microarrays*, vol. 4, no. 2, pp. 228–244, 2015.

[67] A. Anne, A. Bouchardon, and J. Moiroux, “3’-ferrocene-labeled oligonucleotide chains end-tethered to gold electrode surfaces: novel model systems for exploring flexibility of short DNA using cyclic voltammetry,” *Journal of the American Chemical Society*, vol. 125, no. 5, pp. 1112–1113, 2003.

[68] E. Lagally, *Microfluidics and nanotechnology: biosensing to the single molecule limit.* CRC Press, 2014.

[69] J. Das, K. B. Cederquist, A. A. Zaragoza, P. E. Lee, E. H. Sargent, and S. O. Kelley, “An ultrasensitive universal detector based on neutralizer displacement,” *Nature chemistry*, vol. 4, no. 8, p. 642, 2012.

[70] L. Ding, A. M. Bond, J. Zhai, and J. Zhang, "Utilization of nanoparticle labels for signal amplification in ultrasensitive electrochemical affinity biosensors: a review," *Analytica Chimica Acta*, vol. 797, pp. 1–12, 2013.

[71] L.-N. Feng, Z.-P. Bian, J. Peng, F. Jiang, G.-H. Yang, Y.-D. Zhu, D. Yang, L.-P. Jiang, and J.-J. Zhu, "Ultrasensitive multianalyte electrochemical immunoassay based on metal ion functionalized titanium phosphate nanospheres," *Analytical chemistry*, vol. 84, no. 18, pp. 7810–7815, 2012.

[72] V. K. Upadhyayula, "Functionalized gold nanoparticle supported sensory mechanisms applied in detection of chemical and biological threat agents: a review," *Analytica Chimica Acta*, vol. 715, pp. 1–18, 2012.

[73] J. Wang, D. Xu, A.-N. Kawde, and R. Polsky, "Metal nanoparticle-based electrochemical stripping potentiometric detection of DNA hybridization," *Analytical chemistry*, vol. 73, no. 22, pp. 5576–5581, 2001.

[74] J. Zhang, B. P. Ting, M. Khan, M. C. Pearce, Y. Yang, Z. Gao, and J. Y. Ying, "Pt nanoparticle label-mediated deposition of Pt catalyst for ultrasensitive electrochemical immunosensors," *Biosensors and Bioelectronics*, vol. 26, no. 2, pp. 418–423, 2010.

[75] B.-I. Haukanes and C. Kvam, "Application of magnetic beads in bioassays," *Nature Biotechnology*, vol. 11, no. 1, p. 60, 1993.

[76] Y.-T. Chen, A. G. Kolhatkar, O. Zenasni, S. Xu, and T. R. Lee, "Biosensing using magnetic particle detection techniques," *Sensors*, vol. 17, no. 10, p. 2300, 2017.

[77] R. S. Gaster, L. Xu, S.-J. Han, R. J. Wilson, D. A. Hall, S. J. Osterfeld, H. Yu, and S. X. Wang, "Quantification of protein interactions and solution transport using high-density GMR sensor arrays," *Nature nanotechnology*, vol. 6, no. 5, p. 314, 2011.

[78] W. Shen, B. D. Schrag, M. J. Carter, J. Xie, C. Xu, S. Sun, and G. Xiao, "Detection of DNA labeled with magnetic nanoparticles using MgO-based magnetic tunnel junction sensors," *Journal of Applied Physics*, vol. 103, no. 7, p. 07A306, 2008.

[79] L. Ejsing, M. F. Hansen, A. K. Menon, H. A. Ferreira, D. L. Graham, and P. P. Freitas, "Magnetic microbead detection using the planar hall effect," *Journal of Magnetism and Magnetic Materials*, vol. 293, no. 1, pp. 677–684, 2005.

[80] G. Mihajlović, P. Xiong, S. von Molnár, K. Ohtani, H. Ohno, M. Field, and G. J. Sullivan, "Detection of single magnetic bead for biological applications using an InAs quantum-well micro-Hall sensor," *Applied Physics Letters*, vol. 87, no. 11, p. 112502, 2005.

[81] K. Enpuku, T. Minotani, T. Gima, Y. Kuroki, Y. Itoh, M. Yamashita, Y. Katakura, and S. Kuhara, "Detection of magnetic nanoparticles with superconducting quantum interference device (SQUID) magnetometer and application to immunoassays," *Japanese journal of applied physics*, vol. 38, no. 10A, p. L1102, 1999.

[82] S. Xu, V. V. Yashchuk, M. H. Donaldson, S. M. Rochester, D. Budker, and A. Pines, "Magnetic resonance imaging with an optical atomic magnetometer," *Proceedings of the National Academy of Sciences*, vol. 103, no. 34, pp. 12668–12671, 2006.

[83] F. Ludwig, S. Mäuselein, E. Heim, and M. Schilling, "Magnetorelaxometry of magnetic nanoparticles in magnetically unshielded environment utilizing a differential fluxgate arrangement," *Review of scientific instruments*, vol. 76, no. 10, p. 106102, 2005.

[84] M. Barbic and H. ElBidweihy, "Effect of magnetic nanoparticle shape on flux amplification in inductive coil magnetic resonance detection," *Journal of Applied Physics*, vol. 120, no. 10, p. 104506, 2016.

[85] L. McGuinness, Y. Yan, A. Stacey, D. Simpson, L. Hall, D. Maclaurin, S. Prawer, P. Mulvaney, J. Wrachtrup, F. Caruso, *et al.*, "Quantum measurement and orientation tracking of fluorescent nanodiamonds inside living cells," *Nature nanotechnology*, vol. 6, no. 6, p. 358, 2011.

[86] P. Vavassori, V. Metlushko, B. Ilic, M. Gobbi, M. Donolato, M. Cantoni, and R. Bertacco, "Domain wall displacement in Py square ring for single nanometric magnetic bead detection," *Applied Physics Letters*, vol. 93, no. 20, p. 203502, 2008.

[87] S. Sang, Y. Wang, Q. Feng, Y. Wei, J. Ji, and W. Zhang, "Progress of new label-free techniques for biosensors: a review," *Critical reviews in biotechnology*, vol. 36, no. 3, pp. 465–481, 2016.

[88] S. T. Mathews, E. P. Plaisance, and T. Kim, "Imaging systems for westerns: chemiluminescence vs. infrared detection," in *Protein Blotting and Detection*, pp. 499–513, Springer, 2009.

[89] A. Wardeh, I. P. Kay, M. Sabaté, V. Coen, A. Gijzel, J. Ligthart, A. den Boer, P. Levendag, W. van Der Giessen, and P. Serruys, "β-particle–emitting radioactive stent implantation: a safety and feasibility study," *Circulation*, vol. 100, no. 16, pp. 1684–1689, 1999.

[90] S. J. Dwight, B. S. Gaylord, J. W. Hong, and G. C. Bazan, "Perturbation of fluorescence by nonspecific interactions between anionic poly (phenylenevinylene) s and proteins: implications for biosensors," *Journal of the American Chemical Society*, vol. 126, no. 51, pp. 16850–16859, 2004.

[91] T. Kilic, M. Soler, N. Fahimi-Kashani, H. Altug, and S. Carrara, “Mining the potential of label-free biosensors for in vitro antipsychotic drug screening,” *Biosensors*, vol. 8, no. 1, p. 6, 2018.

[92] M. L. Sin, K. E. Mach, P. K. Wong, and J. C. Liao, “Advances and challenges in biosensor-based diagnosis of infectious diseases,” *Expert review of molecular diagnostics*, vol. 14, no. 2, pp. 225–244, 2014.

[93] M. Ritzi-Lehnert, “Development of chip-compatible sample preparation for diagnosis of infectious diseases,” *Expert review of molecular diagnostics*, vol. 12, no. 2, pp. 189–206, 2012.

[94] K. E. Sapsford, K. M. Tyner, B. J. Dair, J. R. Deschamps, and I. L. Medintz, “Analyzing nanomaterial bioconjugates: a review of current and emerging purification and characterization techniques,” *Analytical chemistry*, vol. 83, no. 12, pp. 4453–4488, 2011.

[95] E. Fu, T. Chinowsky, K. Nelson, K. Johnston, T. Edwards, K. Helton, M. Grow, J. W. Miller, and P. Yager, “Spr imaging-based salivary diagnostics system for the detection of small molecule analytes,” *Annals of the New York Academy of Sciences*, vol. 1098, no. 1, pp. 335–344, 2007.

[96] A. Cattamanchi, J. Davis, M. Pai, L. Huang, P. Hopewell, and K. Steingart, “Does bleach processing increase the accuracy of sputum smear microscopy for diagnosing pulmonary tuberculosis?,” *Journal of clinical microbiology*, vol. 48, no. 7, pp. 2433–2439, 2010.

[97] G. M. Whitesides, “The origins and the future of microfluidics,” *Nature*, vol. 442, no. 7101, p. 368, 2006.

[98] T. Footz, S. Wunsam, S. Kulak, H. J. Crabtree, D. M. Glerum, and C. J. Backhouse, “Sample purification on a microfluidic device,” *Electrophoresis*, vol. 22, no. 18, pp. 3868–3875, 2001.

[99] E. Reiter, J. Zentek, and E. Razzazi, “Review on sample preparation strategies and methods used for the analysis of aflatoxins in food and feed,” *Molecular nutrition & food research*, vol. 53, no. 4, pp. 508–524, 2009.

[100] L. Nováková and H. Vlčková, “A review of current trends and advances in modern bio-analytical methods: chromatography and sample preparation,” *Analytica chimica acta*, vol. 656, no. 1-2, pp. 8–35, 2009.

[101] E. S. Kawasaki, “Sample preparation from blood, cells and other fluids,” *PCR protocols: A guide to methods and applications*, vol. 1, 1990.

[102] C. A. Rowe-Taitt, J. P. Golden, M. J. Feldstein, J. J. Cras, K. E. Hoffman, and F. S. Ligler, “Array biosensor for detection of biohazards,” *Biosensors and Bioelectronics*, vol. 14, no. 10-11, pp. 785–794, 2000.

[103] J. P. Chambers, B. P. Arulanandam, L. L. Matta, A. Weis, and J. J. Valdes, “Biosensor recognition elements,” tech. rep., Texas Univ. at San Antonio Dept of Biology, 2008.

[104] J. Valdes, J. Wall Jr, J. Chambers, and M. Eldefrawi, “A receptor-based capacitive biosensor.,” *Johns Hopkins APL Technical Digest*, vol. 9, no. 1, pp. 4–9, 1988.

[105] N. Ferrer-Miralles, J. X. Feliu, S. Vandevuer, A. Müller, J. Cabrera-Crespo, I. Ortmans, F. Hoffmann, D. Cazorla, U. Rinas, M. Prévost, *et al.*, “Engineering regulable escherichia coliβ-galactosidases as biosensors for anti-HIV antibody detection in human sera,” *Journal of Biological Chemistry*, vol. 276, no. 43, pp. 40087–40095, 2001.

[106] G. Rocchitta, A. Spanu, S. Babudieri, G. Latte, G. Madeddu, G. Galleri, S. Nuvoli, P. Bagella, M. Demartis, V. Fiore, *et al.*, “Enzyme biosensors for biomedical applications: Strategies for safeguarding analytical performances in biological fluids,” *Sensors*, vol. 16, no. 6, p. 780, 2016.

[107] S. D. Jayasena, “Aptamers: an emerging class of molecules that rival antibodies in diagnostics,” *Clinical chemistry*, vol. 45, no. 9, pp. 1628–1650, 1999.

[108] E. Engvall and P. Perlmann, “Enzyme-linked immunosorbent assay (ELISA) quantitative assay of immunoglobulin g,” *Immunochemistry*, vol. 8, no. 9, pp. 871–874, 1971.

[109] D. V. Lim, J. M. Simpson, E. A. Kearns, and M. F. Kramer, “Current and developing technologies for monitoring agents of bioterrorism and biowarfare,” *Clinical microbiology reviews*, vol. 18, no. 4, pp. 583–607, 2005.

[110] M. Egholm, O. Buchardt, L. Christensen, C. Behrens, S. M. Freier, D. A. Driver, R. H. Berg, S. K. Kim, B. Norden, and P. E. Nielsen, “PNA hybridizes to complementary oligonucleotides obeying the watson–crick hydrogen-bonding rules,” *Nature*, vol. 365, no. 6446, p. 566, 1993.

[111] O. Brandt and J. D. Hoheisel, “Peptide nucleic acids on microarrays and other biosensors,” *TRENDS in Biotechnology*, vol. 22, no. 12, pp. 617–622, 2004.

[112] A. Ersöz, A. Denizli, A. Özcan, and R. Say, “Molecularly imprinted ligand-exchange recognition assay of glucose by quartz crystal microbalance,” *Biosensors and Bioelectronics*, vol. 20, no. 11, pp. 2197–2202, 2005.

[113] D. B. Xie B., Ramanathan K., “Principles of enzyme thermistor systems: Applications to biomedical and other measurements,” in *Thermal Biosensors, Bioactivity, Bioaffinitty. Advances in Biochemical Engineering/Biotechnology* (B. P. et al., ed.), vol. 64, Springer, 1999.

[114] V. Perumal and U. Hashim, “Advances in biosensors: Principle, architecture and applications,” *Journal of applied biomedicine*, vol. 12, no. 1, pp. 1–15, 2014.

[115] S. P. Mohanty and E. Kougianos, “Biosensors: a tutorial review,” *Ieee Potentials*, vol. 25, no. 2, pp. 35–40, 2006.

[116] L. Ahmad, B. Towe, A. Wolf, F. Mertens, and J. Lerchner, “Binding event measurement using a chip calorimeter coupled to magnetic beads,” *Sensors and Actuators B: Chemical*, vol. 145, no. 1, pp. 239–245, 2010.

[117] Y. Zhang and S. Tadigadapa, “Calorimetric biosensors with integrated microfluidic channels,” *Biosensors and Bioelectronics*, vol. 19, no. 12, pp. 1733–1743, 2004.

[118] M. A. Cooper, “Label-free screening of bio-molecular interactions,” *Analytical and bioanalytical chemistry*, vol. 377, no. 5, pp. 834–842, 2003.

[119] P. Paul, M. Hossain, R. C. Yadav, and G. S. Kumar, “Biophysical studies on the base specificity and energetics of the DNA interaction of photoactive dye thionine: spectroscopic and calorimetric approach,” *Biophysical Chemistry*, vol. 148, no. 1-3, pp. 93–103, 2010.

[120] H. Xi, S. Kumar, L. Dosen-Micovic, and D. P. Arya, “Calorimetric and spectroscopic studies of aminoglycoside binding to AT-rich DNA triple helices,” *Biochimie*, vol. 92, no. 5, pp. 514–529, 2010.

[121] P. Kirchner, J. Oberländer, P. Friedrich, J. Berger, G. Rysstad, M. Keusgen, and M. J. Schöning, “Realisation of a calorimetric gas sensor on polyimide foil for applications in aseptic food industry,” *Sensors and Actuators B: Chemical*, vol. 170, pp. 60–66, 2012.

[122] T. Maskow, K. Wolf, W. Kunze, S. Enders, and H. Harms, “Rapid analysis of bacterial contamination of tap water using isothermal calorimetry,” *Thermochimica acta*, vol. 543, pp. 273–280, 2012.

[123] M. Nirschl, F. Reuter, and J. Vörös, “Review of transducer principles for label-free biomolecular interaction analysis,” *Biosensors*, vol. 1, no. 3, pp. 70–92, 2011.

[124] R. Monošík, M. Stredanskỳ, and E. Šturdík, “Biosensors-classification, characterization and new trends,” *Acta Chimica Slovaca*, vol. 5, no. 1, pp. 109–120, 2012.

[125] M. Pohanka, “Overview of piezoelectric biosensors, immunosensors and DNA sensors and their applications,” *Materials*, vol. 11, no. 3, p. 448, 2018.

[126] G. García-Martinez, E. A. Bustabad, H. Perrot, C. Gabrielli, B. Bucur, M. Lazerges, D. Rose, L. Rodriguez-Pardo, J. Fariña, C. Compère, *et al.*, “Development of a mass sensitive quartz crystal microbalance (QCM)-based DNA biosensor using a 50 MHz electronic oscillator circuit,” *Sensors*, vol. 11, no. 8, pp. 7656–7664, 2011.

[127] M. Pohanka, “The piezoelectric biosensors: Principles and applications,” *Int. J. Electrochem. Sci*, vol. 12, pp. 496–506, 2017.

[128] T. Vo-Dinh and B. Cullum, “Biosensors and biochips: advances in biological and medical diagnostics,” *Fresenius’ journal of analytical chemistry*, vol. 366, no. 6-7, pp. 540–551, 2000.

[129] K. K. Kanazawa and J. G. Gordon II, “The oscillation frequency of a quartz resonator in contact with liquid,” *Analytica Chimica Acta*, vol. 175, pp. 99–105, 1985.

[130] R. Funari, I. Terracciano, B. Della Ventura, S. Ricci, T. Cardi, N. D’Agostino, and R. Velotta, “Label-free detection of gliadin in food by quartz crystal microbalance-based immunosensor,” *Journal of agricultural and food chemistry*, vol. 65, no. 6, pp. 1281–1289, 2017.

[131] C. Yao, T. Zhu, J. Tang, R. Wu, Q. Chen, M. Chen, B. Zhang, J. Huang, and W. Fu, “Hybridization assay of hepatitis B virus by QCM peptide nucleic acid biosensor,” *Biosensors and Bioelectronics*, vol. 23, no. 6, pp. 879–885, 2008.

[132] D. Dell’Atti, S. Tombelli, M. Minunni, and M. Mascini, “Detection of clinically relevant point mutations by a novel piezoelectric biosensor,” *Biosensors and Bioelectronics*, vol. 21, no. 10, pp. 1876–1879, 2006.

[133] H. Chen, Q.-Y. Hu, J.-H. Jiang, G.-L. Shen, R.-Q. Yu, *et al.*, “Construction of supported lipid membrane modified piezoelectric biosensor for sensitive assay of cholera toxin based on surface-agglutination of ganglioside-bearing liposomes,” *Analytica Chimica Acta*, vol. 657, no. 2, pp. 204–209, 2010.

[134] B. L. Leca-Bouvier B.D., “Enzyme for biosensing applications,” in *Recognition Receptors in Biosensors* (Z. M., ed.), pp. 177–220, Springer, 2010.

[135] O. L. Glynn B., “Nucleic acid diagnostic biosensors,” in *Recognition Receptors in Biosensors* (Z. M., ed.), pp. 343–363, Springer, 2010.

[136] Z. Zhang, S. Zhang, and X. Zhang, “Recent developments and applications of chemiluminescence sensors,” *Analytica Chimica Acta*, vol. 541, no. 1-2, pp. 37–46, 2005.

[137] A. G. Brolo, “Plasmonics for future biosensors,” *Nature Photonics*, vol. 6, no. 11, p. 709, 2012.

[138] O. Tokel, F. Inci, and U. Demirci, “Advances in plasmonic technologies for point of care applications,” *Chemical reviews*, vol. 114, no. 11, pp. 5728–5752, 2014.

[139] G. Zanchetta, R. Lanfranco, F. Giavazzi, T. Bellini, and M. Buscaglia, “Emerging applications of label-free optical biosensors,” *Nanophotonics*, vol. 6, no. 4, pp. 627–645, 2017.

[140] X. D. Hoa, A. Kirk, and M. Tabrizian, “Towards integrated and sensitive surface plasmon resonance biosensors: a review of recent progress,” *Biosensors and Bioelectronics*, vol. 23, no. 2, pp. 151–160, 2007.

[141] W. Diao, M. Tang, S. Ding, X. Li, W. Cheng, F. Mo, X. Yan, H. Ma, and Y. Yan, “Highly sensitive surface plasmon resonance biosensor for the detection of HIV-related DNA based on dynamic and structural DNA nanodevices,” *Biosensors and Bioelectronics*, vol. 100, pp. 228–234, 2018.

[142] S. Mariani and M. Minunni, “Surface plasmon resonance applications in clinical analysis,” *Analytical and bioanalytical chemistry*, vol. 406, no. 9-10, pp. 2303–2323, 2014.

[143] C. Boozer, G. Kim, S. Cong, H. Guan, and T. Londergan, “Looking towards label-free biomolecular interaction analysis in a high-throughput format: a review of new surface plasmon resonance technologies,” *Current opinion in biotechnology*, vol. 17, no. 4, pp. 400–405, 2006.

[144] T. Do, F. Ho, B. Heidecker, K. Witte, L. Chang, and L. Lerner, “A rapid method for determining dynamic binding capacity of resins for the purification of proteins,” *Protein expression and purification*, vol. 60, no. 2, pp. 147–150, 2008.

[145] Y. N. Abdiche, A. Miles, J. Eckman, D. Foletti, T. J. Van Blarcom, Y. A. Yeung, J. Pons, and A. Rajpal, “High-throughput epitope binning assays on label-free array-based biosensors can yield exquisite epitope discrimination that facilitates the selection of monoclonal antibodies with functional activity,” *PLoS One*, vol. 9, no. 3, p. e92451, 2014.

[146] Y. Abdiche, D. Malashock, A. Pinkerton, and J. Pons, “Determining kinetics and affinities of protein interactions using a parallel real-time label-free biosensor, the octet,” *Analytical biochemistry*, vol. 377, no. 2, pp. 209–217, 2008.

[147] X. Fan, I. M. White, S. I. Shopova, H. Zhu, J. D. Suter, and Y. Sun, “Sensitive optical biosensors for unlabeled targets: a review,” *Analytica Chimica Acta*, vol. 620, no. 1-2, pp. 8–26, 2008.

[148] P. Kozma, F. Kehl, E. Ehrentreich-Förster, C. Stamm, and F. F. Bier, “Integrated planar optical waveguide interferometer biosensors: A comparative review,” *Biosensors and Bioelectronics*, vol. 58, pp. 287–307, 2014.

[149] B. Cunningham, P. Li, B. Lin, and J. Pepper, “Colorimetric resonant reflection as a direct biochemical assay technique,” *Sensors and Actuators B: Chemical*, vol. 81, no. 2-3, pp. 316–328, 2002.

[150] A. Rothen, “The ellipsometer, an apparatus to measure thicknesses of thin surface films,” *Review of Scientific Instruments*, vol. 16, no. 2, pp. 26–30, 1945.

[151] K. Tiefenthaler and W. Lukosz, “Sensitivity of grating couplers as integrated-optical chemical sensors,” *JOSA B*, vol. 6, no. 2, pp. 209–220, 1989.

[152] F. Höök, J. Vörös, M. Rodahl, R. Kurrat, P. Böni, J. Ramsden, M. Textor, N. Spencer, P. Tengvall, J. Gold, *et al.*, "A comparative study of protein adsorption on titanium oxide surfaces using in situ ellipsometry, optical waveguide lightmode spectroscopy, and quartz crystal microbalance/dissipation," *Colloids and Surfaces B: Biointerfaces*, vol. 24, no. 2, pp. 155–170, 2002.

[153] S. M. Borisov and O. S. Wolfbeis, "Optical biosensors," *Chemical reviews*, vol. 108, no. 2, pp. 423–461, 2008.

[154] A. Chaubey and B. Malhotra, "Mediated biosensors," *Biosensors and bioelectronics*, vol. 17, no. 6-7, pp. 441–456, 2002.

[155] J.-G. Guan, Y.-Q. Miao, and Q.-J. Zhang, "Impedimetric biosensors," *Journal of bioscience and bioengineering*, vol. 97, no. 4, pp. 219–226, 2004.

[156] M. I. Prodromidis, "Impedimetric immunosensors—a review," *Electrochimica Acta*, vol. 55, no. 14, pp. 4227–4233, 2010.

[157] M. J. Schöning and A. Poghossian, "Recent advances in biologically sensitive field-effect transistors (BioFETs)," *Analyst*, vol. 127, no. 9, pp. 1137–1151, 2002.

[158] P. D'Orazio, "Biosensors in clinical chemistry," *Clinica Chimica Acta*, vol. 334, no. 1-2, pp. 41–69, 2003.

[159] D. Grieshaber, R. MacKenzie, J. Voeroes, and E. Reimhult, "Electrochemical biosensors-sensor principles and architectures," *Sensors*, vol. 8, no. 3, pp. 1400–1458, 2008.

[160] A. J. Bard and L. R. Faulkner, *Electrochemical Methods: Fundamentals and Applications*. John Wiley & Sons, second ed., 2001.

[161] P. N. Bartlett, *Bioelectrochemistry: fundamentals, experimental techniques and applications*. John Wiley & Sons, 2008.

[162] K. R. Rogers and M. Mascini, "Biosensors for field analytical monitoring," *Field Analytical Chemistry & Technology*, vol. 2, no. 6, pp. 317–331, 1998.

[163] C. N. LaFratta and D. R. Walt, "Very high density sensing arrays," *Chemical reviews*, vol. 108, no. 2, pp. 614–637, 2008.

[164] J.-W. Choi, K. W. Oh, J. H. Thomas, W. R. Heineman, H. B. Halsall, J. H. Nevin, A. J. Helmicki, H. T. Henderson, and C. H. Ahn, "An integrated microfluidic biochemical detection system for protein analysis with magnetic bead-based sampling capabilities," *Lab on a Chip*, vol. 2, no. 1, pp. 27–30, 2002.

[165] M. Varshney and Y. Li, "Interdigitated array microelectrode based impedance biosensor coupled with magnetic nanoparticle–antibody conjugates for detection of Escherichia coli O157: H7 in food samples," *Biosensors and Bioelectronics*, vol. 22, no. 11, pp. 2408–2414, 2007.

[166] S. E. Fosdick, K. N. Knust, K. Scida, and R. M. Crooks, “Bipolar electrochemistry,” *Angewandte Chemie International Edition*, vol. 52, no. 40, pp. 10438–10456, 2013.

[167] M. A. Zevenbergen, B. L. Wolfrum, E. D. Goluch, P. S. Singh, and S. G. Lemay, “Fast electron-transfer kinetics probed in nanofluidic channels,” *Journal of the American Chemical Society*, vol. 131, no. 32, pp. 11471–11477, 2009.

[168] C. Ma, N. M. Contento, L. R. Gibson, and P. W. Bohn, “Redox cycling in nanoscale-recessed ring-disk electrode arrays for enhanced electrochemical sensitivity,” *Acs Nano*, vol. 7, no. 6, pp. 5483–5490, 2013.

[169] T. Yin and W. Qin, “Applications of nanomaterials in potentiometric sensors,” *TrAC Trends in Analytical Chemistry*, vol. 51, pp. 79–86, 2013.

[170] E. Bakker and E. Pretsch, “Potentiometric sensors for trace-level analysis,” *TrAC Trends in Analytical Chemistry*, vol. 24, no. 3, pp. 199–207, 2005.

[171] A. Manz, N. Graber, and H. á. Widmer, “Miniaturized total chemical analysis systems: a novel concept for chemical sensing,” *Sensors and actuators B: Chemical*, vol. 1, no. 1-6, pp. 244–248, 1990.

[172] S. El Ichi, F. Leon, L. Vossier, H. Marchandin, A. Errachid, J. Coste, N. Jaffrezic-Renault, and C. Fournier-Wirth, “Microconductometric immunosensor for label-free and sensitive detection of gram-negative bacteria,” *Biosensors and bioelectronics*, vol. 54, pp. 378–384, 2014.

[173] R. Spera, F. Festa, N. L. Bragazzi, E. Pechkova, J. LaBaer, and C. Nicolini, “Conductometric monitoring of protein–protein interactions,” *Journal of proteome research*, vol. 12, no. 12, pp. 5535–5547, 2013.

[174] C. Berggren, B. Bjarnason, and G. Johansson, “Capacitive biosensors,” *Electroanalysis*, vol. 13, no. 3, pp. 173–180, 2001.

[175] F. Patolsky and C. M. Lieber, “Nanowire nanosensors,” *Materials today*, vol. 8, no. 4, pp. 20–28, 2005.

[176] I. Lee, X. Luo, J. Huang, X. T. Cui, and M. Yun, “Detection of cardiac biomarkers using single polyaniline nanowire-based conductometric biosensors,” *Biosensors*, vol. 2, no. 2, pp. 205–220, 2012.

[177] P. Bergveld, “Development of an ion-sensitive solid-state device for neurophysiological measurements,” *IEEE Transactions on Biomedical Engineering*, vol. BME-17, no. 1, pp. 70–71, 1970.

[178] A. Tarasov, W. Fu, O. Knopfmacher, J. Brunner, M. Calame, and C. Schönenberger, “Signal-to-noise ratio in dual-gated silicon nanoribbon field-effect sensors,” *Applied physics letters*, vol. 98, no. 1, p. 012114, 2011.

[179] E. Accastelli, G. Cappi, J. Buckley, T. Ernst, and C. Guiducci, "Comparison between front- and back-gating of silicon nanoribbons in real-time sensing experiments," in *Proc. 2013 IEEE 13th IEEE Conference on Nanotechnology (IEEE-NANO)*, pp. 517–520, 2013.

[180] P. Scarbolo, E. Accastelli, F. Pittino, T. Ernst, C. Guiducci, and L. Selmi, "Characterization and modelling of differential sensitivity of nanoribbon-based ph-sensors," in *Proc. 18th International Conference on Solid-State Sensors, Actuators and Microsystems (TRANSDUCERS)*, pp. 2188–2191, June 2015.

[181] S. Rigante *et al.*, "Sensing with advanced computing technology: fin field-effect transistors with high-k gate stack on bulk silicon," *ACS nano*, vol. 9, no. 5, pp. 4872–4881, 2015.

[182] F. Lisdat and D. Schäfer, "The use of electrochemical impedance spectroscopy for biosensing," *Analytical and bioanalytical chemistry*, vol. 391, no. 5, p. 1555, 2008.

[183] T. Bryan, X. Luo, P. R. Bueno, and J. J. Davis, "An optimised electrochemical biosensor for the label-free detection of C-reactive protein in blood," *Biosensors and Bioelectronics*, vol. 39, no. 1, pp. 94–98, 2013.

[184] E. Barsoukov and J. R. Macdonald, *Impedance spectroscopy: theory, experiment, and applications.* John Wiley & Sons, 2018.

[185] M. Carminati, G. Ferrari, D. Bianchi, and M. Sampietro, "Impedance spectroscopy for biosensing: Circuits and applications," *Handbook of Biochips: Integrated Circuits and Systems for Biology and Medicine*, pp. 1–24, 2015.

[186] M. Carminati and G. Ferrari, "Basic techniques for capacitance and impedance measurements," *Capacitance Spectroscopy of Semiconductors*, p. 117, 2018.

[187] R. Garcia-Ramirez, O. Villalta-Gutierrez, and R. Rimolo-Donadio, "Review of CMOS circuit architectures for electrical impedance spectroscopy," in *Proc. IEEE 36th Central American and Panama Convention (CONCAPAN)*, pp. 1–6, 2016.

[188] G. Ferrari and M. Carminati, "Advanced instrumentation for high-resolution capacitance and impedance measurements," *Capacitance Spectroscopy of Semiconductors*, p. 149, 2018.

[189] J. Chen, B. McGaughy, D. Sylvester, and C. Hu, "An on-chip, attofarad interconnect charge-based capacitance measurement (CBCM) technique," in *Proc. IEDM*, pp. 69–72, 1996.

[190] F. Widdershoven, A. Cossettini, C. Laborde, A. Bandiziol, P. P. van Swinderen, S. G. Lemay, and L. Selmi, "A CMOS pixelated nanocapacitor biosensor platform for high-frequency impedance spectroscopy and imaging," *IEEE Transactions on Biomedical Circuits and Systems*, vol. 12, pp. 1369–1382, Dec 2018.

[191] R. M. Foster, “A reactance theorem,” *Bell System Technical Journal*, vol. 3, no. 2, pp. 259–267, 1924.

[192] W. Cauer, “Die verwirklichung von wechselstromwiderständen vorgeschriebener frequenzabhängigkeit,” *Archiv für Elektrotechnik*, vol. 17, no. 4, pp. 355–388, 1926.

[193] K. Murthy and R. Bedford, “Transformation between Foster and Cauer equivalent networks,” *IEEE Transactions on Circuits and Systems*, vol. 25, pp. 238–239, April 1978.

[194] U. Rammelt and G. Reinhard, “On the applicability of a constant phase element (CPE) to the estimation of roughness of solid metal electrodes,” *Electrochimica Acta*, vol. 35, no. 6, pp. 1045–1049, 1990.

[195] J. E. B. Randles, “Kinetics of rapid electrode reactions,” *Discussions of the faraday society*, vol. 1, pp. 11–19, 1947.

[196] M. E. Orazem and B. Tribollet, *Electrochemical impedance spectroscopy*, vol. 48. John Wiley & Sons, 2011.

[197] S. P. Basak, B. Kanjilal, P. Sarkar, and A. P. Turner, “Application of electrical impedance spectroscopy and amperometry in polyaniline modified ammonia gas sensor,” *Synthetic Metals*, vol. 175, pp. 127–133, 2013.

[198] H. Helmholtz, “Studien über electrische Grenzschichten,” *Annalen der Physik*, vol. 243, no. 7, pp. 337–382, 1879.

[199] M. Gouy, “Sur la constitution de la charge électrique à la surface d’un électrolyte,” *Journal de Physique Théorique et Appliquée*, vol. 9, no. 1, pp. 457–468, 1910.

[200] D. L. Chapman, “LI. a contribution to the theory of electrocapillarity,” *The London, Edinburgh, and Dublin philosophical magazine and journal of science*, vol. 25, no. 148, pp. 475–481, 1913.

[201] O. Stern, “Zur theorie der elektrolytischen doppelschicht,” *Zeitschrift für Elektrochemie und angewandte physikalische Chemie*, vol. 30, no. 21-22, pp. 508–516, 1924.

[202] A. Matsumoto and Y. Miyahara, “Current and emerging challenges of field effect transistor based bio-sensing,” *Nanoscale*, vol. 5, pp. 10702 – 10718, 2013.

[203] F. Pittino, “Prospects of nanoelectronic biosensing with high-frequency impedance spectroscopy,” *Ph.D. dissertation, DIEGM, University of Udine, Udine, Italy*, 2015.

[204] E. Stern, J. Klemic, D. Routenberg, P. Wyrembak, D. Turner-Evans, D. LaVan, T. Fahmy, and M. Reed, “Label-free immunodetection with CMOS-compatible semiconducting nanowires,” *Nature*, vol. 445, pp. 519–522, 2007.

[205] L. Yang, “Electrical impedance spectroscopy for detection of bacterial cells in suspensions using interdigitated microelectrodes,” *Talanta*, vol. 74, no. 5, pp. 1621–1629, 2008.

[206] N. Couniot, A. Afzalian, N. Van Overstraeten-Schlögel, L. Francis, and D. Flandre, “Capacitive biosensing of bacterial cells: analytical model and numerical simulations,” *Sensors and Actuators B: Chemical*, vol. 211, pp. 428–438, 2015.

[207] G. S. Kulkarni and Z. Zhong, “Detection beyond the Debye screening length in a high-frequency nanoelectronic biosensor,” *Nano Letters*, vol. 12, no. 2, pp. 719–723, 2012.

[208] F. Pittino, L. Selmi, and F. Widdershoven, “Numerical and analytical models to investigate the AC high-frequency response of nanoelectrode/SAM/electrolyte capacitive sensing elements,” *Solid-State Electronics*, vol. 88, no. 0, pp. 82 – 88, 2013.

[209] S. G. Lemay, C. Laborde, C. Renault, A. Cossettini, L. Selmi, and F. P. Widdershoven, “High-frequency nanocapacitor arrays: Concept, recent developments, and outlook,” *Accounts of Chemical Research*, vol. 49, no. 10, pp. 2355–2362, 2016.

[210] F. Widdershoven, “CMOS Pixelated Capacitive Sensor platform for biosensing and many other applications,” Oct 2016. Smart sensors NEREID workshop.

[211] F. Pittino, P. Scarbolo, F. Widdershoven, and L. Selmi, “Derivation and numerical verification of a compact analytical model for the AC admittance response of nanoelectrodes, suitable for the analysis and optimization of impedance biosensors,” *IEEE Trans. Nanotechnology*, vol. 14, no. 4, pp. 709–716, 2015.

[212] J. Muñoz, R. Montes, and M. Baeza, “Trends in electrochemical impedance spectroscopy involving nanocomposite transducers: characterization, architecture surface and bio-sensing,” *TrAC Trends in Analytical Chemistry*, 2017.

[213] C. Zhu, G. Yang, H. Li, D. Du, and Y. Lin, “Electrochemical sensors and biosensors based on nanomaterials and nanostructures,” *Analytical chemistry*, vol. 87, no. 1, pp. 230–249, 2014.

[214] F. Widdershoven *et al.*, “CMOS biosensor platform,” *Proc. IEDM*, pp. 816–819, 2010.

[215] C. Laborde, F. Pittino, H. Verhoeven, S. Lemay, L. Selmi, M. Jongsma, and F. Widdershoven, “Real-time imaging of microparticles and living cells with CMOS nanocapacitor arrays,” *Nature Nanotechnology*, vol. 10, no. 9, pp. 791–795, 2015.

[216] C. Stagni, C. Guiducci, L. Benini, B. Ricco, S. Carrara, B. Samori, C. Paulus, M. Schienle, M. Augustyniak, and R. Thewes, “CMOS DNA sensor array with

integrated A/D conversion based on label-free capacitance measurement," *IEEE Journal of Solid-State Circuits*, vol. 41, pp. 2956–2964, Dec 2006.

[217] V. Viswam, R. Bounik, A. Shadmani, J. Dragas, A. J. Boos, A. Birchler, J. Müller, Y. Chen, and A. Hierlemann, "High-density CMOS microelectrode array system for impedance spectroscopy and imaging of biological cells," in *Proc. IEEE SENSORS*, pp. 1–3, 2016.

[218] N. Couniot, L. A. Francis, and D. Flandre, "A 16 × 16 CMOS capacitive biosensor array towards detection of single bacterial cell," *IEEE Transactions on Biomedical Circuits and Systems*, vol. 10, pp. 364–374, April 2016.

[219] H. Li, S. Parsnejad, E. Ashoori, C. Thompson, E. K. Purcell, and A. J. Mason, "Ultracompact microwatt CMOS current readout with picoampere noise and kilohertz bandwidth for biosensor arrays," *IEEE Transactions on Biomedical Circuits and Systems*, vol. 12, pp. 35–46, Feb 2018.

[220] C. Stagni, C. Guiducci, L. Benini, B. Ricco, S. Carrara, C. Paulus, M. Schienle, and R. Thewes, "A fully electronic label-free DNA sensor chip," *IEEE Sensors Journal*, vol. 7, pp. 577–585, April 2007.

[221] J. S. Park, T. Chi, A. Su, C. Zhu, J. H. Sung, H. C. Cho, M. Styczynski, and H. Wang, "A high-density CMOS multi-modality joint sensor/stimulator array with 1024 pixels for holistic real-time cellular characterization," in *2016 IEEE Symposium on VLSI Circuits (VLSI-Circuits)*, pp. 1–2, June 2016.

[222] J. Abbott, T. Ye, L. Qin, M. Jorgolli, R. S. Gertner, D. Ham, and H. Park, "CMOS nanoelectrode array for all-electrical intracellular electrophysiological imaging," *Nature nanotechnology*, vol. 12, no. 5, p. 460, 2017.

[223] A. Hierlemann, U. Frey, S. Hafizovic, and F. Heer, "Growing cells atop microelectronic chips: Interfacing electrogenic cells in vitro with CMOS–based microelectrode arrays," *Proceedings of the IEEE*, vol. 99, pp. 252–284, Feb 2011.

[224] V. Viswam, J. Dragas, A. Shadmani, Y. Chen, A. Stettler, J. Müller, and A. Hierlemann, "Multi-functional microelectrode array system featuring 59,760 electrodes, 2048 electrophysiology channels, impedance and neurotransmitter measurement units," in *Proc. 2016 IEEE International Solid-State Circuits Conference (ISSCC)*, pp. 394–396, Jan 2016.

[225] G. N. Angotzi, M. Malerba, F. Boi, E. Miele, A. Maccione, H. Amin, M. Crepaldi, and L. Berdondini, "A synchronous neural recording platform for multiple high-resolution CMOS probes and passive electrode arrays," *IEEE Transactions on Biomedical Circuits and Systems*, vol. 12, pp. 532–542, June 2018.

[226] G. Nabovati, E. Ghafar-Zadeh, A. Letourneau, and M. Sawan, "Towards high throughput cell growth screening: A new CMOS 8 × 8 biosensor array for life

science applications," *IEEE Transactions on Biomedical Circuits and Systems*, vol. 11, pp. 380–391, April 2017.

[227] M. Carminati, G. Ferrari, F. Guagliardo, and M. Sampietro, "Zeptofarad capacitance detection with a miniaturized CMOS current front-end for nanoscale sensors," *Sens Actuators A Phys*, vol. 172, no. 1, pp. 117–123, 2011.

[228] P. Ciccarella, M. Carminati, M. Sampietro, and G. Ferrari, "Multichannel 65 zF rms resolution CMOS monolithic capacitive sensor for counting single micrometer-sized airborne particles on chip," *IEEE Journal of Solid-State Circuits*, vol. 51, pp. 2545–2553, Nov 2016.

[229] E. Stern, R. Wagner, F. J. Sigworth, R. Breaker, T. M. Fahmy, and M. A. Reed, "Importance of the Debye screening length on nanowire field effect transistor sensors," *Nano letters*, vol. 7, no. 11, pp. 3405–3409, 2007.

[230] S. Ingebrandt, "Bioelectronics: sensing beyond the limit," *Nature nanotechnology*, vol. 10, no. 9, p. 734, 2015.

[231] C.-H. Chu, I. Sarangadharan, A. Regmi, Y.-W. Chen, C.-P. Hsu, W.-H. Chang, G.-Y. Lee, J.-I. Chyi, C.-C. Chen, S.-C. Shiesh, *et al.*, "Beyond the Debye length in high ionic strength solution: direct protein detection with field-effect transistors (FETs) in human serum," *Scientific reports*, vol. 7, no. 1, p. 5256, 2017.

[232] C. C. Wong, C. Drews, Y. Chen, T. S. Pui, S. Arya, R. Weerasekera, and A. Rahman, "CMOS based high density micro array platform for electrochemical detection and enumeration of cells," in *Electron Devices Meeting (IEDM), 2013 IEEE International*, pp. 14.2.1–14.2.4, 2013.

[233] C. Ionescu-Zanetti, J. Nevill, D. Di Carlo, K. Jeong, and L. Lee, "Nanogap capacitors: Sensitivity to sample permittivity changes," *Journal of applied physics*, vol. 99, no. 2, p. 024305, 2006.

[234] A. Susloparova, D. Koppenhöfer, X. Vu, M. Weil, and S. Ingebrandt, "Impedance spectroscopy with field-effect transistor arrays for the analysis of anti-cancer drug action on individual cells," *Biosensors and Bioelectronics*, vol. 40, no. 1, pp. 50–56, 2013.

[235] P. van Gerwen, W. Laureyn, W. Laureys, G. Huyberechts, M. O. de Beeck, K. Baert, J. Suls, W. Sansen, P. Jacobs, L. Hermans, and R. Mertens, "Nanoscaled interdigitated electrode arrays for biochemical sensors," *Sensors and Actuators B: Chemical*, vol. 49, no. 1–2, pp. 73 – 80, 1998.

[236] M. Löhndorf, U. Schlecht, T. Gronewold, A. Malavé, and M. Tewes, "Microfabricated high-performance microwave impedance biosensors for detection of aptamer-protein interactions," *Applied Physics Letters*, vol. 87, no. 24, p. 243902, 2005.

[237] G. S. Kulkarni and Z. Zhong, “Fabrication of carbon nanotube high-frequency nanoelectronic biosensor for sensing in high ionic strength solutions,” *Journal of Visualized Experiments: JoVE*, no. 77, e50430, pp. 1–14, 2013.

[238] A. Manickam, A. Chevalier, M. McDermott, A. Ellington, and A. Hassibi, “A CMOS electrochemical impedance spectroscopy (EIS) biosensor array,” *IEEE Transactions on Biomedical Circuits and Systems*, vol. 4, no. 6, pp. 379–390, 2010.

[239] J. Rosenstein, V. Ray, M. Drndic, and K. L. Shepard, “Nanopore DNA sensors in CMOS with on-chip low-noise preamplifiers,” in *2011 16th International Solid-State Sensors, Actuators and Microsystems Conference (TRANSDUCERS)*, pp. 874–877, June 2011.

[240] M. Carminati, “Advances in high-resolution microscale impedance sensors,” *Journal of Sensors*, vol. 2017, pp. 1–15, 2017.

[241] “International Technology Roadmap for Semiconductors.” http://www.itrs2.net/ (accessed October, 2018).

[242] D. Bianchi, G. Ferrari, A. Rottigni, and M. Sampietro, “CMOS impedance analyzer for nanosamples investigation operating up to 150 MHz with sub-aF resolution,” *IEEE Journal of Solid-State Circuits*, vol. 49, pp. 2748–2757, Dec 2014.

[243] N. Couniot, D. Bol, O. Poncelet, L. A. Francis, and D. Flandre, “A capacitance-to-frequency converter with on-chip passivated microelectrodes for bacteria detection in saline buffers up to 575 MHz,” *IEEE Transactions on Circuits and Systems II: Express Briefs*, vol. 62, pp. 159–163, Feb 2015.

[244] F. Pittino, M. Dalla Longa, P. Scarbolo, A. Cossettini, and L. Selmi, “ENBIOS-1D Lab,” May 2016. v1.0. [Online]. Available: https://nanohub.org/resources/biolab, doi: 10.4231/D3Z60C34Q.

[245] P. Scarbolo, F. Pittino, M. Dalla Longa, A. Cossettini, and L. Selmi, “ENBIOS-1D Lab,” Apr 2017. v3.0. [Online]. Available: https://nanohub.org/resources/biolab, doi: 10.4231/D3Z02Z963.

[246] A. Hoxha, P. Scarbolo, A. Cossettini, F. Pittino, and L. Selmi, “ENBIOS-2D Lab,” Oct 2016. v1.0. [Online]. Available: https://nanohub.org/resources/biolabisfet, doi: 10.4231/D3V11VM7D.

[247] A. Cossettini, M. Dalla Longa, P. Scarbolo, and L. Selmi, “Modeling and simulation of small CCMV virus detection by means of high frequency impedance spectroscopy at nanoelectrodes,” in *Proc. 2017 IEEE 17th International Conference on Nanotechnology (IEEE-NANO)*, (Pittsburgh, PA, USA), pp. 416–419, 25–28 July 2017.

[248] A. Cossettini and L. Selmi, “On the response of nanoelectrode impedance spectroscopy measures to plant, animal, and human viruses,” *IEEE Transactions on NanoBioscience*, vol. 17, pp. 102–109, April 2018.

[249] B. Stadlbauer, L. Taghizadeh, J. M. Escalante, C. Heitzinger, A. Cossettini, and L. Selmi, "Bayesian estimation for transport equations for nanocapacitors," in *Proc. SIAM Conference on Uncertainty Quantification (UQ 2018)*, (Garden Grove, CA, USA), pp. 69–70, 16–19 April 2018.

[250] A. Cossettini, P. Scarbolo, J. M. Escalante, B. Stadlbauer, N. Muhammad, L. Taghizadeh, C. Heitzinger, and L. Selmi, "Calibration, compensation, parameter estimation, and uncertainty quantification for nanoelectrode array biosensors," in *Proc. SIAM Conference on Uncertainty Quantification (UQ 2018)*, (Garden Grove, CA, USA), p. 81, 16–19 April 2018.

[251] A. Cossettini and L. Selmi, "Calibration of high-frequency impedance spectroscopy measurements with nanocapacitor arrays," in *Proc. 2nd European Biosensor Symposium (EBS2019)*, (Florence, Italy), 18–21 February 2019.

[252] M. Mase, S. Kawahito, M. Sasaki, Y. Wakamori, and M. Furuta, "A wide dynamic range CMOS image sensor with multiple exposure-time signal outputs and 12-bit column-parallel cyclic A/D converters," *IEEE Journal of Solid-State Circuits*, vol. 40, pp. 2787–2795, Dec 2005.

[253] W. Y. Sinclair, "Integrated circuit test probe," Jan. 18 2005. US Patent 6,844,749.

[254] Datasheet, Aries Electronics Inc., A1924-314-23-2, "23021 CSP STYLE SOCKET .35mm PITCH, 36LD, LGA 2.122mm X 3.168mm," 2014.

[255] IDEX Health & Science, "https://www.idex-hs.com/."

[256] Microcolumn S.r.l., "http://www.microcolumn.it."

[257] S. M. Kurtz, ed., *PEEK biomaterials handbook*. Elsevier, 1st ed., 2011.

[258] Zeus Industrial Products, Inc., "Chemical Resistance." https://www.zeusinc.com/resources/summary-material-properties/chemical-resistance.

[259] Shielding Solutions Ltd., "https://shielding-solutions.com/."

[260] Laser Veronese, "https://www.laserveronese.net/."

[261] 3D Project Lab, "https://www.3dplabudine.it/."

[262] Sigma-Aldrich Corporation, "https://www.sigmaaldrich.com/."

[263] F. Widdershoven (NXP Semiconductors), "PDMS." Private communication.

[264] New Era Pump Systems, Inc., "NE-300 Just Infusion$^{\text{TM}}$ Syringe Pump, https://www.syringepump.com/NE-300.php."

[265] KF Technology, "http://www.kftechnology.it/."

[266] J. S. Park, M. K. Aziz, S. Li, T. Chi, S. I. Grijalva, J. H. Sung, H. C. Cho, and H. Wang, "1024-pixel CMOS multimodality joint cellular sensor/stimulator array for real-time holistic cellular characterization and cell-based drug screening," *IEEE Transactions on Biomedical Circuits and Systems*, vol. 12, pp. 80–94, Feb 2018.

[267] H. Jafari, L. Soleymani, and R. Genov, "16-channel CMOS impedance spectroscopy DNA analyzer with dual-slope multiplying ADCs," *IEEE Transactions on Biomedical Circuits and Systems*, vol. 6, pp. 468–478, Oct 2012.

[268] C. M. Lopez, H. S. Chun, L. Berti, S. Wang, J. Putzeys, C. V. D. Bulcke, J. W. Weijers, A. Firrincieli, V. Reumers, D. Braeken, and N. V. Helleputte, "A 16384-electrode 1024-channel multimodal cmos mea for high-throughput intracellular action potential measurements and impedance spectroscopy in drug-screening applications," in *Proc. 2018 IEEE International Solid-State Circuits Conference - (ISSCC)*, pp. 464–466, Feb 2018.

[269] F. Pittino and L. Selmi, "Use and comparative assessment of the CVFEM method for Poisson-Boltzmann and Poisson-Nernst-Planck three dimensional simulations of impedimetric nano-biosensors operated in the DC and AC small signal regimes," *Computational Methods in Applied Mechanics and Engineering*, pp. 902–923, 2014.

[270] L. Bousse and P. Bergveld, "On the impedance of the silicon dioxide/electrolyte interface," *Journal of Electroanalytical Chemistry and Interfacial Electrochemistry*, vol. 152, no. 1-2, pp. 25–39, 1983.

[271] C. Menzel, T. Lerch, T. Scheper, and K. Schügerl, "Development of biosensors based on an electrolyte isolator semiconductor (EIS)-capacitor structure and their application for process monitoring. Part I. Development of the biosensors and their characterization," *Analytica Chimica Acta*, vol. 317, no. 1-3, pp. 259–264, 1995.

[272] M. H. Abouzar, W. Moritz, M. J. Schöning, and A. Poghossian, "Capacitance–voltage and impedance-spectroscopy characteristics of nanoplate EISOI capacitors," *physica status solidi (a)*, vol. 208, no. 6, pp. 1327–1332, 2011.

[273] Y. Liu and R. W. Dutton, "Effects of charge screening and surface properties on signal transduction in field effect nanowire biosensors," *Journal of Applied Physics*, vol. 106, no. 1, pp. –, 2009.

[274] Y.Wang and G.Li, "Performance investigation for a silicon nanowire FET biosensor using numerical simulation," in *Proc. IEEE Nanotechnology Materials and Devices Conference*, pp. 81–86, 2010.

[275] S. Baumgartner, M. Vasicek, A. Bulyha, and C. Heitzinger, "Optimization of nanowire DNA sensor sensitivity using self-consistent simulation," *Nanotechnology*, vol. 22, no. 42, p. 425503, 2011.

[276] S. Baumgartner and C. Heitzinger, “Existence and local uniqueness for 3d self-consistent multiscale models of field-effect sensors,” *Commun. Math. Sci*, vol. 10, no. 2, pp. 693–716, 2012.

[277] A. Flavell, M. Machen, B. Eisenberg, J. Kabre, C. Liu, and X. Li, “A conservative finite difference scheme for Poisson-Nernst-Planck equations,” *Journal of Computational Electronics*, pp. 1–15, 2013.

[278] F. Pittino and L. Selmi, “A technique to model the AC response of diffuse layers at electrode/electrolyte interfaces and to efficiently simulate impedimetric biosensor arrays for many analyte configurations,” in *Proceedings of the International Conference on Simulation of Semiconductor Processes and Devices (SISPAD)*, pp. 353–356, 2014.

[279] P. Scarbolo, “Electrical characterization and modeling of pH and microparticle nanoelectronic sensors,” *Ph.D. dissertation, DPIA, University of Udine, Udine, Italy*, 2017.

[280] J. Schöberl, “NETGEN an advancing front 2D/3D-mesh generator based on abstract rules,” *Computing and Visualization in Science*, vol. 1, pp. 41–52, 1997.

[281] R. d. L. Kronig, “On the theory of dispersion of X-rays,” *Josa*, vol. 12, no. 6, pp. 547–557, 1926.

[282] H. Kramers, “Diffusion of light by atoms,” *Atti. Congr. Internat. Fisici*, vol. 2, pp. 545–57, 1927.

[283] R. Van Hal, J. C. Eijkel, and P. Bergveld, “A general model to describe the electrostatic potential at electrolyte oxide interfaces,” *Advances in colloid and interface science*, vol. 69, no. 1-3, pp. 31–62, 1996.

[284] A. P. Stogryn, H. T. Bull, K. Rubayi, and S. Iravanchy, “The microwave dielectric properties of sea and fresh water,” in *GenCorp Aerojet, Tech. Rep.*, 1995.

[285] J. Speight, ed., *Lange’s Handbook of Chemistry.* McGraw-Hill, 15th ed., 1999.

[286] G. Klimeck, M. McLennan, S. B. Brophy, G. B. Adams III, and M. S. Lundstrom, “nanoHUB.org: Advancing Education and Research in Nanotechnology,” *IEEE Computers in Engineering and Science (CISE)*, vol. 10, pp. 17–23, 2008.

[287] G. Klimeck, L. K. Zentner, K. P. Madhavan, V. A. Farnsworth, and M. S. Lundstrom, “Network for Computational Nanotechnology – A Strategic Plan for Global Knowledge Transfer in Research and Education,” in *Proc. IEEE Nanotechnology Materials and Devices Conference (IEEE NMDC)*, (The Shilla Jeju, Korea), IEEE, 18–21 October 2011.

[288] K. Madhavan, L. Zentner, V. Farnsworth, S. Shivarajapura, M. Zentner, N. Denny, and G. Klimeck, “nanoHUB.org: Cloud-based Services for Nanoscale Modeling, Simulation, and Education,” *Nanotechnology Reviews*, vol. 2, no. 1, pp. 107–117, 2013.

[289] K. S. Cole and R. H. Cole, “Dispersion and absorption in dielectrics I. Alternating current characteristics,” *The Journal of chemical physics*, vol. 9, no. 4, pp. 341–351, 1941.

[290] J. Powles, “Cole-Cole plots as they should be,” *Journal of molecular liquids*, vol. 56, pp. 35–47, 1993.

[291] F. Widdershoven (NXP Semiconductors), “Signal transduction chain.” Private communication.

[292] A. J. Jerri, *The Gibbs phenomenon in Fourier analysis, splines and wavelet approximations*, vol. 446. Springer Science & Business Media, 2013.

[293] R. I. MacCuspie, N. Nuraje, S.-Y. Lee, A. Runge, and H. Matsui, “Comparison of electrical properties of viruses studied by AC capacitance scanning probe microscopy,” *Journal of the American Chemical Society*, vol. 130, no. 3, pp. 887–891, 2008.

[294] M. Al Ahmad, F. Mustafa, L. M. Ali, J. V. Karakkat, and T. A. Rizvi, “Label-free capacitance-based identification of viruses,” *Scientific reports*, vol. 5, 2015.

[295] D. Zhang, R. Konecny, N. A. Baker, and J. A. McCammon, “Electrostatic interaction between RNA and protein capsid in cowpea chlorotic mottle virus simulated by a coarse-grain RNA model and a Monte Carlo approach,” *Biopolymers*, vol. 75, no. 4, pp. 325–337, 2004.

[296] J. A. Speir, S. Munshi, G. Wang, T. S. Baker, and J. E. Johnson, “Structures of the native and swollen forms of cowpea chlorotic mottle virus determined by X-ray crystallography and cryo-electron microscopy,” *Structure*, vol. 3, no. 1, pp. 63–78, 1995.

[297] D. L. Caspar and A. Klug, “Physical principles in the construction of regular viruses,” in *Cold Spring Harbor symposia on quantitative biology*, vol. 27, pp. 1–24, Cold Spring Harbor Laboratory Press, 1962.

[298] M. Carrillo-Tripp *et al.*, “VIPERdb2: an enhanced and web api enabled relational database for structural virology,” *Nucleic Acids Res*, vol. 37, no. suppl 1, pp. D436–D442, 2009.

[299] R. Francki, “The viruses and their taxonomy,” in *The Plant Viruses. Polyhedral Virions with Tripartite Genomes*, pp. 1–18, Plenum Press, New York, 1985.

[300] R. Konecny *et al.*, “Electrostatic properties of cowpea chlorotic mottle virus and cucumber mosaic virus capsids,” *Biopolymers*, vol. 82, no. 2, pp. 106–120, 2006.

[301] F. Tama and C. L. Brooks, "The mechanism and pathway of pH induced swelling in cowpea chlorotic mottle virus," *Journal of molecular biology*, vol. 318, no. 3, pp. 733–747, 2002.

[302] D. Luque *et al.*, "Epitope insertion at the n-terminal molecular switch of the rabbit hemorrhagic disease virus T=3 capsid protein leads to larger T= 4 capsids," *Journal of virology*, vol. 86, no. 12, pp. 6470–6480, 2012.

[303] E. Angulo and J. Bárcena, "Towards a unique and transmissible vaccine against myxomatosis and rabbit haemorrhagic disease for rabbit populations," *Wildlife Research*, vol. 34, no. 7, pp. 567–577, 2008.

[304] X. Wang *et al.*, "Hepatitis A virus and the origins of picornaviruses," *Nature*, vol. 517, no. 7532, pp. 85–88, 2015.

[305] J. L. Melnick, "Properties and classification of hepatitis A virus," *Vaccine*, vol. 10, no. Suppl 1, pp. S24–S26, 1992.

[306] A. L. Božič, A. Šiber, and R. Podgornik, "How simple can a model of an empty viral capsid be? Charge distributions in viral capsids," *Journal of Biological Physics*, vol. 38, no. 4, pp. 657–671, 2012.

[307] T. J. Dolinsky, J. E. Nielsen, J. A. McCammon, and N. A. Baker, "PDB2PQR: an automated pipeline for the setup of poisson–boltzmann electrostatics calculations," *Nucleic Acids Res*, vol. 32, no. suppl 2, pp. W665–W667, 2004.

[308] C. R. Søndergaard, M. H. Olsson, M. Rostkowski, and J. H. Jensen, "Improved treatment of ligands and coupling effects in empirical calculation and rationalization of pk_a values," *J. Chem. Theory Comput.*, vol. 7, no. 7, pp. 2284–2295, 2011.

[309] M. H. Olsson, C. R. Søndergaard, M. Rostkowski, and J. H. Jensen, "PROPKA3: consistent treatment of internal and surface residues in empirical pk_a predictions," *J. Chem. Theory Comput.*, vol. 7, no. 2, pp. 525–537, 2011.

[310] E. Antezana, "The amino acid masses." [Online]. Available: http://education.expasy.org/student_projects/isotopident/htdocs/aa-list.html. [Accessed: Mar 2017].

[311] A. V. Finkelstein and O. B. Ptitsyn, *Protein Physics.* London, U.K.: Academic, 2002.

[312] M. R. Gunner, J. Mao, Y. Song, and J. Kim, "Factors influencing the energetics of electron and proton transfers in proteins. What can be learned from calculations," *Biochim. Biophys. Acta*, vol. 1757, no. 8, pp. 942–968, 2006.

[313] D. G. Isom, B. R. Cannon, C. A. Castañeda, A. Robinson, and B. García-Moreno E, "High tolerance for ionizable residues in the hydrophobic interior of proteins," *Proc. Natl. Acad. Sci. U.S.A.*, vol. 105, no. 46, pp. 17784–17788, 2008.

[314] D. G. Isom, C. A. Castañeda, B. R. Cannon, P. D. Velu, and B. García-Moreno E, “Charges in the hydrophobic interior of proteins,” *Proc. Natl. Acad. Sci. U.S.A.*, vol. 107, no. 37, pp. 16096–16100, 2010.

[315] UniProt Consortium *et al.*, “Ongoing and future developments at the universal protein resource,” *Nucleic Acids Res*, vol. 39, no. suppl 1, pp. D214–D219, 2011.

[316] C. Putnam, “Protein calculator v3.4,” 2016. [Online]. Available: http://protcalc.sourceforge.net/. [Accessed: Mar 2017].

[317] A. Siber, A. L. Bozic, and R. Podgornik, “Energies and pressures in viruses: contribution of nonspecific electrostatic interactions,” *Phys. Chem. Chem. Phys.*, vol. 14, pp. 3746–3765, 2012.

[318] M. Aubouy, E. Trizac, and L. Bocquet, “Effective charge versus bare charge: an analytical estimate for colloids in the infinite dilution limit,” *J. Phys. A*, vol. 36, no. 22, p. 5835, 2003.

[319] J. Eden, P. R. Gascoyne, and R. Pethig, “Dielectric and electrical properties of hydrated bovine serum albumin,” *J. Chem. Soc., Faraday Trans. 1*, vol. 76, pp. 426–434, 1980.

[320] D. Kim and A. E. Herr, “Protein immobilization techniques for microfluidic assays,” *Biomicrofluidics*, vol. 7, no. 4, p. 041501, 2013 and references therein.

[321] D. Luque *et al.*, “Self-assembly and characterization of small and monodisperse dye nanospheres in a protein cage,” *Chemical Science*, vol. 5, no. 2, pp. 575–581, 2014.

[322] R. H. Cheng, V. S. Reddy, N. H. Olson, A. J. Fisher, T. S. Baker, and J. E. Johnson, “Functional implications of quasi-equivalence in a T= 3 icosahedral animal virus established by cryo-electron microscopy and X-ray crystallography,” *Structure*, vol. 2, no. 4, pp. 271–282, 1994.

[323] V. S. Reddy, H. A. Giesing, R. T. Morton, A. Kumar, C. B. Post, C. L. Brooks III, and J. E. Johnson, “Energetics of quasiequivalence: computational analysis of protein-protein interactions in icosahedral viruses,” *Biophysical journal*, vol. 74, no. 1, pp. 546–558, 1998.

[324] W. K. Pratt, *Digital image processing: PIKS Scientific inside*, vol. 4. Wiley-interscience Hoboken, New Jersey, 2007.

[325] Y. Wang, B. Cheng, X. Wang, E. Towie, C. Riddet, A. Brown, S. Amoroso, L. Wang, D. Reid, X. Liu, *et al.*, “Variability-aware tcad based design-technology co-optimization platform for 7nm node nanowire and beyond,” in *VLSI Technology, 2016 IEEE Symposium on*, pp. 1–2, IEEE, 2016.

[326] A. Asenov, S. M. Amoroso, L. Gerrer, F. Adamu-Lema, V. P. Georgiev, and X. Wang, “Tcad-based design technology co-optimization for variability in

nanoscale soi finfets," in *Integrated Nanodevice and Nanosystem Fabrication*, pp. 235–272, Pan Stanford, 2017.

[327] R. C. Smith, *Uncertainty quantification*, vol. 12 of *Computational Science & Engineering.* Society for Industrial and Applied Mathematics (SIAM), Philadelphia, PA, 2014. Theory, implementation, and applications.

[328] B. V. Rosić, A. Kučerová, J. Sýkora, O. Pajonk, A. Litvinenko, and H. G. Matthies, "Parameter identification in a probabilistic setting," *Engineering Structures*, vol. 50, no. Supplement C, pp. 179 – 196, 2013. Engineering Structures: Modelling and Computations (special issue IASS-IACM 2012).

[329] E. S. Jackson and W. J. Fitzgerald, "Introduction to bayesian methods for biosensor design," *Handbook of Biosensors and Biochips*, 2008.

[330] A. Papoulis and S. U. Pillai, *Probability, random variables, and stochastic processes.* Tata McGraw-Hill Education, 2002.

[331] H. W. Engl and P. Kügler, "Nonlinear inverse problems: theoretical aspects and some industrial applications," in *Multidisciplinary methods for analysis optimization and control of complex systems*, pp. 3–47, Springer, 2005.

[332] M. Kern, *Numerical Methods for Inverse Problems.* John Wiley & Sons, 2016.

[333] N. Metropolis, A. W. Rosenbluth, M. N. Rosenbluth, A. H. Teller, and E. Teller, "Equation of state calculations by fast computing machines," *The Journal of Chemical Physics*, vol. 21, no. 6, pp. 1087–1092, 1953.

[334] W. K. Hastings, "Monte Carlo sampling methods using Markov chains and their applications," *Biometrika*, vol. 57, no. 1, pp. 97–109, 1970.

[335] B. W. Silverman, *Density estimation for statistics and data analysis.* Routledge, 2018.

[336] J. Bezanson *et al.*, "Julia: The Julia programming language, v1.0," 2012–2018. https://julialang.org/.

[337] F. Widdershoven (NXP Semiconductors), "Post-processing calibration." Private communication.

[338] F. Widdershoven (NXP Semiconductors), "Charge detector analysis." Private communication.

[339] Cadence Design Systems, Inc., "Cadence IC 6.1.6."

[340] Nanoscale Integration and Modeling (NIMO) Group, Arizona State University, "Predictive Technology Model." http://ptm.asu.edu/.

[341] Y. Cao, T. Sato, M. Orshansky, D. Sylvester, and C. Hu, "New paradigm of predictive MOSFET and interconnect modeling for early circuit simulation," in *Proceedings of the IEEE 2000 Custom Integrated Circuits Conference (CICC)*, pp. 201–204, IEEE, 2000.

[342] C. E. Housecroft, C. G. Palivan, K. Gademann, W. Meier, M. Calame, V. Mikhalevich, X. Zhang, E. Piel, M. Szponarski, A. Wiesler, *et al.*, "'active surfaces' as possible functional systems in detection and chemical (bio) reactivity," *CHIMIA International Journal for Chemistry*, vol. 70, no. 6, pp. 402–412, 2016.

[343] R. J. Good, "Contact angle, wetting, and adhesion: a critical review," *Journal of adhesion science and technology*, vol. 6, no. 12, pp. 1269–1302, 1992.

[344] F. Widdershoven (NXP Semiconductors), "Emulsion experiments." Private communication.

[345] The MathWorks, Inc., "bwarea."
https://it.mathworks.com/help/images/ref/bwarea.html.

[346] C. Laborde, "High-frequency impedance spectroscopy at CMOS nanocapacitor arrays," *Ph.D. dissertation, MESA+ Institute for Nanotechnology, University of Twente, Enschede, The Netherlands*, 2016.

[347] Q. Zhu, T. Merelle, F. Widdershoven, and S. V. Huffel, "Signal classification algorithm for the detection of abrupt jumps in CMOS nanoelectrode biosensor applications," in *Proceedings BSI*, pp. 129–132, 2012.

[348] F. Widdershoven (NXP Semiconductors), "Influence of particle charge on admittance change." Private communication.

[349] Wolfram Research, Inc., "Mathematica, Version 10.0."